ATMOSPHERIC HETEROGENEOUS REACTIONS OF CHLORINE AND BROMINE CONTAINING MOLECULES: A LABORATORY STUDY

THÈSE N^{O} 2403 (2001)

PRÉSENTÉE AU DÉPARTEMENT DE GÉNIE RURAL

ÉCOLE POLYTECHNIQUE FÉDÉRALE DE LAUSANNE

POUR L'OBTENTION DU GRADE DE DOCTEUR ÈS SCIENCES

PAR

Arnaud AGUZZI
Physicien diplômé de l'Université de Lausanne
de nationalités suisse et française et originaire de Porrentruy (JU)

acceptée sur proposition du jury:

Dr M. J. Rossi, directeur de thèse
Dr W. Harbich, rapporteur
Prof. P. Mirabel, rapporteur
Dr G. Moortgat, rapporteur
Prof. H. van den Bergh, rapporteur

Lausanne, EPFL
2001

A Hortense,
Evan et Hugo.

A mes parents.

Version Abrégée

Cette thèse est une étude en laboratoire de réactions hétérogènes impliquant des molécules réservoirs de brome et de chlore sur des surfaces de sels alcalins, qui sont caractéristiques de la couche limite marine ainsi que sur des surfaces de glace représentatives des conditions rencontrées dans la basse stratosphère. Le but est d'obtenir des valeurs fiables des coefficients de collage γ ainsi que la connaissance des mécanismes de réaction, en vue d'extrapolation aux conditions atmosphériques. Les expériences ont été effectuées dans un réacteur à écoulement de type cellule Knudsen (à parois teflonnées), couplé à un spectromètre de masse.

Les réactions de $BrONO_2$ avec les sels alcalins solides ont été étudiées à température ambiante. Les coefficients de collage γ_0 de $BrONO_2$ sur NaCl et KBr sont $\gamma_0 = 0.31 \pm 0.10$ et $\gamma_0 = 0.32 \pm 0.09$, respectivement. Sur NaCl, on observe BrCl, Br_2 et HCl comme produits, tandis que Br_2 et HBr sont observés sur KBr. HCl et HBr sont les produits de réactions sur NaCl et KBr, respectivement, avec la formation de HNO_3 qui résulte de l'hydrolyse de $BrONO_2$ avec les traces de H_2O condensée sur l'échantillon de sel. Avec NaCl, nous avons observé Br_2, formé par la décomposition hétérogène de $BrONO_2$ avec les échantillons solides de KBr. Les réactions d'échange d'halogène sont compétitives avec l'hydrolyse et la décomposition qui se produisent également sur les sels dit non–réactifs ($NaNO_3$, Na_2SO_4). Une grande vitesse de collage initiale ($0.2 < \gamma_0 < 0.4$) et un rendement de l'ordre de 50 % de Br_2 ont été observés sur les sels non–réactifs avec un bilan de masse complet pour Br_2.

Le système $ClONO_2$–sels a été réinvestigé. Nous avons conduit des expériences sur des sels aussi bien réactifs (NaCl, KBr) que non réactifs ($NaNO_3$, Na_2SO_4). L'hydrolyse de $ClONO_2$ n'a pas été observée, contrairement à la décomposition hétérogène qui se produit sur les sels non réactifs, avec un rendement de Cl_2 de (25 ± 5) %.

Des simulations numériques ont été effectuées en utilisant un modèle en boîte unidimensionnel pour évaluer l'impact de la chimie hétérogène sur les sels marins dans les conditions de la couche limite marine. La chimie du chlore et du brome est activée par les réactions hétérogènes se déroulant sur NaCl et KBr, considérés dans le modèle comme les uniques sources de chlore et de brome. Les simulations incluant la phase gaseuze et la chimie hétérogène du chlore ont révélé: 1) Dénitrification de la troposphère (conversion des NO_y en nitrates solides). 2) Accroissement du pouvoir oxydatif de la troposphère par libération d'atomes de chlore. Lorsque qu'en plus la chimie du brome est prise en compte dans le modèle, la réaction de recombinaison de NO_2 avec BrO amplifie la dénitrification de la troposphère via la formation de $BrONO_2$. Les calculs montrent que $BrONO_2$ est le réservoir bromé le plus important sous condition de $[NO_x]$ élevée, alors que sous condition de $[NO_x]$ faible, c'est HOBr qui est l'espèce réservoir la plus importante.

Le collage de HNO_3 sur la glace, des solutions solides d'acide sulfurique et des solutions ternaires (STS) a été étudié dans la gamme de température 180–211 K. Le coefficient de

collage γ diminue de 0.3 à 180 K à 0.06 à 211 K. La représentation d'Arrhenius montre deux régimes distincts. A basse température (180–190 K) γ a une valeur constante de 0.3, tandis que pour T>195 K, on trouve une énergie d'activation négative de $E_a = -7 \pm 1$ kcal/mol. A une température donnée, γ est indépendant de [HNO_3], ce qui confirme l'ordre 1 en [HNO_3] de la loi de vitesse. Les valeurs de γ pour HNO_3 sur les solutions solides de H_2SO_4/H_2O décroissent linéairement en fonction de la concentration de la solution de 0.20 (0.10) à 10 wt % H_2SO_4 à 0.05 (0.03) à 98 wt % H_2SO_4 à 180 K (200 K). La valeur de γ pour HNO_3 sur les STS de $H_2SO_4/HNO_3/H_2$ est égale à 0.10 ± 0.03 dans l'intervalle 185–195 K. Pour chaque température, la composition de l'interface a été préservée par un flux externe approprié de H_2O.

La vitesse d'hydrolyse de Br_2O sur les surfaces de glaces est grande dans la gamme de température 180–210 K. A une température donnée, la cinétique est apparemment de premier ordre en [Br_2O]. La dépendance négative observée en fonction de la température conduit à une valeur de l'énergie d'activation $E_a = -2.3 \pm 0.6$ kcal/mol. Ces observations suggèrent un mécanisme d'adsorption complexe, impliquant que l'interaction de Br_2O avec la glace n'est pas une réaction élémentaire.

L'hydrolyse de $BrONO_2$ a été mesurée sur des glaces "bulk" (B), condensées (C) et monocristalline (SC) dans la gamme de température de 180–210 K. Pour tous les types de glace, HOBr et Br_2O ont été détectés comme produits. Pour toutes les températures, la loi de vitesse est de premier ordre avec [$BrONO_2$], avec γ de l'ordre de 0.3 à 180 K. La dépendance négative de la cinétique de l'hydrolyse de $BrONO_2$ sur des glaces pures observée en fonction de la température conduit à une valeur de l'énergie d'activation E_a de -2.0 ± 0.2, -2.1 ± 0.2 et -6.6 ± 0.3 kcal/mol sur les échantillons (C), (B) et (SC), respectivement, mettant ainsi en évidence l'importance du type de substrat pour la cinétique. Doper les échantillons de glace avec HBr mène à la formation de Br_2, précédée de l'hydrolyse de $BrONO_2$. La représentation d'Arrhenius, dans ce cas, correspond à une énergie d'activation de $E_a = -1.2 \pm 0.2$ kcal/mol.

Nous avons étudié les propriétés structurales de la région proche de la surface de différents échantillons de glace dopés avec HX (X = Cl,Br). Essentiellement, nous nous sommes focalisés sur la dépendance temporelle de la concentration de surface [HX] en utilisant la réaction rapide de titration $XONO_2 + HX \rightarrow X_2 + HNO_3$. Ces expériences révèlent que HX est localisé dans une région d'épaisseur I bien définie, proche de la surface du substrat. Les molécules de HX composant l'interface sont immédiatement disponibles pour la réaction de titration, quelque soit le flux de $XONO_2$. Dans la gamme de température de 190–200 K, nous avons mesuré une valeur de $I^{HCl} = 43 \pm 16$, 250 ± 50 et 444 ± 120 pour les glaces (SC), (C) et (B), respectivement, et une valeur $I^{HBr} = 110 \pm 15$ nm sur une glace (C) à 205 K. Finalement, nous avons déterminé le coefficient de diffusion massique de HX (D_{HX}) en modélisant nos résultats selon les lois de Fick de la diffusion. Nous avons obtenu les valeurs de $D_{HCl} = 4.5 \cdot 10^{-15} - 1.0 \cdot 10^{-12}$ cm^2/s à 190 K et $D_{HBr} = (6.5 \pm 3.0) \cdot 10^{-15}$ cm^2/s à 205 K.

Abstract

This thesis deals with a laboratory study of heterogeneous reactions involving bromine and chlorine containing reservoir species on alkali salt substrates which are relevant to the marine boundary layer, and on ice substrates which are relevant to the lower stratosphere. The aim is to obtain reliable data on uptake coefficients γ and reaction mechanisms for the sake of extrapolation of results obtained in the laboratory to atmospheric conditions. The experiments have been performed in a Teflon coated Knudsen flow reactor equipped with a quadrupole mass spectrometer.

The reactions of $BrONO_2$ with solid alkali halides have been studied at ambient temperature. The initial uptake coefficients γ_0 of $BrONO_2$ on NaCl and KBr substrates are $\gamma_0 = 0.31 \pm 0.10$ and $\gamma_0 = 0.32 \pm 0.09$, respectively. For NaCl substrates BrCl, Br_2 and HCl and for KBr both Br_2 and HBr are observed as products. HCl and HBr result from the interaction of NaCl and KBr, respectively, with HNO_3 generated in the hydrolysis of $BrONO_2$ with H_2O condensed on the salt sample. Using NaCl we observed Br_2 which is formed from heterogeneous $BrONO_2$ decomposition occurring on solid KBr samples. Halogen exchange reactions are competing with hydrolysis and decomposition which also take place on non–reactive salts ($NaNO_3$, Na_2SO_4). A high rate of initial uptake ($0.2 \leq \gamma_0 \leq 0.4$) and a Br_2 yield on the order of 50 % are observed on non–reactive salts with a closed mass balance for Br_2.

The $ClONO_2$–salt system has been reinvestigated. Experiments on NaCl, KBr (reactive salts) and on $NaNO_3$ and Na_2SO_4 (non–reactive salts) have been performed. The hydrolysis of $ClONO_2$ was not observable in contrast to heterogeneous decomposition which occurred on non–reactive salts with a Cl_2 yield of (25 ± 5) %.

Calculations have been performed using a 0–D box model in order to observe the effects of heterogeneous chemistry on sea salt in the marine boundary layer. Chlorine and bromine chemistry is activated by heterogeneous reactions occurring on NaCl and KBr which are the sole sources of chlorine and bromine in the model. Simulations performed with chlorine heterogeneous chemistry and gas phase chemistry indicate: 1) Denitrification of the troposphere (NO_y converted to solid nitrates). 2) Increase of the oxidative capacity of the troposphere by the release of Cl atoms. When bromine chemistry is added to the model, the recombination reaction of NO_2 with BrO leads to an increase of tropospheric denitrification through formation of $BrONO_2$. Calculations show that at high $[NO_x]$, the most important bromine reservoir is $BrONO_2$, while at low $[NO_x]$ HOBr is the most important bromine reservoir.

The uptake of HNO_3 on ice, solid sulfuric acid solutions and solid ternary solutions

(STS) has been investigated at 180 to 211 K. The uptake coefficient γ decreases from 0.30 at 180 K to 0.06 at 211 K. The Arrhenius representation shows two distinct regimes. The first at low temperatures (180–190 K) shows a constant value γ of 0.3, whereas the second regime at $T > 195$ K corresponds to an activation energy of $E_a = -7 \pm 1$ kcal/mol. At a fixed temperature, γ is independent of $[HNO_3]$ thus confirming a rate law first order in $[HNO_3]$. The γ values of HNO_3 on H_2SO_4/H_2O solid solutions linearly decreases from 0.20 (0.10) at 10 wt % H_2SO_4 to 0.05 (0.03) at 98 wt % H_2SO_4 at 180 K (200 K). The γ values of HNO_3 with STS of $H_2SO_4/HNO_3/H_2O$ is equal to 0.10 ± 0.03 in the temperature range 185–195 K at conditions where the composition of the interface was held constant at the given temperature by adding an external flow of H_2O.

Br_2O hydrolysis on ice surfaces occurs rapidly in the chosen temperature range of 180 to 210 K. At a fixed temperature the uptake kinetics follow an apparent first order rate law in $[Br_2O]$. The observed negative temperature dependence leads to an activation energy E_a for heterogeneous hydrolysis of -2.3 ± 0.6 kcal/mol. These facts point towards a complex reaction mechanism implying that the interaction of Br_2O with ice is not an elementary reaction.

$BrONO_2$ hydrolysis has been measured on bulk (B), condensed (C) and single crystal (SC) ice in the temperature range 180–210 K. On all types of ice, HOBr and Br_2O are observed as products. At a fixed temperature the rate law is first order in $[BrONO_2]$ with $\gamma \approx 0.3$ at 180 K. The observed negative temperature dependence leads to an activation energy E_a for the hydrolysis of $BrONO_2$ on pure ice of -2.0 ± 0.2, -2.1 ± 0.2 and -6.6 ± 0.3 kcal/mol on (C), (B) and (SC) ice, respectively, pointing towards different kinetics of $BrONO_2$ on these different types of ice. Doping the ice samples with HBr leads to the formation of Br_2, preceded by $BrONO_2$ hydrolysis. The Arrhenius representation corresponds to an activation energy of $E_a = -1.2 \pm 0.2$ kcal/mol.

We investigated the structural properties of the near–surface region of various types of HX (X = Cl or Br) doped ice. Basically, we studied the time dependent [HX] in the interface region using the fast reaction titration $XONO_2 + HX \rightarrow X_2 + HNO_3$. These experiments reveal that HX is located near the surface of the substrate in a well defined region of thickness I. The HX molecules composing the interface are immediately available for the titration reaction, whatever the flow of $XONO_2$. In the temperature range 190–200 K, we measured a value of $I^{HCl} = 43 \pm 16$, 250 ± 50 and 444 ± 120 nm for (SC), (C) and (B) ices, respectively and $I^{HBr} = 110 \pm 15$ nm on (C) ice at 205 K. Finally, we assessed the bulk diffusion coefficient for HX, D_{HX} by modeling our results according to Fick's laws of diffusion. We obtained values of $D_{HCl} = 4.5 \cdot 10^{-15} - 1.0 \cdot 10^{-12}$ cm^2/s at 190 K and $D_{HBr} = (6.5 \pm 3.0) \cdot 10^{-15}$ cm^2/s at 205 K.

Contents

Chapter 1

Introduction

The earth's atmosphere is composed of several layers as depicted in Figure 1.1. We are in contact with the boundary layer of the troposphere where most of the weather occurs, such as rain, snow and clouds. The troposphere extends from the earth surface to about 8 to 15 km (dependent upon the time of year and latitude). The lower 2 km is referred to as the planetary boundary layer (PBL) in which of course human activity deposits most of its waste. Above the troposphere is the stratosphere, an important region in which effects such as the ozone hole events occur. The narrow region between these two parts of the atmosphere is called the tropopause. Above the stratosphere is the mesosphere from ~ 50 to ~ 85 km, separated from the stratosphere by the mesopause. Above the mesosphere, one finds the thermosphere.

The composition of the atmosphere is dominated by molecular nitrogen and oxygen as displayed in Table 1.1. Many other compounds are present in trace amounts such as methane (CH_4) and ozone (O_3).

Table 1.1: Composition of the atmosphere for dry air at ground level in continental areas.

Gas	Formula	Percent by volume
Nitrogen	N_2	78.08
Oxygen	O_2	20.94
Argon	Ar	0.934
Carbon Dioxide	CO_2	0.033
Neon	Ne	0.00182
Helium	He	0.00052
Methane	CH_4	0.00015
Ozone	O_3	0.000001–0.000004

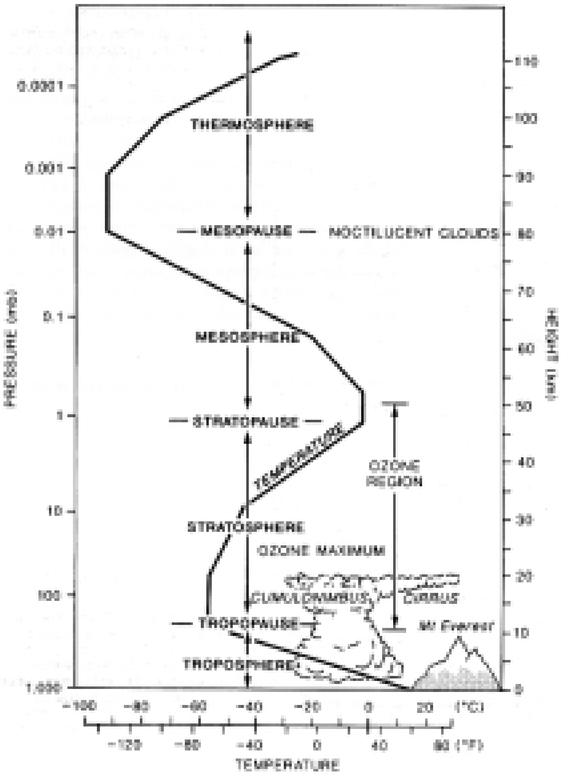

Figure 1.1: Typical variation of temperature with altitude at mid–latitudes in the different regions of the atmosphere.

Ozone, naturally produced in trace amounts in the atmosphere, consists of three atoms of oxygen bonded together. It is found in both the stratosphere (about 90 % of the total atmospheric loading) and the troposphere (about 10 %). Ozone is an important greenhouse gas in the troposphere. In the stratosphere, ozone forms a protective layer shielding the Earth from ultraviolet radiation and subsequent harmful health effects on humans and the environment. In the troposphere, oxygen molecules and ozone react with appropriate precursor gases by oxidization and lead to smog formation.

During the last two centuries, human activities have changed the chemical balance, which may lead to significant global climate change. The manufactured thus anthropogenic chlorofluorocarbons (CFC's), invented in 1928, are known today for their dramatic effects on the stratospheric ozone layer. They are involved in powerful catalytic cycles that destroy ozone and lead to the so–called "ozone hole" over the poles (Sections 1.4 and 1.5).

Other dramatic examples of Man's influence on the atmosphere is the increase of carbon dioxide (CO_2) and nitrogen oxides ($NO_x = NO + NO_2$) due mostly to fossil fuel burning. CO_2 concentration has passed from 280 to 360 ppm, from the start of the

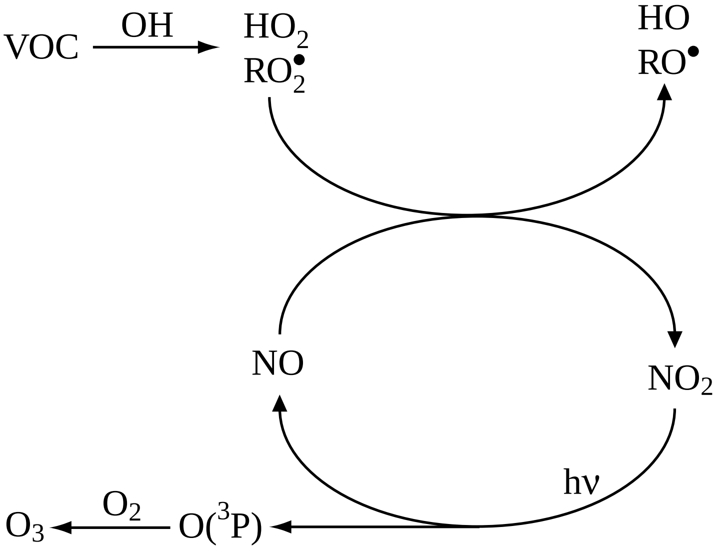

Figure 1.2: Scheme of the reactions involved in ozone formation in the presence of volatile organic compounds (VOC) and nitrogen oxides (NO_x).

industrial revolution (1850) to now. The CO_2 levels are important because it contributes to the greenhouse effect leading to global warming. NO_x plays an important role in both polluted and unpolluted atmospheres because it contributes to the oxidation capacity of the troposphere (Sections 1.1 and 1.2).

1.1 Tropospheric Ozone

Tropospheric ozone is known to be formed via NO_2 photolysis (reactions (1.1) and (1.2)) as suggested for the first time by Blacet [1952].

$$NO_2 + h\nu(\lambda \lesssim 420nm) \rightarrow NO + O(^3P) \tag{1.1}$$

$$O(^3P) + O_2 \xrightarrow{M} O_3 \tag{1.2}$$

High levels of NO_x (NO_2 + NO) are clearly associated with anthropogenic emissions, but there are also small contributions to emission owing to natural processes. Small concentrations of O_3 can be formed by the simultaneously presence of volatile organic compounds (VOC) and nitrogen oxides (NO_x) as displayed in Figure 1.2. The tropospheric VOC degradation by OH radicals leads to the formation of the $RO_2^\bullet$ which reacts with NO to form NO_2. Ozone is then formed via the photolysis of NO_2 according to reactions (1.1) and (1.2).

Finally, periodic intrusions of stratospheric air provide an additional source of tropospheric ozone. Due to its lifetime, 1–2 days in the PBL, ozone is an active player in both day and night tropospheric chemistry.

Tropospheric ozone has detrimental impacts on human health as well as on the productivity of both managed and natural vegetation. It also serves as an important mediator for the chemical transformations of a variety of other pollutants.

1.2 Oxidation Capacity of the Troposphere

The concentrations of the principal oxidants present in the atmosphere, such as OH radical, NO_3, O_3 and H_2O_2 greatly influence the oxidation capacity (also called oxidation efficiency or oxidation power) of the troposphere. These oxidant species interact with each other and with the trace gases emitted at the earth's surface and determine the lifetime of the atmospheric compounds. The major oxidant of the troposphere is the OH–radical which is produced by ozone photolysis [Levy, 1971; Thompson, 1992]. The absorption of solar UV radiation of wavenlengths shorter than 325 nm by O_3 generates molecular oxygen (O_2) and electronically excited oxygen atoms ($O(^1D)$):

$$O_3 + h\nu(\lambda \lesssim 325nm) \rightarrow O_2 + O(^1D) \tag{1.3}$$

which possess enough energy to react with H_2O to produce two OH–radicals:

$$O(^1D) + H_2O \rightarrow 2OH \tag{1.4}$$

For each ozone molecule destroyed, two OH radicals are formed. Other sources for OH–radicals may be the photolysis of nitrous acid (HONO) [Finlayson–Pitts and Pitts, 1986] or the photolysis of formaldehyde (CH_2O) according to the following reaction scheme:

$$CH_2O + h\nu \rightarrow H + HCO \tag{1.5}$$

$$H + O_2 \rightarrow HO_2 \tag{1.6}$$

$$HO_2 + NO \rightarrow OH + NO_2 \tag{1.7}$$

Reactions with OH initiate the oxidation and removal of most trace gas from the atmosphere. The OH–radical is very reactive towards most of the hydrocarbons (RH) and undergoes hydrogen abstraction reations which initiate RH oxidation according to:

$$RH + OH \rightarrow R + H_2O \tag{1.8}$$

Reaction (1.8) is followed by additional reactions leading to the oxidation of the hydrocarbon. In Appendix A hydrocarbon oxidation using methane (CH_4) as an example is described for polluted (NO_x rich environment) and unpolluted (NO_x poor environment) areas.

Chlorine atoms may also play an important role in tropospheric chemistry because they also react very efficiently with RH according to the following initiation reaction to oxidation:

$$RH + Cl^{\bullet} \rightarrow R + HCl \tag{1.9}$$

Reaction (1.9) is in general much faster than reaction (1.8) depending on the hydrocarbon. As we will see later (Section 1.8.1), Cl atoms may come from heterogeneous reactions on sea–salt aerosols of chlorine reservoir molecules. An increase of halogen concentration may influence the oxidation capacity in the troposphere and may contribute to the tropospheric ozone loss observed during Arctic sunrise.

1.3 Sudden Tropospheric Polar Ozone Loss

First noted in 1985, this event occurs at the Arctic sunrise, during March and April, at which tropospheric ozone levels fall from 30–40 ppb to negligible concentrations [Barrie, 1988; Bottenheim, 1990]. During the ozone loss period, ozone concentrations show a strong anti–correlation to the concentration of bromine compounds in the boundary layer. Therefore, bromine chemistry appears to be the likely cause of the effect [Barrie, 1988; Bottenheim, 1990; Impey, 1997 and 1999]. Bromine atoms can be produced by photolysis of Br_2 and BrCl and react with ozone to form bromine monoxyde and molecular oxygen according to:

$$Br^{\bullet} + O_3 \rightarrow BrO + O_2 \tag{1.10}$$

During the Arctic winter the turbulent seas produce a large number of sea salt particles which are deposited all over the ice pack. It is thought that the onset of sunlight can trigger the release of bromine from these built–up deposits [McConnell, 1992]. In Section 1.8.1 the activation of bromine from sea salt aerosol is discussed.

While the phenomenon of sudden tropospheric Arctic loss was discovered at about the same time as the Antarctic stratospheric ozone hole, it has received little media interest and thus investigation, presumably as it poses no obvious threat to life. Nevertheless, the study of the Arctic tropospheric ozone loss has revealed some interesting

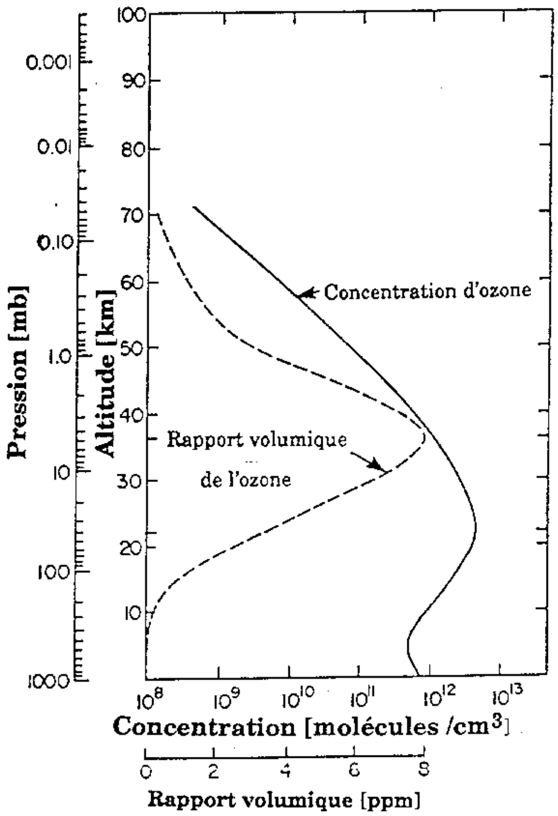

Figure 1.3: Typical ozone concentration profile as a function of altitude at mid–latitudes (yearly average).

chemistry in which heterogeneous interactions play a key role in tropospheric ozone depletion.

1.4 Stratospheric Ozone Loss

As displayed in Figure 1.3 the relative ozone concentration begins to increase at about 10 km in altitude, reaches a relative maximum of 8 ppm around 30 km to finally returns to a low level (0.2–0.3 ppm) at about 70 km. In absolute numbers the maximum of its stratospheric concentration occurs around 22 km with a value of about $5 \cdot 10^{12}$ molecule/cm^3 (Figure 1.3).

In the stratosphere, the ozone concentration is maintained by the equilibrium of four basic equations forming the well known Chapman mechanism evoked in the 1930s (reactions (1.11) to (1.14)).

$$
\begin{aligned}
O_2 + h\nu &\rightarrow 2O^{\bullet} && (1.11)\\
O^{\bullet} + O_2 &\xrightarrow{M} O_3 && (1.12)\\
O_3 + h\nu &\rightarrow O_2 + O^{\bullet} && (1.13)\\
O_3 + O^{\bullet} &\rightarrow 2O_2 && (1.14)
\end{aligned}
$$

The first step of the Chapman mechanism (reaction (1.11)) consists of the photodissociation of molecular oxygen (O_2) by ultraviolet (UV) photons of $\lambda \leq 220$ nm encountered at high altitude. The results of this step is the production of two oxygen atoms which interact with O_2 to produce O_3 (reaction (1.12)). The third body M in reaction (1.12) carries away the excess thermal energy resulting from the recombination reaction (1.12) leading to O_3 which creates a temperature inversion above the tropopause (see Figure 1.1) which is limiting the exchange of air masses between the stratosphere and the troposphere.

Conversely, O_3 strongly absorbs radiation in the wavelength range 240 to 320 nm and photodissociates to form one oxygen molecule and one oxygen atom (reaction (1.13)); most importantly, O_3 may react with an oxygen atom to form two molecules of oxygen (reaction (1.14)).

However, the Chapman mechanism is not sufficient to account quantitatively for the O_3 concentration encountered in the natural stratosphere. In the 1960s, the assessed O_3 budget was incorrect as it was overestimated by the Chapman theory by a factor of two. Hampston [1964] suggested in 1964 that the reactions of hydrogen oxides with O_3 would result in a catalytic cycle that would enhance O_3 loss in the Chapman model. Crutzen showed in 1971 that catalytic cycles produced by the reactions of nitrogen oxides with O_3 are important in stratospheric chemistry [Crutzen, 1971]. In 1974, work performed by Molina and Rowland [1974] elucidated the effect of chlorine containing compounds on that chemistry. The catalytic cycle added to the Chapman model is as follows:

$$
\begin{aligned}
X^{\bullet} + O_3 &\rightarrow XO^{\bullet} + O_2 && (1.15)\\
XO^{\bullet} + O^{\bullet} &\rightarrow X^{\bullet} + O_2 && (1.16)
\end{aligned}
$$

where $X^{\bullet}$ is a free radical catalyst representing $H^{\bullet}$, $OH^{\bullet}$, $NO^{\bullet}$, $Cl^{\bullet}$, $Br^{\bullet}$ or $I^{\bullet}$. This cycle results in the following net reaction:

$$2O_3 \rightarrow 3O_2 \qquad (1.17)$$

The catalyst $X^\bullet$ is regenerated in reaction (1.16) which explains that this reaction sequence corresponds to a chain reaction. Termination steps exist that prevent total stratospheric O_3 depletion. Examples of termination steps are the following:

$$OH^\bullet + NO_2^\bullet \xrightarrow{M} HNO_3 \tag{1.18}$$

$$Cl^\bullet + HO_2^\bullet \rightarrow HCl + O_2 \tag{1.19}$$

Chlorofluorocarbons and Stratospheric Chemistry

During the 1970s, a series of measurements performed by Lovelock [1974] threw new light on the atmospheric fate of man–made compounds: the Chlorofluorocarbons, better known as CFC's. Their high chemical stability allows them to diffuse through the troposphere where they are emitted by men, and reach the stratosphere where they can be photolysed. The photodissociation of CFC's results in the release of a chlorine atom (reaction (1.20) as example). As shown by Molina and Rowland [1974], the chlorine atoms released react with O_3 resulting in $ClO^\bullet$. It will react with O atoms in the background stratosphere and will initiate a catalytic cycle similar to the one described above. $Cl^\bullet$ atoms are very efficient ozone scavengers: one molecule of Cl can potentially destroy between 10^4 and 10^5 molecules of ozone.

$$CF_2Cl_2 + h\nu \rightarrow {}^\bullet CF_2Cl + Cl^\bullet \tag{1.20}$$

$$Cl^\bullet + O_3 \rightarrow ClO^\bullet + O_2 \tag{1.21}$$

$$ClO^\bullet + O^\bullet \rightarrow Cl^\bullet + O_2 \tag{1.22}$$

The cycle describes by reactions (1.20) to (1.22) has the following termination reactions:

$$Cl^\bullet + CH_4 \rightarrow HCl + CH_3 \tag{1.23}$$

$$ClO^\bullet + NO_2^\bullet \xrightarrow{M} ClONO_2 \tag{1.24}$$

The atmospheric liffetime of the CFC's are in the range 50 to 200 years. Since the 1940's, an immense chlorine reservoir has been formed in the atmosphere by extensive production and concomitant emission of CFC's, and all this chlorine is essentially available for ozone depletion. Halons, an other man–made compounds, are similar to CFC's but contain bromine, which will provide a source of stratospheric bromine. Potential ozone destruction by bromine atoms is a hundred times higher than that of chlorine atoms on a per atom basis.

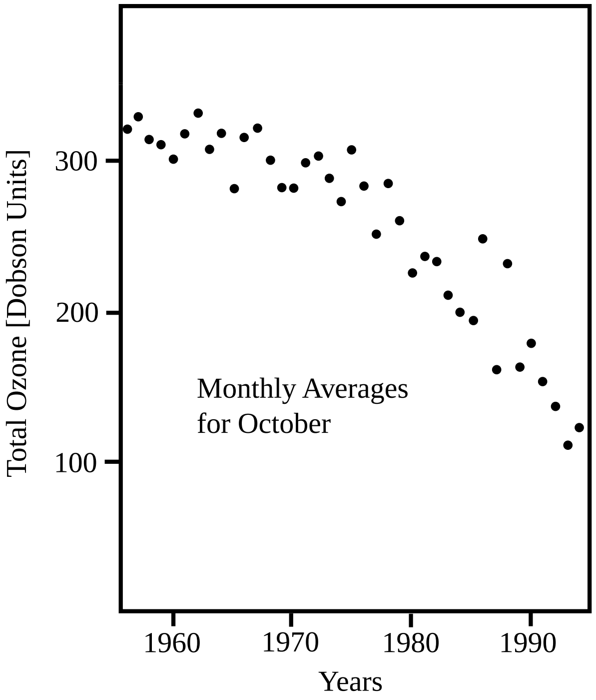

Figure 1.4: October mean column ozone over Halley Bay, Antarctica from 1956 to 1994 [Jones, 1995].

1.5 The Antarctic Ozone Hole

In 1985, Farman *et al.* of the British Antarctic Survey showed that ozone was disappearing over Antarctica during this southern hemisphere spring period [Farman, 1985]. The springtime ozone levels decreased to unprecedented levels, with each succeeding year being worse than the year before (Figure 1.4). This landmark paper set in motion a series of intensive field campaigns, analysis efforts, satellite investigations, and laboratory studies that have nearly fully characterized the processes that control Antarctic ozone. These large antarctic ozone losses are now better known as "The Antarctic Ozone Hole".

Using a Dobson spectrometer based at Halley Bay the British Antarctic Survey had measured a steady decrease of stratospheric ozone levels in spring since the 1950's. In the mid–80's this trend had reached such an extent that their measurements showed a dramatic reduction in the local concentration of stratospheric ozone in the month of October. Certainly this was a regional effect and in that respect had to be connected with the specific meteorological conditions encountered over the Antarctic and in particular the yearly formation of a vortex that isolates the high altitude air mass from the global stratosphere during most of the polar winter. This feature alone cannot account for the trend observed in the ozone loss. It was tempting to correlate this negative evolution in the ozone concentration with the occurrence of CFC's. Starting from there it was possible to come up with a new mechanism: the very low temperatures achieved (193 K) in the Antarctic vortex causes most of the water vapor present to condense into ice particles which together happen to form what is called Polar Stratospheric Clouds (PSC's, see Section 1.6.2). The simultaneous occurrence of PSC's and local ozone minima inside the vortex led to the hypothesis that heterogeneous chemistry could actually play a significant role within this gigantic atmospheric reactor (the size of a continent).

What happens is that the chlorine reservoir molecules such as HCl and $ClONO_2$ are chemically converted to species such as HOCl or Cl_2 (reactions (1.25) and (1.26)) through their interactions with the surface of the ice particles [Molina, 1987].

$$ClONO_2 + H_2O(ice) \rightarrow HOCl + HNO_3 \tag{1.25}$$

$$ClONO_2 + HCl(ads) \rightarrow Cl_2 + HNO_3 \tag{1.26}$$

To top it all denitrification of the air mass imprisoned in the vortex also takes place through the adsorption of HNO_3 onto the PSC's. A longer and more intense solar radiation is required to initiate the photolysis of HNO_3 that will return the necessary $NO_2^\bullet$ needed in the chain termination reaction (1.24).

Again the Antarctic ozone hole is an extreme yet regional phenomenon due essentially to the very peculiar meteorological conditions that prevail above this polar region. But the community of atmospheric scientists learned a great deal on the coupling of chemical and dynamical atmospheric processes from its regular occurrence. The two main lessons were on the one hand the assertion of the important role played by halogenated trace gases in the balance of stratospheric ozone, and on the other hand the emergence of a type of chemistry until then neglected in the atmospheric context, namely heterogeneous chemistry.

For the ozone depletion problem is now acknowledged as a global one: in the mid–latitudes (30 to 70°) measurements show an average reduction of approximately 5 % in the ozone concentration over the past two decades.

1.5.1 Catalytic Loss of Stratospheric Ozone

The principal loss processes for ozone involve chlorine oxide (ClO) and bromine oxide (BrO). We will present the catalytic reactions associated with both compounds.

ClO–ClO Reaction

Chlorine monoxide, $ClO^\bullet$, the most abundant chlorine containing species forms the dimer Cl_2O_2 which is stored all through the winter. Come spring with the first sunlight and it is readily photolysed to form atomic chlorine. The amount of active chlorine available for catalytic ozone destruction becomes consequently quite high.

$$
\begin{aligned}
ClO^\bullet + ClO^\bullet &\xrightarrow{M} Cl_2O_2 && (1.27)\\
Cl_2O_2 + h\nu &\rightarrow Cl^\bullet + ClOO^\bullet && (1.28)\\
ClOO^\bullet &\xrightarrow{M} Cl^\bullet + O_2 && (1.29)\\
2[Cl^\bullet + O_3 &\rightarrow ClO^\bullet + O_2] && (1.30)
\end{aligned}
$$

The net reaction of the above cycle (reactions (1.27) to (1.30)) is the following reaction:

$$2O_3 + h\nu \rightarrow 3O_2 \qquad (1.31)$$

ClO–BrO Reaction

A second reaction of nearly comparable effect to the ClO–ClO reaction is the BrO–ClO reaction [McElroy, 1986]. This catalytic cycle consists of the following set of reactions:

$$
\begin{aligned}
ClO^\bullet + BrO^\bullet &\rightarrow Br^\bullet + OClO && (1.32)\\
&\rightarrow Br^\bullet + ClOO && (1.33)\\
&\rightarrow BrCl + O_2 && (1.34)\\
BrCl + h\nu &\rightarrow Cl^\bullet + Br^\bullet && (1.35)\\
Br^\bullet + O_3 &\rightarrow BrO^\bullet + O_2 && (1.36)\\
Cl^\bullet + O_3 &\rightarrow ClO^\bullet + O_2 && (1.37)
\end{aligned}
$$

This reaction scheme leads to the same net reaction as in the ClO–ClO catalytic cycle (reaction (1.31)).

As in the ClO–ClO reaction, this last reaction scheme does not require free oxygen atoms. Anderson *et al.* [1989b] calculated that this reaction accounts for a loss rate that is about half that of the ClO–ClO reaction. Similar ozone loss rates are calculated by Salawitch *et al.* [1993] for the northern polar winter of 1992.

ClO–O Reaction

A third loss process is the conventional catalytic loss process of ClO with free oxygen atoms via the following two reactions:

$$ClO^{\bullet} + O^{\bullet} \rightarrow Cl^{\bullet} + O_2 \tag{1.38}$$

$$Cl^{\bullet} + O_3 \rightarrow ClO^{\bullet} + O_2 \tag{1.39}$$

The net reaction of the above cycle (reactions (1.38) and (1.39)) is the following reaction:

$$O^{\bullet} + O_3 \rightarrow 2O_2 \tag{1.40}$$

Salawitch *et al.* [1993] calculated that this process accounts for less than 15 % of the observed ozone loss. Anderson *et al.* [1989a] indicate that this last catalytic cycle is much less important in the polar regions than the ClO–ClO and ClO–BrO reaction schemes.

The termolecular self–reaction of ClO (reaction (1.27)) and the resulting cycle (reactions (1.28) to (1.30)) is believed to be responsible for approximately 75 % of the ozone destruction in the 13 to 19 km region in the Antarctic ozone hole [Anderson, 1991]. The cycle involving ClO + O (reactions (1.38) to (1.40)) account for approximately 5 % and the remainder is due to the ClO–BrO interaction (reactions (1.32) to (1.37)) [Anderson, 1991].

1.6 Particles in the Atmosphere

Particulate matter in the atmosphere may be solid or liquid and of a diameter varying roughly between 2 nm and 100 μm. These aerosols undergo Brownian diffusion and do not settle via gravity at a significant rate. The larger particles, however, fall quickly. Aerosols may be directly emitted into the atmosphere (primary particles) or may be formed by different chemical processes (secondary particles).

Tropospheric particles include the following:

- **Sea salt particles**: see Section 1.6.1.
- **Sulfate aerosols**: primarily produced from the nucleation of sulfuric acid, act as cloud condensation nuclei [Pandis, 1995].
- **Water droplets**: allow a wide range of aqueous chemistry, rapid uptake of sulfuric and nitric acids leading to acid rains.
- **Soot**: generally produced from combustion of fossil fuels (vehicle emissions, biomass burning), direct injection by aircraft emissions are of particular concern

[Lary, 1999], ability to convert NO_2 to HONO [Kalberer, 1999; Al–Abadleh, 2000; Alcala–Jornod, 2000; Stadler, 2000].

- **Dust**: produced by wind action upon dry land, rich in calcium, aluminium, iron and silicon [Pandis, 1995], provide alkaline surfaces on which SO_2 and NO_x can be adsorbed [Dentener, 1996; Herring, 1996].

Stratospheric particles comprise the following:

- **Polar stratospheric clouds (PSC)**: see Section 1.6.2.
- **Sulfate aerosols**: produced analogously to tropospheric sulfate aerosols, provide surfaces able to regenerate halogens and thus enable global stratospheric ozone loss.

1.6.1 Sea–Salt Aerosols

Marine aerosol present in the troposphere consists of small sulfate particles and larger sea–salt aerosol particles containing chloride and bromide. Table 1.2 shows the composition of sea–alt aerosol particles based on the assumption that the aerosol composition is identical to that of seawater [Miller, 1972]. This condition is mostly verified in a "clean atmosphere".

Table 1.2: Composition of sea–salt particles in clean atmospheres.

Species	Percent by weight	Species	Percent by weight
Cl^-	55.04	Na^+	30.61
SO_4^{2-}	7.68	Mg^{2+}	3.69
Ca^{2+}	1.16	K^+	1.1
Br^-	0.19	Carbon	0.0035 – 0.0087
Al^{3+}	0.00046 – 0.0055	Ba^{2+}	0.00014
I^-	0.00014	Fe^{3+}	0.00005 – 0.0005
NO_3^-	0.000003 – 0.002		

Data taken from Miller *et al.* [1972] based upon the composition of marine water.

Sea–salt aerosols are produced by the wave action of the sea during which water drops with a wide range of sizes, from less than 0.1 μm to more than 100 μm are whipped up. As evaporation of water occurs in the droplets, the salt becomes more and more concentrated. If the relative humidity (rh) is below the deliquescence point of NaCl (∼ 75 % rh) complete evaporation may occur resulting in solid salt particles. The maximum number concentration of sea–salt aerosol is found at low altitude in coastal regions, and concentrations of Cl^- in the free troposphere are typically between a fraction and two orders of magnitude smaller than those in the marine boundary layer [Graedel and Keene, 1995].

1.6.2 Polar Stratospheric Cloud Particles

One can distinguish between two classes of PSC's: type I and II, with the first split into two different kinds. Type Ia PSC's are believed to consist of nitric acid trihydrate (NAT) solid particles, because NAT is the more stable binary form of HNO_3/H_2O solutions under stratospheric conditions [Hanson and Mauersberger, 1988]. Type Ib PSC's may be supercooled ternary solution droplets ($H_2SO_4/HNO_3/H_2O$) generated from sulfate aerosols [Carslaw, 1994], while type II very likely consist of ice crystals [Turco, 1989] that form when the temperature falls below 188 K (– 85 °C). Type II PSC's are relatively large, with a diameter of at least 10 μm, while type I PSC's are much smaller than type II, with a particle diameter on the order of 0.1 to 1 μm. However, in the lower stratosphere the chemical composition of PSC particles is still not well known [Schreiner, 1999].

1.7 Source of Reactive Halogen Species in the Atmosphere

The sources of halogen compounds have been a topic of intense discussion for a long time. Today, even if all is not well known, the following main sources have been identified.

1.7.1 Tropospheric Sources

Photolytically unstable halocarbons can act as precursors of halogen atoms in the troposphere. Contrary to the mechanisms in the stratosphere, only compounds photolyzing at a wavelength above 290 nm will release reactive halogen species in the troposphere. Man–made CFC's have a long lifetime in the boundary layer, therefore they are not a reactive halogen source in the troposphere. Less stable species, such as CH_3Cl or CH_2Cl_2 emitted by algae in the oceans, are an important source of chlorine atoms in the boundary layer [Graedel and Keene, 1995].

The main source of reactive bromine are the organic compounds CH_3Br and $CHBr_3$ that originate from both anthropogenic and natural sources [Khalil, 1993; Lary, 1996]. Oceans provide an important amount of these species. CH_3Br is probably the most abundant bromine reservoir [Khalil, 1993; Lary, 1996] whose anthropogenic sources are due to biomass burning and its use as an agricultural fumigant. Recently Lee–Taylor and Holland [2000] proposed the decomposition of litter by wood–rotting fungi as a potential source of CH_3Br. Table 1.3 shows the most important chlorine and bromine atoms source in the troposphere.

Table 1.3: Organohalogen compound concentrations in the boundary layer and the respective photolytic lifetimes.

Gas	Formula	Concentration$^{(a)}$	Lifetime$^{(b)}$
Methyl Chloride	CH_3Cl	$\sim$ 600 ppt	$\sim$ 1.5 years
Dichloromethane	CH_2Cl_2	$\sim$ 30 ppt	200 days
Methyl Bromide	CH_3Br	10–15 ppt	1.3 years
Bromoform	$CHBr_3$	0.2–0.3 ppt	20 Days

(a) Kaye, 1994. (b) WMO Report, 1995.

Yokouchi *et al.* [2000] and Rhew *et al.* [2000] identify high emission rates of methyl halides from terrestrial–coastal ecosystems. Rhew *et al.* [2000] show that both methyl halides, CH_3Br and CH_3Cl, are released to the atmosphere from all vegetation zones of two coastal salt marshes in southern California (Mission Bay marsh and San Dieguito lagoon). They have measured very large fluxes of CH_3Br and CH_3Cl in a strong correlation with an average molar ratio of roughly 1:20, respectively. These measurements suggest that salt marshes and their vegetation, even if they contribute less than 1 % of the global surface area, may produce roughly 10 % of the total fluxes of atmospheric CH_3Br and CH_3Cl. The work performed by Yokouchi *et al.* [2000] report evidence of significant CH_3Cl emission from warm coastal land, particularly from tropical islands. High levels of methyl chloride were correlated with levels of α–pinene (a compound which comes from terrestrial plants), suggesting that the source of CH_3Cl is terrestrial. Both Yokouchi *et al.* and Rhew *et al.* invoke biological reactions to produce methyl halides.

Oxidation-reduction reactions taking place in an inorganic medium may be sources of methyl halides (and other organic halogens) as described by Keppler *et al.* [2000]. They find that, in soils and sediments, halide ions can be alkylated during the oxidation of organic matter such as Fe(III). When the available halide ion is chloride, bromide or iodide, the reaction products are CH_3Cl, CH_3Br or CH_3I, respectively.

1.7.2 Stratospheric Sources

The chlorine budget has been the first and the most thoroughly investigated and is now well estimated [Prather and Watson, 1990]. Over 80 % of chlorine originates from the man–made CFC's and HCF's (hydrochlorofluorocabons). The other 20 % come from natural sources, such as CH_3Cl emitted from the oceans reaching the stratosphere because of its long tropospheric lifetime.

There are no known sources of bromine in the stratosphere. CH_3Br, $CBrF_3$ and $CBrClF_2$ are the three main anthropogenic compounds that can reach the stratosphere due to their long lifetime in the troposphere [Lary, 1996].

Emission of halocarbons is one of the major source of reactive halogen in the atmosphere. But as we will see in the following Section, heterogeneous reactions on sea salt aerosols in the marine boundary layer or PSC particles in the lower stratosphere are important sources of halogen release mechanisms.

1.8 The Importance of Heterogeneous Chemistry in the Atmosphere

The importance of heterogeneous chemistry in the atmosphere has been clearly demonstrated. In the stratosphere, heterogeneous reactions on PSC particles convert chlorine containing reservoir species into photolyzed active chlorine species which lead to ozone depletion [Solomon, 1988]. In the troposphere, heterogeneous processes taking place on dry particles (sea salt aerosols) or liquid droplets (deliquescent sea salt aerosols) act as reactive halogen sources [Finlayson–Pitts and Johnson, 1988; Fenter, 1996, Abbatt, 1998].

1.8.1 Activation of Halogen from Sea Salt Aerosols

As discussed in Section 1.6.1, sea–salt aerosols (or salt covered surfaces) represent a large reservoir of halogens in the atmosphere. Several heterogeneous processes releasing reactive halogen species have been proposed to date.

The reaction of nitrogen oxides on NaX or KX (X = Cl, Br) is known to release XNO and XNO_2 [Finlayson–Pitts and Johnson, 1988; Benhke, 1992 and 1993; Fenter, 1996] via the following reactions (Figure 1.5.a):

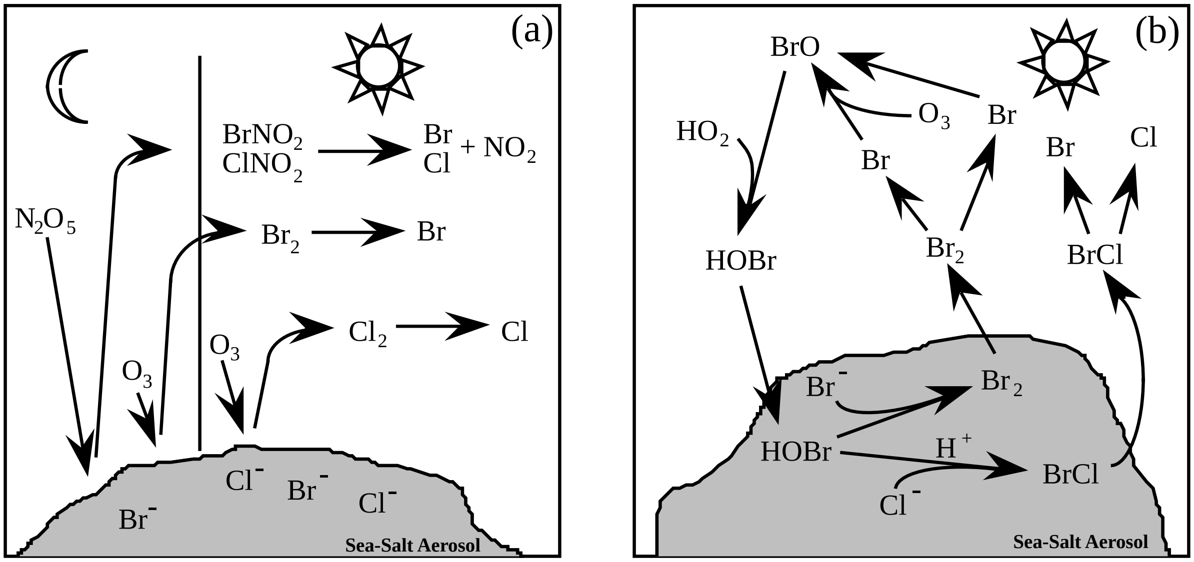

Figure 1.5: (a) Heterogeneous processes on sea–salt aerosols involving N_2O_5 and O_3 liberating active halogen species in the troposphere. (b) Heterogeneous processes on sea–salt aerosols proposed by Vogt *et al.* [1996].

$$N_2O_5 + NaX \rightarrow XNO_2 + NaNO_3 \quad (1.41)$$

$$2NO_2 + NaX \rightarrow XNO + NaNO_3 \quad (1.42)$$

XNO and XNO_2, the primary product of these reactions, are photolyzed rapidly in the early morning hours [Wayne, 1995] and release halogen atoms. This mechanism would be most effective in relatively polluted air with high NO_x concentrations.

Oum *et al.* [1998a/b] proposed the direct reaction of O_3 on sea–salt aerosol as a source of active halogen. The release of Cl_2 [Oum, 1998a] and Br_2 [Oum, 1998b] has been observed in laboratory studies. While Cl_2 is generated from the photolysis of O_3 in the presence of sea–salt aerosols above their deliquescence point, Br_2 is formed in the nighttime reaction of O_3 with frozen sea–water. Both Cl_2 and Br_2 generate halogen atoms upon photolysis (Figure 1.5.a).

Other heterogeneous mechanisms have been proposed [Fan and Jacob, 1992; Mozurkewitch, 1995; Vogt, 1996; Mochida, 1998], mechanisms in which HOBr plays an important role. Vogt *et al.* [1996] proposed a process based on the uptake of HOBr on salt substrates (Figure 1.5.b). HOBr can react on the surface with Cl^- forming BrCl (reaction (1.43)), which can hydrolyze back to HOBr (reaction (1.44)) or react with Br^- to form Br_2 (reaction (1.45)).

$$HOBr(aq) + Cl^- + H^+ \rightarrow BrCl(aq) + H_2O \quad (1.43)$$

$$BrCl(aq) + H_2O \rightarrow HOBr(aq) + Cl^- + H^+ \quad (1.44)$$

$$BrCl(aq) + Br^- \rightarrow Br_2(aq) + Cl^- \quad (1.45)$$

Br_2 and BrCl can then return to the gas phase where they are photolysed and react with O_3 to form halogen oxides. In this reaction scheme one HOBr molecule can release up to two Br atoms per cycle. Once a catalytic cycle (reactions (1.15) and (1.16) on page 7) has started, the reactive halogen species concentrations increase in an exponential manner, which is called "Bromine Explosion" [Platt, 1995; Wennberg, 1999].

Recently, measurements performed by Foster *et al.* [2001], using atmospheric pressure chemical ionization–mass spectrometry, show the presence of Br_2 and BrCl in the arctic troposphere, 125 cm above the snow level. Br_2 and BrCl mixing ratio up to 25 and 35 ppt have been observed, however they did not observe Cl_2. Br_2/BrCl mixing ratios are anti–correlated with tropospheric O_3 concentrations. As BrCl and Br_2 trends are similar, they suggest a common source, namely the heterogeneous reaction of HOBr with chloride and bromide sea–salts aerosols [Foster, 2001].

1.8.2 Activation of Halogen from PSC Particles

In the stratosphere, the most well–known heterogeneous reactions convert the inactive species HCl and $ClONO_2$ into photolytically labile Cl_2 species (reaction (1.50)) and the active N_2O_5 species into less reactive HNO_3 (reaction (1.46)). The net effect of theses processes is to decrease NO_x levels and increase stratospheric ClO_x and HO_x levels. However, in the stratosphere other heterogeneous reactions may take place on PSC type I as well as on PSC type II (ice) particles leading to the activation of chlorine and bromine:

$$N_2O_5(g) + HCl(c) \rightarrow ClNO_2(g) + HNO_3(s) \quad (1.46)$$

$$HOCl(g) + HCl(s) \rightarrow Cl_2(g) + H_2O(s) \quad (1.47)$$

$$HOBr(g) + HCl(s) \rightarrow BrCl(g) + H_2O(s) \quad (1.48)$$

$$ClONO_2(g) + H_2O(s) \rightarrow HOCl(g) + HNO_3(s) \quad (1.49)$$

$$ClONO_2(g) + HCl(s) \rightarrow Cl_2(g) + HNO_3(s) \quad (1.50)$$

$$BrONO_2(g) + H_2O(s) \rightarrow HOBr(g) + HNO_3(s) \quad (1.51)$$

$$BrONO_2(g) + HCl(s) \rightarrow BrCl(g) + HNO_3(s) \quad (1.52)$$

Reaction (1.46) converts HCl into nitryl chloride, $ClNO_2$. In the spring, when the sun comes up, $ClNO_2$ is rapidly photolyzed to produce Cl atoms and NO_2, but this NO_2 can then sequester chlorine in the form of $ClONO_2$, a stable chlorine reservoir. Chlorine activation seems to be more important via $ClONO_2$ heterogeneous reactions than via N_2O_5 reactions on PSC particles.

On ice, the hydrolysis of $ClONO_2$ and $BrONO_2$ initially proceeds at comparable rates. However, toward midlatitudes the atmospheric aerosol particles are largely concentrated H_2SO_4/H_2O mixtures, and on this kind of surfaces the $ClONO_2$ uptake decreases, leading at these latitudes to a less important chlorine activation than the corresponding bromine activation. In addition, the hydrolysis of $ClONO_2$ on pure ice samples (reaction (1.49)) is less efficient than the corresponding reaction involving $BrONO_2$ (reaction (1.51)); $ClONO_2$ hydrolysis is prone to surface saturation on solid ice samples, whereas $BrONO_2$ hydrolysis is a continuous source of HOBr [Oppliger, 1997; Allanic, 1997], showing that HOBr becomes an important intermediate in bromine chemistry.

These reactions produce chlorine or/and bromine containing species (Cl_2, Br_2 or BrCl) which are then released into the gas phase. These latter species rapidly photolyse to form free chlorine and bromine atoms involved in stratospheric ozone loss.

1.9 Motivation and Plan of the Thesis

Three major axis compose Atmospheric Sciences, which are:

- Field Measurements
- Laboratory Experiments
- Numerical Modeling of the Atmoshpere

The present work belongs to the second category. The goal of this thesis is to increase the amount of kinetic and chemical data that need to be included in numerical models of ozone. Heterogeneous reactions constitute a major part of the hidden chemistry of the atmosphere, and one of the aim of this work is to study the kinetics of certain reactions involving halogen containing species. The determination of the rate laws and the reaction mechanism enables the extrapolation to stratospheric or tropospheric conditions.

In Chapter 2, the chosen experimental apparatus which has been used in this work is described in detail. Chapter 3 will go through the synthesis procedure that was designed in order to prepare the gaseous reactants used in this work. At the end of this Chapter, the preparation of the different solid substrates is described which include salt samples (relevant to the troposphere), ice, doped–ice, frozen sulfuric acid and solid ternary solutions (STS) of $HNO_3/H_2SO_4/H_2O$ (relevant to the stratosphere).

Two Sections (A and B) follow which deal each with a specific region of the atmosphere.

Part A, composed of Chapters 4 and 5, is devoted to the study of a particular aspect of heterogeneous chemistry relevant to the lower troposphere involving salt particles from the marine boundary layer. Chapter 4 reports the kinetics of the interaction of $BrONO_2$, for the first time, and $ClONO_2$ on salt samples such as NaCl, KBr, $NaNO_3$ and Na_2SO_4, whereas Chapter 5 deals with the numerical simulation of the marine chemistry in the presence of salt aerosol particles using a simple chemical–radiative box model including heterogeneous chemistry. Based on night–time measurements, Spicer *et al.* postulated in 1998 an unknown source of Cl_2 in the marine boundary layer [Spicer, 1998]. We show that one possible contributing heterogeneous reaction may be the one studied in Chapter 4.

Part B is composed of Chapters 6, 7 and 8 and is concerned with the heterogeneous chemistry relevant to the upper troposphere and lower stratosphere. Chapter 6 examines the interaction of nitric acid (HNO_3) with low temperature ice substrates, such as water ice, frozen sulfuric acid and solid ternary solutions (STS) of sulfuric and nitric acids and water. Chapter 7 describes the investigation of the interaction of $BrONO_2$ with different types of ice, doped–ice with HBr, after having given a brief description of the Br_2O/ice system related to halogen activation on PSC particles. Finally, in Chapter 8 the properties of the HCl/ice and HBr/ice interface are presented.

Chapter 2

Experimental Set-Up

In this chapter we describe the Knudsen reactor specifically designed for the study of heterogeneous reactions equipped with a mass spectrometer (MS). The Knudsen cell is a low pressure flow reactor that operates under molecular flow conditions [Golden, 1973]. This low pressure regime ($P_{tot} < 1$ mTorr) presents two major advantages. First, gas–wall collisions are greatly favored over gas phase collisions. Second, the gaseous reactant interacts with the condensed sample in the absence of limiting gas phase diffusion; this means that crucial parameters such as the residence time, τ, and the collision frequency, Z_1, can be determined by gas kinetic theory. The gas–wall collision frequency per molecule per cm^2 per second is defined by:

$$Z_1 = \frac{< c >}{4V} = \frac{1}{4V}\sqrt{\frac{8RT}{\pi M}} \tag{2.1}$$

where <c> is the mean molecular speed of the gas species, M the molecular mass in kg/mol, R the ideal gas constant, T the gas temperature in Kelvin and V the reactor volume.

2.1 General Description of the Apparatus

The apparatus, shown schematically in Figure 2.1, consists of a standard vacuum line from which gas phase reactants are introduced into the flow reactor: the Knudsen flow reactor is displayed in gray–tone in Figure 2.1. The studied heterogeneous reactions take place in this reactor located on top of the vacuum chamber which houses the mass spectrometer.

The vacuum line is evacuated by a diffusion pump and is used to produce, store and mix gaseous (G) or liquid (L) reactants. Gaseous species are introduced into the Knudsen cell through different inlets such as a capillary of 0.1 mm diameter, a 3 mm

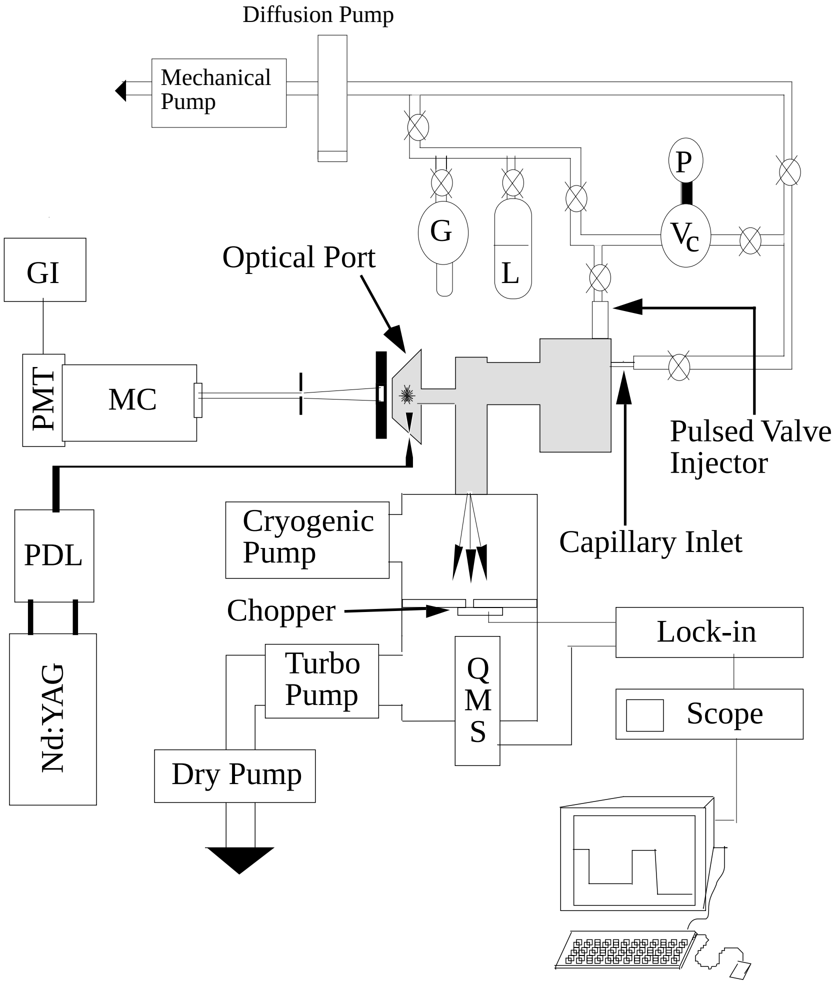

Figure 2.1: Schematic outline of the apparatus. Knudsen flow reactor is depicted in gray.

inner diameter Teflon tube and a pulsed solenoid valve (General Valve, Series 9, 2 mm diameter orifice). The pressure in the calibrated volume (V_c) is measured by a Baratron pressure gauge (P). From the pressure drop in V_c, we determine the flow rate of the gas under study using the ideal gas relation. Typical flow rates obtained are on the order of 10^{14} to 10^{16} molecule/s. The gaseous species leave the reactor through an orifice of variable diameter (1, 4, 8 or 14 mm) and forms an effusive molecular beam, which is monitored by an electron impact quadrupole mass spectrometer QMS (Balzers QMA 421) lodged in the lower part of the differentially pumped vacuum chamber. In the absence of reaction, one determines the escape rate constant, k_{esc}, which corresponds to the effusive loss out of the reactor. This effusion rate depends only on the gas–wall collision frequency (Z_1) given by equation (2.1) and the escape orifice surface (A_h).

$$k_{esc} = Z_1 A_h \tag{2.2}$$

By changing the escape orifice, one affects k_{esc} thus the residence time, τ, in the reactor, which is given by the following equation:

$$k_{esc} = \frac{1}{\tau} \tag{2.3}$$

The instantaneous concentration, [C], in the reactor also depends on the the selected orifice size according to the following equation:

$$[C] = \frac{N}{V} = \frac{F}{k_{esc} V} \tag{2.4}$$

where N is the total number of molecules in the reactor and F the flow rate of molecules entering into the reactor.

The choice of Phase Sensitive Detection (PSD) was made to discriminate the signal emanating from the molecular beam against the background signal owing to further interactions of the reactants with the walls of the detection chamber. To this end the beam effusing from the cell is modulated by a tunable chopping wheel (20–350Hz) located just above the ionization zone of the mass spectrometer. The PSD is then processed by a lock–in amplifier (SRS 830). Alternatively, optical detection was used with a monochromator (MC) and a PMT–gated integrator (GI). The Nd:YAG pumped dye laser (PDL) provides the excitation light.

2.2 Low Pressure Flow Reactor: The Knudsen Cell

The Knudsen cell used in this study consists of two compartments: one used for the reference experiment and the second containing the condensed substrate of interest (see Figures 2.2 and 2.3). The sample compartment can be isolated by an O–ring sealed movable plunger. The internal reactor surfaces, which are made of Pyrex glass and stainless steel, are entirely FEP–Teflon (Dupont) coated to limit potential interactions between gas phase molecules and the walls. The versatility of this reactor in the context of heterogeneous studies has been discussed by Caloz *et al.* [1997].

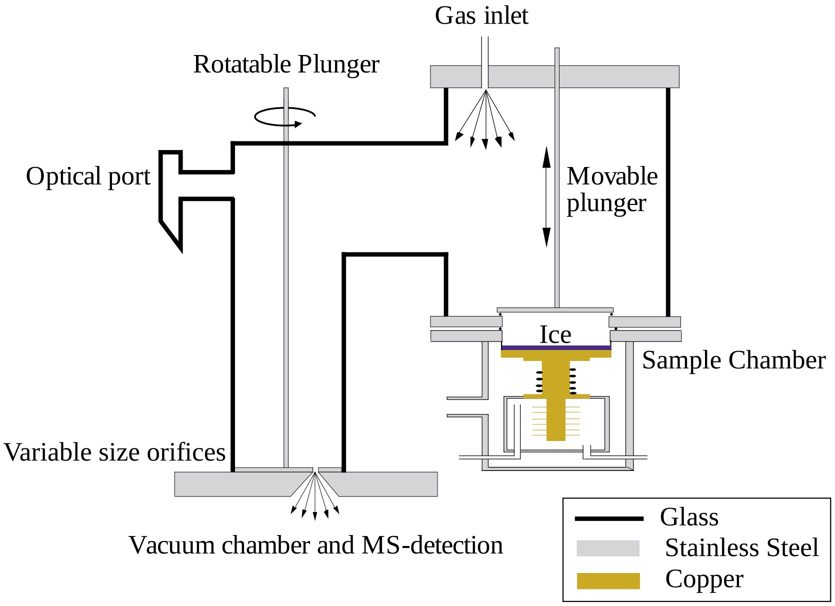

Figure 2.2: Schematic drawing of the Knudsen flow reactor.

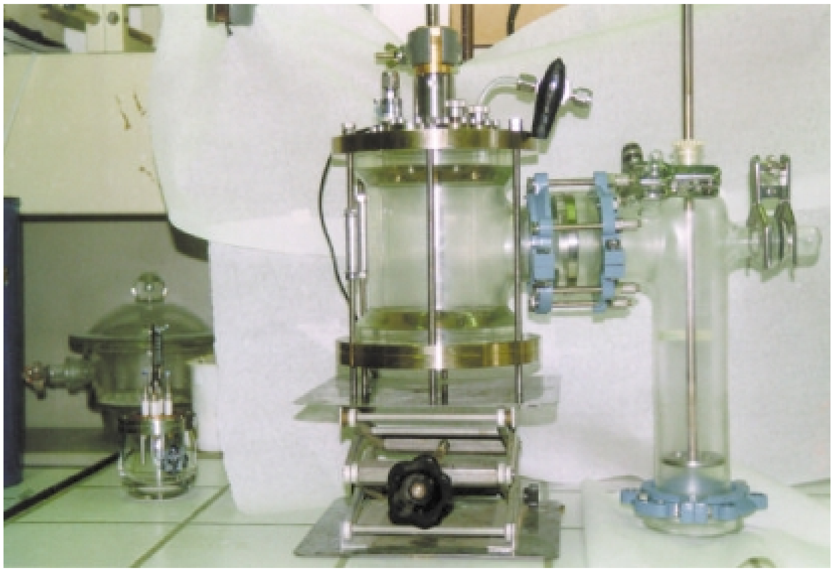

Figure 2.3: Photographic view of the Knudsen flow reactor.

The relevant dimensions of the reactor are summarized in Table 2.1.

Table 2.1: Knudsen cell parameters.

Parameter	Value
Volume of the reactor: V	1830 cm^3 (without optical port)
	2000 cm^3 (with optical port)
Estimated surface area (total)	1300 cm^2
Sample surface area: A_s	17 cm^2
Escape rate constant k_{esc} (a)	
– for the 1 mm orifice	$0.01 \cdot (T/M)^{1/2} s^{-1}$
– for the 4 mm orifice	$0.24 \cdot (T/M)^{1/2} s^{-1}$
– for the 8 mm orifice	$0.79 \cdot (T/M)^{1/2} s^{-1}$
– for the 14 mm orifice	$1.77 \cdot (T/M)^{1/2} s^{-1}$

(a) Values determined by experiment; T and M are the temperature and the molecular mass, respectively.

2.3 Determination of the Uptake Coefficient

In molecular flow conditions, each molecule that enters the reactor volume collides with the walls until it is lost by reaction, with a probability γ, or leaves the cell through the escape orifice, with k_{esc}. Using the different possibilities for the inlet, one may perform two types of experiments, namely continuous flow (or steady state) and pulsed valve experiments.

2.3.1 Continuous Flow Experiment

A constant flow rate F^{in} of molecules is admitted into the reactor through the capillary or the 3 mm ID inlet. Once steady–state is established in the cell, the equation $F^{in} = F^{out}$ results in the following relation in the absence of reaction:

$$\frac{dN}{dt} = F^{in} - F^{out} = F^{in} - k_{esc}N_0 = 0 \tag{2.5}$$

$$\Longrightarrow N_0 = \frac{F^{in}}{k_{esc}} \tag{2.6}$$

where F^{in} is the flow rate entering the reactor and N_0 the number of molecules in the reactor before opening the sample compartment by lifting the plunger. When the reactive surface is exposed to the gas phase a flow steady state is established and may be expressed by:

$$\frac{dN}{dt} = F^{in} - k_{esc}N_r - k_{uni}N_r = 0 \tag{2.7}$$

This leads to N_r, the number of molecules in the reactor, given by equation (2.8):

$$N_r = \frac{F^{in}}{k_{esc} + k_{uni}} \tag{2.8}$$

where k_{uni} refers to the first order rate constant for the net uptake of gas by the reactive surface. N_r may therefore be seen as the number of surviving molecules leaving the reactor. Substituting the flow entering into the reactor, F^{in}, from equations (2.6) and (2.8), one can express k_{uni} by the following relation:

$$k_{uni} = k_{esc} \cdot \frac{N_0 - N_r}{N_r} \tag{2.9}$$

The mass spectrometer probes the effusive molecular beam leaving the reactor, and the mass spectrometric (MS) signal is directly proportional to the flow of molecules leaving the reactor. Thus, k_{uni} can be determined from the ratio of the intensities of the MS signal levels:

$$k_{uni} = k_{esc} \cdot \left(\frac{I_0}{I} - 1\right) \tag{2.10}$$

where I_0 and I are the intensities of the MS signal before and during the reaction, respectively. This value of k_{uni} depends on the geometrical characteristics of the reactor (surface sample area and cell volume). It is convenient to express the kinetic result in the form of a non–dimensional uptake coefficient, γ defined according to equation (2.11):

$$\gamma = \frac{k_{uni}}{Z_1 A_s} = \frac{k_{uni}}{\omega} \tag{2.11}$$

where A_s is the sample surface area. This uptake coefficient represents the fraction in per cent of total collisions that leads to the net removal of the reactant species from the gas phase. A typical steady state experiment is displayed in Figure 2.4.

2.3.2 Pulsed Valve Experiment

Pulses of reactive molecules are admitted into the cell during the short opening period of the solenoid valve on the millisecond time scale. Having isolated the reactive sample, one injects a first pulse which is called a ”reference pulse“ (Figure 2.5). The corresponding

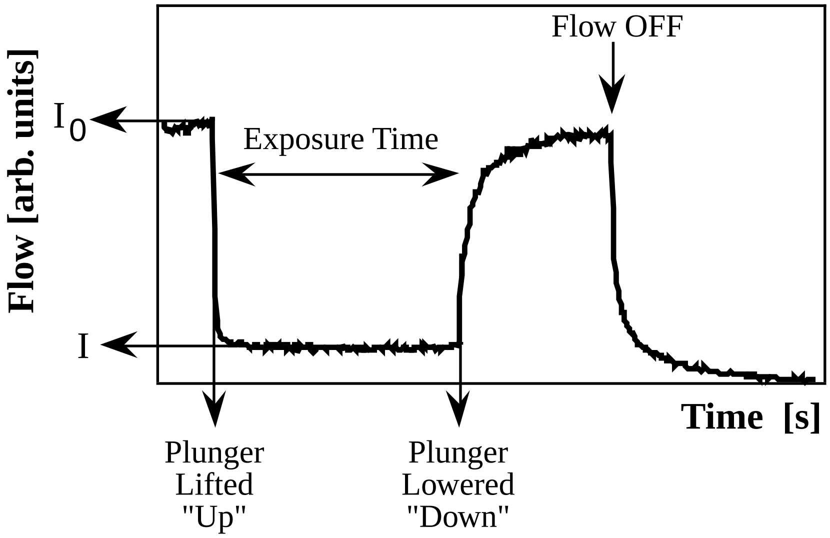

Figure 2.4: Typical steady–state experiment of HNO_3 on bulk ice performed in the 14 mm diameter orifice reactor at 200 K at $F^{i}_{HNO_3} = 1.2 \cdot 10^{14}$ molecule/s leading to $\gamma = 0.16$.

MS signal decay following a single exponential gives us a measured value of k_{esc} for the reactant according to relation (2.12):

$$\frac{dN}{dt} = -k_{esc}N \tag{2.12}$$

The so–called "reactive pulse“ displayed in Figure 2.5 is the pulse obtained when the reactive sample is exposed to the same amount of molecules introduced into the reactor via the pulsed valve compared to the reference pulse. The resulting MS signal, assuming that the process is first order, is again a single exponential decay, whose constant is k_{dec}. The decay obtained with the sample compartment open is the sum of k_{esc} and k_{uni}, the first order rate constant for heterogeneous reaction. Thus by comparing the two pulses, one obtains:

$$k_{uni} = k_{dec} - k_{esc} \tag{2.13}$$

By applying the same procedure outlined in the above section, we obtain the γ value according to equation (2.11).

The pulsed valve technique has two major advantages with respect to the continuous flow experiments:

- The injected dose of reactant can be minimized, typically down to 10^{14} molecules per pulse. This represents only a few percent of a formal monolayer which is equivalent to approximately 10^{15} molecule/cm^2 for our sample. This means:

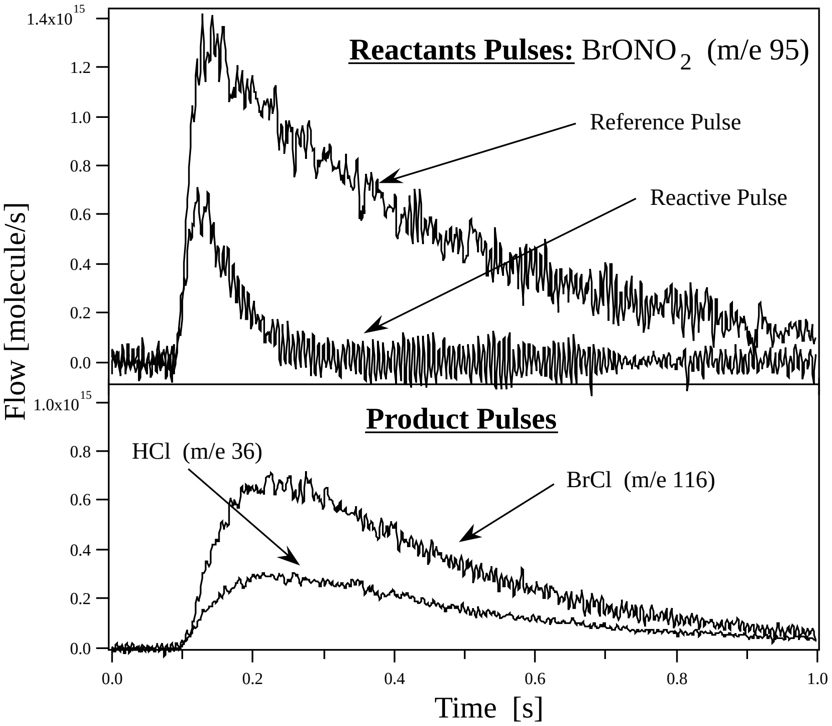

Figure 2.5: Typical pulsed–valve experiment of BrONO$_2$ (monitored at m/e 95) on NaCl–powder performed in the 14 mm diameter orifice reactor leading to $\gamma_0 = 0.3$. The reference pulse is monitored with the sample compartment closed, while the reactive pulse corresponds to the same injected dose (in this case, the dose of BrONO$_2$ is $4.7 \cdot 10^{14}$ molecules) in the presence of the substrate. The lower panel indicates the release into the gas phase of the products, namely BrCl (m/e 116), HCl (m/e 36) and Br$_2$ (not shown) in a yield of 45, 22 and 6 %, respectively, following reaction .

1. Desorption can be separated from adsorption on the time scale of the pulse [Chaix, 1998; Fluckiger, 1998].
2. Fast surface saturation processes observed during a steady state experiment can be avoid leading to the true initial uptake coefficient γ_0.

- As shown in Figure 2.5, the expected products may also be monitored. The shape of the product pulses and the delay in product appearance may give us additional information in terms of potential interaction of the product(s) with the condensed phase (see also Figure 7.5 on page 133.

2.4 The Low Temperature Support (LTS)

In order to study heterogeneous reactions relevant to the lower stratosphere, it is important to have a tool in order to cool our samples to temperatures of stratospheric interest. For this purpose a support capable of cooling solids or solutions to 130 K has been used. A schematic view of the low temperature support (LTS) is shown in Figure 2.6.

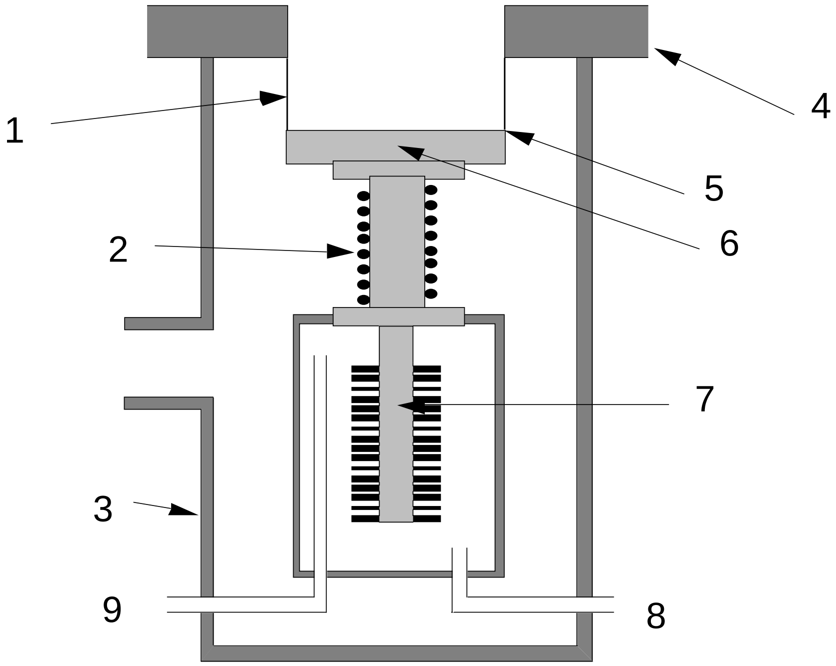

Figure 2.6: Schematic drawing of the low temperature support (LTS). **1** thin stainless steel wall (0.2 mm), **2** heating wires around the copper core, **3** evacuated stainless steel jacket, **4** stainless steel flange, **5** welded steel–copper connection, **6** sample dish (gold–plated copper), **7** copper core immersed in the heat exchanger, **8** compressed air inlet, **9** compressed air outlet.

The gold–plated sample dish is connected to a heat exchanger for cooling and is resistively heated by an electrical wire. The cooling of the copper core in the heat exchanger is achieved by a cold compressed air flow circulating through a coil immersed in liquid nitrogen. The desired temperature is maintained with a precision of ± 0.5 K by a PID temperature controller (Eurotherm 906D) which alternates cycles of heating and cooling. The copper plate is thermally insulated from the Knudsen cell's lower flange by thin walls (0.2 mm thick). Evacuating the internal volume of the LTS prevents any convective heat transfer between the temperature controlled elements and ambient laboratory air. Two type T thermocouples, one connected to the center and one to the edge of the copper plate, ensure that the radial temperature gradient is never larger than 2 K even at the lowest attainable temperature (130 K).

The different types of low temperature samples and the way to obtain them are described in the following Chapter in Section 3.9.2 on page 40.

2.5 The High Temperature Support (HTS)

In order to study the importance of adsorbed water in the heterogeneous chemistry of reactions in relation with sea–salt aerosol, we have used a support in which samples may be heated up to 750 K inside the low–pressure environment of the Knudsen Cell. The support is used both in sample preparation as well as a means of drying substrates. The principle of the HTS is similar to that of the LTS. The heated copper dish is insulated from the Knudsen reactor by a thin feathered stainless steel wall (Figure 2.7). The copper dish is heated by three resistive cartridges, and cold water is circulated in the base flange in order to prevent any heating of the O–rings. The internal surfaces are nickel coated and the temperature is measured using two thermocouples placed in the middle and at the edge of the copper plate. The temperature can be adjusted accurately by changing the voltage applied to the heating cartridges. Because the samples are at low pressure, thermal conduction between the sample and the heated copper support is improved by a thin layer of liquid gallium.

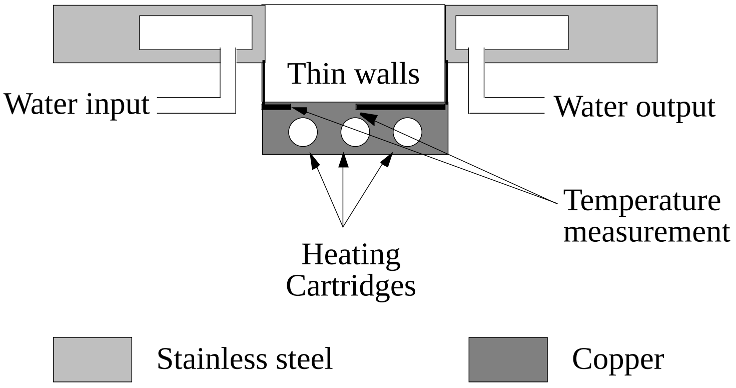

Figure 2.7: Schematic drawing of the high temperature support (HTS). It can be operated from room temperature up to 700 K.

2.6 Error and Uncertainties

The range of uptake coefficients that are accessible to measurements using the Knudsen cell reactor described above lies in the range $10^{-6} < \gamma < 1$ [Caloz, 1997]. This large dynamic range of γ is made possible by changing the escape orifice area, and thus k_{esc} by two orders of magnitude. The escape rate constant, k_{esc}, is directly measured in pulsed–valve experiments with a maximum uncertainty of 10 % [Caloz, 1997].

In steady–state experiments, the use of equation (2.10) in the determination of k_{uni} implies an uncertainty proportional to the error in the ratio of $\frac{I_0}{I}$ and k_{esc}. The former depends on the signal–to–noise characteristics of the instrument and varies as a function of the flow, amplification and QMS settings. Generally, in steady–state experiments the ratio $\left(\frac{I_0}{I}\right)$ is determined with little error ($\cong$ 10 %) if, during an exposure of the solid sample, the signal falls into the range of 0.1 to 0.9 of the initial signal (I_0).

Other sources of error could be the exposure of the reactant species to a rather large non Teflon coated surface in the sample holder, particularly during the use of the gold–plated LTS. To take into account the interaction of non Teflonated surfaces, we routinely performed blank experiment using the different empty supports. We regularly performed calibrations to take into account the QMS setup parameters, such as ionization efficiency or SEM voltage, which depend on the mass spectrometer age and may affect mass balances.

Thus the total error in the determination of the net uptake coefficient must be evaluated on a case–by–case basis, but usually does not exceed 30 %.

Chapter 3

Reactant Synthesis and Purification

Laboratory studies of heterogeneous reactions require to master many synthesis procedures because most of the species we mention in this work are not commercially available. In order to obtain good quality data, we have to prepare reactants as pure as possible. As we reduce the impurities, the primary and secondary reaction products are more easily identified using mass spectrometric methods.

In this chapter we will describe the synthesis and purification procedures for compounds we have prepared for the study of heterogeneous reactions relevant to the atmosphere. These species are namely HNO_3, BrCl, N_2O_5, Cl_2O, $ClONO_2$, Br_2O, HOBr, and finally $BrONO_2$, whose heterogeneous interactions with polar substrates, such as salt and ice, is the main subject of this work. After every synthesis run, the purity of the different samples was checked in the Knudsen flow reactor using mass spectrometry.

3.1 HNO_3

HNO_3 has been prepared from a mixture of liquid HNO_3 (90 %, Fluka AG) stabilized in H_2SO_4 (98 %, Fluka AG) in a ratio of 1:3 v/v. The base peak is observed at m/e 46 (NO_2^+), and the parent peak, observed at m/e 63, is in general less than 4 % of the main peak. HNO_3 has been used in this work as a reactant as well as a doping acid. A typical mass spectrum of HNO_3 is displayed in Figure 3.1.

3.2 BrCl

Gaseous BrCl is obtained by mixing a small amount of Br_2 with an excess of Cl_2 in a 5 l flask at room temperature according to reaction (3.1) following the procedure described by Stull *et al.* [1971]:

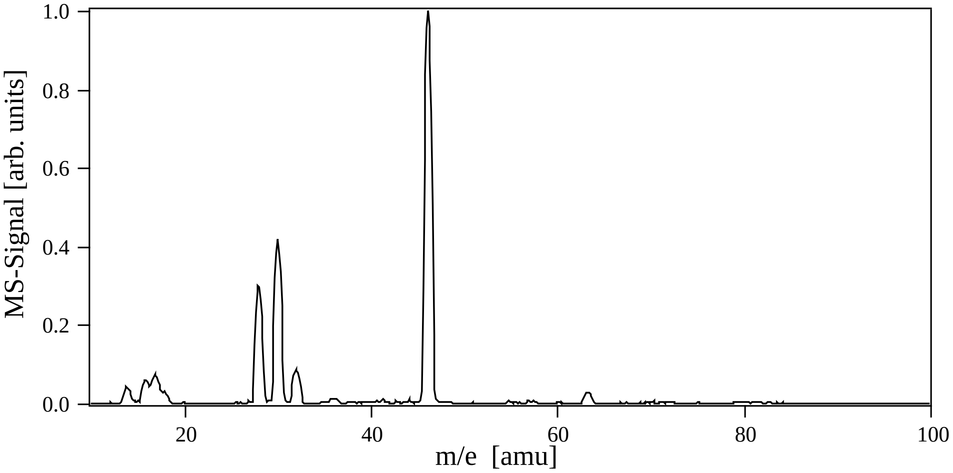

Figure 3.1: Mass spectrum of HNO_3. m/e 46 (NO_2^+) is used to monitored HNO_3.

$$Br_2 + Cl_2 \rightarrow 2BrCl \tag{3.1}$$

Our mixtures typically contained 80% Cl_2, 18% BrCl and 2% Br_2. The mixture is distilled at 200 K in order to remove excess Cl_2.

3.3 N_2O_5

Dinitrogen pentoxide is prepared by reacting pure NO_2 with excess ozone following the procedure described by Fenter *et al.* [1996] according to the reactions (3.2) and (3.3):

$$NO_2 + O_3 \rightarrow NO_3 + O_2 \tag{3.2}$$

$$NO_2 + NO_3 \rightarrow N_2O_5 \tag{3.3}$$

The challenge is to reduce the formation of HNO_3 which occurs by hydrolysis of N_2O_5 according to the following reaction:

$$N_2O_5 + H_2O \rightarrow 2HNO_3 \tag{3.4}$$

The outgoing O_3/O_2 mixture from the ozone generator (Fischer, model 502) of approximate ratio 5 % v/v is passed through a P_2O_5 trap to eliminate the residual water before mixing with dried NO_2. The final mixture is condensed in a cold trap at approximately 180 K resulting in a white solid powder.

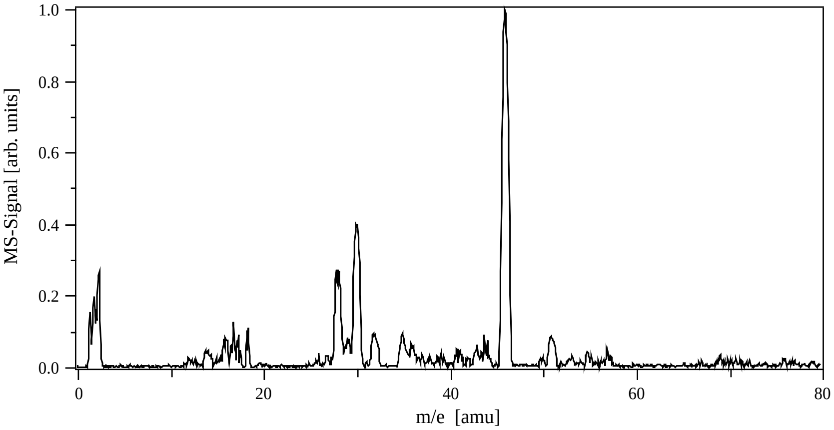

Figure 3.2: Mass spectrum of $ClONO_2$. The main peak at m/e 46 (NO_2^+) has been used to monitor $ClONO_2$; m/e 51 corresponds to the ClO^+ fragment of $ClONO_2$.

3.4 Cl_2O

Dichlorine monoxide is synthesized from reaction (3.5) according to the procedure described in Knauth *et al.* [1979]. The resulting product is a orange–brown liquid which is purified by distillation at 160 K in order to remove unreacted Cl_2. However, there is still Cl_2 in the trap because Cl_2O slowly decomposes during storage periods at 190 K.

$$2Cl_2 + 3HgO \rightarrow Cl_2O + HgCl_2 \cdot 2HgO \tag{3.5}$$

3.5 $ClONO_2$

Chlorine nitrate is synthesized from the reaction of Cl_2O with excess N_2O_5 following the procedure described by Timonen *et al.* [1994] according to reaction (3.6):

$$Cl_2O + N_2O_5 \rightarrow 2ClONO_2 \tag{3.6}$$

The mixture is kept in a cold methanol bath at 245 K during 20 minutes in order to accelerate the reaction after which it is subsequently kept at 195 K during 24 hours in order to complete the reaction. The major impurities are Cl_2 and N_2O_5. The Cl_2 impurity is removed by distillation at 180 K in a bromobutane bath cooled with liquid nitrogen. The $ClONO_2/N_2O_5$ mixture is then distilled at 220 K to remove N_2O_5 and the distillate is collected in a clean trap at 77 K. After purification no impurities have been observed within our analytical sensitivity and the remaining product is a bright yellow liquid. A mass spectrum of $ClONO_2$ is shown on Figure 3.2.

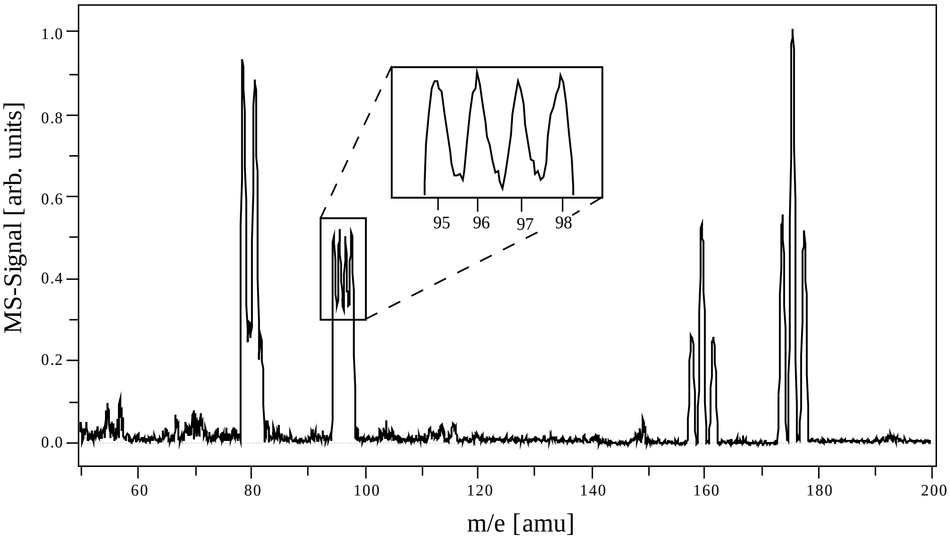

Figure 3.3: Mass spectrum of Br_2O. The base peak at m/e 176 (Br_2O^+) indicates the presence of Br_2O; m/e 95 and 97 correspond to the BrO^+ fragment of Br_2O. HOBr (m/e 96 and 98) and Br_2 (m/e 158, 160 and 162) are still detectable after purification of the sample.

3.6 Br_2O

Dibromine monoxide was synthesised from the reaction of Br_2 with HgO, in analogy to the Cl_2/Cl_2O system according to reaction (3.7) [Tevault *et al.*, 1978]:

$$2Br_2 + HgO \rightarrow Br_2O + HgBr_2 \tag{3.7}$$

Approximately 50 g of HgO powder were placed in a 2 l glass flask equipped with an in– and outlet valve, which was evacuated to a pressure of approximately 4 kPa (40 mbar). Br_2 was degassed and dried over P_2O_5. The flask was subsequently filled with 130 mbar Br_2. After waiting for 5 minutes for the reactants and products to come to equilibrium, the gases were pumped through a second trap cooled at 77 K. This process was repeated several times to obtain sufficient quantities of BrOBr collected in the cold trap at 77 K. The temperature of the trap was then raised to about 200 K, and Br_2 was removed by pumping. Towards the end of the pumping period of 6–9 hours, a brown powder remained in the trap. A mass spectrum of Br_2O is displayed in Figure 3.3 with the base peak at m/e 176 (Br_2O^+) which unambiguously reveals the presence of Br_2O. The trap also contains HOBr (m/e 96 and 98) and Br_2 as impurities. Important quantities of water remain in the batch of Br_2O coming from water absorbed on HgO. Even after pumping, the impurities remain adsorbed in the trap.

3.7 HOBr

Hypobromous acid is prepared from an aqueous solution according to the protocol described in Dancer [1863] (reactions (3.8) and (3.9)). Liquid Br_2 (5 ml) is added, during 30 minutes, drop by drop to 150 ml of distilled H_2O at ambient temperature in which 24.5 g of $AgNO_3$ has previously been dissolved. Then the mixture is agitated during 10 additional minutes.

$$Br_2 + AgNO_3 \rightarrow BrNO_3 + AgBr \tag{3.8}$$

$$BrNO_3 + H_2O \rightarrow HOBr + HNO_3 \tag{3.9}$$

The second step consists of a vacuum distillation where the condenser temperature is hold at 273 K, the resulting distillate is collected at 230 K in a trap containing 20 ml of 20 % wt H_2SO_4 to stabilize HOBr in solution. In this study no uptake experiment of HOBr on polar substrates have been performed, HOBr have been produced in order to calibrate MS signals, because HOBr as been observed as reaction product (Chapter 7). A typical mass spectrum of HOBr is displayed in Figure 3.4.

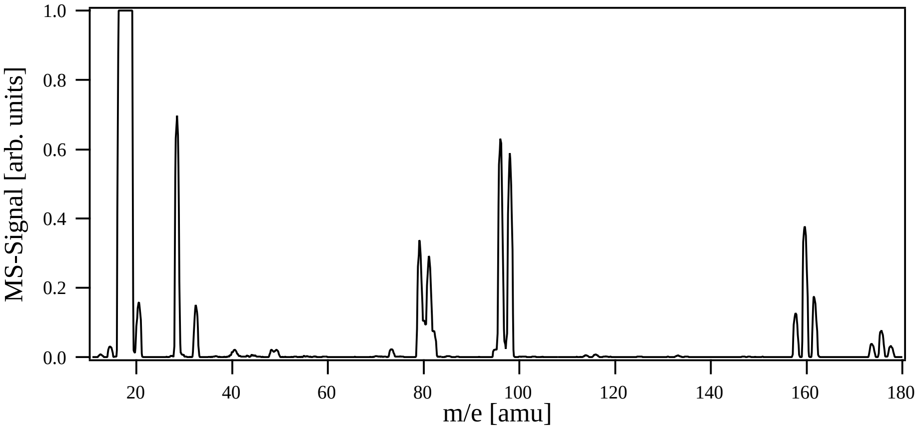

Figure 3.4: Mass spectrum of HOBr. The parents peaks at m/e 96 or 98 are used to monitored HOBr. HOBr contribution at m/e 95 and 97 (BrO^+) are small, less than 4 %. Br_2 (m/e 158, 160 and 162) and Br_2O (m/e 174, 176 and 178) are always observed as impurities in different extends.

3.8 $BrONO_2$

Bromine nitrate is synthesized from the reaction of $ClONO_2$ with Br_2 according to reaction (3.10) following the procedure described by Wilson *et al.* [1987]. $ClONO_2$ is mixed with Br_2 in a molar ratio of 3:1 in a trap at 77 K. Before condensation $ClONO_2$ and Br_2 are passed across a P_2O_5 trap in order to dry the reactants.

$$ClONO_2 + Br_2 \rightarrow BrONO_2 + BrCl \tag{3.10}$$

The mixture is kept at ambient temperature for an hour and condensed in a cold trap at 200 K in a cold circulation bath during 12 hours. Unreacted Br_2, $ClONO_2$ and other impurities are removed by pumping for 2–3 hours at a temperature range of 200 to 220 K. The remaining product is a solid yellow substance. However Br_2, BrCl and sometimes Br_2O are still remaining in the trap as impurities even after long periods of pumping. Mixing bromine and chlorine–containing compounds always leads to the formation of BrCl. A mass spectrum of $BrONO_2$ is shown in Figure 3.5. The base peak is at m/e 46 (NO^+), but we did not use m/e 46 to monitor $BrONO_2$ in order to avoid any confusion with other species contributing to this mass. We chose to monitor $BrONO_2$ at m/e 95 (BrO^+) which is an unambiguous marker for $BrONO_2$ as long as HOBr is either absent or present in known quantities such that an appropriate correction may be performed at m/e 95. The typical ratio of m/e 46 to 95 is 20:1.

The successful synthesis of Br_2O suggested a new way for the preparation of $BrONO_2$ via reaction (3.11):

$$Br_2O + N_2O_5 \rightarrow 2BrONO_2 \tag{3.11}$$

However, this approach has been unsuccessful because the Br_2O decomposition at the reaction temperature of 240 K was too rapid. An excess of Br_2O leads to the formation of a bright–yellow powder, but the MS–signal of the vapor pressure over this powder did not indicate the presence of $BrONO_2$. An excess of N_2O_5 did not lead to the formation of $BrONO_2$ either.

3.9 Substrate Preparation

3.9.1 Salt Samples

In order to gauge the importance of diffusion of the reactants into the bulk of the salt substrates different surface presentations have been used: grains of defined average size, powder, spray deposited thin films and single crystals. All salts were commercially available: NaCl, KBr, $NaNO_3, Na_2SO_4$ from Fluka A.G. The powders were obtained by grinding grains of average diameter 350–500 μm in a ball mill and were subsequently sieved to isolate different size ranges from 35 to 160 μm. Spray deposited thin films

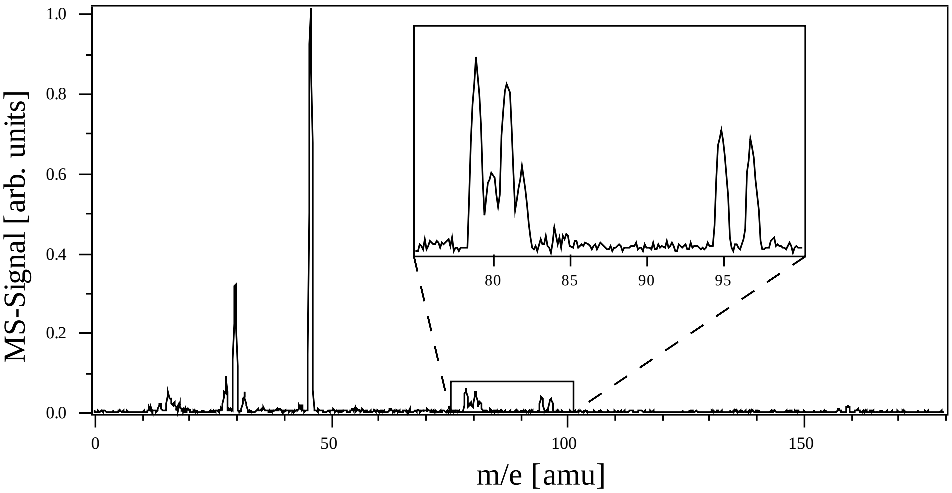

Figure 3.5: Mass spectrum of $BrONO_2$. The m/e 95 and 97 (BrO^+) signals are used to monitor $BrONO_2$. The typical ratio of the MS–signal at m/e 46 and 95 (or 97) is 20:1. Br_2 (m/e 158, 160 and 162) and BrCl (m/e 114, 116 and 118) are sometimes observed as impurities.

were obtained using a salt solution saturated in methanol. The solution is sprayed on a 50 mm diameter glass flat heated to a temperature of 400 K. The solvent immediately evaporates and the salt formed a coherent thin film on the glass flat as shown by SEM pictures (Figure 3.6). The mass of the salt generally ranges from 3 to 10 mg leading to surface densities of 0.15 to 0.5 mg/cm^2 leading to a coherent thin film as displayed in Figure 3.6. Optical windows of NaCl and KBr used in IR spectroscopy were employed as reactive substrates of single crystal type (Bicron Corporation).

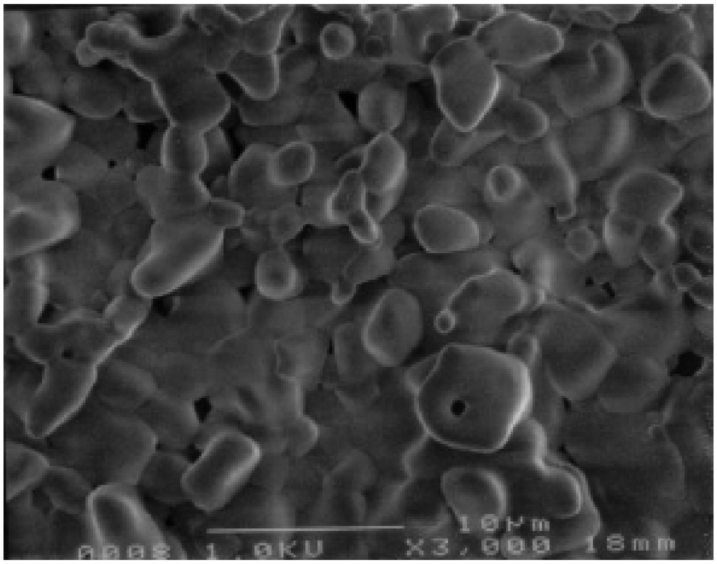

Figure 3.6: Typical scanning electron microscope image (SEM) of the methanol spray–deposited KBr showing the lack of internal surface area.

In order to study the role of absorbed H_2O on the salt samples in heterogeneous reactions we used a heated sample holder described in detail in Section 2.5. In general, the samples are pumped overnight after introduction into the Knudsen cell in order to eliminate residual water. However, there is a quantity of adsorbed water remaining on the salt substrate which Finlayson–Pitts and co–workers have called the quasi–liquid layer (QLL) [Beichert, 1996]. Using this support, we heated the sprayed substrate up to 550 K. Most of the adsorbed water desorbed during heating so we could observe the effect of the lack of H_2O on the reaction kinetics. We have performed several SS experiments in order to measure the uptake of H_2O on dried salt, but the rate of uptake is very slow. It is in the range of the detection limit of our experiment ($\gamma < 10^{-5}$).

3.9.2 Low Temperature Samples

The ice samples were prepared using the low temperature support described in Section 2.4. Various types of ice were obtained according to the following procedures:

- Sample referred to as **"Bulk ice" (B)**: Liquid deionized water is poured into the sample dish prior to any experiment. The water is then degassed by freeze–pump–thaw cycles and finally cooled down to a chosen temperature in about 15 minutes in order to perform the uptake experiment.

- Sample referred to as **"Single crystal ice" (SC)**: Liquid deionized water is poured into the sample dish like for (B) samples, but the rate of cooling was much slower in the temperature range 273 to 240 K. The temperature decrease was set to –0.3 K/min according to the procedure described by Knight [1996].
  At present one does not have an optical characterization for pure (SC) samples, but we notice that (SC) appeared to the eye as being more transparent than (B) samples. In addition, experiments performed on (SC) samples show distinctly different kinetics compared to the one performed on (B) samples [Chaix, 1998; ibid. in Chapter 7]

- Sample referred to as **"Condensed ice" (C)**: Gas phase water vapor is deposited onto the cold support at 150 K; the empty support is attached to the reactor and subsequently cooled down to the desired temperature with the plunger lowered, such that the sample compartment is sealed off. When the chosen temperature is reached (150 K), the plunger is lifted and the sample dish is exposed to a water flow of the order of 10^{14} to 10^{19} molecule/s during several minutes. This results in sample thicknesses in the range 250 nm to a few μm.

- Sample referred as to **”HX–doped ice“**: Gas phase HX vapor (X = Cl, Br, NO_3), is deposited on the ice surface (B, C or SC) during several minutes. An initial flow rate of HX on the order of 10^{15} molecule/s is used to adsorb approximately 10 formal monolayers of HX at the interface.

The frozen H_2SO_4 samples have been prepared in two steps. First, a (B) ice sample was prepared at 150 K by freezing a small amount of liquid H_2O in order to protect the gold–plated sample support from the corrosive action of H_2SO_4. Subsequently, a liquid H_2SO_4 solution was slowly added to the bulk ice layer which froze right away so as to avoid any concentration gradient or dilution in the bulk. Both thickness layers are generally of the same order, typically 0.5 cm. The solid ternary solution (STS) samples consisting of $H_2SO_4/HNO_3/H_2O$ were prepared in the same manner as the frozen H_2SO_4/H_2O samples.

Most of the experiments performed on low temperature samples were carried out with an external H_2O flow ($F^{ext}_{H_2O}$) in order to keep the sample in thermodynamic equilibrium. The external water flow is adjusted so that no change can be observed at m/e 18 upon opening and closing the sample chamber of the Knudsen flow reactor. At steady state the partial pressure of H_2O observed during an uptake experiment is equivalent to the equilibrium vapor pressure for the ice sample, P_w, given by the following equation:

$$P_w = \frac{F^{ext}_{H_2O}}{k_{esc}V} \cdot RT \tag{3.12}$$

The equilibrium vapor pressure calculated using equation (3.12) provides a final check of the sample temperature measured by two type T thermocouples.

3.9.3 Doping Acids

Several experiments were performed on ice samples doped by various acids whose sources are presented as follows:

- **HCl** was produced by reacting sulfuric acid (H_2SO_4) on dry NaCl at room temperature under vacuum conditions according to the following reaction:

  $$H_2SO_4 + 2NaCl \rightarrow 2HCl + Na_2SO_4 \tag{3.13}$$

  The gaseous HCl is then trapped in a bulb at liquid nitrogen (LN) temperature. A mass spectrum of HCl is displayed in Figure 3.7 (upper panel). HCl is monitored at m/e 36 (base peak).

- **HBr** was transferred in a trap, kept at LN temperature, from a bottle (Messer Griesheim) and purified from Br_2 contamination by distillation. A mass spectrum of HBr (monitored at m/e 82) is displayed in Figure 3.7 (lower panel). No Br_2 is observed at m/e 158, 160 and 162.

- **HNO_3** synthesis was presented above (section 3.1)

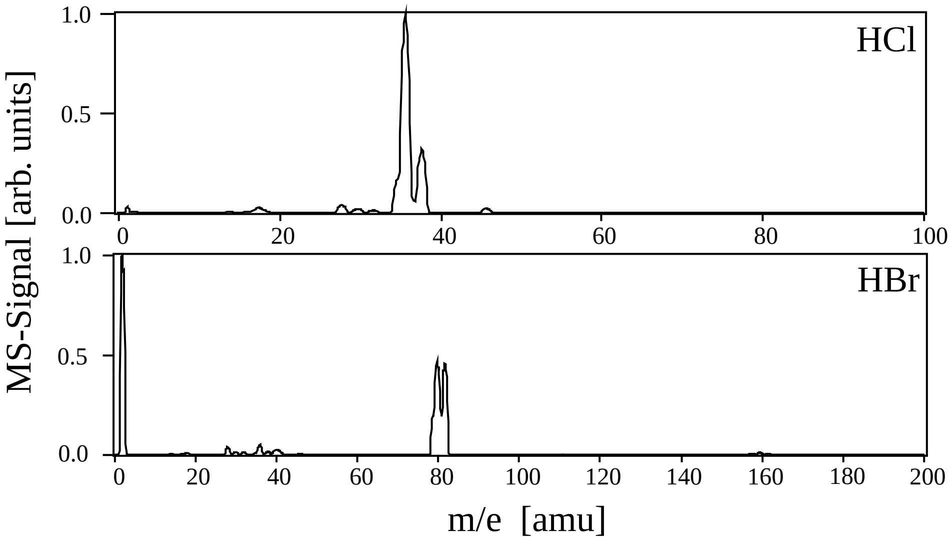

Figure 3.7: Mass spectrum of HCl (upper panel) and HBr (lower panel).

Part A: Heterogeneous Reactions Relevant to the Troposphere

Chapter 4

Interaction of $BrONO_2$ and $ClONO_2$ with Salts

4.1 Introduction

Marine aerosol present in the troposphere consists of small sulfate particles and larger sea–salt aerosol particles containing chloride and bromide, which are generated by breaking waves on the ocean's surface. The salt particles contribute most of the total aerosol mass [Harrison, 1998]. The presence of $BrONO_2$ and $ClONO_2$, two important halogen reservoirs, may have an important impact on the oxidizing potential of the Earth's troposphere by reacting with sea–salt aerosol particles [Sander, 1996; Finlayson–Pitts, 1989]. The heterogeneous reactions of $BrONO_2$ and $ClONO_2$ with solid alkali halides may contribute to halogen activation in the marine atmosphere by releasing Cl_2, Br_2 or BrCl in cases where NO_x is present in significant quantities. It is only recently that halogen activation processes on sea–salt aerosols have begun to be studied [Zetzsch, 1992]. The formation of $BrONO_2$ and $ClONO_2$ is known to occur in the atmosphere via the radical recombination reaction of XO with NO_2 following reaction (4.1), where X = Br, Cl.

$$XO + NO_2 \xrightarrow{M} XONO_2 \qquad (4.1)$$

The destruction of $XONO_2$ occurs through photolysis and heterogeneous loss. In the troposphere, we typically expect a peak concentration level of 110 and 280 ppt for $BrONO_2$ and $ClONO_2$, respectively, at a NO_x level of 100 ppb (polluted air mass) and an aerosol surface–to–volume ratio of 10 $\mu m^2/cm^3$. For these box model calculations it was assumed that the sea–salt aerosol concentration was constant and that both bromine and chlorine are present in equal concentrations. The corresponding $BrONO_2$

and $ClONO_2$ levels decrease to 0.7 and 7 ppt at a NO_x level of 1 ppb. The box model used for these calculations is described in Chapter 5.

The heterogeneous reactions of $ClONO_2$ with solid NaCl and KBr have already been studied in a fast flow tube reactor [Timonen, 1994] and a Knudsen flow reactor [Caloz, 1996]. They proceed according to the following reactions:

$$
\begin{aligned}
ClONO_2 + NaCl &\rightarrow Cl_2 + NaNO_3 &\quad (4.2)\\
ClONO_2 + KBr &\rightarrow BrCl + KNO_3 &\quad (4.3)
\end{aligned}
$$

$ClONO_2$ reacting with solid NaCl leads to the formation of Cl_2. The primary reaction product from reaction (4.3), BrCl, is partly released from KBr and partly undergoes a fast secondary reaction resulting in Br_2 and KCl which in turn generates Cl_2 according to reaction (4.2) [Caloz, 1996]. The heterogeneous reactions of $BrONO_2$ with solid NaCl and KBr have not been studied to date, however, we expect the following reactions in analogy to the reactions with $ClONO_2$:

$$
\begin{aligned}
BrONO_2 + NaCl &\rightarrow BrCl + NaNO_3 &\quad (4.4)\\
BrONO_2 + KBr &\rightarrow Br_2 + KNO_3 &\quad (4.5)
\end{aligned}
$$

The release of halogen or interhalogen compounds according to reactions (4.2) to (4.5) may have an influence on tropospheric chemistry. First, as the chlorine concentration increases and the reaction rate constants of Cl interacting with hydrocarbons are significantly larger than those for OH, we may expect a change in the oxidizing potential of the troposphere [Finlayson–Pitts, 1986; Crutzen, 1995]. Second, observations strongly indicate that tropospheric ozone can be rapidly destroyed by small amounts of active bromine in the polar regions . During polar sunrise in the Arctic, it has been observed that low ozone concentrations coincided with high BrO concentrations [Barrie, 1988; Hausmann, 1994; Wagner, 1998; McElroy, 1999]. Recently, high BrO concentrations have been observed in the troposphere at midlatitudes as well [Hebestreit, 1999].

The focus of the present Chapter involves the study of the heterogeneous processes of $BrONO_2$ and $ClONO_2$ on solid salts which may in part occur as marine aerosols. An important goal of the present study is to measure the kinetics of reactions (4.4) and (4.5) and to determine the identity of the primary reaction products as well as potential fast secondary reactions which may mask the primary reactions. Together with the heterogeneous reactions of HOCl and HOBr on salt [Mochida, 1998], these reactions result in the release of molecular halogens and interhalogens in the atmosphere.

Because of the recent interest in $BrONO_2$, several measurements of the properties of $BrONO_2$ have been reported. For example, the electronic structure of $BrONO_2$ [Dianxun, 1996], its heat of formation and the rate constant for its thermal decomposition [Orlando, 1996] have been measured recently. Here, we will also consider the interaction of $ClONO_2$ with non–reactive salts in order to further probe the reactivity of $ClONO_2$ towards solid salts and compare its behavior to $BrONO_2$. We highlight the importance of water absorbed on the salt surface in relation to heterogeneous reactions as suggested by Beichert and Finlayson–Pitts [1996]. In addition, a simple chemical kinetic model describing heterogeneous reactions is proposed to explain the ionic exchange at the salt interface.

4.2 Experimental Apparatus

The experiments have been performed in the Knudsen cell reactor described in detail in Chapter 2. The characteristics of the reactor used for this study are summarized in Table 4.1.

Table 4.1: Knudsen cell parameter.

Parameter	Value
Volume of the reactor: V	1830 cm^3
Estimated surface area (total)	1300 cm^2
Sample surface area: A_s	19.6 cm^2
Gas number concentration: [C] (a)	(1–100) x 10^{10} cm^{-3}
Surface collision frequency: ω (b)	$\omega = 2A_s \cdot (T/M)^{1/2} s^{-1}$
Escape rate constant: k_{esc} (c)	
for the 4 mm orifice	$0.24 \cdot (T/M)^{1/2} s^{-1}$
for the 8 mm orifice	$0.79 \cdot (T/M)^{1/2} s^{-1}$
for the 14 mm orifice	$1.77 \cdot (T/M)^{1/2} s^{-1}$

(a) Calculated using the relation $F^i = V \cdot k_{esc} \cdot [C]$ where F^i is the flow entering the cell and [C] the concentration. (b) T and M are the temperature and the molecular weight of molecule C, respectively. (c) Value determined by experiment.

The uptake coefficient γ is obtained according to $\gamma = \frac{k_{uni}}{\omega}$ where ω is the collision frequency of the gas with the reactive surface calculated from gas kinetic theory (Table 4.1): $\omega = 50\ s^{-1}$ for $BrONO_2$; k_{uni} is the unimolecular rate constant obtained by the experiments and corrected according to equation (4.8).

Table 4.2: Loss of $BrONO_2$ on the PTFE–Teflon–coated supports.

Sample support	A_{PTFE} $[cm^2]$ $^{(a)}$	ω $[s^{-1}]$ $^{(b)}$	k_{uni}^{PTFE} $[s^{-1}]$	γ
Cup 1	120	330	4	0.010 ± 0.005
Cup 2	100	270	6	0.022 ± 0.006
Plate	60	170	11	0.110 ± 0.050

(a) A_{PTFE} = surface area of PTFE. (b) ω = collision frequency on PTFE.

4.3 Interaction of $BrONO_2$ with the Teflon–Coated Sample Support

$BrONO_2$ interacts with the empty Teflon–coated sample support. Therefore, the value of the measured rate constant k_{uni}^{obs} must be corrected in order to obtain the true value of the rate constant, k_{uni}, for the heterogeneous reaction of $BrONO_2$ with the salt sample. When the plunger is lifted, there are two additional loss processes; one on the salt, and the other on the Teflon coat of the sample support. The total rate constant obtained from experiments for $BrONO_2$ disappearance, k_{uni}^{obs}, may then be expressed as the sum of two contributions according to equation (4.6):

$$k_{uni}^{obs} = k_{uni}^{PTFE} + k_{uni} \tag{4.6}$$

where k_{uni}^{PTFE} represents the loss on the empty Teflon–coated support and k_{uni} the loss on the salt surface sample. We may normalize k_{uni}^{PTFE} to unity surface area according to equation (4.7):

$$k_{uni}^{PTFE} = \hat{k}^{PTFE} \cdot A_{PTFE} \tag{4.7}$$

where A_{PTFE} is the surface area of the Teflon–coated empty sample support and $\hat{k}^{PTFE}$ is the corresponding surface–area normalized rate constant expressed in $s^{-1} \cdot cm^{-2}$. With these relations the true value of k_{uni} for the interaction of $BrONO_2$ on salts may be obtained from the following equation:

$$k_{uni} = k_{uni}^{obs} - \hat{k}^{PTFE} \cdot A_{PTFE}^{*} \tag{4.8}$$

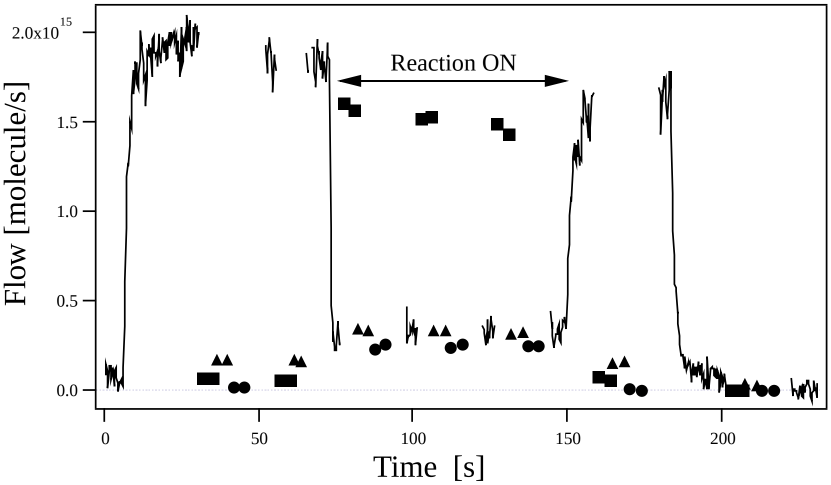

Figure 4.1: Typical steady state uptake experiment of $BrONO_2$ on NaCl performed in the 14 mm diameter orifice reactor at $F^{in}_{BrONO_2} = 1.8 \cdot 10^{15}$ molecule s^{-1} leading to $\gamma_0 = 0.25 \pm 0.13$. $BrONO_2$ (solid line) is monitored at m/e 95, BrCl (■) is detected at m/e 116, Br_2 (▲) at m/e 160 and HCl (•) at m/e 36, with yields of 88, 4 and 18 %, respectively.

where A^*_{PTFE} is the effective Teflon surface of the sample support exposed to $BrONO_2$ in an uptake experiment: $A^*_{PTFE} = A_{PTFE} - A_s$. Typical corrections for k^{obs}_{uni} are of the order of 1 to 5 s^{-1}. For instance, $ClONO_2$ does not interact with Teflon under identical experimental conditions. Table 4.2 displays values of k^{PTFE}_{uni} of $BrONO_2$ for the different empty PTFE Teflon–coated sample supports we have used.

4.4 $BrONO_2$ on NaCl

We have performed steady–state (SS) and pulsed–valve (PV) uptake experiments on different types of solid NaCl. The stoichiometry of the reaction is given by equation (4.9):

$$BrONO_2(g) + NaCl(s) \rightarrow BrCl(g) + NaNO_3(s) \tag{4.9}$$

where BrCl is released from the NaCl sample. Typical SS and PV experiments are displayed in Figures 4.1 and 4.2, respectively.

When solid NaCl is exposed to $BrONO_2$ a rapid drop of the signal at m/e 95 is observed in SS experiments, which is correlated with a rapid increase of BrCl monitored at m/e 116. Br_2 (m/e 160) and HCl (m/e 36) are also observed which appeared both unexpectedly (Figure 4.1).

The average uptake coefficient of $BrONO_2$ which was determined according to $\gamma = \frac{k_{uni}}{\omega}$, where k_{uni} has been obtained by equation (4.8), is large and leads to a mean value

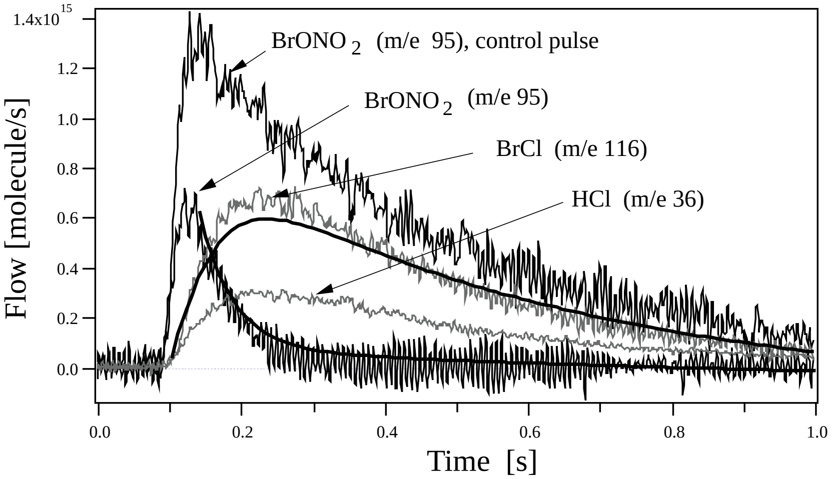

Figure 4.2: Typical pulsed valve uptake experiment of $BrONO_2$ on NaCl performed in the 14 mm diameter orifice reactor leading to $\gamma_0 = 0.30 \pm 0.09$. The dose of $BrONO_2$ is $4.7 \cdot 10^{14}$ molecules. Solid lines represent simulation results using the set of parameters of Table 4.7 on page 65.

of $\gamma_0 = 0.31 \pm 0.10$ which is obtained by considering all uptake experiments on all types of solid NaCl, such as powder, grain, thin film and single crystal using the 14, 8 and 4 mm diameter orifice reactor. The initial uptake coefficient γ_0 is independent of the flow rate of $BrONO_2$ entering the reactor ($F^i_{BrONO_2}$) and thus of the concentration of $BrONO_2$ into the reactor for a specific aperture. Because we observed no saturation of the sample during the experiments carried out on grain, powder and single crystal substrates, we will only consider the initial uptake coefficient γ_0, because $\gamma_{ss} = \gamma_0$, where γ_{ss} is the uptake coefficient at steady–state conditions.

Table 4.3: Initial uptake γ_0 for $BrONO_2$ + NaCl.

Salt–type	No of expts	γ_0
Grain	27	0.31 ± 0.12
Powder	6	0.33 ± 0.11
Sprayed thin film	11	0.32 ± 0.12
Single crystal	3	0.20 ± 0.10
	Weighted mean value:	0.31 ± 0.10

The value of γ_0 decreases by a factor of two in going from the 14 mm to the 4 mm orifice, which is not significantly different given the experimental uncertainty. These results allow us to draw the conclusion that for NaCl powder and grain γ_0 is independent

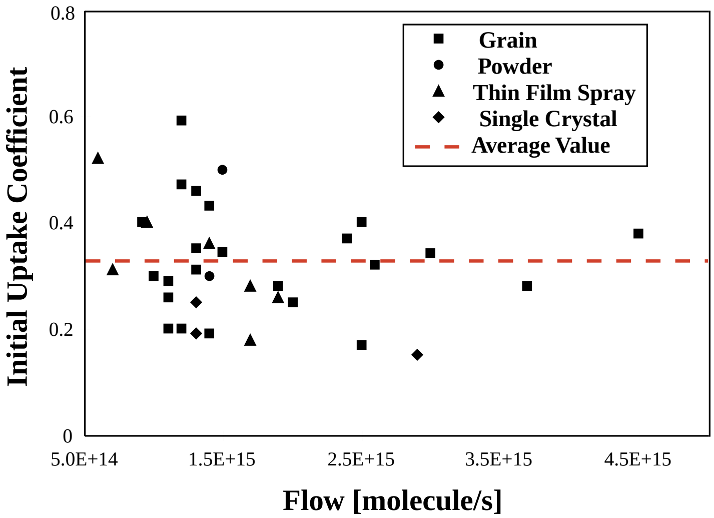

Figure 4.3: Initial uptake coefficient γ_0 of $BrONO_2$ interacting with different types of solid NaCl as a function of $F^{in}_{BrONO_2}$. The 14, 8 and 4 mm escape orifices have been used. The average γ_0 value is 0.31 ± 0.10 and is independent of $F^{in}_{BrONO_2}$ for grains and powder samples.

of $F^{in}_{BrONO_2}$ for all escape orifices confirming an apparent first–order rate law for the uptake rate constant k_{uni} obtained from equation (4.8). However, for samples of low surface area such as thin films and single crystal substrates, a decrease of γ_0 with increasing $F^{in}_{BrONO_2}$ is observed owing to saturation of the uptake in line with numerical modeling results discussed later (see Section 4.10).

The γ_0 values for $BrONO_2$ on all types of solid NaCl versus $F^{in}_{BrONO_2}$ are presented in Figure 4.3 and confirm the absence of a flow rate dependence for large surface area substrates. Table 4.3 shows the mean value of γ_0 for the four different types of substrates which is independent of sample presentation. The detailed data are presented in Table B.1 in Appendix B on page 173.

To confirm the absence of diffusion of $BrONO_2$ into the bulk of solid NaCl we have performed SS uptake experiments as a function of the mass of NaCl. No dependence of γ_0 on the mass of NaCl presented as grain and thin film samples has been observed as displayed in Figure 4.4.

This result is primarily a consequence of the high value of γ_0 which prevents $BrONO_2$ from diffusing into the bulk of the sample. In this case the pore diffusion theory proposed by Keyser *et al.* does not apply [Keyser, 1991, 1993] and no correction to the raw uptake data should be performed. The yield of the primary product BrCl is (80 ± 20) %, where the uncertainty limits are due to the calibration error of the MS–signal. Br_2 whose yield is of the order of 10 % may be generated in the self–reaction of $BrONO_2$ in analogy to HOBr reacting with NaCl [Mochida, 1998]. HCl may be formed as a secondary

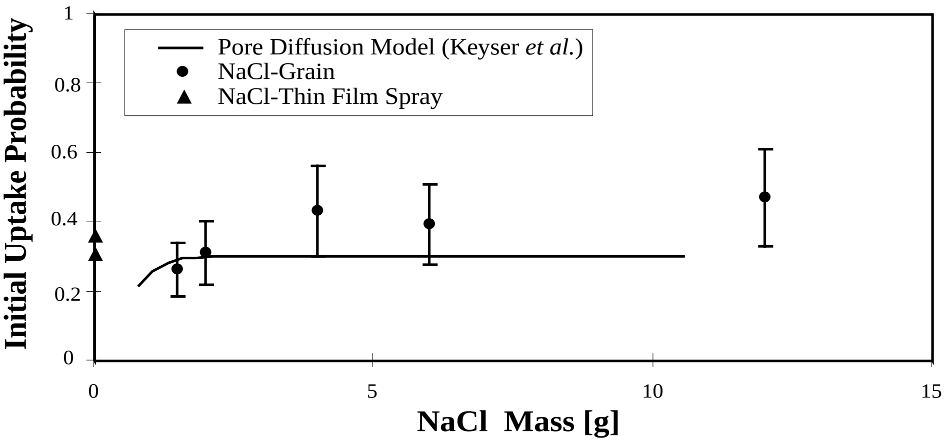

Figure 4.4: Mass dependence of γ_0 for $BrONO_2$ interacting with solid NaCl. The measured value of γ_0 for thin films of NaCl does not follow the pore diffusion model proposed by Keyser *et al.* [1991, 1993].

product from the hydrolysis of $BrONO_2$ leading to HNO_3 and HOBr. We propose a comprehensive mechanism starting with reaction (4.9), which is in competition with reactions (4.10) to (4.15):

$$BrONO_2(g) + H_2O(ads) \rightarrow HNO_3(g) + HOBr(g) \tag{4.10}$$

Reaction (4.10) is the hydrolysis of $BrONO_2$ taking place on the surface of NaCl and competes with the reaction of interest, reaction (4.9). No definite proof of reaction (4.10) can be given because neither HNO_3 nor HOBr are observed. The interaction of HNO_3 with solid NaCl rapidly leads to HCl [Fenter, 1994] and the heterogeneous reaction of HOBr on solid NaCl leads to BrCl [Mochida, 1998] according to reactions (4.11) and (4.12), respectively.

$$HNO_3(g) + NaCl(s) \rightarrow HCl(g) + NaNO_3(s) \tag{4.11}$$
$$HOBr(g) + NaCl(s) \rightarrow BrCl(g) + NaOH(s) \tag{4.12}$$

Br_2 may be formed in the self reaction of $BrONO_2$ in analogy to the heterogeneous reaction of HOBr on solid NaCl [Mochida, 1998]. The decomposition of $BrONO_2$ leads to the following products according to reactions (4.13) to (4.15).

$$2BrONO_2(g) \rightarrow Br_2O(g) + N_2O_5(g) \tag{4.13}$$
$$Br_2O(g) \rightarrow Br_2(g) + \frac{1}{2}O_2(g) \tag{4.14}$$
$$N_2O_5(g) + H_2O \rightarrow 2HNO_3(g) \tag{4.15}$$

HNO_3, obtained from the hydrolysis of N_2O_5, reacts on solid NaCl to HCl in reaction (4.11). However, Br_2 may also be generated in the self reaction of HOBr [Mochida, 1998] in addition to reaction (4.14). Both mechanisms probably contribute to the formation of Br_2. We have also performed some SS experiments of Br_2O interacting with solid NaCl in which Br_2O was monitored at m/e 176. The initial uptake coefficient γ_0 has been measured and is of the order of 10^{-2} [Santschi, 1999]. The uptake leads to the formation of Br_2, BrCl and HOBr with the main product in fact being Br_2. The most probable reaction path to Br_2 is the heterogeneous decomposition of Br_2O on solid NaCl according to reaction (4.14).

Table 4.4: Initial uptake γ_0 for $BrONO_2$ on non–reactive salts, such as $NaNO_3$ and Na_2SO_4.

Salt–type	Mass [g]	Flow [molecule/s]	γ_0	Br_2–Yield [%]
$NaNO_3$–grain	6.0	$1.0 \cdot 10^{15}$	0.53 ± 0.08	43 ± 13
$NaNO_3$–grain	6.1	$1.1 \cdot 10^{15}$	0.39 ± 0.08	35 ± 10
$NaNO_3$–grain	6.1	$1.2 \cdot 10^{15}$	0.39 ± 0.09	30 ± 9
$NaNO_3$–grain	6.0	$1.4 \cdot 10^{15}$	0.24 ± 0.10	38 ± 11
$NaNO_3$–grain	6.0	$1.9 \cdot 10^{15}$	0.20 ± 0.11	35 ± 10
$NaNO_3$–grain	8.0	–	0.21 ± 0.08	–
Na_2SO_4–grain	6.0	$2.8 \cdot 10^{15}$	0.21 ± 0.11	38 ± 11
Na_2SO_4–grain	7.0	–	0.20 ± 0.10	–

4.5 $BrONO_2$ on $NaNO_3$ and Na_2SO_4

To clearly obtain proof of the decomposition pathway, we performed LIF (Laser Induced Fluorescence) investigations of NO_2 ($\lambda_{\text{exc}} = 440$ nm) combined with uptake experiments of $BrONO_2$ on non–reactive salts such as $NaNO_3$ and Na_2SO_4. We use LIF detection to unambiguously monitor NO_2, because all possible decomposition products, such as NO, NO_2, N_2O_5 or HNO_3 all contribute to m/e 46. The mean values of the uptake coefficients of $BrONO_2$ on these non–reactive salts are $\gamma_0 = 0.33 \pm 0.12$ and $\gamma_0 = 0.20 \pm 0.01$ on $NaNO_3$ and Na_2SO_4, respectively, where uncertainties are one standard deviation. Uptake experiments are summarized in Table 4.4.

When we start the uptake experiment by lifting the plunger we observed a rapid decrease of the partial pressure of $BrONO_2$ and the prompt appearance of the reaction products Br_2 and BrCl. The latter, whose yield is less than 5 %, is probably due to contamination of the salt sample with chloride. The yield of Br_2 is (37 ± 11) % so that the bromine mass balance is closed within experimental uncertainty. We undertook LIF detection of NO_2 during $BrONO_2$ uptake experiment on non–reactive salts in order to detect the possible formation of NO_2 or N_2O_5. No NO_2 has been found beyond the detection limit of $2.0 \cdot 10^9$ molecule/cm^3. A Na_2SO_4 sample which was previously exposed to $BrONO_2$ gave rise to a MS–signal at m/e 46 during heating in situ up to 500 K. This same signal at m/e 46 was absent when a pure Na_2SO_4 sample was heated in situ in the absence of $BrONO_2$. Similar experiments on $NaNO_3$ were inconclusive because control experiments with neat $NaNO_3$ also resulted in a MS–signal at m/e 46, probably owing to decomposition. Under the assumption that the MS–signal at m/e 46 corresponds to HNO_3, the product of hydrolysis, we are able to close the nitrogen mass balance in the experiments of $BrONO_2$ interacting with Na_2SO_4.

4.6 $BrONO_2$ on KBr

SS and PV experiments have been performed following reaction (4.16) on KBr substrates whose presentation included grain, sprayed thin film and single crystal:

$$BrONO_2(g) + KBr \rightarrow Br_2(g) + KNO_3(s) \tag{4.16}$$

where Br_2 is released from the KBr sample. Figure 4.5 displays a typical SS experiments of the interaction of $BrONO_2$ with solid KBr grains with the reactor orifice set at 14 mm, while Figure 4.6 displays a typical PV experiment using the same reactor orifice. We have performed a few experiments using the 4 mm diameter orifice, but we realized that the kinetics of reaction (4.16) was too rapid to extract a γ_0 value.

The observed products were Br_2 monitored at m/e 160, which is the main product of the interaction, and HBr detected at m/e 82, which results from the hydrolysis of $BrONO_2$ in a secondary reaction in analogy to the formation of HCl in experiments involving NaCl (reaction (4.11)). HBr has not been observed in PV experiments (Figure 4.6).

Table 4.5 presents a summary of the whole set of data (Table B.2 in Appendix B) of the γ_0 values of $BrONO_2$ with KBr and leads to the following conclusions. First, the mean value of γ_0 is constant and independent of the flow rate with $\gamma_0 = 0.32 \pm 0.09$, a result displayed in Figure 4.7. This points to an apparent first order rate law for the uptake of $BrONO_2$ on solid KBr as was the case for solid NaCl. Second, we observed a decrease in the yield of Br_2 with increasing flow rate as shown in Figure 4.8. At low

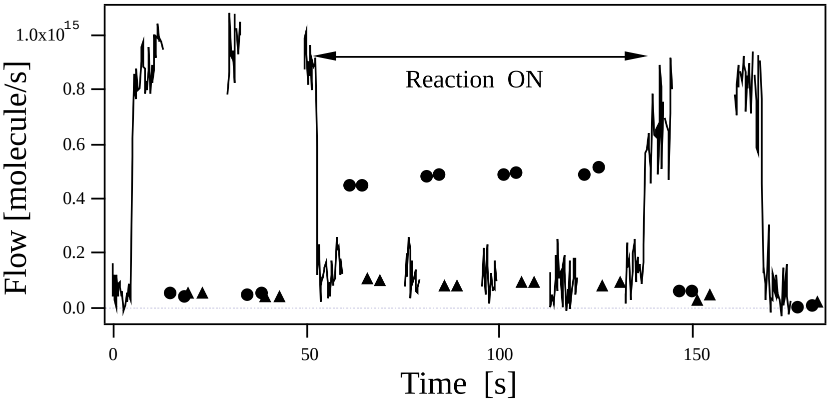

Figure 4.5: Typical steady state uptake experiment of $BrONO_2$ on KBr performed in the 14 mm diameter orifice reactor at $F^i_{BrONO_2} = 0.9 \cdot 10^{15}$ molecule s^{-1} leading to $\gamma_0 = 0.30 \pm 0.11$. $BrONO_2$ (solid line) is monitored at m/e 95, Br_2 (●) at m/e 160 and HBr (▲) at m/e 82. The Br_2 and HBr yields are 70 % and 11 %, respectively.

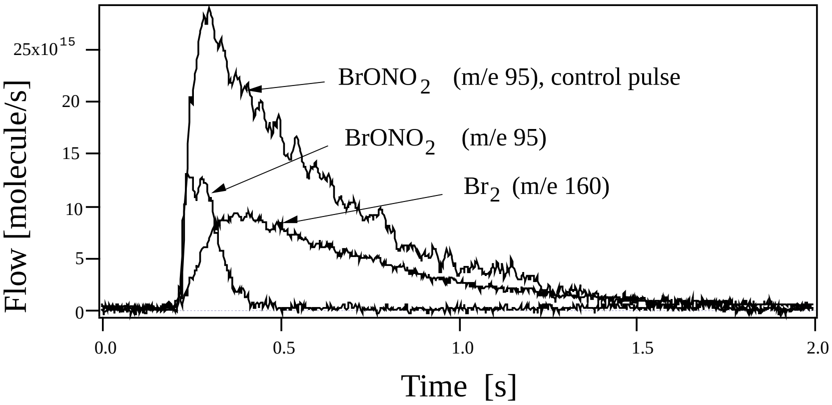

Figure 4.6: Typical pulsed valve uptake experiment of $BrONO_2$ on KBr performed in the 14 mm diameter orifice reactor leading to $\gamma_0 = 0.38 \pm 0.11$ using a dose of $BrONO_2$ is $1.2 \cdot 10^{16}$ molecules. No HBr was detected in the PV experiments. The Br_2 yields is 52 %.

flow rates of up to $1.0 \cdot 10^{15}$ molecule·s^{-1}, the Br_2–yield is (70 ± 10)% and drops to (45 ± 5) % for high values of $F^i_{BrONO_2}$.

We conclude that at high flow rates of $BrONO_2$ the self–reaction (4.13) of $BrONO_2$ leading to decomposition is increasingly competing with the heterogeneous reaction on KBr (reaction (4.16)). We therefore propose a mechanism consisting of the heterogeneous reaction (4.16) of $BrONO_2$ on KBr, hydrolysis (4.10) and self–reaction (4.13) of $BrONO_2$ taking place on the salt surface. Both products of $BrONO_2$ hydrolysis given in reaction (4.10) react with KBr. The interaction of HNO_3 with KBr [Fenter, 1994], reaction (4.17), and the heterogeneous reaction of HOBr with solid KBr, reaction (4.18) [Mochida, 1998], have been studied in detail before:

Table 4.5: Initial uptake γ_0 for $BrONO_2$ + KBr.

Salt–type	No of expts	γ_0
Grain	27	0.34 ± 0.12
Sprayed thin film	5	0.29 ± 0.11
Single crystal	1	0.20 ± 0.10
	Weighted mean value:	0.32 ± 0.09

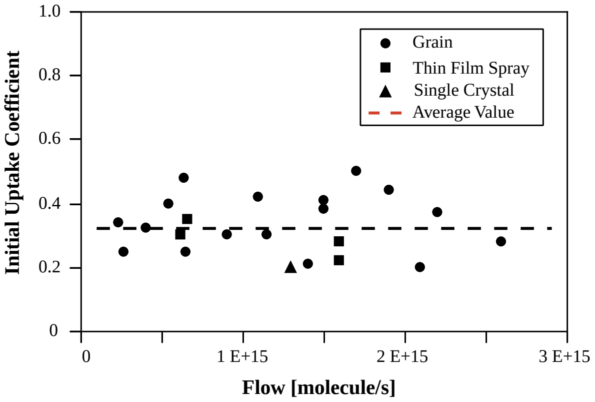

Figure 4.7: Initial uptake coefficient γ_0 of $BrONO_2$ interacting with different types of solid KBr as a function of $F^i_{BrONO_2}$. The 14 and 8 mm escape orifice have been used. The average γ_0 value is 0.32 ± 0.09 and is independent of $F^i_{BrONO_2}$ for salt grain.

$$HNO_3(g) + KBr(s) \rightarrow HBr(g) + KNO_3(s) \tag{4.17}$$

$$HOBr(g) + KBr(s) \rightarrow Br_2(g) + KOH(s) \tag{4.18}$$

The HBr released in reaction (4.17) is only observed in SS experiments. The HBr–yield decreases with increasing $F^i_{BrONO_2}$ as has been observed for Br_2 formed in reaction (4.16). We assume that Br_2 is in part formed in the self reaction of $BrONO_2$ as outlined in reactions (4.13) and (4.14). In conclusion, there may be three source reactions for Br_2, namely reaction (4.14), (4.16) and (4.18), and one reaction releasing HBr following reaction (4.17).

4.7 $ClONO_2$ on NaCl and KBr

The heterogeneous interaction of $ClONO_2$ with solid NaCl [Finlayson–Pitts, 1989; Timonen, 1994; Caloz, 1996] and KBr [Caloz, 1996] leading to halogen exchange products

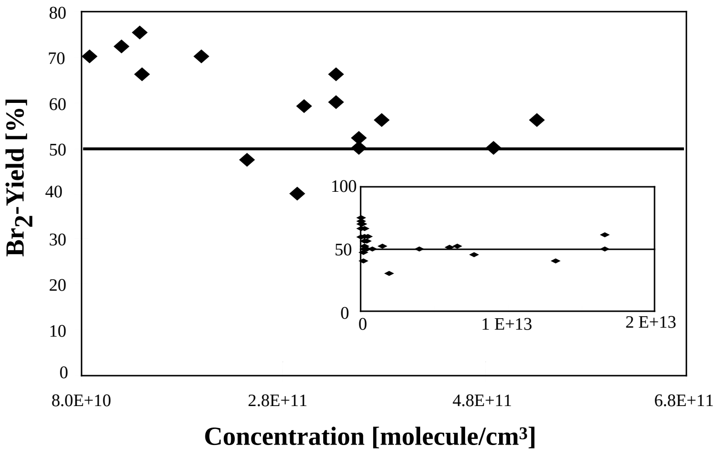

Figure 4.8: Br_2–yield for the heterogeneous reaction of $BrONO_2$ on KBr. At small $BrONO_2$ concentrations of the order of 0.9 to $2 \cdot 10^{11}$ molecule $\cdot$ cm^{-3} the yield is (70 ± 10) % and at larger concentrations of up to $2 \cdot 10^{13}$ molecule $\cdot$ cm^{-3} the yield drops to a limiting value of (50 ± 20) %. The insert shows the Br_2–yield on a large concentration scale.

Cl_2, Br_2 and BrCl has been studied before. It proceeds according to the following reactions:

$$ClONO_2(g) + NaCl(s) \rightarrow Cl_2(g) + NaNO_3(s) \tag{4.19}$$

$$ClONO_2(g) + KBr(s) \rightarrow BrCl(g) + KNO_3(s) \tag{4.20}$$

In this Section, we present additional experiments on solid NaCl and KBr in order to study potential heterogeneous decomposition pathways of $ClONO_2$ which are becoming apparent at longer residence times using the 14 and 8 mm diameter escape orifices of the Knudsen cell. To this end we have also performed experiments on non–reactive samples, such as $NaNO_3$ and Na_2SO_4 (Section 4.8), in order to gauge the importance of the heterogeneous decomposition pathway in relation to the heterogeneous halogen exchange reaction.

Figure 4.9 shows a typical SS experiment on KBr together with the rate of formation of BrCl, Br_2 and KBr.

The heterogeneous reaction of $ClONO_2$ on NaCl, reaction (4.19), only leads to Cl_2 which is formed with a yield of 103 ± 15 %. The initial uptake coefficients are displayed in Table B.3 in Appendix B. The average rate of uptake is $\gamma_0 = 0.10 \pm 0.05$, independent of $F^{in}_{ClONO_2}$, which confirms a rate law first order in $ClONO_2$ and agrees with the previously measured value of $\gamma = 0.23 \pm 0.06$ [Caloz, 1996]. The reaction of $ClONO_2$ with KBr is more complex than the one on NaCl. The detected products are Br_2, Cl_2 and BrCl in order of their appearance, which has been established in PV experiments.

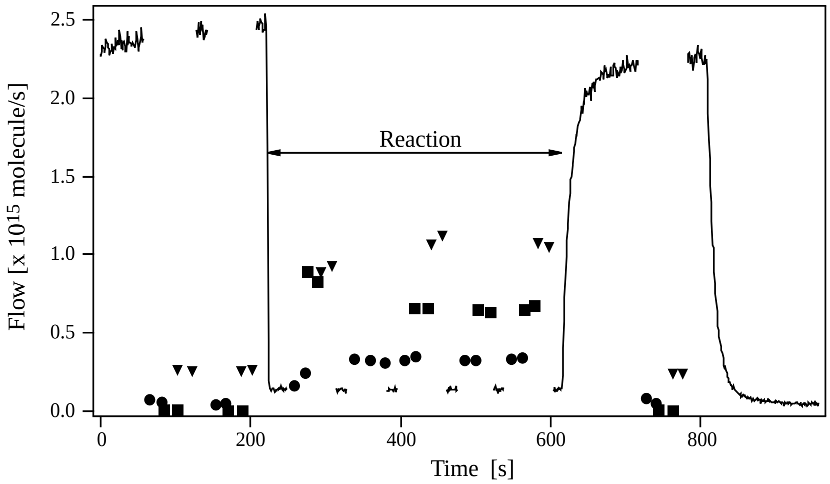

Figure 4.9: Typical steady state experiment of $ClONO_2$ on KBr–powder consisting of grains in the range 160–250 μm using the 4 mm diameter orifce reactor. $F^{in}_{ClONO_2} = 2.5 \cdot 10^{15}$ molecule/s (solid line) corresponding to a concentration of $2.8 \cdot 10^{12}$ molecule/cm^3 led to an uptake coefficient $\gamma_0 = 0.13 \pm 0.08$. The Br_2 (■), Cl_2 (▼) and BrCl (•) yields are (35 ± 10) %, (40 ± 12) % and (15 ± 7) %, respectively.

When $ClONO_2$ reacts with KBr, BrCl is expected to be the primary product generated in a 100 % yield according to reaction (4.20).

The secondary reaction (4.21) converts BrCl to Br_2 in a fast reaction whose initial uptake coefficient is given in Table 4.6. As an example, $\gamma_0 = 0.14 \pm 0.05$ for reaction (4.21) in the 4 mm diameter orifice reactor. When sufficient KCl has accumulated on the sample surface, $ClONO_2$ also reacts with KCl to form Cl_2 following reaction (4.22).

$$\begin{aligned} BrCl(g) + KBr(s) &\rightarrow Br_2(g) + KCl(s) && (4.21) \\ ClONO_2(g) + KCl(s) &\rightarrow Cl_2(g) + KNO_3(s) && (4.22) \\ Cl_2(g) + KBr(s) &\rightarrow BrCl(g) + KCl(s) && (4.23) \end{aligned}$$

Cl_2 formed in reaction (4.22) may then react on KBr to release additional amounts of BrCl according to reaction (4.23). Table B.3 in Appendix B displays the uptake coefficients γ_0 of $ClONO_2$ interacting with NaCl and KBr which are in good agreement with the values obtained by Caloz *et al.* [1996] for the large orifice reactor and Koch *et al.* [1998] using the diffusion tube technique. The uptake kinetics of $ClONO_2$ on solid NaCl and KBr using the 4 mm diameter aperture reactor are also displayed in Table B.3. As was the case for $BrONO_2$ we note a decrease of γ_0 by a factor of two upon increasing the gas phase residence time approximately by a factor of 10. Figure 4.10 displays the yields of Br_2, Cl_2 and BrCl for the interaction of $ClONO_2$ with KBr as a function of

Table 4.6: Kinetics of Cl_2, Br_2 and BrCl on NaCl and KBr resulting from pulsed valve experiments.

Gaseous Species	Orifice [mm]	γ_{NaCl}	γ_{KBr}
Cl_2	14	n.u.	$3.0 \cdot 10^{-2}$
	4	n.u.	$2.4 \cdot 10^{-2}$
Br_2	14	$4.0 \cdot 10^{-3}$	$3.0 \cdot 10^{-3}$
	8	n.u.	–
	4	n.u.	$3.0 \cdot 10^{-3}$
BrCl	14	$6.0 \cdot 10^{-2}$	–
	8	$3.0 \cdot 10^{-2}$	–
	4	$1.0 \cdot 10^{-2}$	$1.4 \cdot 10^{-1}$

n.u. = no uptake

the concentration of $ClONO_2$ in the 4 mm diameter orifice reactor. At low values of of typically 10^{14} molecule/s Br_2–formation in 100 % yield is observed. With increasing $F^{in}_{ClONO_2}$ a gradual appearance of Cl_2 and BrCl is observed. These observations are in qualitative agreement with the mechanism proposed above.

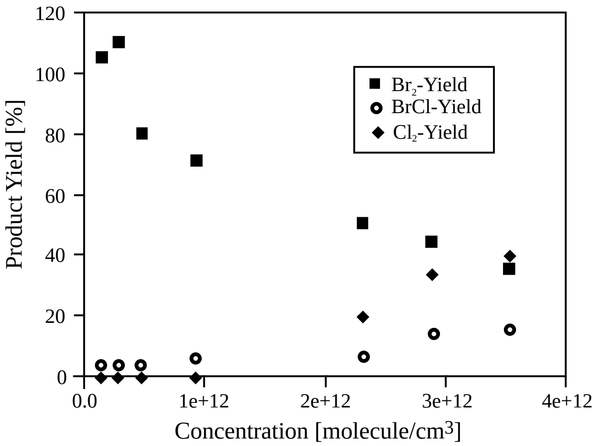

Figure 4.10: Product yields from steady state experiments for the interaction of $ClONO_2$ on KBr as a function of the concentration of $ClONO_2$. At low [$ClONO_2$], Br_2 is observed in 100 % yield, whereas the Br_2–yield (■) decreases at high [$ClONO_2$] and Cl_2 (◊) and BrCl (•) both start to appear.

4.8 $ClONO_2$ on $NaNO_3$ and Na_2SO_4

We have performed experiments of $ClONO_2$ on non–reactive salts such as $NaNO_3$ and Na_2SO_4. Figure 4.11 displays a typical experiment of $ClONO_2$ interacting with $NaNO_3$.

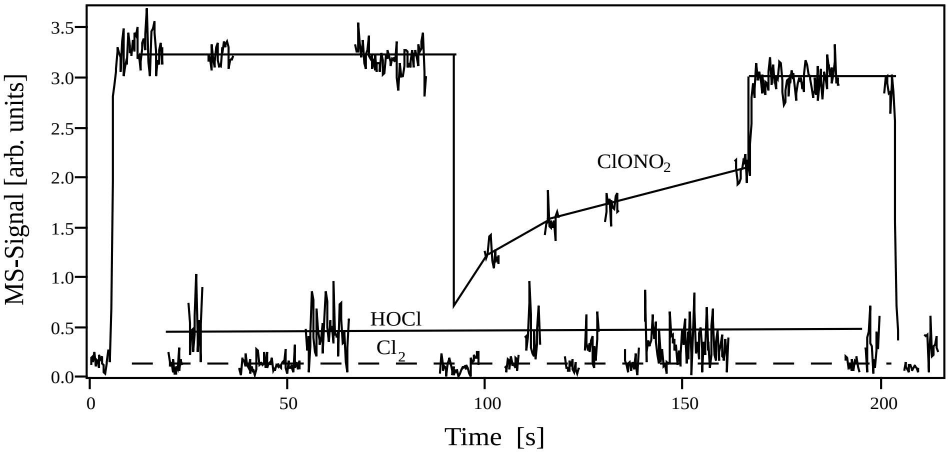

Figure 4.11: The heterogeneous interaction of $ClONO_2$ on non–reactive salt $NaNO_3$. The initial uptake coefficient is $\gamma_0 = 0.20 \pm 0.08$ for the 14 mm diameter orifice reactor using $F^{i}_{ClONO_2} = (3.0 \pm 0.2) \cdot 10^{15}$ molecule/s. HOCl is only observed when significant amounts of H_2O are adsorbed on $NaNO_3$. HOCl is not found when $NaNO_3$ is dried by prolonged pumping at 10^{-5} Torr at 300 K.

An average uptake coefficient of $\gamma_0 = 0.24 \pm 0.10$ has been observed on both solid salts, with the detailed results displayed in Table B.4 in Appendix B. On Na_2SO_4, the product of the decomposition, Cl_2, was observed at a yield of (27 ± 7) %, which is not negligible. Contrary to $BrONO_2$, where the Br_2 mass balance is closed, only a little more than half of the chlorine is accounted for. We expected HOCl as a product of the $ClONO_2$ hydrolysis taking place on the solid salt surface but observed none when the salt had been pumped overnight. A yield of approximately 10 % of HOCl was observed on"wet“ salt (see Table B.4). With no ionic exchange taking place in these experiments, we observe a pronounced saturation of the sample surface (Figure 4.11). We conclude from these control experiments that the hydrolysis of $ClONO_2$ is too slow to be competitive with the effusion out of the Knudsen reactor thus leading to the conclusion that $ClONO_2$ is more stable than $BrONO_2$. However, $ClONO_2$ may heterogeneously decompose to Cl_2 even on reactive salt substrates which has not been observed before. The uptake coefficients of $ClONO_2$ on salt obtained in the present work are in good agreement with the literature [Caloz, 1996; Koch, 1998] and are of the same order of magnitude as the results obtained in the flow tube experiments performed by Timonen *et al.* [1994]. They found Cl_2 as the sole product with an uptake coefficient of

$\gamma = (4.6 \pm 3.0) \cdot 10^{-3}$ after correction for internal diffusion. Timonen *et al.* conclude that the true uptake coefficient γ is about 20 times smaller than the values reported here for the reaction (4.2) [Timonen, 1994]. Owing to the large value of γ_0 it is not possible to test the pore diffusion theory as displayed in Figure 4.4. We insist that it is inappropriate to apply a correction to the raw data obtained by Timonen *et al.* [1994]. We therefore compare their raw data with our values for γ_0. In fact, we note a good agreement between the two data sets.

4.9 The Role of Water

In order to study the role of H_2O in the heterogeneous reaction of $BrONO_2$ and $ClONO_2$ on salt, we generally used spray deposited thin film substrates of 3 to 10 mg mass. Using the high temperature support up to temperatures of 550 K one may observe the desorption of water absorbed on the salt sample. The sample is heated in vacuum until no more H_2O desorption is observable. The amount of H_2O desorbing from the surface of a fresh KBr–sprayed thin film sample which had been pumped for 15 minutes before the start of the thermal desorption experiment is approximately $1.2 \cdot 10^{19}$ molecules, which corresponds to 10^5 formal monolayers of H_2O. If the same type of sample had been pumped at 10^{-5} Torr over night at ambient temperature the amount of H_2O that could be thermally desorbed is approximately $5 \cdot 10^{17}$ molecules corresponding to $5 \cdot 10^3$ formal monolayers, a factor of 20 lower than the quantity desorbed from a sample pumped for only 15 minutes. We conclude that there remains a sufficient amount of H_2O on the sample which may enable heterogeneous reactions involving ionic exchange reactions even if the sample had been pumped for long periods of time at pressures less than 10^{-5} Torr.

Figure 4.12 shows results on $BrONO_2$ interacting with a sprayed thin film of NaCl at constant $F^{i}_{BrONO_2}$. The first experiment ("wet“ case) represents the uptake of $BrONO_2$ on a NaCl sample which was pumped overnight (Figure 4.12(a)) whereas the second ("dry“ case) displays $BrONO_2$ uptake on a sample which has gone through a heating cycle prior to exposure and had therefore lost a few hundred monolayers of absorbed H_2O (Figure 4.12(b)). In both cases the same value of $\gamma_0 = 0.30 \pm 0.09$ has been observed similar to results on the interaction of NO_3 with alkali halide salts obtained by Seisel *et al.* [1999]. In this case there is no change of γ as opposed to what Davies *et al.* [1998] and De Haan *et al.* [1997] have observed in the study of the heterogeneous reaction of HNO_3 with NaCl and synthetic sea salt, respectively. As shown by Finlayson–Pitts and co–workers the decrease of γ as a function of the sample heating

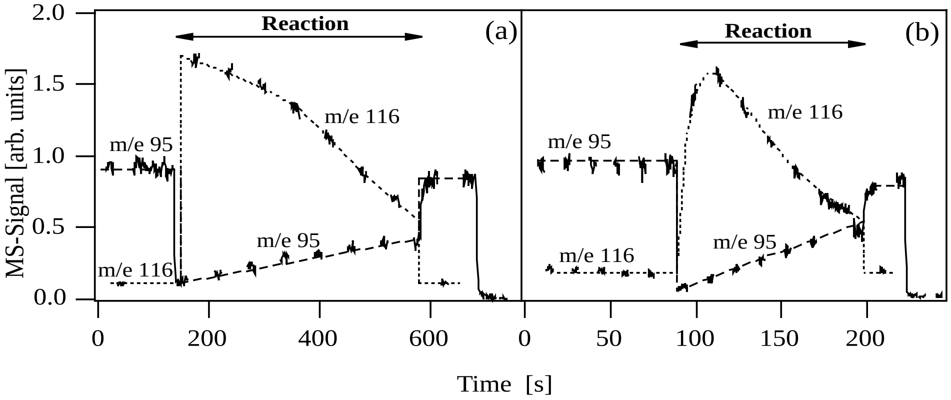

Figure 4.12: The role of absorbed H_2O in the reaction of $BrONO_2$ on a spray–coated thin film of NaCl. For both experiments $F^i_{BrONO_2} = 1.2 \cdot 10^{15}$ molecule/s monitored at m/e 95. (a) Prompt rate of formation of BrCl (m/e 116) an a freshly prepared salt sample, which had not been heated. (b) Delayed rate of formation of BrCl (m/e 116) using a previously heated sample. In the two experiments, the uptake coefficient of $BrONO_2$ remains the same.

time appears approximately after 4 hours. In our uptake experiments the salt samples have been heated between 40 minutes and 2 hours, enough to restore the H_2O partial pressure to background levels. We conclude that the experimental conditions of De Haan and Finlayson–Pitts and the present ones are probably equivalent as far as the H_2O content of the sample is concerned. This leads us to the interesting conclusion that γ_0 of $BrONO_2$ interacting with salt depends less on the amount of H_2O absorbed on the surface than γ_0 of HNO_3 on salt. Although we observe no change in γ_0 between dry and wet conditions, the rate of formation of the main product BrCl in the dry case is delayed with respect to the wet case where BrCl promptly appears after the start of the uptake experiment. In addition, saturation of the uptake appears more rapidly in the dry case (Figure 4.12(b)). The BrCl partial pressure decreases on the time scale of 2 minutes which we attribute to the build–up of $NaNO_3$ and which slows down the reaction in the dry case. In comparison, we still observe the formation of BrCl after 7 minutes in the wet case, Figure 4.12(a). The present results confirm the importance of water in heterogeneous ionic exchange reactions in good agreement with the work of Finlayson–Pitts and co–workers who expounded on the role of a quasi–liquid layer (QLL) on top of the sample surface [Beichert, 1996], which is now believed to be concentrated on specific defects of the crystal structure [De Haan, 1997]. Some authors postulate that H_2O is trapped on surface defects which leads to the presence of small "pools" on the sample surface [Davies, 1998; Weis, 1999]. Product nitrate, remaining on the sample surface, recrystallizes to form separate microcrystallites [Davies, 1998; Allen, 1996] which have been experimentally observed with increasing extent of reaction.

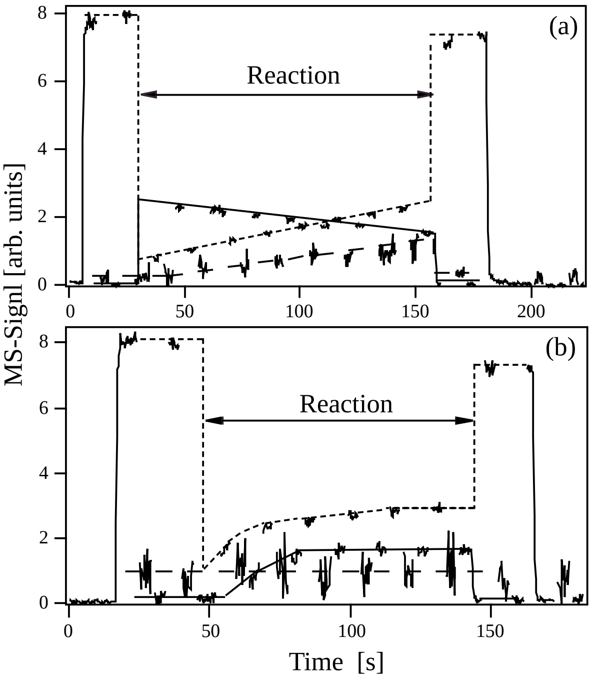

Figure 4.13: The role of absorbed H_2O in the reaction of $ClONO_2$ on Na_2SO_4–powder. For both experiments $F^i_{ClONO_2} = 9.0 \cdot 10^{15}$ molecule/s (dotted line). (a) Sample pumped for 15 minutes prior to uptake experiment and Cl_2 (solid line) appears promptly. A low rate of formation of HOCl (dashed line) is also observed. (b) Sample pumped in the reactor overnight at 10^{-5} Torr at 300 K. No HOCl observed and formation of Cl_2 is delayed compared to "wet" case displayed in panel (a).

Figure 4.13 displays the results of the uptake of $ClONO_2$ on non–reactive Na_2SO_4–powder. Figure 4.13(a) shows an experiment performed on Na_2SO_4 pumped for only 15 minutes. We note a rapid decrease of the MS–signal for $ClONO_2$ corresponding to a high value of $\gamma_0 = 0.32 \pm 0.07$. Cl_2 immediately appears and a low rate of formation of HOCl resulting from the hydrolysis of $ClONO_2$ is also observed with approximate yields of Cl_2 and HOCl of 35 % and 10 %, respectively. In Figure 4.13(b), $ClONO_2$ uptake on dry Na_2SO_4–powder pumped overnight and heated for 1 hour prior to the uptake experiment is displayed. Approximately 30 formal monolayers of water have been desorbed upon heating with an incandescent lamp (dry case). The value of γ_0 of $ClONO_2$ for the dry case is similar to the wet case. The saturation of $ClONO_2$ uptake on the dry surface appears more quickly and no prompt formation of Cl_2 has been observed, in agreement with the results on $BrONO_2$ uptake on NaCl presented above. In addition, no formation of HOCl has been observed in the dry case (Figure 4.13(b)). In conclusion, it seems that H_2O has a catalytic effect on heterogeneous reactions of ionic exchange on salts, in agreement with what has been observed before [Beichert, 1996; Davies, 1998; De Haan, 1997; Weis, 1999].

4.10 Modelling of Experimental Results

In order to understand the mechanism of the heterogeneous interaction of $BrONO_2$ and $ClONO_2$ with solid alkali substrates, we fitted the experimental results to the Langmuir–Hinshelwood model of adsorption which will be used throughout this work [Adamson, 1976]. We consider that the gas molecules interact with a surface site (ss) located on the salt surface in an effective bimolecular reaction whose rate is proportional to the number of free surface sites and the concentration of the molecules in the gas phase. The model used in this study is described by the following equations:

$$G + ss \leftrightarrows L \qquad k_1, k_2 \tag{4.24}$$

$$G + ss \leftrightarrows A \qquad k_3, k_4 \tag{4.25}$$

$$A \rightarrow P + Q + ss \qquad k_5 \tag{4.26}$$

where G is the gas phase species, ss is a free surface site, L is an adsorbed species on the surface which does not react, A is an adsorbed species which leads to formation of products, P is the product released into the gas phase and Q is a solid product which remains on the substrate surface. In this model, we consider two paths for the loss of G: $BrONO_2$ or $ClONO_2$ adsorb to the surface on two different types of surface sites characterized by k_1 and k_3. One fraction of $BrONO_2$ adsorbed on the salt leads to a species (L) which will not react and therefore will only lead to surface saturation. The other fraction generates a reactive adsorbed state described by A in the model which will react with the ions present in the QLL or on defect sites of the sample surface leading to products. Once A has reacted, a surface site ss is returned to the interface in process k_5 and may partake in renewed adsorption. The adjustable parameters in this model are the five kinetic constants (k_1 to k_5) and the total number of ss (S_0). The best fit has been obtained using the set of kinetic parameters displayed in Table 4.7 in which we present the parameters expressed in two unit systems.

The first one (bold characters) is the unit system for our experimental configuration and its surface to volume ratio. The second represents the parameters expressed in transferable units, which corresponds to unit surface–to–volume ratio, independent of the system used to perform the uptake experiment. A description of both unit systems has been presented by Tabor *et al.* [1994]. The term $(k_1 + k_3)S_0$ corresponds to the rate of loss of G and is equal to 17 s^{-1} which leads to $\gamma_0 = 0.34$. This is the experimental

Table 4.7: Set of kinetic parameters used in the modelling.

Parameter	Units [(a)]	Numerical Value [(a)]
S_0	**molecule**	$\mathbf{1.00 \cdot 10^{16}}$
	molecule · cm^2	$5.10 \cdot 10^{14}$
k_1	$\mathbf{molecule^{-1} \cdot s^{-1}}$	$\mathbf{1.00 \cdot 10^{-15}}$
	$cm^2 \cdot molecule^{-1} \cdot s^{-1}$	$1.96 \cdot 10^{-14}$
k_2	$\mathbf{s^{-1}}$	**2.00**
	$cm^{-1} \cdot s^{-1}$	$2.20 \cdot 10^{-2}$
k_3	$\mathbf{molecule^{-1} \cdot s^{-1}}$	$\mathbf{7.00 \cdot 10^{-16}}$
	$cm^2 \cdot molecule^{-1} \cdot s^{-1}$	$1.37 \cdot 10^{-14}$
k_4	$\mathbf{s^{-1}}$	$\mathbf{5.00 \cdot 10^{-2}}$
	$cm^{-1} \cdot s^{-1}$	$5.50 \cdot 10^{-3}$
k_5	$\mathbf{s^{-1}}$	**30.0**
	$cm^{-1} \cdot s^{-1}$	$3.30 \cdot 10^{-1}$

(a) Bold characters represent the rate constants expressed for the present experimental system, the others are transferable units for unity surface–to–volume ratio.
Rate constants in units of $cm^{-1} \cdot s^{-1}$ are calculated using the value
$A_s/V = 19.6/1830 = 1.1 \cdot 10^{-2}$ cm^{-1}.

mean value of γ_0 for both $BrONO_2$ + NaCl and $BrONO_2$ + KBr obtained in this study. The rate of evaporation of G from the sample surface is given by k_2 and k_4 which are small compared to k_5. This is consistent with the fact that no evaporation of $BrONO_2$ has been observed experimentally once $F^i_{BrONO_2}$ was abruptly halted. In addition, no regeneration of surface sites is observed when $F^i_{BrONO_2}$ is halted, which indicates surface poisoning to a certain degree, probably owing to the build–up of nitrate (Q). The rate of appearance of P is given by k_5, which is high as revealed in Figure 4.14.

We use $S_0 = 10^{16}$ for a surface area of 20 cm^2 as the initial condition. The surface processes compete against the rate of escape of the gaseous species G and P. By varying the rate of escape of G and P we may simulate the different orifices of the flow reactor. In the interest of simplicity we have neither taken into account the hydrolysis of G nor the self–reaction of reactants, reactions (4.10) and (4.13), respectively. The results obtained in the modeling calculations are displayed in Figures 4.14 and 4.2 (page 50). Figure 4.14 shows the simulations performed for typical SS experiments. Panel a and b display uptake experiments of the reaction $BrONO_2 + NaCl \rightarrow BrCl + NaNO_3$ for

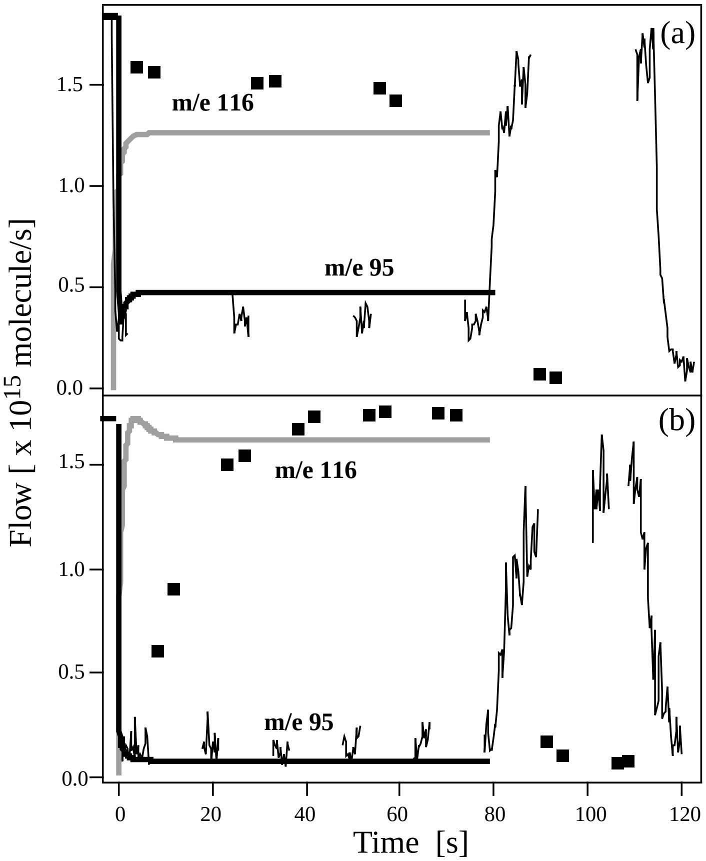

Figure 4.14: Modelling of typical SS experiments. Comparison of experiment and model (lines). (a) Simulation results for the interaction of $BrONO_2$ (m/e 95, solid bold line) on NaCl–powder for the 14 mm diameter orifice and $F^i_{BrONO_2} = 1.8 \cdot 10^{15}$ molecule/s, BrCl monitored at m/e 116 (broken line). (b) Simulation results for the interaction of $BrONO_2$ (m/e 95, solid bold line) on NaCl–powder for the 4 mm diameter orifice and $F^i_{BrONO_2} = 1.7 \cdot 10^{15}$ molecule/s using the same set of parameters as in case (a). See Table 4.7 for the list of the different parameters.

the 14 and 4 mm diameter orifice, respectively. One notes that the calculated curves fit the experimental results of the SS and PV experiments in the 14 mm diameter orifice, Figure 4.14(a) and Figure 4.2, quite well. Using the set of parameters presented in Table 4.7 which best fit our experimental data obtained in the 14 mm reactor one notes that the initial uptake calculated for the 4 mm reactor is well reproduced but that the modeled rate of BrCl formation is too fast which is not unexpected owing to the extreme simplicity of the used reaction mechanism. Table 4.6 shows that BrCl reacts on NaCl according to a γ of 0.01 in the 4 mm escape reactor. However, the secondary reaction of BrCl with NaCl have not been taken into account in this model which may explain the prompt rate of formation of BrCl in the simulations in the 4 mm escape reactor.

Table 4.8 displays values of the modeled γ_0 as a function of $F^i_{BrONO_2}$. Generally, it is

Table 4.8: Calculated γ_0 for the interaction of $BrONO_2$ with NaCl.

Experiment type	Orifice [mm]	Flow [molecule/s]	Dose [molecule]	γ_0^{sim}	γ_0^{exp}
SS	14	$1.0 \cdot 10^{13}$		0.22	–
SS	14	$9.1 \cdot 10^{13}$		0.20	–
SS	14	$9.1 \cdot 10^{14}$		0.20	0.40
SS (a)	14	$1.6 \cdot 10^{15}$		0.22	0.29
SS	14	$3.0 \cdot 10^{15}$		0.19	0.34
SS	14	$1.0 \cdot 10^{16}$		0.16	–
SS	14	$1.0 \cdot 10^{17}$		0.02	–
PV (b)	14		$4.7 \cdot 10^{14}$	0.29	0.31
SS (c)	4	$1.6 \cdot 10^{15}$		0.12	0.19
SS	4	$2.5 \cdot 10^{15}$		0.11	0.17
PV	4		$1.1 \cdot 10^{15}$	0.30	0.22

(a) Experiment displayed in Figure 4.14(a).

(b) Experiment displayed in Figure 4.2 on page 50.

(c) Experiment displayed in Figure 4.14(b).

seen that the model adsorption parameters simultaneously reproduce the experimental uptake rate for both orifice reactors, 14 mm and 4 mm. The model exhibits a small decrease of γ for the 4 mm diameter orifice reactor which is in fact experimentally observed. At high flow rates of the order of 10^{17} molecule/s, the model results predict $\gamma_0 = 0.02$, which we confirmed experimentally. This means that the saturation of the surface sites is increasing in importance at those high $BrONO_2$ flow rates.

4.11 Conclusion

The heterogeneous reaction and the hydrolysis of $BrONO_2$ or $ClONO_2$ leads to halogen activation. These reactions convert inorganic that is inactive halogens to active ones in the troposphere. This contributes to an increase of the halogen concentration and therefore to a change of the oxidizing potential of the troposphere and enhances the importance of halogen–based catalytic cycles responsible for ozone depletion.

We have measured the uptake coefficients of $BrONO_2$ on solid NaCl and KBr for the first time. BrCl, Br_2 and HCl are observed as products for the $BrONO_2$ reaction with NaCl, whereas Br_2 and HBr are the observed products in the reaction of $BrONO_2$ with KBr. The mean values of the uptake coefficients for $BrONO_2$ on NaCl and KBr are $<\gamma_0>= 0.31 \pm 0.10$ and $<\gamma_0>= 0.32 \pm 0.09$, respectively. The kinetics of $BrONO_2$ on reactive salts do not depend on surface presentation, including powder, grain, single crystal or coherent thin film. Therefore, we conclude that there is no diffusion of $BrONO_2$ into the salt substrate in agreement with the high value of γ. Because of the fast uptake of $BrONO_2$ on sea–salts, the life time of $BrONO_2$ in the marine troposphere is expected to be short. Under typical marine boundary layer conditions we have 10 salt aerosol particles per cm^3 each with an average diameter of 2 μm. At 300 K the rate constant for diffusion ($1.3 \cdot 10^{-3}$ s^{-1}) and for heterogeneous reaction ($2 \cdot 10^{-3}$ s^{-1}) are comparable and result in an overall rate constant for $BrONO_2$ disappearance of $8 \cdot 10^{-4}$ s^{-1} leading to an atmospheric lifetime of just over 20 minutes.

The production of Br_2 observed in the reaction $BrONO_2$ + NaCl and $BrONO_2$ + non–halogen containing salt such as $NaNO_3$ and Na_2SO_4 leads us to conclude that there is a self–reaction of $BrONO_2$ according to the net reaction $2\ BrONO_2 \rightarrow Br_2 + 1/2\ O_2 + N_2O_5$. For the $BrONO_2$/KBr system the self–reaction probably occurs too, but we are unable to distinguish it from the halogen exchange reaction. The production of HCl and HBr in the $BrONO_2$/NaCl and $BrONO_2$/KBr systems, respectively, stems from the hydrolysis of $BrONO_2$ on the salt substrate according to the reaction $BrONO_2 + H_2O \rightarrow HOBr + HNO_3$. The observation of HCl and HBr is, however, not a direct proof for the hydrolysis, because we neither observed HOBr nor HNO_3, owing to fast secondary reactions. The competition between reaction, self–reaction and hydrolysis of $BrONO_2$ may play an important role in the marine troposphere. In the presence of atmospheric humidity, the ratio between these three reactive pathways of $BrONO_2$ may change in favor of the hydrolysis, which leads to the formation of HOBr.

The role of H_2O is of great importance in heterogeneous chemistry on salts. The sea–salt particles in the marine troposphere are deliquescent because of the prevailing high relative humidity. Our laboratory results performed on humid and dry salt samples show no significant difference in the initial uptake coefficient γ_0 whereas the rate of product formation seems to be a strong function of the amount of adsorbed H_2O which emphasizes its catalytic role. In addition, the yield of hydrolysis products HCl and HBr are a sensitive function of the moisture content of the salt substrates. The results obtained in experiments of $ClONO_2$ interacting with reactive salts are in good agreement with the results obtained by Caloz *et al.* [1996] and Timonen *et al.* if we only take their raw data for comparison [Timonen, 1994]. We have shown that $ClONO_2$ decomposes on surfaces of $NaNO_3$ and Na_2SO_4 leading to the formation of Cl_2. The appearance of Cl_2 in the decomposition of $ClONO_2$ on non–reactive salts is a new fact, and the active chlorine so formed could contribute to a change in the oxidative potential of the troposphere. Recently, an unknown source of Cl_2 has been postulated based on the measurement of nighttime Cl_2 in the marine boundary layer [Spicer, 1998]. The hydrolysis of $ClONO_2$ on salts is less important than in the case of $BrONO_2$ and only appears where the halogen exchange reaction is not enabled such as is the case on non–reactive salts. The unexpected self–reaction or decomposition of $BrONO_2$ or $ClONO_2$ leaves the halogen concentration unchanged.

Chapter 5

Numerical Simulation of the Chemistry of the Marine Boundary Layer

In order to gauge the importance of heterogeneous reactions occurring on salt substrates which we studied in our laboratory on the chemistry of the marine boundary layer, we used a box model involving all the relevant chemical and radiative processes. The numerical solution is obtained using the code LSODE [Hindmarsh, 1983] which is the solver of the CHEMKIN package. In this Chapter we will describe the model and then present some examples of scenarios that have been modeled.

5.1 Model Description

The model is a 0–D chemical-radiative box model including both homogeneous and heterogeneous atmospheric chemistry and photochemistry, excluding atmospheric transport.

5.1.1 Chemical Mechanism

Homogeneous chemistry

In order to build the chemical mechanism, one first selects homogeneous reactions (85 reactions) that are relevant to the atmosphere. These homogeneous reactions as well as their corresponding rate constants are summarized in Tables C.1 in Appendix C. Photochemistry is also taken into account. The photolyzable species considered in this model are displayed in Table C.2 in Appendix C with the corresponding photolysis rate constant, J, calculated for 30°N at ground level (25 reactions). We accepted this homogeneous mechanism as satisfying when it was able to predict concentrations of radicals (OH, NO_3, HO_2, ...) without heterogeneous chemistry that are in good agreement with typical measured atmospheric concentrations.

Heterogeneous chemistry

Although CHEMKIN is a gas-phase chemical model, it is possible to take into account heterogeneous reactions by considering the estimated surface area A/V [Müller, 1994]. We have to introduce heterogeneous reactions as pseudo–homogeneous reactions whose rate constants depend on a particular surface–to–volume ratio and introduce the reaction rate constant according to:

$$k = \omega\gamma = \sqrt{\frac{8RT}{\pi M}}\frac{A}{4V}\gamma \tag{5.1}$$

where T is the temperature, R the gas constant, M the molecular weight, γ the uptake coefficient and A/V the surface area.

In order to introduce heterogeneous reactions into the code, one has to consider the reactions as effectively bimolecular by introducing an effective concentration of the solid samples as if it were a gas. As an example let us consider the following heterogeneous reaction:

$$BrONO_2 + NaCl \xrightarrow{\gamma = 0.31} BrCl + NaNO_3 \tag{5.2}$$

The rate of this reaction is first order in $BrONO_2$ (see Chapter 4) and is given by:

$$Rate = k[BrONO_2] \tag{5.3}$$

in units of molecule/s cm^3 and $k = \omega\gamma = \sqrt{\frac{8RT}{\pi M}\frac{A}{4V}}\gamma$. To introduce this reaction into the code, we need to consider a concentration of NaCl expressed in molecule/cm^3. The rate is then expressed as:

$$Rate = k'[NaCl]_0[BrONO_2] \tag{5.4}$$

where k' = k/$[NaCl]_0$ with k given by equation (5.1), and $[NaCl]_0$ is the initial NaCl concentration. therefore k' remains constant during the whole heterogeneous activation period. The 15 heterogeneous reactions involved in this model are displayed in Table 5.1 as well as their pseudo first order rate constant k [s^{-1}] calculated for a surface–to–volume ratio A/V = 10^{-7} cm^2/cm^3 at 300 K. The justification of the use of such a model excluding surface saturation is that the rate of uptake of $BrONO_2$ on NaCl and KBr is constant and independent of the extent of the heterogeneous reaction (Chapter 4). To date, no $BrONO_2$ has been observed in the atmosphere and one of the goals of these simulations is to describe the possible behavior of $BrONO_2$ in the marine boundary layer (MBL).

Table 5.1: Heterogeneous reactions used in the model with γ values resulting from Knudsen cell studies. k [s^{-1}] has been calculated according to equation (5.1) for a surface–to–volume ratio A/V = 10^{-7} cm^2/cm^3 at 300 K.

Reaction	γ	k [s^{-1}]	Reference
$HNO_3 + NaCl \rightarrow HCl + NaNO_3$	$2.8 \cdot 10^{-2}$	$2.2 \cdot 10^{-5}$	Fenter, 1994
$HNO_3 + KBr \rightarrow HBr + KNO_3$	$2.8 \cdot 10^{-2}$	$2.2 \cdot 10^{-5}$	Fenter, 1994
$N_2O_5 + NaCl \rightarrow ClNO_2 + NaNO_3$	$5.0 \cdot 10^{-4}$	$3.0 \cdot 10^{-7}$	Fenter, 1996
$N_2O_5 + KBr \rightarrow BrNO_2 + KNO_3$	$2.0 \cdot 10^{-3}$	$1.2 \cdot 10^{-6}$	Fenter, 1996
$ClONO_2 + NaCl \rightarrow Cl_2 + NaNO_3$	$2.3 \cdot 10^{-1}$	$1.5 \cdot 10^{-4}$	Caloz, 1996
$ClONO_2 + KBr \rightarrow BrCl + KNO_3$	$3.5 \cdot 10^{-1}$	$2.2 \cdot 10^{-4}$	Caloz, 1996
$BrNO_2 + KBr \rightarrow Br_2 + KNO_3$	$3.0 \cdot 10^{-1}$	$1.7 \cdot 10^{-4}$	Caloz, 1998
$ClNO_2 + KBr \rightarrow BrNO_2 + KCl$	$1.3 \cdot 10^{-4}$	$9.1 \cdot 10^{-8}$	Caloz, 1998
$HOBr + KBr \rightarrow Br_2 + KOH$	$3.0 \cdot 10^{-1}$	$1.9 \cdot 10^{-4}$	Mochida, 1998
$HOBr + NaCl \rightarrow BrCl + NaOH$	$4.0 \cdot 10^{-2}$	$2.6 \cdot 10^{-5}$	Mochida, 1998
$NO_3 + NaCl \rightarrow Cl + NaNO_3$	$4.6 \cdot 10^{-2}$	$3.7 \cdot 10^{-5}$	Seisel, 1999
$BrCl + KBr \rightarrow Br_2 + KCl$	$1.4 \cdot 10^{-1}$	$8.2 \cdot 10^{-5}$	This work
$Cl_2 + KBr \rightarrow BrCl + NaNO_3$	$3.0 \cdot 10^{-2}$	$2.3 \cdot 10^{-5}$	This work
$BrONO_2 + NaCl \rightarrow BrCl + NaNO_3$	$3.1 \cdot 10^{-1}$	$1.6 \cdot 10^{-5}$	This work
$BrONO_2 + KBr \rightarrow Br_2 + KNO_3$	$3.2 \cdot 10^{-1}$	$1.7 \cdot 10^{-5}$	This work

Saturation effects

In Section 5.5, we will present calculations in which the salt substrate is consumed and where the rate constant for the heterogeneous reaction therefore decreases with time in contrast to equation (5.4). The rate of reaction may be expressed by the following expressions:

$$Rate = k''[NaCl][BrONO_2] \tag{5.5}$$

$$k'' = k/[NaCl]_0 \tag{5.6}$$

where $[NaCl]_0$ is the initial salt concentration in formula units/cm^3. The rate of the heterogeneous reaction decreases with decreasing NaCl concentration at constant $[NaCl]_0$ owing to consumption. This calculation has been performed using realistic salt concentrations as initial concentrations in the model runs.

5.1.2 Model Set-Up

In all examples presented below, calculations are run during 9 days. The first 2 days are run without heterogeneous processes, in order to let the system reach steady state. During the following 5 days, during which the heterogeneous processes are activated, salt substrates are introduced in order to enable heterogeneous chemistry. The heterogeneous chemistry is subsequently "switched off“ or disabled during the remaining 2 days in order to see if any effect of the heterogeneous activation period on the global gas phase chemistry may be observed.

Initial conditions

All the calculations have been performed at 300 K at a total pressure of 1 atm in order to simulate tropospheric chemical processes in the boundary layer. A latitude of 30°N has been chosen and the runs have been performed between January first and tenth.

As initial conditions, one introduces the concentrations of the primary pollutants which are directly emitted into the troposphere, such as NO_x, hydrocarbons as well as a few important secondary pollutants which are formed in reactions of primary pollutants, such as O_3 and HNO_3. The latter pollutants have been produced during the first two days of the run where no salt surface was available for activating the heterogeneous chemistry. The species which have been introduced at $t = 0$ are displayed in Table 5.2. In addition, no emission of source gases has been taken into account.

No chlorine– and bromine–containing source gases have been introduced in the model initially. In each run chlorine– and bromine–containing species are released from the condensed phase in heterogeneous chemical processes displayed in Table 5.1. It is well known that the ratio of Br^-/Cl^- is of the order of 1/600 in sea salt. We therefore used this value for the KBr/NaCl ratio in calculations simultaneously involving chloride and bromide surfaces. As this value corresponds to a volume ratio, the used surface ratio between the two salts is about 70 according to the assumption that the salts are homogeneously mixed. The total volume of NaCl (V_{NaCl}) and KBr (V_{KBr}) are proportional to the third power of the radius of the NaCl and KBr spherical particles, while the total surface of NaCl (S_{NaCl}) and KBr (S_{KBr}) go with r^2_{NaCl} and r^2_{KBr}, respectively.

Table 5.2: Initial concentrations in molecules/cm^3 used in Section 5.2.

Species	Concentration [molecule/cm^3]	Species	Concentration [molecule/cm^3]
NaCl	$1.0 \cdot 10^{15}$	KBr	0
N_2	$2.0 \cdot 10^{19}$	NO	$1.0 \cdot 10^{1}$
NO_2	$3.6 \cdot 10^{10}$	NO_3	$1.8 \cdot 10^{8}$
N_2O_5	$2.0 \cdot 10^{8}$	O_2	$4.5 \cdot 10^{18}$
H_2O	$6.0 \cdot 10^{17}$	CH_4	$1.0 \cdot 10^{13}$
C_2H_6	$1.0 \cdot 10^{11}$	O_3	$1.0 \cdot 10^{12}$
CO_2	$7.0 \cdot 10^{15}$	HNO_3	$3.6 \cdot 10^{10}$

$$\frac{V_{KBr}}{V_{NaCl}} = \frac{1}{600} \Longrightarrow r_{NaCl} = r_{KBr}\sqrt[3]{600} \tag{5.7}$$

$$\frac{S_{KBr}}{S_{NaCl}} = \frac{4\pi r_{KBr}^2}{4\pi r_{KBr}^2 \sqrt[3]{600^2}} = \frac{1}{\sqrt[3]{600^2}} = \frac{1}{71.1} \tag{5.8}$$

From the known KBr/NaCl volume ratio, equation (5.7) establishes a relationship between the effective radius of both spherical salt particles. Equation (5.8) yields the surface ratio between the two salts using $r_{\mathrm{NaCl}} = r_{\mathrm{KBr}}\sqrt[3]{600}$ which leads to a surface ratio of about 70.

Several runs have been performed at different salt concentrations. We note that NaCl is consumed already after 2 to 3 hours if its mass is of the order of $1{\cdot}10^{10}$ formula unit/cm^3. This salt concentration is comparable to the gas–phase concentration. This means that the heterogeneous chemistry on salts is very efficient in the presence of marine aerosols. On the other hand, if the salt concentration is high the reactions on the salt substrates may occur without significant salt substrate depletion. In order to observe the possible effects of heterogeneous chemistry on the relevant gas phase species during a few days, salt concentrations have been chosen to be of the order of $1{\cdot}10^{15}$ formula unit/cm^3.

5.2 The Effect of the Surface–to–Volume Ratio on the Heterogeneous Kinetics

For this example the only parameter which was varied was the total surface area (A/V) of all particles within the reference volume of 1 cm^3. In this case the A/V values were 0, 1, 10 and 100 $\mu m^2/cm^3$. The results are displayed in Figures 5.1, 5.2 and 5.3. These initial examples clearly show the effect of the heterogeneous chemistry in the presence of particles of a given surface–to-volume ratio:

- Denitrification of the planetary boundary layer by converting NO_y to solid nitrates which may eventually settle to ground (Figure 5.1).
- Change of the oxidative capacity of the troposphere by increase of the Cl atom concentration (see ethane in Figure 5.2).
- Injection of volatile chlorine into the troposphere and formation of chlorine reservoir compounds (Figure 5.3). This phenomenon is commonly called chlorine activation.

Figure 5.1 shows the results of calculations for relevant nitrogen oxides. All nitrogen oxides disappear very rapidly on the time scale of one to several days in the presence of high A/V ratios, especially at a "surface“ concentration of 100 $\mu m^2/cm^3$.

Figure 5.2 presents a different set of key species in the troposphere, namely OH, HO_2, C_2H_6 and O_3. Clearly, we observe no influence on the maximum values of OH and HO_2. As an example of a tropospheric hydrocarbon, we choose ethane rather than methane because ethane reacts more rapidly in the troposphere in line with the presence of higher hydrocarbons in the troposphere. The ethane (C_2H_6) concentrations decrease with increasing surface–to-volume ratio A/V as expected. As Cl atoms are released into the gas phase (Figure 5.3), and as the C_2H_6 oxidation by Cl is approximately 250 time faster than the analogous reactions involving OH-radicals ($k_{Cl} = 5.7 \cdot 10^{-11}$ cm^3/s, $k_{OH} = 2.4 \cdot 10^{-13}$ cm^3/s), it is not surprising that more C_2H_6 is consumed. These oxidation reactions are characterized by the production of HCl which is a stable reservoir molecule of chlorine.

One may observe that the increase of the A/V ratio of the salt substrates results in a decrease of the O_3 concentration after few days. This is probably due to the disappearance of NO_2 (Figure 5.1), whose photolysis leads to the production of tropospheric O_3 [Blacet, 1952] and therefore is not replaced.

Figure 5.3 shows the concentrations of the chlorine containing species as well as the results obtained for the resulting solid nitrate concentrations. One may note that all species, except $ClNO_2$ and $ClONO_2$, show similar behaviour at high A/V values. These latter two species may further react in secondary reactions as has been observed in laboratory studies [Caloz, 1996 and 1998; Aguzzi, 1999]. The calculated Cl atom concentrations are in good agreement with indirect measurements [Wingenter, 1996; Boudries, 2000]. The resulting $NaNO_3$ concentration shows the extent of heterogeneous chemistry, the final concentration of nitrate at high A/V values corresponds to about $7 \cdot 10^{10}$ molecule/cm^3, which is equal to the sum of all available NO_y thus satisfying the mass balance.

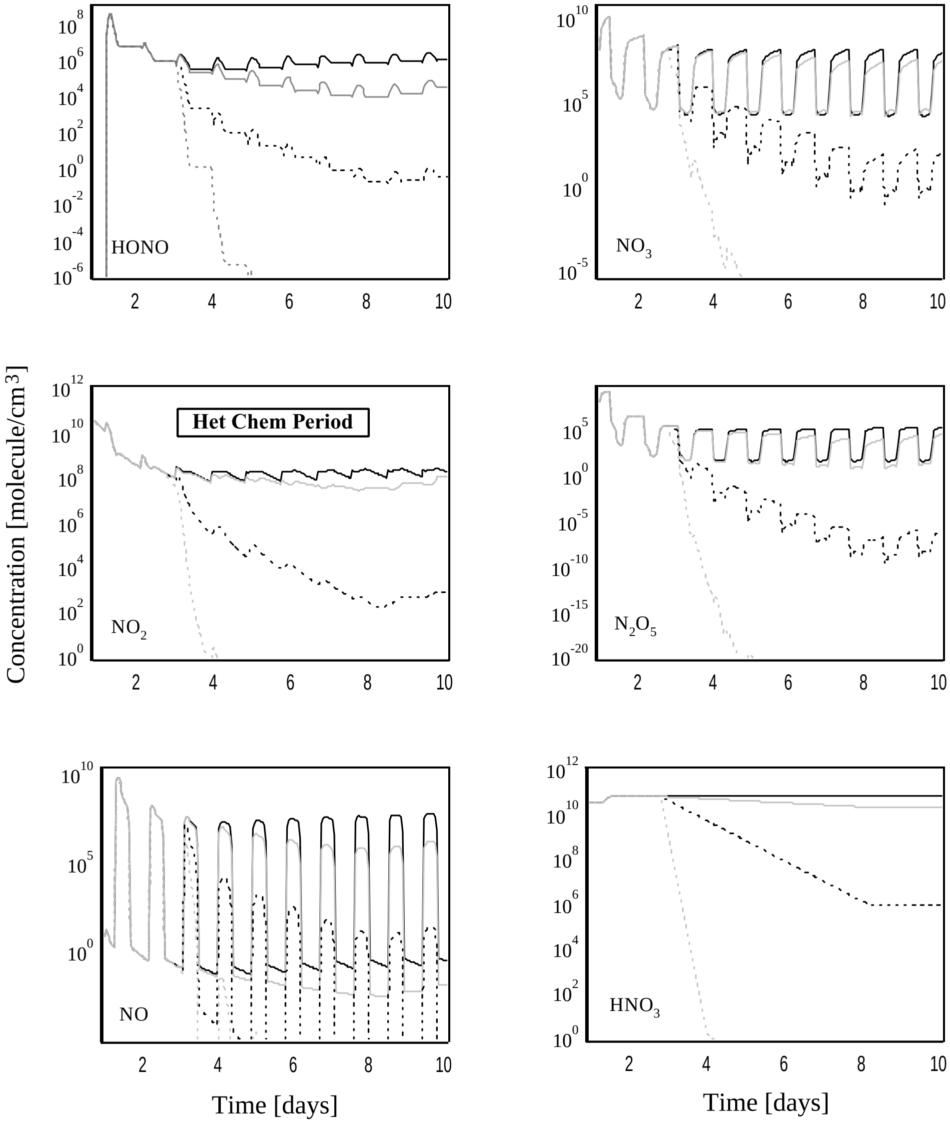

Figure 5.1: Display of the concentration of several species of the NO_y family, in molecule/cm^3, as a function of time in days. Each graph contains 4 curves, the solid black line results from calculations obtained with no aerosol, the solid gray, the dotted black and the dotted gray lines result from calculations using A/V = 1, 10 and 100 μm^2/cm^3, respectively.

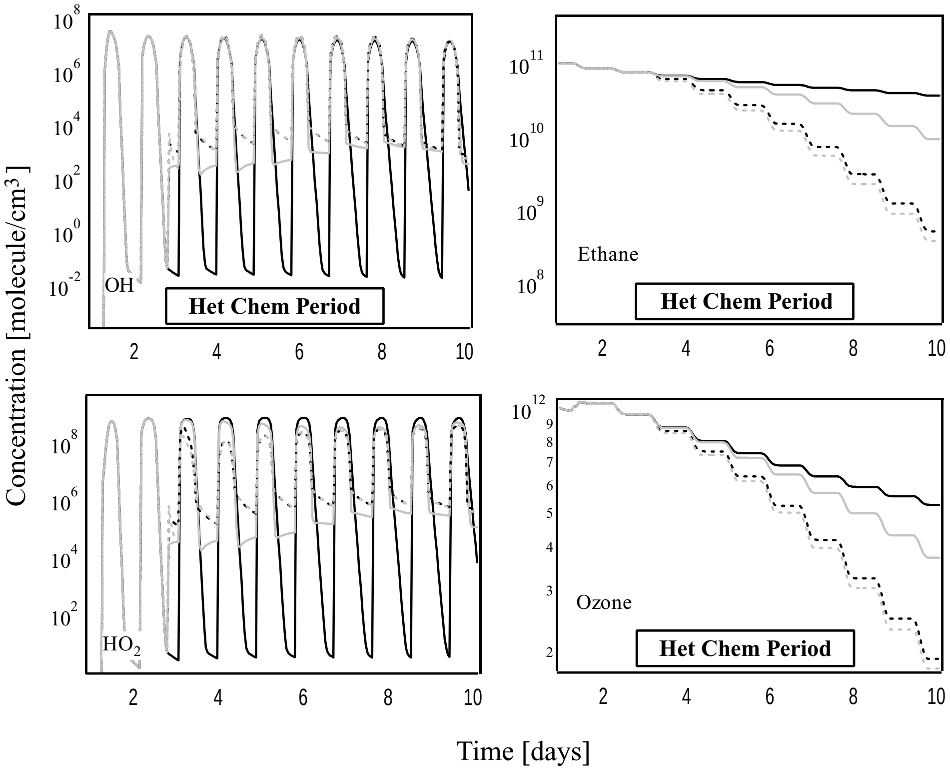

Figure 5.2: Display of species concentrations of key atmospheric importance in the troposphere, in molecule/cm^3, as a function of time in days. Each graph contains 4 curves, the solid black line results from calculations obtained with no aerosol, the solid gray, the dotted black and the dotted gray lines result from calculations using A/V = 1, 10 and 100 μm^2/cm^3, respectively.

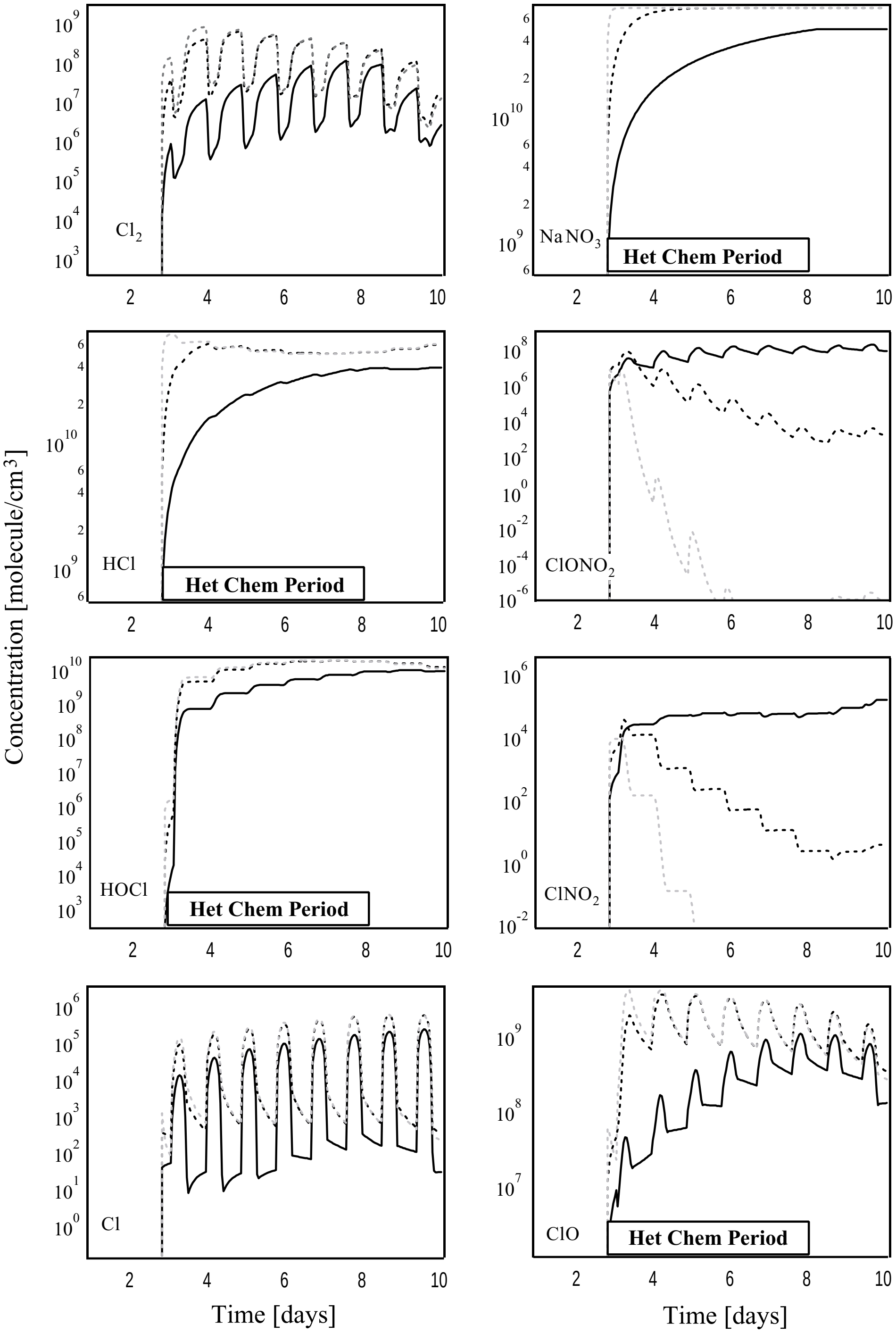

Figure 5.3: Display of volatile chlorine containing species concentrations, in molecule/cm^3, as a function of time in days. Each graph contains 3 curves, the solid black, the dotted black and the dotted gray lines result from calculations using A/V = 1, 10 and 100 μm^2/cm^3, respectively.

5.3 Atmospheric Chemistry in the Presence of Solid Chloride and Bromide Containing Salt Without Surface Saturation

In this Section, bromine has been added to the chlorine chemistry by setting an initial value for the KBr concentration of $1{\cdot}10^{15}$ molecule/cm^3 in contrast to Section 5.2 where it was set equal to zero. No other change has been made with respect to Section 5.2. The following results have been obtained for a clean air mass with an initial NO_x level of 1.5 ppb. Typical sea salt aerosol concentrations in the marine boundary layer (MBL) are approximately 5 to 30 cm^{-3} depending on meteorological conditions [Blanchard, 1987; O'Dowd, 1993]. For this reason, the surface–to–volume ratio has been set to 10 μm^2/cm^3, which corresponds to a particle concentration of 13 cm^{-3} using an aerosol diameter of $D_p = 0.5$ μm.

Bromine chemistry is thought to have a different effect compared to chlorine chemistry. In the troposphere, the bromine chemistry differs from the chlorine chemistry because abstraction reactions of Br atoms with hydrocarbons are known to be slow. For instance, the reactions of Br atoms with alkanes are sufficiently slow so that they are negligible in the atmosphere [Wallington, 1989; Barnes, 1989]. A notable exception is the fast hydrogen abstraction reaction of Br with formaldehyde leading to HBr and formal radical ($HCO^\bullet$). Therefore, bromine atoms do not play an as important a role in the initiation of hydrocarbon oxidation processes as chlorine atoms do.

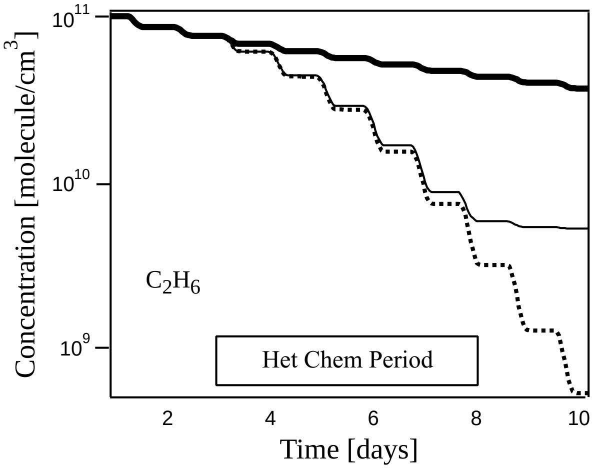

Figure 5.4: Ethane concentrations for three different cases. Bold solid line represents the base case, that is no aerosol present, the dotted line shows the concentration with chlorine and the thin solid line corresponds to the case where both chlorine and bromine substrates are added to gas phase chemistry. Calculations have been performed at A/V = 10 μm^2/cm^3.

Figure 5.4 shows an example of a hydrocarbon oxidation by displaying the ethane (C_2H_6) concentration as a function of time. The bold solid line shows the C_2H_6 behaviour in the presence of OH-radicals only, that is chlorine and bromine concentrations are set to zero. The dotted line displays C_2H_6 in the presence of chlorine substrates, that is no bromine is available for heterogeneous chemistry, while the thin solid line shows C_2H_6 with both chlorine and bromine substrates available for heterogeneous chemistry. One may observe that the introduction of KBr–containing aerosols in the simulations kept the level of C_2H_6 constant once the heterogeneous reactions are switched off at the beginning of day eight. However, it did not affect the C_2H_6 concentration during the heterogeneous activation period. When the heterogeneous chemistry is turned off, no more Cl– and Br–atoms are released in the gas–phase from the aerosol. The major Cl atom source is then the ClO–ClO reaction, but the ClO self–reaction (reaction (5.9)) is slower by a factor of 10 compared to the ClO–BrO reactions (5.10 to 5.12).

$$ClO + ClO \xrightarrow{k_{5.9} = 2.9 \cdot 10^{-13}} Cl_2O_2 \tag{5.9}$$

$$BrO + ClO \xrightarrow{k_{5.10} = 1.0 \cdot 10^{-12}} BrCl + O_2 \tag{5.10}$$

$$\xrightarrow{k_{5.11} = 6.8 \cdot 10^{-12}} Br + OClO \tag{5.11}$$

$$\xrightarrow{k_{5.12} = 6.1 \cdot 10^{-12}} Br + ClOO \tag{5.12}$$

where the rate constants k are expressed in $cm^3 \cdot s^{-1}$. However, when the heterogeneous activation period is over, the rate of the bimolecular ClO–BrO reaction is reduced by a factor of 10000 or more, due to the strong decrease of the ClO and BrO concentrations displayed in Figure 5.5 such that Cl– and Br–atoms do not result from the ClO–BrO reaction. To try to explain the C_2H_6 behavior in the presence of bromine and chlorine substrates, let us consider the HOCl concentration over the same period (Figure 5.5). One observes that in the presence of chlorine and bromine substrates the HOCl mixing ratio is lower compared to the situation where only chlorine substrates are present. HOCl is formed by the gaseous reaction of ClO with HO_2. If the ClO concentration is low, it will result in a low HOCl concentration. However, HOCl photolysis will produce Cl–atom and OH radicals according to the following reaction:

$$HOCl \xrightarrow{h\nu} Cl + OH \tag{5.13}$$

We note that we will obtain more Cl–atoms due to a higher HOCl mixing ratio if only chlorine substrates are present than when chlorine and bromine substrates are present together. This means a larger decrease of C_2H_6 in the case of chlorine only compared to the presence of chlorine and bromine owing to a larger Cl–atom precursor concentration in the former case. We may note in Figure 5.5, that HCl is an important Cl–atom reservoir.

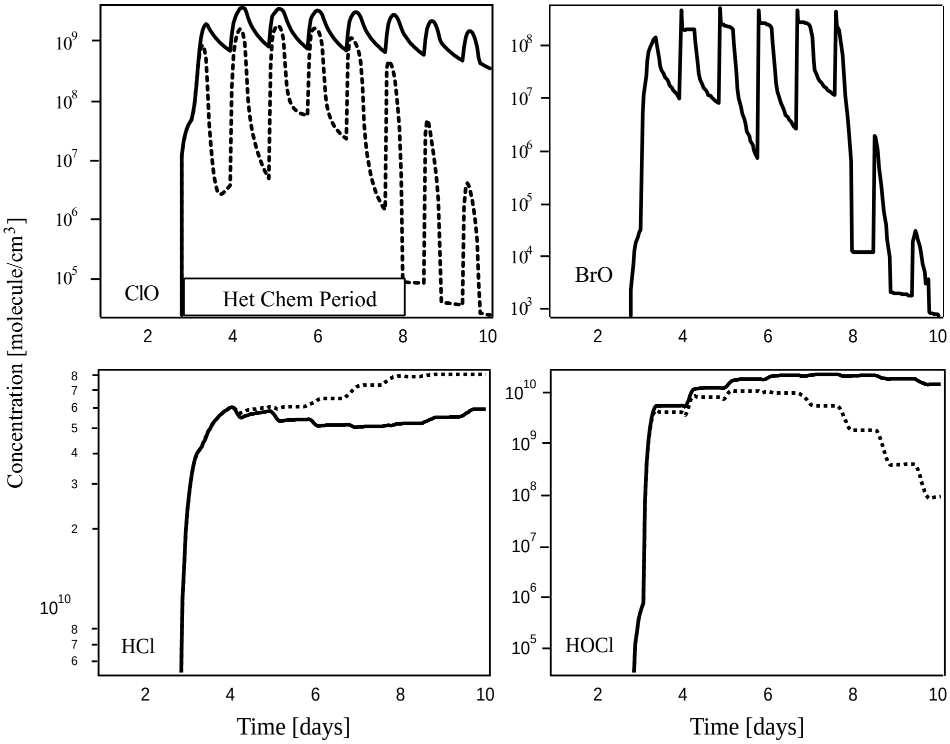

Figure 5.5: ClO, BrO, HCl and HOCl concentrations. Each graph compares the concentrations between the absence (solid line) and the presence (dashed line) of bromine chemistry. Calculations have been performed using A/V = 10 $\mu m^2/cm^3$.

Figure 5.5 displays ClO (top left panel) and BrO (top right panel) concentrations. The top left panel shows the ClO concentration as a function of time when only chlorine heterogeneous chemistry is on (thin solid line), and when chlorine and bromine chemistry are on together (dashed line). One may note that the abundance of ClO in the gas phase is higher in the absence of bromine, because of the absence of the reaction with BrO. This is a consequence of the coupling of bromine with chlorine chemistry. Bromine compounds are participating in reactions involving gaseous chlorine species and thus liberating chlorine in its active form. In the presence of BrO, ClO may react according to reaction (5.14), followed by the faster reaction (5.15) leading to the release of one Cl–atom.

$$BrO + ClO \rightarrow Br + ClOO \tag{5.14}$$

$$ClOO \xrightarrow{M} Cl + O_2 \tag{5.15}$$

Figure 5.6 displays the concentrations of NO$_y$ resulting, from calculations performed

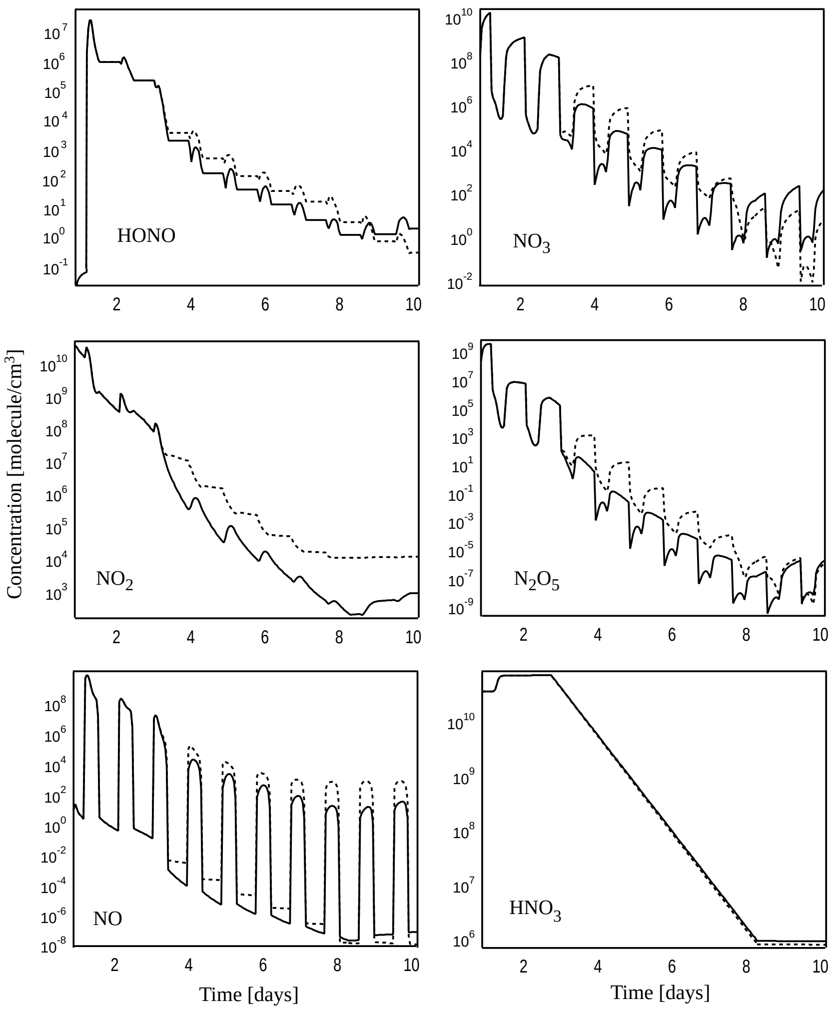

Figure 5.6: Display of NO_y species concentrations. Each graph contains two curves, dotted lines involved only chlorine substrates, while solid lines take into account chlorine and bromine–containing substrates. Calculations have been performed using A/V = 10 $\mu m^2/cm^3$.

exclusively with chlorine chemistry (dotted line), and with both chlorine and bromine salts present in the simulations (solid lines). We have already noted that the introduction of chlorine heterogeneous reactions into the gas-phase box–model leads to the denitrification of the troposphere by converting NO_x into solid nitrates (Figure 5.1). When bromine heterogeneous reactions are added, one may note for instance that the HNO_3 concentration is not affected by the addition of bromine chemistry, in contrast to the other NO_y species. As displayed in Figure 5.1, the HNO_3 mixing ratio remains constant in the absence of any solid substrate. By introducing solid substrates in the model, one may note that the HNO_3 concentration is not influenced by Br–containing substrates. The HNO_3 behavior in our box–model is governed by its interaction with solid NaCl, characterized by its relatively high rate compared to rate of the reaction of HNO_3 on KBr. In general when heterogeneous chemistry is active, the concentration of

NO_y decreases by a factor 10 with both chlorine and bromine chemistry in the model, because an additional sink of NO_x is added by the rapid reactions of BrO with NO and NO_2.

Figure 5.7 shows the concentrations of $BrONO_2$ and HOBr, two important bromine reservoirs. The formation of $BrONO_2$ is known to occur in the atmosphere via the recombination reaction of BrO with NO_2, while HOBr is formed via the reactions of Br_2 with OH radicals and BrO with HO_2 in the gas phase. One may note a $BrONO_2$ concentration of 0.7 ppt and a HOBr concentration up to approximately 40 ppt at a NO_x level of 1.5 ppb (clean air mass) in Figure 5.7. We notice the large discrepancy between these two different bromine reservoirs. While the HOBr formation does not depend on NO_x chemistry, $BrONO_2$ production, as we will see in Section 5.4, is greatly influenced by the NO_x concentration.

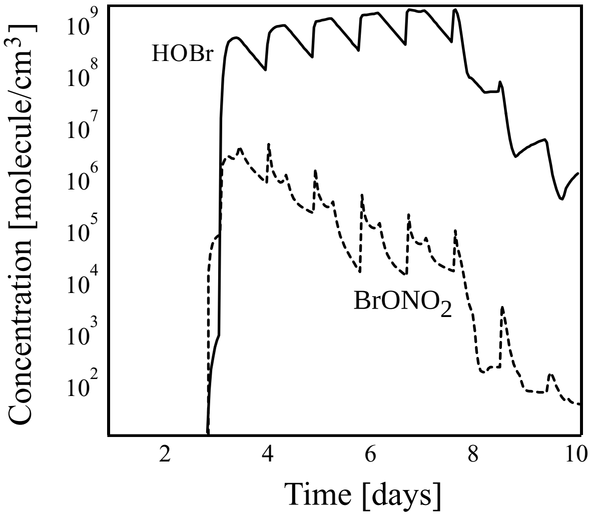

Figure 5.7: HOBr (solid line) and $BrONO_2$ (dashed line) concentrations. Calculations have been performed using A/V = 10 $\mu m^2/cm^3$ and 1.5 ppb of NO_x.

The left panel of Figure 5.8 displays the concentrations of BrCl (dotted line), Br_2 (bold solid line) and Cl_2 (thin solid line) when the chlorine and bromine containing salt substrate is exposed to a NO_x level of approximately 2 ppb (clean air mass). The most abundant species generated from heterogeneous reactions is BrCl with a mixing ratio of up to 32 ppt. Br_2 mixing ratios of up to 50 ppt have been observed in a chlorine free atmosphere and 11 ppt when both chlorine and bromine chemistry were active. When no bromine substrate is involved in the simulations, the Cl_2 mixing ratio may increase up to 25 ppt and reaches 1 ppt when bromine and chlorine substrates are present (Table 5.3).

The right panel in Figure 5.8 shows the total amount of active halogen X_{act} =

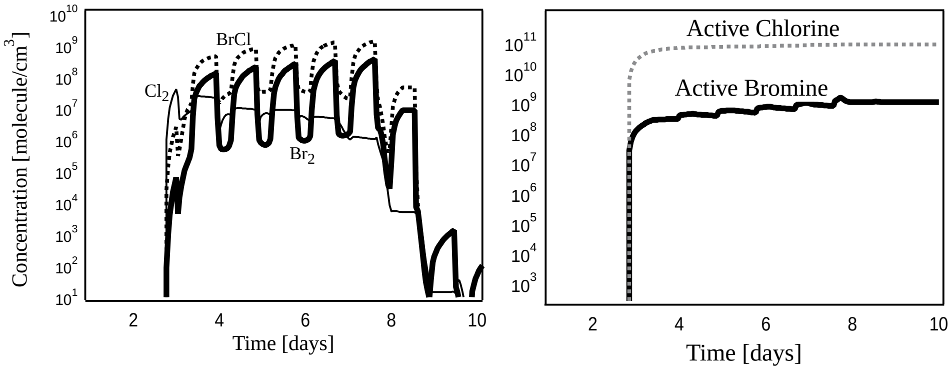

Figure 5.8: Left panel: BrCl (dotted line), Br_2 (bold solid line) and Cl_2 (thin solid line) concentrations. Right panel: Total active halogen resulting resulting from bromine and chlorine chemistry. Calculations have been performed using A/V = 10 $\mu m^2/cm^3$ at 1.5 ppb of NO_x.

$X+X_2+HX+XO+HOX+XONO_2$, with X = Br, Cl liberated into the gas phase during and after the heterogeneous activation period. Chlorine and bromine species reach concentrations of $8 \cdot 10^{10}$ (3.3 ppb) and $2 \cdot 10^9$ (80 ppt) molecule/cm^3, respectively, which is in good agreement with values reported in the literature [Wayne, 1995; Hebestreit, 1999].

Measurements performed by Foster *et al.* [2001] are also displayed in Table 5.3. They report results from measurements of Br_2, BrCl and Cl_2 in the troposphere of the high Arctic, ∼ 125 cm above the snow level. They observed BrCl and Br_2 mixing ratios of up to 35 and 25 ppt, respectively. However they did not detect Cl_2 above the detection limit of 2 ppt of their chemical ionization–mass spectrometer (CIMS) in agreement with the expectations of our simple box model numerical simulation.

Measurements performed at Alert, Canada by Foster *et al.* [2001] and the present calculations refer to two different locations. Calculations have been performed for a latitude of 30°N, while Alert lies at approximately 82°N. However, it appears that the halogen concentrations follow the same trend at both latitudes, that is no Cl_2 detected, BrCl being the most abundant species and the Br_2 mixing ratio lying between the one for Cl_2 and BrCl concentrations. Br_2 photolysis rate constant have been calculated for the Alert latitude as $J_{Br_2} = 9.5 \cdot 10^{-4}$ s^{-1}, which is smaller by a factor of 15 compared to the one used in the box–model. This fact may explain the relatively low Br_2 mixing ratio obtained in the present box model. The high reactivity of Cl_2 in the atmosphere may explain the absence of Cl_2 in both simulations and measurements performed by Foster *et al.* [2001]. BrO measurements performed by McElroy *et al.* [1999] reveal mixing ratios in the range of 50–100 ppt in the Arctic, which has been assumed to be uniformly distributed in the PBL. Compared to our calculated BrO mixing ratios, one

Table 5.3: Halogen and bromine oxide maximum concentrations at 30°N resulting from calculations with chlorine (Cl), bromine (Br) and chlorine–bromine (Cl–Br) containing salt substrates compared to field measurements.

Species	Cl	Br	Cl–Br	Foster[(a)]	McElroy[(b)]	Hebestreit[(c)]
Cl_2	25 ppt	–	1 ppt	–	–	–
Br_2	–	50 ppt	11 ppt	25 ppt	–	–
BrCl	–	–	32 ppt	35 ppt	–	–
BrO	–	48 ppt	17 ppt	–	50–100 ppt	86 ppt

(a) Measurements performed by Foster *et al.* [2001] in the Arctic during polar sunrise.

(b) BrO observations from a high–altitude aircraft, assuming that all BrO resides within the PBL (< 1 km) [McElroy, 1999].

(c) DOAS measurements of BrO at the Dead Sea [Hebestreit, 1999].

observes that our box model underestimates the BrO concentrations. The measurements of McElroy *et al.* have been performed in the Arctic during the end of April 1997, while our simulations are performed during the first ten days of January at 30°N.

DOAS measurements performed from 27 May to 25 June 1997 at the Dead Sea (31°N) show BrO mixing ratios up to 86 ppt [Hebestreit, 1999]. Our box model underestimated the BrO mixing ratios for this case as expected. During the May–June period, the daylight period is longer than in January and photolysis reactions are faster, which means that more Br_2 and BrCl may photolyse to produce increased Br–atom concentrations. These Br–atoms may then react with O_3 to increase the tropospheric BrO concentrations.

Large fluxes of reactive gas phase Br–atoms, which may react with O_3, may result from the condensed–phase reaction of HOBr and halide ions in deliquescent sea salt aerosols and lead to the production of BrCl and Br_2 according to the following reaction scheme [Vogt, 1996; Impey, 1999; Foster, 2001]:

$$HOBr + Br^-, Cl^- + H^+ \rightarrow Br_2, BrCl + H_2O \quad (5.16)$$

$$Br_2 + h\nu \rightarrow 2Br \quad (5.17)$$

$$BrCl + h\nu \rightarrow Br + Cl \quad (5.18)$$

$$Br + O_3 \rightarrow BrO + O_2 \quad (5.19)$$

This mechanism does not require any concentration of NO_x to produce halogen atoms. One may note that the halide ion is present as HX (X = Cl, Br). In our case, we did not consider deliquescent sea salt aerosols for the sake of simplicity. Partial justification may be derived from the observations presented in Chapter 4, where no change of the uptake kinetics of $BrONO_2$ has been observed in going from "dry" to "wet" salt samples.

Mochida *et al.* [1998] measured large uptake coefficients of HOBr on solid NaCl and KBr substrates leading to the production of BrCl and Br_2 (reactions (5.20) and (5.21)).

$$HOBr + NaCl \xrightarrow{\gamma = 0.04} BrCl + NaOH \tag{5.20}$$

$$HOBr + KBr \xrightarrow{\gamma = 0.30} Br_2 + KOH \tag{5.21}$$

In order to assess the potential role of HOBr in releasing Br_2 and BrCl from sea salt aerosols, we performed calculations with the same initial conditions as described on the top of page 81, and run the box model with and without HOBr heterogeneous reactions, whereas the homogeneous reactions of HOBr have been left in the box model. The Br–containing volatile compounds, Br_2 (left panel of Figure 5.9) and BrCl (right panel of Figure 5.9), resulting from the absence (dotted line) and the presence (gray line) of the heterogeneous reactions of HOBr are displayed in Figure 5.9.

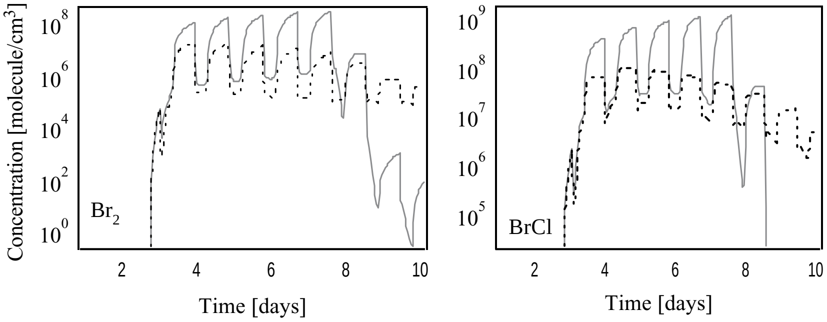

Figure 5.9: Volatile Br–containing species concentrations. Gray lines correspond to HOBr heterogeneous reactions with NaCl and KBr present, while dotted lines correspond to HOBr heterogeneous reactions absent from the simulation in a clean air mass. HOBr homogeneous chemistry and photochemistry are active in both situations.

Figure 5.9 shows that the addition of HOBr heterogeneous reactions on NaCl and KBr in the mechanism increases the amount of volatile bromine containing species. Owing to the high HOBr concentrations in comparison with $BrONO_2$ and owing to the fast uptake kinetics, HOBr heterogeneous reactions are responsible for approximately 95 and 90 % of all BrCl and Br_2 generated and released into the gas phase at low NO_x concentrations, respectively.

The effect of bromine chemistry on ozone is dramatic as displayed in Figure 5.10 which presents a comparison between a case without heterogeneous chemistry (solid black line), one with only chlorine chemistry (gray line) and a third with both chlorine and bromine (dotted black line).

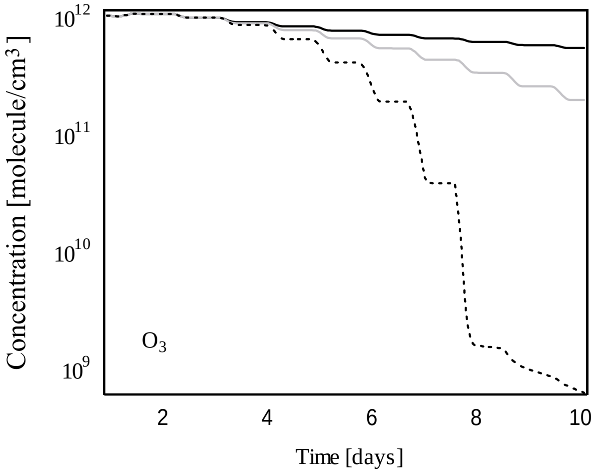

Figure 5.10: Comparison of O_3 concentrations for three different simulations. The solid black line shows the O_3 concentration when no reactive substrate is available, that is no chlorine and bromine chemistry is activated, the gray line involved only chlorine chemistry, while the dashed black line takes into account both chlorine and bromine chemistry. Calculations have been performed using A/V = 10 μm^2/cm^3.

Following the suggestion of one referee, two homogeneous reactions have been omitted in the present model. They are:

$$OH + HNO_3 \xrightarrow{M} NO_3 + H_2O \tag{5.22}$$

$$Br + CH_2O \rightarrow HCO + HBr \tag{5.23}$$

Several runs have been performed including both reactions. The main results are displayed in Figures 5.11, 5.12 and 5.13.

According to Figure 5.11 one may observe that especially at the end of the halogen activation period the decrease of the Br level is balanced by the increase in HBr following the introduction of reactions (5.22) and (5.23). The most important effect of the addition of reactions is observed on ozone concentration which is reduced by a factor of 30 with respect to zero aerosol situation. Without reactions (5.22) and (5.23) the model predicts that the ozone concentration will be depleted by a factor of 1500. Reaction (5.23) therefore has a attenuating effect on tropospheric ozone depletion because CH_2O represents an efficient sink for reactive bromine. If reactions (5.22) and (5.23) are introduced separately into the model, one may note that reaction (5.22) ($OH + HNO_3 + M$) has a negligible effect on concentrations considered in the present box model.

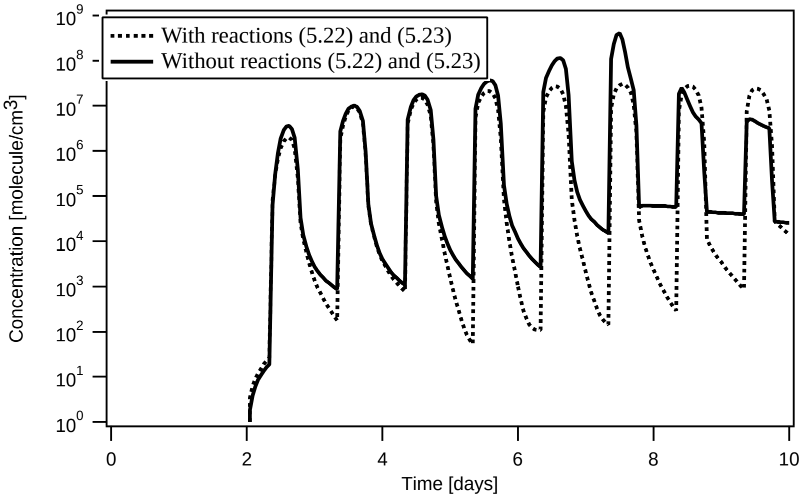

Figure 5.11: Comparison of Br concentrations with and without reactions (5.22) and (5.23). Calculations have been performed using A/V = 10 μm^2/cm^3.

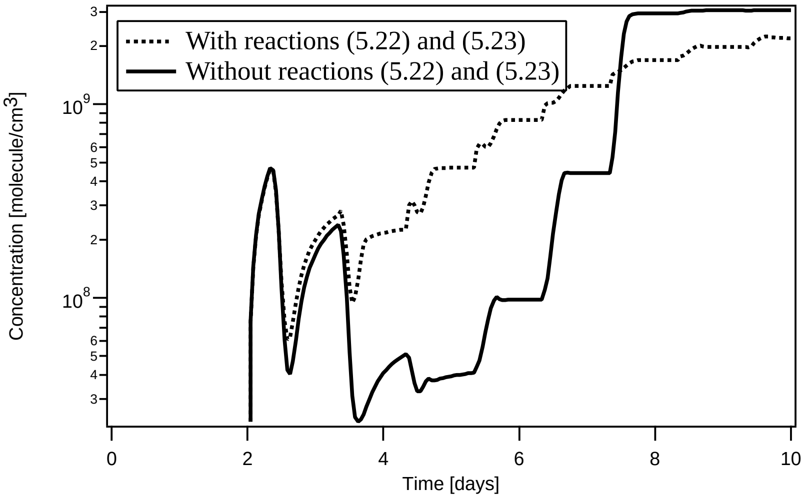

Figure 5.12: Comparison of HBr concentrations with and without reactions (5.22) and (5.23). Calculations have been performed using A/V = 10 μm^2/cm^3.

5.4 Heterogeneous Reactions Involving BrONO$_2$

As discussed in Chapter 4, BrONO$_2$ reacts very efficiently with salt surfaces according to:

$$BrONO_2 + NaCl \xrightarrow{\gamma = 0.31} BrCl + NaNO_3 \qquad (5.24)$$

$$BrONO_2 + KBr \xrightarrow{\gamma = 0.32} Br_2 + KNO_3 \qquad (5.25)$$

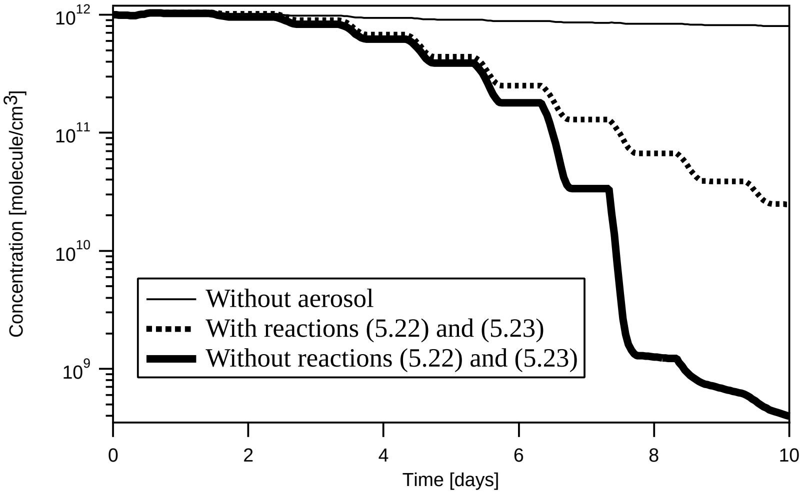

Figure 5.13: Comparison of HBr concentrations with and without reactions (5.22) and (5.23). Calculations have been performed using A/V = 10 μm^2/cm^3. All other parameters are the one from Figure 5.10.

The formation of $BrONO_2$ in the atmosphere occurs in the reaction of bromine oxide (BrO) with NO_2 according to:

$$BrO + NO_2 \xrightarrow{M} BrONO_2 \tag{5.26}$$

Thus the formation of $BrONO_2$ greatly depends on the NO_x concentrations in contrast to HOBr. Figure 5.14 displays the formation of $BrONO_2$ at 1.5 and 150 ppb of NO_x. One may observe a $BrONO_2$ peak concentration of 0.5 and 120 ppt at NO_x levels of 1.5 and 150 ppb, respectively. When the heterogeneous chemistry is halted (day 8), the $BrONO_2$ mixing ratio may reach up to 1 ppb in polluted areas.

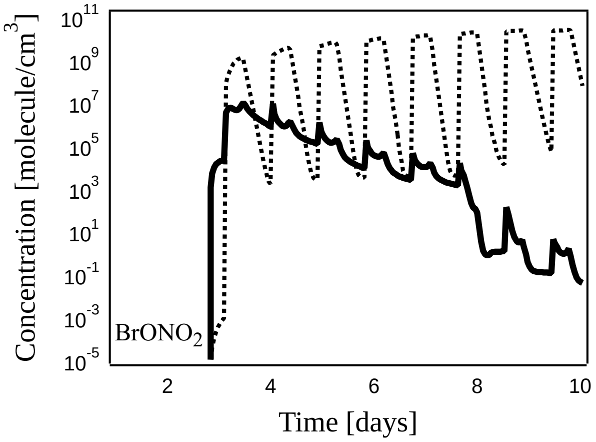

Figure 5.14: $BrONO_2$ production at $[NO_x]$ = 1.5 (solid line) and 150 ppb (dotted line). Calculations have been performed using A/V = 10 μm^2/cm^3.

Figure 5.15 shows the production of $BrONO_2$ as a function of NO_x for two different salt concentrations. On the one hand, an unlimited reservoir of salt has been considered on the order of 10^{15} formula units/cm^3, and on the other hand, the salt reservoir has been limited to be of the order of 10^{12} formula units/cm^3. One may note in both cases identical rates of $BrONO_2$ production.

Figure 5.16 displays the volatile Br–containing species, namely Br_2 (left panel) and BrCl (right panel) resulting from calculations performed at a NO_x mixing ratio of 150 ppb with (solid line) and without (dotted line) $BrONO_2$ heterogeneous reactions in the mechanism.

One may recognize that the production of Br_2 and BrCl is greatly influenced by the presence/absence of $BrONO_2$ at high NO_x mixing ratio. More than 99 % of the volatile bromine results from the heterogeneous reactions of $BrONO_2$ with solid alkali halides, such as NaCl and KBr in polluted areas. At low NO_x mixing ratio the yield of Br_2 and BrCl due to the presence of $BrONO_2$ is less than 2 % of the total Br–containing species in our box model. As we may see in Figure 5.9, HOBr heterogeneous reactions produce more than 90 % of the volatile bromine species whereas the release of bromine due to $BrONO_2$ is insignificant in a clean air mass of low NO_x content. Depending on the level of NO_x, one may distinguish two different chemical mechanisms for volatile bromine release. At low NO_x level over the Arctic, for instance, HOBr seems to be the major source of atmospheric bromine, while at high NO_x mixing ratio $BrONO_2$ uptake on salt seems to be the most important source of bromine–containing compounds.

The influence of the heterogeneous reactions involving $BrONO_2$ on O_3 is presented in Figure 5.17. O_3 concentrations have been obtained according to four situations: (1) no aerosol present in the system (thin solid line), (2) only chlorine chemistry activated

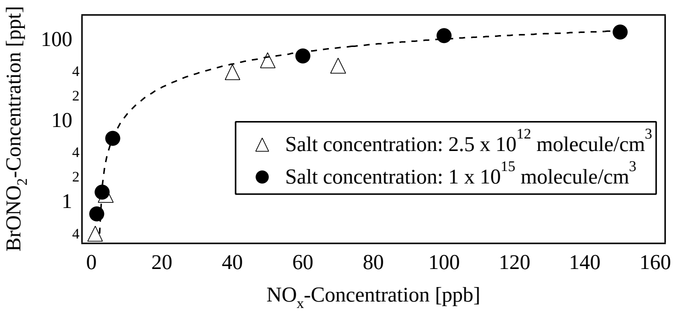

Figure 5.15: Peak concentration of $BrONO_2$ as a function of NO_x right after the beginning of the heterogeneous activation period. Full circles refer to an unlimited supply of salt at $1.0{\cdot}10^{15}$ formula unit/cm^3, the open triangles represent a salt concentration of $2.5{\cdot}10^{12}$ formula unit/cm^3. Calculations have been performed using $A/V = 10\ \mu m^2/cm^3$.

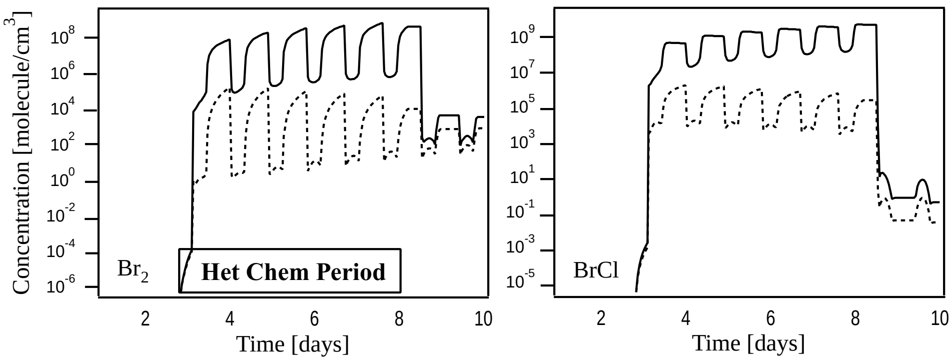

Figure 5.16: Volatile Br–containing species, Br_2 (left panel) and BrCl (right panel) at $[NO_x]$ = 150 ppb. Dotted line: $BrONO_2$ heterogeneous reactions are off ($\gamma = 0.0$); solid line: $BrONO_2$ heterogeneous reactions are active ($\gamma = 0.3$). Calculations have been performed using A/V = 10 $\mu m^2/cm^3$.

(thin dotted line), (3) $BrONO_2$ heterogeneous reactions eliminated from the mechanism (bold solid line), (4) complete reaction mechanism (dotted bold line). While chlorine chemistry reduces O_3 concentration by "only" 60 %, the effect of all heterogeneous bromine reactions leads to more than 99 % depletion of O_3. One may note that $BrONO_2$ heterogeneous reactions contribute up to 50 % to O_3 destruction with respect to the case where these reactions have been removed from the mechanism.

5.5 Saturation Effects

We performed a few calculations where saturation effects on salt substrates have been introduced. The way to perform such simulations is described in Section 5.1.1. The simulation, which has been performed at A/V = 10 $\mu m/cm^3$ show rapid disappearance of the reactive salt. No more salt is available for heterogeneous chemistry after a few hours as is shown in Figure 5.18. Therefore, the rate of the heterogeneous chemistry is lowered in agreement with the decrease of the salt concentration. The NaCl concentration is of the order of 10^{11} formula unit/cm^3, thus fixing the KBr concentration at $3 \cdot 10^8$ formula unit/cm^3. These mixing ratios are quite reasonable according to $[Na^+] = 1.3 \cdot 10^{11}$ molecule/cm^3 measured at the Bermuda Islands (32°N) in January [Gong, 1997].

Figure 5.19 shows the behavior of some NO_y species. It becomes apparent that the denitrification of the troposphere is strongly reduced when saturation effects are taken into account.

The case where saturation has been taken into account shows little change in ozone concentration compared to a calculation where no aerosol was involved (Figure 5.20). The solid line shows, the O_3 mixing ratio in the absence of any aerosols. The gray line

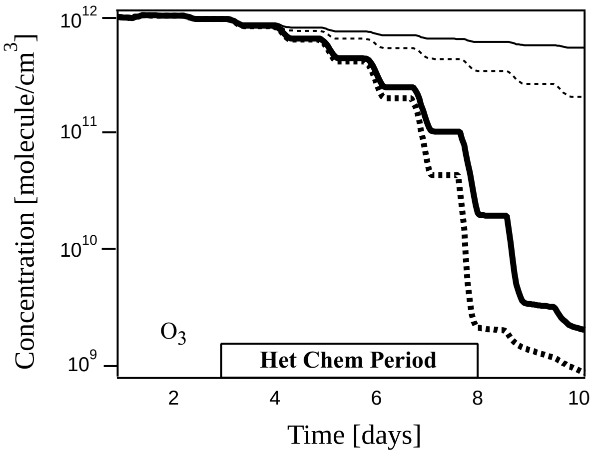

Figure 5.17: Ozone concentration for four different scenarios: no aerosol (thin solid line), chlorine chemistry only (thin dotted line), chlorine and bromine chemistry without the heterogeneous reactions involving $BrONO_2$ (bold solid line) and all reactions are involved in the model (bold dotted line). Calculations have been performed using A/V = 10 $\mu m^2/cm^3$ at 150 ppb of NO_x.

represents the case without saturation while the dotted line displays the O_3 concentration when saturation is included in the model. Ozone depletions up to 10 % have been observed when saturation effects are taken into account, which is relatively small compared to cases where more than 99 % O_3 is destroyed in the absence of saturation. This clearly indicates that the change in the ozone mixing ratio observed in Section 5.3 (Figure 5.10) was mainly due to the destruction of NO_2 whose photolysis initiates O_3 formation (reactions (1.1) and (1.2) on page 3).

The fast depletion of reactive salts renders the heterogeneous chemistry ineffective after injection of volatile chlorine and bromine containing species into the troposphere. Figure 5.21 displays the production of these volatile compounds: Cl_2 (left panel), Br_2 and BrCl, solid and dotted lines, respectively (right panel). We observe at the start of the heterogeneous chemistry on day 3, a rapid rate of production of these halogen compounds during the night, then a slower release during the days thereafter. Initial mixing ratios for Cl_2, BrCl and Br_2 are 170, 0.2 and 10^{-4} ppt, respectively. The amount of Cl_2 resulting from the calculations are within the same range of the one measured by Spicer *et al.* [1998], who report measured values between 10 and 150 ppt.

When saturation effects are taken into account the total simulated active halogen release in the troposphere are 6.8 ppb for chlorine– and 13 ppt for bromine–containing halogen compounds. Active halogen mixing ratios are in good agreement with the values of 3.8 ppb and 20 ppt, respectively, reported by Wayne *et al.* [1995]. Actually, it seems that tropospheric bromine–containing species may occasionally reach mixing ratio of up

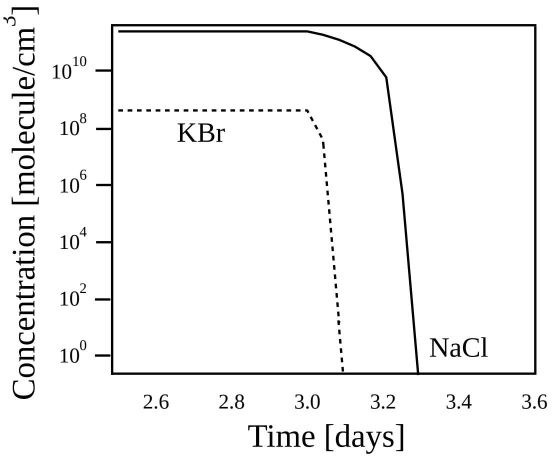

Figure 5.18: NaCl (solid line) and KBr (dotted line) as a function of time when saturation effects are introduced.

to 100 ppt [Hebestreit, 1999].

5.6 Conclusion

We performed calculations using a 0–D box model in order to observe the possible effects of heterogeneous chemistry on sea salt substrates in the marine boundary layer (MBL). 15 heterogeneous reactions of bromine and chlorine containing species have been added to 85 gas phase reactions and 25 photolysis reactions whose photolysis rate constant, J, have been calculated at ground level for 30°N and for the time of 1 to 10 January. We did not introduce any gaseous sources of chlorine and bromine, such as Cl_2, Br_2 or BrCl, instead Cl and Br atoms are generated from the aerosol particles (NaCl, KBr) after photolysis. No emissions of NO_x have been taken into account. For the sake of simplicity we have not considered deliquescent particles as it should be the case for applications in the MBL.

Simulations performed in an atmosphere free of Br–containing aerosol particles already indicates the principal changes occurring when chlorine heterogeneous chemistry is added to gas phase chemistry. The main observed effects are the denitrification of the troposphere because NO_y is converted to solid nitrates, and the increase of the oxidative capacity of the troposphere because of increasing concentrations of Cl atoms. Chlorine atoms may subsequently destroy ozone. The higher the surface–to–volume ratio of the aerosol particles, in the range from 0 to 100 $\mu m^2/cm^3$, the more these effects will be important.

The additional sink represented by the reaction of NO_2 with BrO leads to an increase of the tropospheric denitrification through formation of $BrONO_2$ when bromine chem-

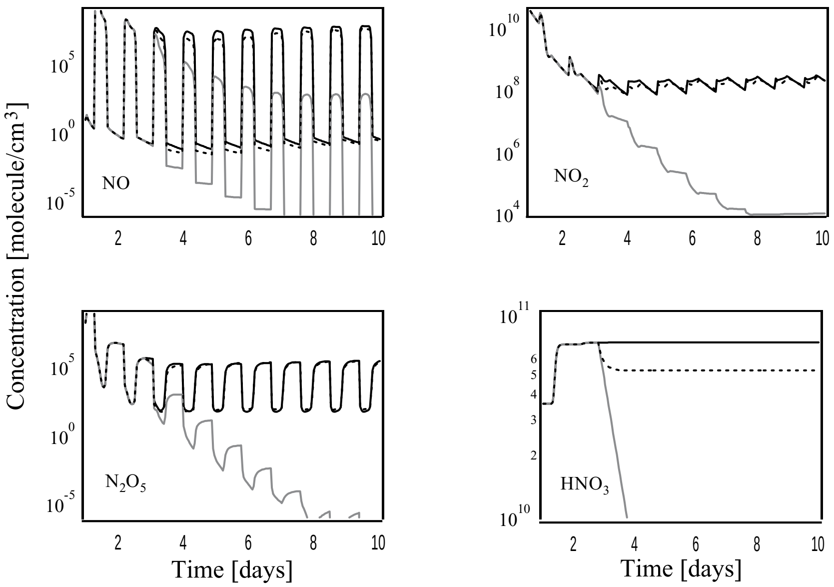

Figure 5.19: Display of some NO_y species. The solid black line corresponds to the reference case (no aerosol), the dotted line results from calculations performed with saturation effects and the gray solid line shows the case without saturation.

istry is added to chlorine chemistry. Halogen release (Cl_2, Br_2 and BrCl) is important at calculated mixing ratios which are comparable to recent measurements performed in the Arctic [Foster, 2001]. Bromine–containing species seem to have a strong capacity to destroy ozone. Depending on the NO_x mixing ratio, the most important bromine reservoir is different in going from a clean to a polluted area. Calculations show that at high NO_x concentrations, the most important bromine reservoir is $BrONO_2$, while at low NO_x HOBr is the most important bromine reservoir. We can conclude from these simulations that HOBr and $BrONO_2$ are the most important bromine reservoirs in the troposphere.

By introducing saturation of the salt substrate into the box-model, which may perhaps correspond to a more realistic situation, in that the solid salt reservoirs are consumed within a few hours, heterogeneous reactions are loosing their efficiency.

In conclusion, in scenarios presented above without and with saturation effects, heterogeneous reactions on salt substrates are very efficient in releasing volatile halogen compounds in the troposphere and may not be neglected in a realistic simulation of tropospheric boundary layer chemistry. We will insist that no emission and transport have been taken into account. The use of a chemical–radiative–transport model would have less dramatic effects on O_3 due to the possible dilution created by the transport phenomenon.

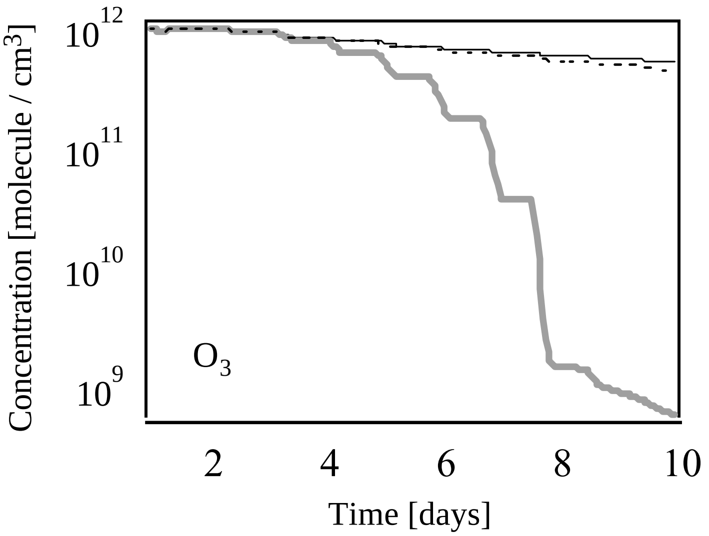

Figure 5.20: Display of the O_3 concentration as a function of time. The solid black line corresponds to the reference case (no aerosol), the dotted line results from calculations performed with saturation effects and the bold gray solid line shows the case without saturation. Calculations have been performed using A/V = 10 $\mu m^2/cm^3$ at 1.5 ppb of NO_x.

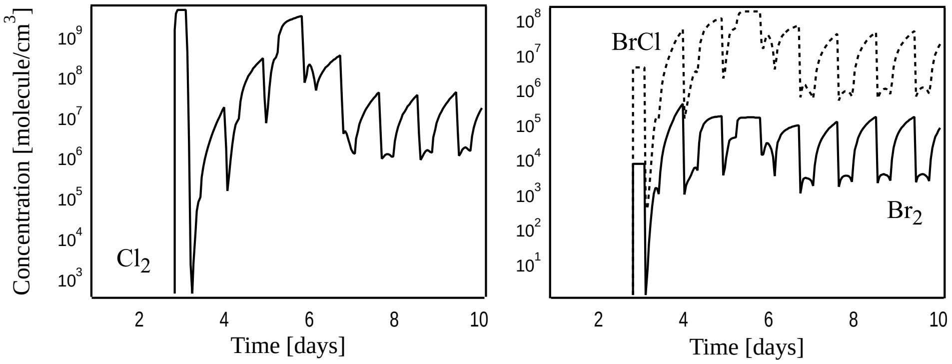

Figure 5.21: The release of volatile halogen–containing compounds. Cl_2 is displayed in the left panel, Br_2 (solid line) and BrCl (dotted line) are displayed on the right panel. Peak concentrations of 170, 0.2 and 10^{-4} ppt for Cl_2, BrCl and Br_2 have been observed in a clean air mass. Calculations have been performed using A/V = 10 $\mu m^2/cm^3$ at 1.5 ppb of NO_x.

Part B: Heterogeneous Reactions Relevant to the Stratosphere

Chapter 6

Interaction of Nitric Acid with Ice, Frozen Sulfuric Acid and Solid Ternary Solutions

6.1 Introduction

Nitric acid, HNO_3, plays a key role in atmospheric chemistry in that it is an important trace gas and NO_x reservoir that influences ozone and cloud formation. In particular the formation of cirrus clouds in the upper troposphere may be promoted by HNO_3 because of the influence of HNO_3 on aerosol activation transforming aerosol particles into cloud condensation nuclei [Laaksonen, 1997].

Upper tropospheric and lower stratospheric measurements at 54° N latitude over western Europe yielded HNO_3 mixing ratios between 760 and 1200 ppt [Lelieveld, 1997]. In the lower stratosphere, HNO_3 mixing ratios up to 2500 ppt have been observed over the western/central Pacific at midlatitudes (37° - 57° N) with a mean value of 1510 ppt [Singh, 1997]. Free tropospheric measurements performed by LeBel *et al.* [1990] at altitudes below 6 km resulted in a HNO_3 mixing ratio between 20 and 760 ppt over the northeastern Pacific Ocean and between 20 and 560 ppt over the western United–States. These results point to the importance of the occurrence of HNO_3 throughout the atmosphere.

In the atmosphere, the main source of HNO_3 is known to be the homogeneous reaction $OH + NO_2 + M$. However, for high latitudes and in the absence of sunlight the key reaction for the formation of HNO_3 in the lower stratosphere or upper troposphere is the following heterogeneous hydrolysis proceeding on background H_2SO_4 aerosol particles [Evans, 1985]:

$$N_2O_5(g) + H_2O(s) \rightarrow 2HNO_3(s) \tag{6.1}$$

Reaction (6.1) is fast with an uptake coefficient on the order of 0.1 in the temperature range 201 to 230 K on 60 wt % H_2SO_4 [Hanson, 1997]. The destruction of HNO_3 occurs through photodissociation whose yield is approximately 1 from 200 to 315 nm [Johnston, 1974], resulting in OH–radical production. Heterogeneous processes of HNO_3 on stratospheric ice particles may result in the formation of polar stratospheric cloud (PSC) Type I particles which are thought to consist of nitric acid trihydrate (NAT), $HNO_3 \cdot 3H_2O$ which is a stable binary form of HNO_3/H_2O under stratospheric conditions [Hanson and Mauersberger, 1988].

Other important sources of HNO_3 may be the hydrolysis of $ClONO_2$ and $BrONO_2$ proceeding on sulfuric acid aerosols according to reactions (6.2) and (6.3), respectively.

$$\begin{aligned} ClONO_2(g) + H_2O(s) &\rightarrow HOCl(g) + HNO_3(s) \quad (6.2) \\ BrONO_2(g) + H_2O(s) &\rightarrow HOBr(g) + HNO_3(s) \quad (6.3) \end{aligned}$$

These reactions have been found to be fast on sulfuric acid [Hanson, 1996; 1998] and on pure ice [Allanic, 1997; Oppliger, 1997]. Reactions (6.2) and (6.3) form adsorbed HNO_3 leading to amorphous HNO_3/H_2O mixtures [Zondlo, 1998] and gaseous HOCl and HOBr, respectively, when taking place on ice or PSC Type I particles [Abbatt, 1992; Hanson, 1995].

The focus of the present work lies in the kinetic study of the heterogeneous adsorption of HNO_3 on low temperature solid samples, such as pure water ice, H_2SO_4 frozen solutions and solid ternary solutions (STS) of $H_2SO_4/HNO_3/H_2O$.

The first point on which we will insist is that pure ice samples may be covered by more than one HNO_3 formal monolayer (ML) before the H_2O vapor pressure starts to decrease as opposed to the results obtained by Peter *et al.* [1994], who have concluded that the rate of evaporation of pure ice begins to decrease when a monolayer of NAT is formed on its surface. This is in agreement with studies performed by Tolbert and Middlebrook [1990] who showed that uncoated ice evaporated faster than ice coated with a formal monolayer of NAT. This is at variance with our results which show that the rate of evaporation of H_2O over ice starts to decrease once several formal monolayers of HNO_3 have been deposited.

The second goal of this chapter is to demonstrate that the use of a Knudsen flow reactor to study HNO_3 uptake on low temperature surfaces leads to identical results compared to the ones obtained in laminar flow tube experiments [Hanson, 1992]. Moreover, in view of the sometimes conflicting results of the uptake coefficient of HNO_3 on ice we were able to show, that we obtained consistent kinetic results using both steady state and time– resolved experimental methods. Our methodology rests on a correction scheme which accurately takes into account desorption of HNO_3 from the internal walls of the reaction vessel, a factor wich is particularly important in the case of as sticky a molecule as HNO_3. Recent measurements performed by Tolbert and co–workers in a Knudsen reactor resulted only in a lower limit of the uptake of HNO_3 on ice [Zondlo, 1997; 1998] which in fact is lower by a factor of 13 and 450 at 185 and 211 K, respectively, compared to the present results. Nevertheless, their study has the advantage that the condensed phase is probed *in situ* by FTIR absorption concomitantly with the kinetic measurement of HNO_3 uptake on ice.

We performed uptake experiments of HNO_3 on ice, H_2SO_4/H_2O and saturated ternary solutions of $H_2SO_4/HNO_3/H_2O$ in the temperature range 180–211 K using a FEP–Teflon–coated Knudsen reactor equipped with a mass spectrometer (MS) described in details in Chapter 2. Two types of experiments have been performed, namely steady state (SS) and pulsed–valve (PV) experiments. A typical PV experiment is shown in Figure 6.1 whereas a typical SS experiment is presented in Figure 6.2.The characteristic parameters of the reactor are presented in Table 4.1. Note that the sample surface area is $A_s = 17.0\ cm^2$ for the low temperature support (see Section 2.4). The collision frequency of HNO_3 is calculated from gas kinetic theory (see Table 4.1) to result in $\omega = 74\ s^{-1}$ at T = 300 K.

6.2 Interaction of HNO_3 with the Reactor Walls

The key parameter needed to obtain the uptake coefficient γ is the escape rate constant k_{esc}. Ideally, the value of k_{esc} given by gas kinetic theory only depends on the molecular mass of the gas phase species at a fixed temperature (Table 4.1). The case of HNO_3 is more complex as noticed by Fenter *et al.* [1994]. HNO_3 is a sticky compound, whose concentration on the reactor walls is different for SS and PV experiments owing to differing partial pressures. In PV experiments the MS signal decays faster than expected when calculated by the expression given in Table 4.1. We thus obtain an apparent value of the escape rate constant which is larger than the theoretical value. On the other hand, the MS signal decays more slowly in SS experiments when we halt the incoming flow of HNO_3 because of sustained desorption of HNO_3 from the internal walls of the Knudsen reactor. It therefore leads to k_{esc} values that are smaller than expected. The

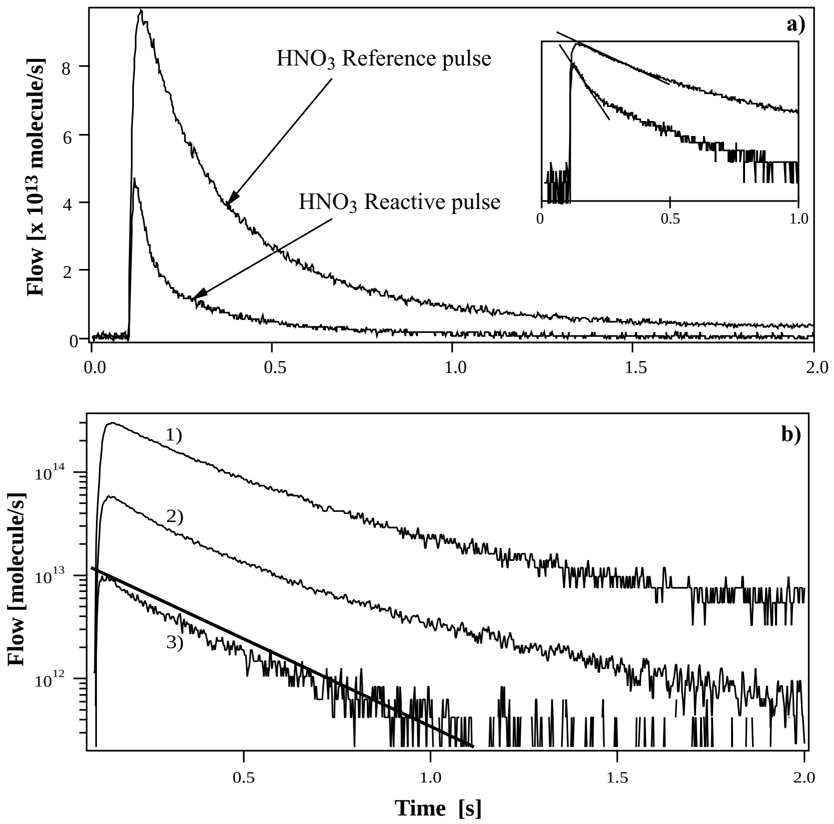

Figure 6.1: Panel a): Typical pulsed valve experiment of HNO_3, monitored at m/e 46, on bulk ice performed in the 14 mm diameter orifice reactor at 180 K using a dose of HNO_3 of $3.5 \cdot 10^{13}$ molecules leading to $\gamma = 0.28$. Panel b): Reference pulses of HNO_3 using a dose of 1) $1 \cdot 10^{14}$ molecules, 2) $2 \cdot 10^{13}$ molecules and 3) $3 \cdot 10^{12}$ molecules reveal complex behavior of HNO_3 on FEP–Teflon. The line represents the decay of a hypothetical non–interacting molecule of mass 63 resulting in $k_{esc} = 3.9$ s^{-1}.

escape rate constant is therefore not the same for both types of experiments as displayed in Tables D.1 to D.4 in Appendix D.

The observations in SS and PV experiments are qualitatively understood in terms of HNO_3 adsorption onto and desorption from the FEP–Teflon walls of the flow reactor. In PV experiments the walls of the Knudsen reactor act as a sink for HNO_3; before injection of a HNO_3 pulse, the Teflon coated reactor walls are devoid of HNO_3. When HNO_3 is injected into the reactor on the ms time scale, it will adsorb on the Teflon coat that is applied to the total internal reactor surface and will thus disappear faster from the gas phase than it would on a non–reactive surface. In SS experiments the internal surfaces of the Knudsen flow reactor are covered with adsorbed HNO_3 whose coverage depends on the flow rate of HNO_3 into the reactor, hence on the partial pressure of HNO_3, P_{HNO_3}. In order to determine k_{esc}, the flow of HNO_3 is halted and the resulting

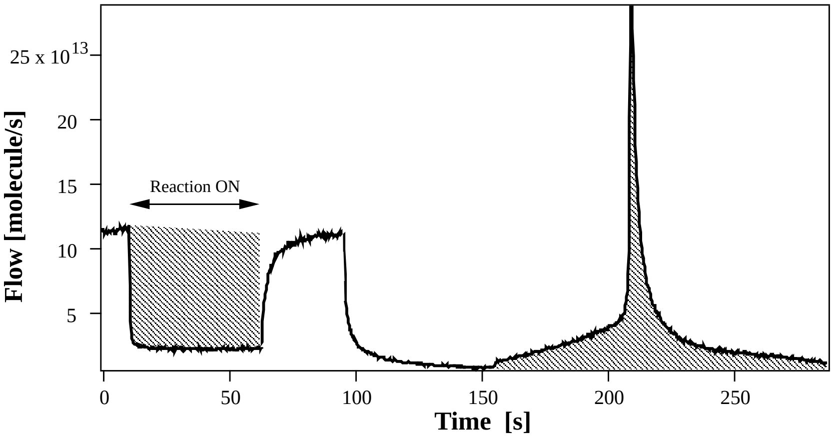

Figure 6.2: Typical steady–state experiment of HNO_3 on bulk ice performed in the 14 mm diameter orifice reactor at 200 K at $F^i_{HNO_3} = 1.2 \cdot 10^{14}$ molecule/s leading to $\gamma = 0.16$. The first half of the trace represents the uptake of HNO_3 on ice, while the second shows the desorption of HNO_3 from the support upon warming. Both integrals represented by dashed areas are equal, thus pointing towards a closed mass balance.

decay of P_{HNO_3} whose rate of change directly leads to k_{esc} is monitored. However, during the decrease of P_{HNO_3} owing to the interaction of HNO_3 with the condensed phase, adsorbed HNO_3 desorbs from the Teflon–coated internal surfaces which act like a reservoir for HNO_3 and therefore give rise to a HNO_3 source term. The net result is a decrease in k_{esc} owing to the replenishment of gas phase HNO_3 (P_{HNO_3}) with formerly adsorbed HNO_3 thus leading to an effect in k_{esc} opposite to the one observed in PV experiments. Using the 14 mm escape orifice reactor, we calculate a value of k_{esc} of 3.9 s^{-1} for HNO_3 according to gas kinetic theory, whereas PV experiments obtain k_{esc} of (5 ± 1) s^{-1} and SS experiments result in $k_{esc} = (2 \pm 1)$ s^{-1}. In all experiments we measured k_{esc} for the specific experimental conditions before each uptake experiment and used this value to determine γ.

Regarding PV experiments a simple model has been developed by Fenter *et al.* [1994] to separate wall contributions from escape. The decrease of both reference and reactive MS signals can be approximated by a double exponential decay. The insert of Figure 6.1.a shows the decay of both pulses. The effects of the internal reactor surfaces for a PV experiment are present to approximately the same extent in both pulses and therefore almost cancel. Although the HNO_3–FEP Teflon interaction has not been studied quantitatively in this work we would like to stress that the present measurement is a difference measurement of the initial slopes as shown in the insert of **Figure 6.1.a**, whereby the complex decay pertaining to the reference pulse cancels to a large extent.

A detailed discussion of the chemical–kinetic mechanism of the interaction of HNO_3 with the FEP–coated internal walls of the Knudsen flow reactor is clearly outside the scope of this work. However, a look at **Figure 6.1.b** which displays the decay of the MS signal of HNO_3 as a function of time at three different doses underlines the strong sensitivity of the decay rate and thus the gas lifetime of HNO_3 on the dose or its initial transient partial pressure. Three qualitative observations may be made based upon inspection of the three reference experiments presented in **Figure 6.1.b**:

- The initial slope of MS signal 3) and 2) is larger than the reference representing a non–interacting molecule of mass 63. The slope of signal 1) pertaining to a dose larger by a factor of approximately 30 compared to signal 3) is equal to the theoretical reference of $k_{esc} = 3.9\ s^{-1}$. This is consistent with increasing HNO_3 desorption from the wall even during the decay with increasing HNO_3 dose.

- At a low dose (signal 3)) there is no lingering "memory" effect of desorbing HNO_3 as the MS signal fairly rapidly goes to zero. At high dose such as for signal 1) so much HNO_3 has adsorbed onto the Teflon walls that they become a (pseudo–) steady–state source of HNO_3 after approximately 2 s at a level of 2.3 % of the initial amplitude of the MS signal. This then means that the walls act as a steady–state reservoir for HNO_3 at high dose akin to high continuous flow rates.

- The mechanism of the HNO_3–interaction with the FEP–coated internal walls of the Knudsen flow reactor is complex, that is non–exponential, and merits perhaps a study in its own right.

In contrast to PV experiments a correction to the measured value of γ_{obs} has to be applied in SS experiments. Figure 6.3 shows a typical SS experiment where I_0 and I are the observed MS intensities obtained during an uptake experiment. In a SS experiment there is steady state between HNO_3 adsorption and desorption processes on the internal surfaces of the Knudsen flow reactor before opening the sample chamber as well as during the uptake experiment. When the condensed phase is exposed to the gas phase at t = 15 s, a fast partial pressure drop of HNO_3 occurs, because the ice substrate acts as a cryogenic pump. Owing to the decrease of the HNO_3 partial pressure, the steady state between the rate of HNO_3 adsorption and desorption on the walls is perturbed. A significant amount of HNO_3 molecules desorb from the walls during the reaction, thus increasing the MS–signal at m/e 46 so that the level observed during the reaction is higher than it would be in the ideal case of a non–sticky molecule.

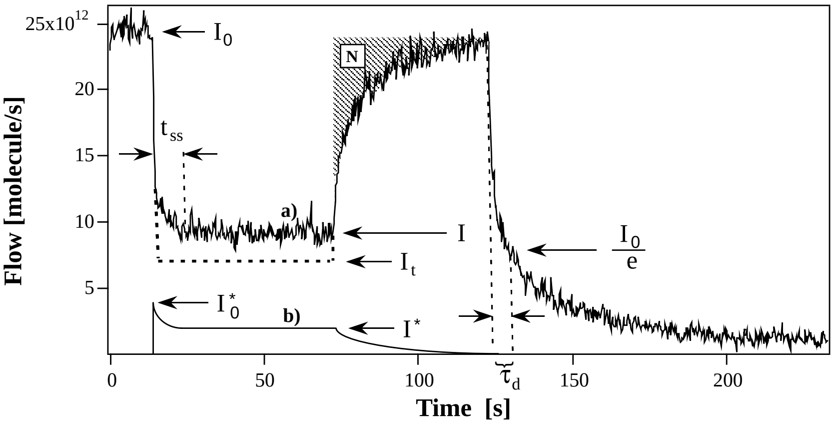

Figure 6.3: Bold trace a) shows an experimental MS signal of HNO_3 at m/e 46 observed at 210 K, the dashed line represents the expected signal if there were no wall contribution during the uptake experiment. The bold trace b) is the calculated additional source of HNO_3 in order to correct the value of the HNO_3 uptake coefficient (see text for details).

6.2.1 Correction of the Observed Uptake Coefficient in Steady State Experiments

To correct the experimental γ_{obs} value, one makes the following assumptions. First, the hatched area displayed in Figure 6.3 resulting from the sluggish recovery of the initial MS signal level of HNO_3 upon closing the sample compartment corresponds to the number of molecules, N, which desorb from the walls during the reaction. If no HNO_3 stuck to the walls during a SS experiment, the HNO_3 MS signal would rise instantaneously on the chosen time scale at the end of the uptake experiment, and would therefore not be delayed as observed in Figures 6.2 and 6.3. The second assumption is that this additional source of HNO_3 appearing during reaction contributes to a partial albeit hypothetical flow rate I_0^* given by $I_0^* = \frac{N}{t_{ss}}$ molecule/s, where t_{ss} is the time necessary to reach steady state during the uptake. When the HNO_3 flow rate is halted at t = 125 s, one may determine the rate constant for HNO_3 desorption from the internal walls, $k_d = \frac{1}{\tau_d}$, by measuring the time, τ_d, necessary to observe the decay of the MS signal to $\frac{I_0}{e}$ (see Figure 6.3). All τ_d values are in the range 10 to 20 s, which results in the desorption kinetics of HNO_3 from the walls falling in the range between 0.05 and 0.10 s^{-1}. The measured values of t_{ss} measured upon HNO_3 uptake seem to be a multiple of τ_d measured at the end of the uptake experiment (Figure 6.3).

Figure 6.3 displays an experimental trace obtained at a substrate temperature of 210 K (trace a)). We make the assumption that the dashed line just below a) would be the true (calculated) SS signal level if there was no contribution from HNO_3 desorbing from the internal surfaces. The reactor walls are considered as a constant source of

HNO_3 during the uptake experiment because of the large reservoir of HNO_3 extending over 1300 cm^2 of the internal reactor area. In this case, one may express the true uptake coefficient γ_t by equation (6.4) if I_t were known. Trace b) in Figure 6.3 shows the calculated additional HNO_3 flow rate I^* at steady state due to the desorption of N molecules of HNO_3 from the walls. Before opening the sample compartment, there is no additional flow as there is steady state between the rate of adsorption and desorption of HNO_3. Upon opening the sample chamber at t = 15 s, the N molecules of HNO_3 desorb from the walls and react on the ice sample according to γ_t, which may be expressed by equation (6.5).

$$\gamma_t = \frac{k_{esc}}{\omega} \cdot \left(\frac{I_0}{I_t} - 1\right) \tag{6.4}$$

$$\gamma_t = \frac{k_{esc}}{\omega} \cdot \left(\frac{I_0^*}{I^*} - 1\right) \tag{6.5}$$

Equation (6.4) gives the true uptake coefficient γ_t for the external source, while equation (6.5) results in the identical value for γ_t due to HNO_3 desorbing fom the walls (internal source). This equation system is made up of 2 equations with 3 unknowns: γ_t, I^*, I_t and 3 known parameters: I_0, I (measured), I_0^* (calculated, see above). Both equations have been set equal to each other, and by making the assumption that $I^* = I - I_t$, the resolution of this system leads to the following expression for γ_t:

$$\gamma_t = \gamma_{obs} + \frac{k_{esc} \cdot N}{\omega \cdot t_{ss} \cdot I} \tag{6.6}$$

where $\gamma_{obs} = \frac{k_{esc}}{\omega} \cdot \left(\frac{I_0}{I} - 1\right)$ is the experimental value for the uptake obtained using the measured initial and final MS signal intensities I_0 and I in relations (2.10) and (2.11), k_{esc} is the escape rate constant, N the total number of HNO_3 molecules desorbing from the walls, ω the collision frequency with the reactive surface and t_{ss} the time necessary to reach steady state after lifting up the plunger: t_{ss} is of the same order as the decay time of the MS signal once the HNO_3 flow rate has been halted.

6.3 The Heterogeneous Interaction of HNO_3 on Ice

6.3.1 Kinetic Results

We have performed steady–state (SS) and pulsed–valve (PV) experiments on two different types of ice, namely bulk ice (B) and condensed ice (C) at temperatures from 180 up to 211 K. Typical uptake experiments of nitric acid on ice are shown in Figures 6.1.a and 6.2. Most of the experiments have been carried out using the 14 diameter orifice reactor.

Figure 6.1.a shows a PV experiment performed at 180 K. The large pulse is the reference pulse whose decay is given by $k_{esc} = 4.3$ s^{-1}. The small pulse is the reactive one, with the sample chamber open, resulting in $k_{dec} = 23.9$ s^{-1} corresponding to an uptake coefficient of 0.28 ± 0.08, where uncertainties are determined by the MS signal noise. The insert in Figure 6.1.a shows the semilogarithmic plot of both the reference as well as the reactive pulse. Deviations from first order decay kinetics are apparent for both pulses at late times, in keeping with the complications discussed above. Figure 6.2 shows a SS experiment performed at 200 K. When the ice sample is exposed to HNO_3 a rapid drop of the MS signal at m/e 46 is observed and a steady state level is reached after a few seconds (t_{ss}) corresponding to $\gamma = 0.16 \pm 0.05$ at 200 K. When the sample chamber is closed at t = 60 s in order to stop the uptake, we observe that the MS signal increases only slowly to reach its initial level, which we attribute to adsorption of HNO_3 onto the reactor walls as discussed above. Subsequently, the flow rate of HNO_3 entering the reactor is halted and the temperature of the support is increased at t = 155 s with the movable plunger open in order to let HNO_3 evaporate from the previously exposed ice substrate. The evaporation rate is at a maximum at t = 215 s and corresponds to the peak signal displayed in Figure 6.2 which appears at 218 ± 3 K using the 14 mm escape reactor orifice. In all uptake experiments the number of HNO_3 molecules condensing onto both types of ice (B, C) is equal to the number desorbing from the condensed phase upon increasing the temperature thus resulting in a closed mass balance in the uptake experiments such as those shown in Figure 6.2.

The results on the uptake kinetics of HNO_3 on ice are displayed in Tables D.1 to D.5 (Appendix D) for the temperature range 180 to 211 K. We note the discrepancy of k_{esc} determined in PV and SS experiments which has been assigned to the contribution of the reactor walls. In PV experiments, k_{esc} is increased due to HNO_3 loss on the reactor walls, whereas in SS experiments, k_{esc} is smaller owing to HNO_3 desorption from the walls, as discussed above. In PV experiments k_{esc} is twice as large as in SS experiments. At a specific temperature, the uptake coefficient γ_{obs} obtained in PV and SS experiments are independent of the dose and the flow entering the reactor, respectively, and therefore of the concentration of HNO_3. This confirms a first order rate law for the uptake process whose rate constant k_{uni} has been obtained from equation (2.13) for PV experiments and from equation (2.10) for SS experiments. Although the observed γ values obtained in SS experiments are in general 15 % smaller than the ones obtained in PV experiments, they are indistinguishable as shown in the Arrhenius representation displayed in Figure 6.4

once the correction according to equation (6.6) has been applied to the SS experiments. Not all γ values have been corrected owing to experimental problems. At 180, 190, 200 and 210 K, γ values displayed in Figure 6.4 have been shifted for clarity by +0.5 K and –0.5 K for SS and PV experiments, respectively,in keeping with uncertainties of the temperature measurement.

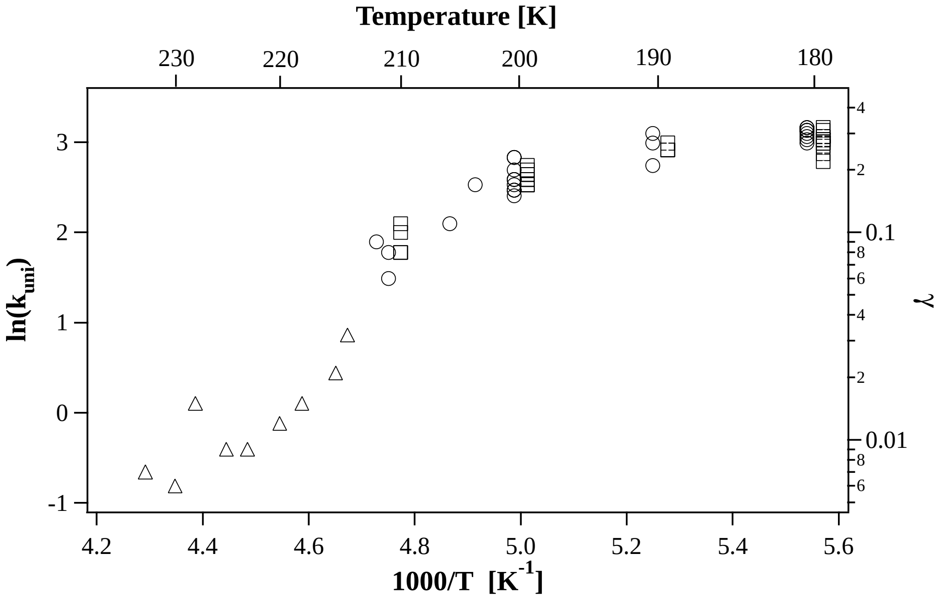

Figure 6.4: Arrhenius representation of the uptake rate constant of HNO_3 on bulk ice and condensed ice (confounded), obtained in pulsed valve (squares) and steady state (circles) experiments, the latter of which are corrected using equation (6.6). The triangles are preliminary results obtained by Cox and co-workers [Fernandez, 2001].

Figure 6.4 clearly shows two distinct regimes of temperature dependence. In the high temperature regime, k_{uni} or γ changes faster with temperature compared to the low temperature regime. The uptake coefficient γ drops from 0.30 at 180 K to 0.06 at 211 K and therefore corresponds to a negative temperature dependence. At these relatively high temperatures, the low values of γ may be attributed to a significant evaporation rate, resulting in a significant decrease of the net HNO_3 uptake, on the order of a factor of 5 akin to the uptake coefficient of $D_2^{18}O$ on $D_2^{16}O$ ice samples [Chaix, 1998]. The transition temperature between these two regimes is approximately (195 ± 5) K, similar to the transition temperature for $D_2^{18}O$ observed by Chaix *et al.* [1998]. At $T < 195$ K, we did not observe any temperature dependence of γ which was constant at $\gamma = 0.26 \pm 0.09$. From the temperature dependence of k_{uni} observed at $T > 195$ K, we have determined an activation energy of $E_a = -6.8 \pm 1.0$ kcal/mol for the adsorption process of HNO_3 on both types of ice. Despite the simple first order rate law for HNO_3 adsorption on pure ice, its negative temperature dependence of k_{uni} and γ leads to a complex adsorption mechanism. In Section D we present modeling results of our experimental kinetic data according to a Langmuir–Hinshelwood mechanism involving a precursor to HNO_3 adsorption.

Table 6.1: Uptake coefficients γ of HNO_3 on ice.

T [K]	γ	Experimental Technic/Detection	References
185	> 0.02	Knudsen reactor/MS, FTIR–RAS	Zondlo *et al.*, 1998
191	≥ 0.30	Flow tube/CIMS	Hanson, 1992
197	$0.3\,^{+0.7}_{-0.1}$	Flow tube/MS	Leu, 1988
200	≥ 0.20	Flow tube/CIMS	Hanson, 1992
200	0.30	Knudsen reactor/MS	Seisel *et al.*, 1998
211	$\gamma_0 \geq 0.005$	Knudsen reactor/MS, FTIR–RAS	Zondlo *et al.*, 1997
	$\gamma_{ss} = 0.0002$	Knudsen reactor/MS, FTIR–RAS	Zondlo *et al.*, 1997
218	> 0.20	Flow tube/MS	Abbatt, 1997
180	0.29 ± 0.07	Knudsen reactor/MS	This work
190	0.26 ± 0.03	Knudsen reactor/MS	This work
200	0.18 ± 0.02	Knudsen reactor/MS	This work
210	0.09 ± 0.02	Knudsen reactor/MS	This work

CIMS: Chemical Ionization Mass Spectroscopy. MS: Mass Spectroscopy.
FTIR–RAS: Fourier Transform Infra Red Reflection–Absorption Spectroscopy.

Table 6.1 summarizes the kinetic results obtained in this study as well as previous results obtained in other laboratories [Leu, 1988; Hanson, 1992; Abbatt, 1997; Zondlo, 1997, 1998; Seisel, 1998]. The uptake coefficients γ_0 for HNO_3 on ice samples reported here (Tables D.1 to D.5) are in good agreement with the lower limits reported by Hanson [1992] at 191 K and 200 K. As shown in Table 6.1, most of the authors using the flow tube technique only give lower limits for the uptake coefficient of HNO_3 on ice owing to the large value of γ. Abbatt [1997] obtains a γ value higher than 0.2 at 218 K which appears to be too large at this temperature compared to our result at 210 K. Due to rate–limiting gas phase diffusion of HNO_3, flow tube experiments can only give limited information in the case of rapid kinetics such as in the present case. Zondlo *et al.* [1997, 1998] give lower limits for the initial uptake coefficient γ_0 obtained in their Knudsen reactor, and γ_{ss} is significantly smaller when steady state is reached, amounting to a factor of 300. At 211 K, we observe partial saturation of the ice sample as was observed by Zondlo *et al.* as well. The low γ values found by Tolbert and co–workers [Zondlo, 1997, 1998] may perhaps be explained by wall contributions during HNO_3 uptake. Their experimental apparatus has a large ratio of internal to reactive surface area which may possibly lead to significant quantities of HNO_3 desorbing from the reactor walls. This in turn would lead to higher than expected values of the partial pressure of HNO_3 at steady state conditions resulting in a small net HNO_3 uptake on the ice and thus to low γ values.

6.3.2 Condensed Phase Product

The investigations of the uptake of HNO_3 on ice samples for a temperature range of 180 to 200 K show constant uptake over the time scale of 50 s (Figure 6.2). We have performed prolonged uptake experiments of HNO_3 interacting with the condensed ice (C) substrate in order to determine the mean stochiometric ratio between H_2O and HNO_3 in the condensed phase. This type of experiment allowed us to determine the average concentration of the condensed substrate from mass balance arguments at certain selected discontinuities of the HNO_3 partial pressure curve with time. It has been performed on condensed ice whose thickness and temperature are shown in Table 6.2 as well as the results obtained for n, which is the ratio of H_2O remaining in the condensed phase to HNO_3 condensed on the ice sample when abrupt changes in P_{HNO_3} appear at t = 210 and 550 s as displayed in Figure 6.5a and 6.5b, respectively. Raw data are displayed in Figure 6.5, where panels a) and b) show experiments performed on condensed ice samples at 180 and 200 K, respectively. We recorded both HNO_3 (m/e 46) and H_2O (m/e 18) in order to obtain an accurate mass balance for both components at any given point in time. Abrupt changes of the partial pressure of HNO_3 have been observed at m/e 46 at t = 550 s (Figure 6.5b) and t = 210/640 s (Figure 6.5a) at 200 and 180 K, respectively.

The abrupt change of the HNO_3 partial pressure is assumed to be a change of the phase of the sample (phase transition). Concurrently, we have measured the number of H_2O molecules that have desorbed from the ice sample by monitoring the partial pressure of H_2O at m/e 18. When we compare the number of H_2O molecules making up the sample prior to the uptake experiment and the number of H_2O molecules which have desorbed at a given time, one is able to determine the quantity of ice remaining on the support at any given time. For instance, in the case displayed in Figure 6.5b we have condensed $2.87 \cdot 10^{19}$ H_2O molecules, resulting in an ice sample of approximately 670 nm. During the HNO_3 uptake experiment $2.82 \cdot 10^{19}$ H_2O molecules have desorbed from the sample surface. Therefore $5.3 \cdot 10^{17}$ H_2O molecules still remain on the support at 550 s. At the same time, $5.9 \cdot 10^{17}$ HNO_3 molecules have been adsorbed on the ice sample, leading to a mean stochiometric ratio between H_2O and HNO_3 in the condensed phase of n = 0.9. The n values obtained are displayed in Table 6.2. The ice surface was not equilibrated by an external H_2O flow, in order to be able to follow the change in the H_2O MS signal at m/e 18.

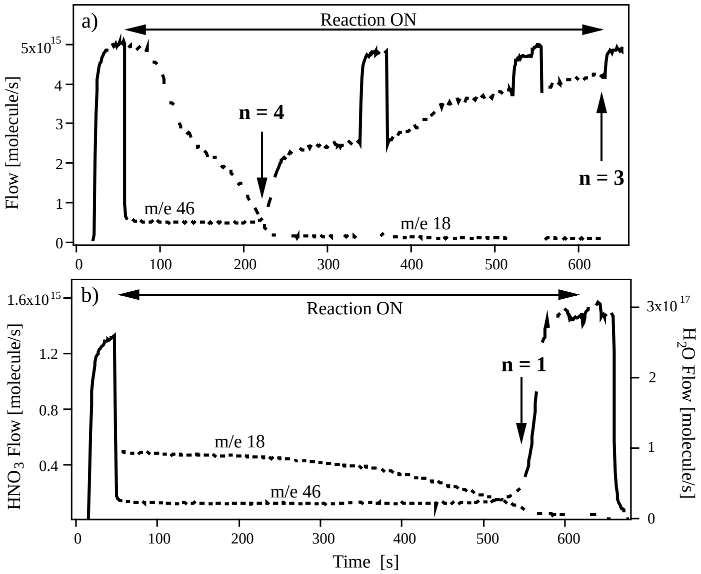

Figure 6.5: Steady state uptake experiments of HNO_3 (m/e 46) on condensed ice on a long time scale at a) 180 K using the 14 mm orifice reactor and b) 200 K using the 8 mm orifice reactor. H_2O has been monitored at m/e 18. The mean concentration ratio HNO_3:H_2O of the condensed mixture is expressed as n.

At 180 K, we observe two distinct levels of HNO_3 during the uptake (Figure 6.5a) in contrast to experiments performed at 200 K (Figure 6.5b) and 190 K (not shown). At 200 K (Figure 6.5b) we calculate a mean composition of the solid substrate of $HNO_3 \cdot 1H_2O$ at t = 550 s. The ratio calculated at 180 K and t = 210 s shows a mean composition of the solid substrate of $HNO_3 \cdot 4H_2O$ when the net uptake of HNO_3 begins to decrease. At the end of the uptake at t = 640 s we found a mean composition of $HNO_3 \cdot 3H_2O$ (see Figure 6.5a). At this temperature, which is below the ice frost point, we apparently obtain a mean stoichiometry corresponding to NAT across the average of the condensed phase, namely HNO_3:H_2O = 1:3 when it is exposed for a long time to gaseous HNO_3. In contrast, at 190 K and 200 K one obtains an average condensed phase having a mean stoichiometry of HNO_3:H_2O = 1:1 at long HNO_3 exposure. We emphazise that the present mass balance argument only addresses the average composition of the condensed phase at any one time, and that possible inhomogeneities in sample composition as probed by depth profiling are therefore not accessible.

Figure 6.6 shows the phase diagram of the HNO_3/H_2O system obtained by Hanson

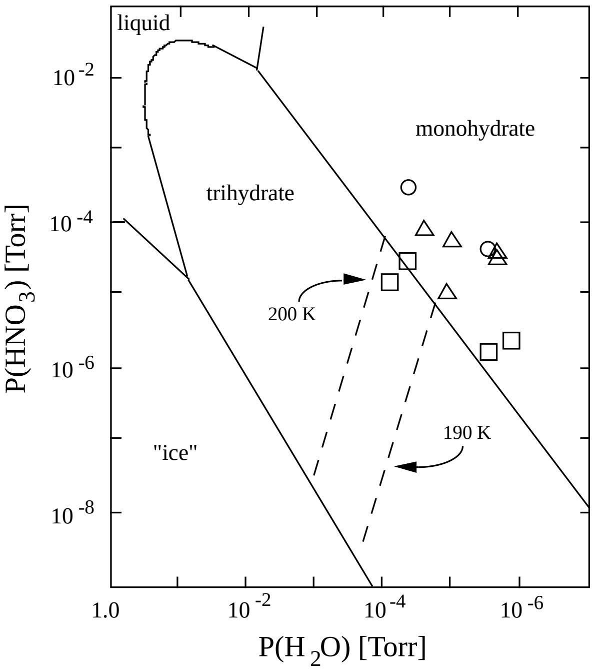

Figure 6.6: HNO_3/H_2O phase diagram with partial pressures of HNO_3 plotted against pressure of H_2O observed during prolonged uptake experiments of HNO_3 on ice at 180 K (□), 190 K (◯) and 200 K (△). Solid lines are the coexistence curves and dashed lines are measured pressures over trihydrates observed by Hanson and Mauersberger [1988] at a fixed temperature (NAT phase diagram from Hanson and Mauersberger [1988]).

and Mauersberger [1988] including the partial pressures of both HNO_3 and H_2O observed from our prolonged uptake experiments of HNO_3 on ice. Partial pressures have been measured at steady state after an abrupt change attributed to a phase transition such as displayed in Figure 6.5. Experiments performed at 180 K reveal partial pressures corresponding to the coexistence curve between trihydrate and monohydrate, which is in good agreement with the results from mass balance experiments (n = 3, Figure 6.5a, t=640 s). At 190 and 200 K, the observed partial pressures clearly correspond to those of HNO_3 monohydrate or some undefined mixture for $n > 1$ (Figure 6.5b, t=550 s), in agreement with results shown in Table 6.2.

However, it must be pointed out that the present experiments do not distinguish between crystalline and amorphous phases of the same stoichiometry. In order to more precisely describe the phases, spectroscopic studies of the condensed phase must be carried out as has recently been done by Zondlo *et al.* [1997, 1998].

Table 6.2: Mean composition of the $HNO_3 \cdot nH_2O$ condensed phase. Experiments performed on condensed ice samples.

T [K]	C [(a)] [molecules]	h [(b)] [nm]	HNO_3(cond) [molecules]	n	t [(c)] [s]	P(HNO_3) [Torr]	P(H_2O) [Torr]
180	$4.50 \cdot 10^{18}$	100	$9.01 \cdot 10^{17}$	4.1 (d)	160	$1.6 \cdot 10^{-6}$	$2.6 \cdot 10^{-6}$
180	$4.50 \cdot 10^{18}$	100	$1.21 \cdot 10^{18}$	3.0 (e)	560	$2.4 \cdot 10^{-6}$	$1.3 \cdot 10^{-6}$
180	$4.65 \cdot 10^{19}$	1100	$8.80 \cdot 10^{17}$	4.5 (f)	185	$1.6 \cdot 10^{-5}$	$8.7 \cdot 10^{-5}$
180	$4.65 \cdot 10^{19}$	1100	$1.34 \cdot 10^{18}$	2.8 (f)	530	$3.4 \cdot 10^{-5}$	$4.4 \cdot 10^{-5}$
190	$2.78 \cdot 10^{18}$	65	$6.31 \cdot 10^{17}$	1.2	145	$4.1 \cdot 10^{-5}$	$2.5 \cdot 10^{-6}$
190	$9.01 \cdot 10^{19}$	2120	$1.12 \cdot 10^{18}$	1.1	2450	$3.3 \cdot 10^{-4}$	$4.5 \cdot 10^{-5}$
200	$1.19 \cdot 10^{19}$	280	$4.39 \cdot 10^{17}$	1.8	120	$3.5 \cdot 10^{-5}$	$1.9 \cdot 10^{-6}$
200 (g)	$1.42 \cdot 10^{19}$	330	$1.64 \cdot 10^{18}$	1.2	230	$6.0 \cdot 10^{-5}$	$9.7 \cdot 10^{-6}$
200 (g)	$2.87 \cdot 10^{19}$	670	$5.85 \cdot 10^{17}$	0.9	495	$1.0 \cdot 10^{-5}$	$1.1 \cdot 10^{-5}$
200	$3.89 \cdot 10^{19}$	916	$1.47 \cdot 10^{18}$	1.1	401	$8.0 \cdot 10^{-5}$	$2.3 \cdot 10^{-5}$
200	$1.11 \cdot 10^{20}$	2610	$4.01 \cdot 10^{18}$	1.1	740	$3.0 \cdot 10^{-5}$	$1.9 \cdot 10^{-6}$

(a) Number of H_2O molecules condensed on the cold support.

(b) Thickness of the condensed ice sample ($\rho = 0.92$ gr cm^{-3}).

(c) Time at which the phase transition has been observed after the opening of the sample compartment.

(d) Value measured at t = 220 s in Figure 6.5.a.

(e) Value measured at t = 620 s in Figure 6.5.a.

(f) Same type of experiment as displayed in Figure 6.5.a.

(g) Experiments performed using the 8 mm aperture reactor.

6.3.3 HNO_3 Diffusion in Ice

The prolonged uptake experiments allow us to determine the amount of HNO_3 which adsorb on the ice sample before the H_2O partial pressure monitored at m/e 18 begins to decrease in the reactor for instance at t $\cong$ 250 s on and at the transition t $\cong$ 550 s displayed in Figure 6.5b. The results are displayed in Table 6.3, where the amounts of absorbed HNO_3 are expressed in formal monolayers (ML) of HNO_3 assuming that one HNO_3 formal monolayer corresponds to $5 \cdot 10^{14}$ molecule/cm^2. One observes for the first case that between 10 and 35 ML of HNO_3 have been adsorbed on the ice sample whereas at the transition point between 50 and 500 ML have been adsorbed.

The phase transition appears after a delay of the order of 200 sec, during which the HNO_3 molecules can diffuse into the bulk of the ice. Fick's first law (equation (6.7)) describes a stationary process of molecular diffusion and was used to calculate the effective distance of penetration of HNO_3, d, into the bulk.

$$J = -D\frac{\partial C(x,t)}{\partial x} \tag{6.7}$$

where J is the flux of HNO_3 which may be expressed in our case by:

$$J = \frac{F^{in} - F^{out}}{A_s} \tag{6.8}$$

where F^{in} and F^{out} is the HNO_3 flow entering and leaving the reactor in molecule·s^{-1}, D is the diffusion coefficient of HNO_3 in the ice and $\frac{\partial C}{\partial x}$ is the concentration gradient of HNO_3 in the condensed ice sample. This gradient may be approximated by a linear relationship using the known amount of HNO_3 taken up into the unknown volume $V = A_s \cdot d$. The gradient of HNO_3 in the ice substrate may therefore be expressed using the following expression:

$$-\frac{\partial C(x,t)}{\partial x} \approx \frac{C(0,t) - C(h,t)}{d} = \frac{N(HNO_3)}{Vd} \tag{6.9}$$

where $N(HNO_3) = (F^{in} - F^{out})\cdot t$ is the quantity of HNO_3 molecules adsorbed on the ice sample during the time t. By substituting equations (6.8) and (6.9) into Fick's first law, equation (6.7), one obtains the following known equation for d, the diffusion length:

$$d = \sqrt{Dt} \tag{6.10}$$

Under the conditions that Fick's law is applicable to our experimental conditions, one obtains the well known relation for the diffusion length, whose values are displayed in Table 6.3. At low temperatures (180, 190 K) one obtains a mean value of 15 ± 8 nm and at 200 K a mean diffusion length of 68 ± 22 nm is obtained at the phase transition with $D = 1.37 \cdot 10^{-2610/T}$ measured by Thibert and Dominé [1998] for single crystal ice. If the condensed phase is amorphous, the results displayed in Table 6.3 are lower limits for the diffusion length. At 180 K, the diffusion length represents 10 % of the remaining ice thickness, whereas at 190 and 200 K the diffusion length is of the order of 100% of the remaining substrate on the support at phase transition. If we take a value 100 times larger for D as has been observed repeatedly in the literature for amorphous or bulk ice substrates, the penetration depths d increase accordingly by a factor of ten. The message is that even at 180 K HNO_3 may have sufficient time to diffuse across the condensate in order to change the bulk composition.

Table 6.3: Quantity of HNO_3 in ML adsorbed on the condensed ice sample, mean distance d of penetration of HNO_3 into the bulk and thickness h of the condensate.

T [K]	Adsorbed HNO_3/ML	d $^{(a)}$ [nm]	h [nm]
180	16 $^{(b)}$/106 $^{(c)}$	3.7 $^{(b)}$/8.6 $^{(c)}$	102 $^{(b)}$/87 $^{(c)}$
180	20/104	3.9/9.0	741/94
190	14/74	8.7/19.1	56/22
190	10/132	12.0/24.8	2052/28
200	15/52	15.6/39.8	219/35
200	35/193	22.4/54.0	252/45
200	16/69	44.1/78.4	346/85
200	24/173	33.3/70.3	257/50
200	35/472	41.3/97.0	1976/101

$^{(a)}$ $d = \sqrt{Dt}$, where $D = 1.37 \cdot 10^{-2610/T}$ [Thibert, 1998].

$^{(b)}$ Measured when H_2O partial pressure begins to decrease.

$^{(c)}$ Measured at the phase transition.

6.4 The Interaction of HNO_3 on Frozen H_2SO_4/H_2O

We performed SS uptake experiments of HNO_3 on solid frozen H_2SO_4/H_2O samples at different concentrations from 10 to 98 % at two different temperatures of 180 and 200 K. Two types of SS experiments were performed, namely one with and one without external water flow whose primary purpose is to equilibrate the substrate interface. Figure 6.7 shows typical SS experiments ($F^{in}_{HNO_3} = 10^{14}$ molecule/s) without external water flow performed at 180 K at three different H_2SO_4 concentrations, namely 17, 60 and 98 % wt H_2SO_4. One observes a constant HNO_3 rate of uptake at 17 and 60 % wt H_2SO_4 solid samples, whereas partial saturation of the uptake rate is observed on 98 % wt H_2SO_4 sample.

The initial uptake coefficients obtained on frozen H_2SO_4 solutions are displayed in Figure 6.8 whose uncertainties are of the order of 20 %. These γ values have not been corrected according to equation (6.6). As discussed above regarding the interaction of HNO_3 on pure ice, the correction applied would be negligible at high HNO_3 flow rate, such as used in the interaction of HNO_3 on frozen H_2SO_4/H_2O. The top and bottom panels in Figure 6.8 show the results measured at 180 and 200 K, respectively. At both temperatures one observes the same behaviour. In experiments performed without external H_2O flow (open squares in Figure 6.8), the uptake coefficient decreases with

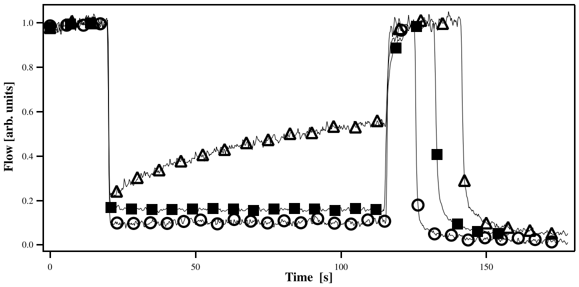

Figure 6.7: Steady state uptake experiments of HNO_3 at 180 K on H_2SO_4/H_2O frozen solutions without H_2O external flow at three different H_2SO_4 concentrations: 17 wt % (◯), 60 wt % (■) and 98 wt % (△).

increasing H_2SO_4 concentration. The H_2O partial pressure inside the reactor gradually decreases during an uptake experiment without balancing H_2O flow. By pumping on the sample at a given concentration of H_2SO_4, the H_2SO_4 concentration at the surface may increase because of evaporation of H_2O and limiting condensed phase diffusion of H_2O. This may lead to a change in the concentration at the interface during an uptake experiment. One notes that even at the lowest H_2SO_4 concentration, γ is smaller than for both types of pure ice samples. The uptake coefficient decreases from 0.3 to 0.2 at 180 K and from 0.2 to 0.1 at 200 K in going from pure ice to a 10 wt % H_2SO_4 solid solution. At 98 wt % H_2SO_4, γ drops to 0.05 and 0.03 at 180 K and 200 K, respectively. Figure 6.8 shows that between these two limits of H_2SO_4 concentration, γ linearly decreases by a factor of 10 for experiments performed without external H_2O flow.

In the experiments performed with an external H_2O flow (full diamonds in Figure 6.8) one observes a constant uptake coefficient at H_2SO_4 concentrations ≤ 60 wt % of $\gamma = 0.210 \pm 0.005$ at 180 K and at H_2SO_4 concentrations ≤ 70 wt %, $\gamma = 0.10 \pm 0.02$ at 200 K, where uncertainties correspond to one standard deviation. Beyond this threshold of 60 wt % H_2SO_4 γ rapidly decreases to reach values of the order of 0.01. We also observe saturation of the uptake kinetics of HNO_3 on the H_2SO_4 frozen sample at these high H_2SO_4 concentrations such as displayed in Figure 6.7. At 180 K the saturation of the uptake rate appears at 90 wt % H_2SO_4, while at 200 K it already occurs at 60 wt % H_2SO_4. Therefore, Figure 6.8 only displays the initial uptake coefficient γ_0 for these latter conditions. Generally, the steady state uptake coefficient γ_{ss} is smaller by up to a factor of two compared to γ_0 as shown in Figure 6.7.

Table 6.4 summarizes the results of the present and previous work performed on liquid [Tolbert, 1988; Reihs, 1990; Van Doren, 1991] and frozen H_2SO_4 solutions [Hanson, 1992]. We observe the same trend in γ values as Reihs *et al.* [1990] observed on

Table 6.4: Uptake coefficients γ of HNO_3 on H_2SO_4/H_2O.

T [K]	γ	wt % H_2SO_4	References
188	0.25 ± 0.05	15 – 87	Reihs *et al.*, 1990 (a)
191	≥ 0.30	57.7	Hanson, 1992 (b)
200	≥ 0.20	57.7	Hanson, 1992 (b)
223	0.07 ± 0.01	15 – 87	Reihs *et al.*, 1990 (a)
230	0.002	75	Tolbert *et al.*, 1988 (a)
283	0.11 ± 0.01	73	Van Doren *et al.*, 1991 (a)
180	0.207 ± 0.005	≤ 60	This work (b)
	$0.21 \Rightarrow 0.05$ (c)	> 60	This work(b)
200	0.10 ± 0.02	≤ 70	This work (b)
	0.007 ± 0.005	> 70	This work (b)

(a) Liquid solutions (or droplets). (b) Frozen crystalline solid. (c) See Figure 6.8.a)

liquid H_2SO_4. The mechanism proposed for the interaction of HNO_3 on H_2SO_4 at low temperature consists of both solvation and aqueous phase reaction of HNO_3. The lower γ obtained at higher H_2SO_4 concentration results from the solubility limitation of HNO_3 in H_2SO_4 on the sample surface [Reihs, 1990]. The condensed phase products of the interaction of HNO_3 on solid H_2SO_4 substrates may be of two different compositions. One possibility is the formation of a HNO_3 hydrate on the H_2SO_4 surface. FTIR experiments performed by Iraci *et al.* [1994] have shown the growth of NAT in/on both liquid and crystalline H_2SO_4 films. The second possibility may be the formation of a saturated ternary solution when HNO_3 is added to H_2SO_4.

6.5 The Interaction of HNO_3 on Solid Ternary Solutions (STS) of $HNO_3/H_2SO_4/H_2O$

SS and PV experiments have been performed on solid ternary solutions (STS) at different temperatures relevant to the lower stratosphere. Carslaw *et al.* [1994] calculated the composition of $H_2SO_4/HNO_3/H_2O$ aerosols resulting in PSC formation in the temperature range 185 and 200 K. We have performed uptake experiments on STS using these calculated compositions. The solid samples were prepared in the same way as described earlier for H_2SO_4 samples and the ice surface was equilibrated by an external H_2O flow. When the plunger is lifted without a HNO_3 flow entering the reactor, one observes a

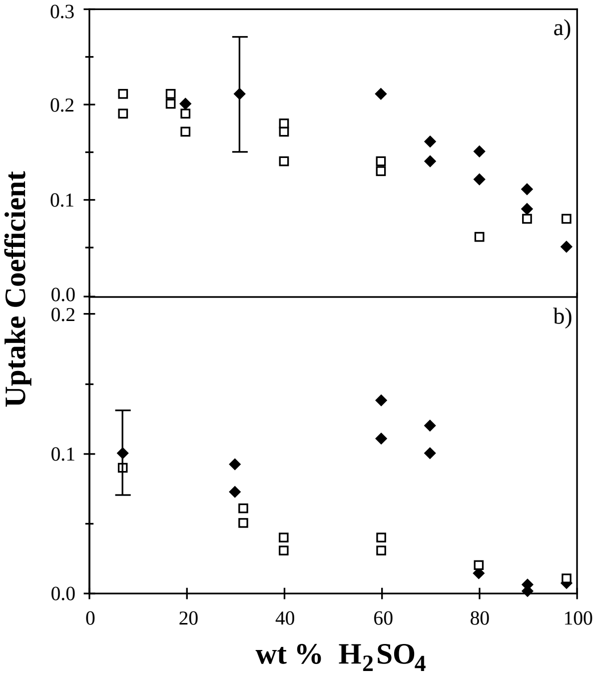

Figure 6.8: Uptake coefficient γ of HNO_3 on H_2SO_4/H_2O frozen solutions as a function of H_2SO_4 concentration. Open squares represent uptake experiments performed without an external H_2O flow rate and full diamonds represent experiments with an additional H_2O flow rate to equilibrate the ice sample at a) 180 K, b) 200 K. Statistical uncertainties have been determined to be ± 30 % for each individual measurement owing to signal noise and the uncertainty in the HNO_3 calibration.

HNO_3 partial pressure which has been taken into account in the calculation of γ.

The results are shown in Table 6.5. The γ values obtained on STS samples in the temperature range 185 to 195 K are constant and centered around a mean value of $\gamma = 0.10 \pm 0.03$ over the whole temperature range, thus for all compositions. At 200 K the STS composition is calculated to be 60 wt % H_2SO_4 and 0.1 wt % HNO_3. Due to the small amount of HNO_3 in the STS composition at 200 K, the corresponding HNO_3 uptake coefficient has been assumed to be the same as the one obtained for a binary frozen solution of 60 wt % H_2SO_4, namely $\gamma = 0.1$ at 200 K (Figure 6.8). No saturation of the rate of HNO_3 uptake on STS has been observed for the concentration range studied. In relation to the interaction of HNO_3 on pure ice, the γ value for the interaction of HNO_3 on cold STS samples is lower by a factor 2–3. The presence of HNO_3 (in excess of 1 % wt) dissolved in H_2SO_4 decreases the rate of uptake of HNO_3 on low temperature samples compared to pure ice.

Table 6.5: Uptake coefficient of HNO_3 on solid ternary solutions of $H_2SO_4/HNO_3/H_2O$.

T [K]	H_2SO_4 [(a)] [wt %]	HNO_3 [(a)] [wt %]	Flow [molecule s^{-1}]	k_{esc} [s^{-1}]	γ_{obs} [(b)]
185	1	20	$4.3 \cdot 10^{14}$	1.6	0.11
185	1	20	$5.4 \cdot 10^{14}$	1.6	0.11
185	1	20	$7.7 \cdot 10^{14}$	1.4	0.12
190	5	40	$9.5 \cdot 10^{13}$	2.2	0.08
190	5	40	$2.3 \cdot 10^{14}$	2.1	0.12
192	20	20	$5.4 \cdot 10^{14}$	1.9	0.12
192	20	20	$7.4 \cdot 10^{14}$	1.7	0.10
195	50	1	$3.4 \cdot 10^{14}$	1.9	0.09
195	50	1	$6.0 \cdot 10^{14}$	2.1	0.08

(a) STS compositions from Carslaw *et al.* [1994].

(b) No correction has been applied on γ values due to large HNO_3 flow rates used in these experiments (see Section 6.6 for details).

6.6 Chemical Kinetic Modeling of Experimental Results of HNO_3 Interacting with Ice

In order to understand the mechanism of the adsorption of HNO_3 on ice samples, we fitted our experimental results using a Langmuir–Hinshelwood model as described previously [Aguzzi, 1999]. The proposed model consists of a set of two equations, representing a series of two elementary processes (equations (6.11) and (6.12)).

$$G + ss \rightleftarrows A \qquad k_1, k_{-1} \tag{6.11}$$

$$A \rightleftarrows B + ss \qquad k_2, k_{-2} \tag{6.12}$$

Equation (6.11) considers that the gaseous HNO_3 (G) interacts with a free surface site ss located on the ice surface leading to a precursor species (A) in an effective bimolecular reaction. The rate of this reaction is therefore proportional to the number of free surface sites ss and to the HNO_3 concentration in the gas phase. The second step, equation (6.12) takes into account the liberation of a free ss by the formation of a new species (B). This step sets free surface sites which are again available to interact with G, thus avoiding any surface saturation, as it has been experimentally observed. Equation

(6.12) may correspond to the diffusion process of adsorbed HNO_3, A, into deeper layers of the bulk.

We run the model according to two different procedures. First, one performs calculations using only with equation (6.11) whose results are presented in Figure 6.9a1–3. Subsequently both equations are used whose results are displayed in Figure 6.9b1–3. The running numbers 1 to 3 represent HNO_3 uptake experiments performed at three different HNO_3 flow rates entering the reactor at 200 K, namely a high ($8 \cdot 10^{15}$ molecule/s), a medium ($1 \cdot 10^{14}$ molecule/s) and a low ($8 \cdot 10^{12}$ molecule/s) HNO_3 flow rate, respectively. In the interest of simplification we did not consider the wall contribution of HNO_3 sticking on Teflon as has been discussed above. The results displayed in Figure 6.9 show a comparison between experimental MS signals (solid lines) and calculations (dotted lines) at 200 K.

Table 6.6: Set of parameters used in the modelling.

Parameters	Units [(a)]	Numerical value [(a)]
S_0	**molecule**	$\mathbf{1.6 \cdot 10^{16}}$
	molecule cm^{-2}	$9.4 \cdot 10^{14}$
k_1	**molecule^{-1} s^{-1}**	$\mathbf{8.7 \cdot 10^{-16}}$
	cm^2 molecule^{-1} s^{-1}	$1.5 \cdot 10^{-14}$
k_{-1}	**s^{-1}**	$\mathbf{0.5 \cdot 10^{-3}}$
	cm^{-1} s^{-1}	$4.6 \cdot 10^{-6}$
k_2	**s^{-1}**	**5.0**
	cm^{-1} s^{-1}	85.0
k_{-2}	**molecule^{-1} s^{-1}**	$\mathbf{0.1 \cdot 10^{-16}}$
	cm^2 molecule^{-1} s^{-1}	$1.7 \cdot 10^{-16}$

[(a)] Bold characters represent the rate constants expressed for the present experimental system, the other are transferable units for unity surface–to–volume ratio. Rate constants in units of cm^{-1} s^{-1} are calculated using the value $A_s/V = 17/1830 = 9.3 \cdot 10^{-3}$ cm^{-1}.

The adjustable parameters in this model are the four kinetic constants (k_1, k_{-1} and k_2, k_{-2}) and the total number of surface sites ss (S_0). The best fits, presented in Figure 6.9, have been obtained using the set of kinetic parameters displayed in Table 6.6. As described earlier [Tabor, 1994; Aguzzi, 1999], the bold characters in Table 6.6 are values expressed for our specific experimental configuration whereas the other are expressed in transferable units independent of the experimental apparatus used.

The term $k_1 \cdot S_0$ corresponds to the rate of loss from the gas phase of the G species and is equal to 14 s^{-1} which leads to a γ value of 0.19 according to equation (2.11) using a calculated collision frequency ω of 74 s^{-1}. This is the experimental mean value of γ for the interaction of HNO_3 with pure ice at 200 K obtained in this study. In Figure 6.9b1–3, one notes the excellent agreement between the calculated curves (dotted lines) and the experimental results (solid lines). The calculated rate of HNO_3 uptake displayed in Figure 6.9a1 shows that using a high HNO_3 flow rate, one rapidly reaches the initial level due to rapid saturation of the free surface sites ss. No saturation is observed when a precursor species is introduced in the adsorption mechanism as displayed in Figure 6.9b1: the calculated rate of uptake fits quite well the experimental result. Using a medium HNO_3 flow rate, both calculated and experimental uptake curves are the same in both runs (cases a2 and b2). Calculations overestimate uptake experiments performed using a low HNO_3 flow rate as displayed in Figure 6.9c3. This stems from the fact that we did not consider the amount of HNO_3 desorbing from the reactor wall. In this last case, the wall effect contributes an additional HNO_3 flow of $1 \cdot 10^{12}$ molecule/s, which is the difference between experimental and calculated flow rates. This fact confirms that at low HNO_3 flow rate the correction on the kinetics is more important than at high flow, where the HNO_3 wall contribution is negligible.

6.7 Conclusion

We have measured the uptake of HNO_3 on both vapor–condensed (C) as well as bulk (B) ice in the temperature range 180 to 211 K. The Arrhenius representation shows two distinct regimes of temperature dependence. At low temperatures ($T < 195$ K), the kinetics of adsorption is constant and relatively high ($\gamma \sim 0.3$). At higher temperature, we have determined an activation energy of $E_a = -7 \pm 1$ kcal/mol. For a specific temperature, γ is independent of the HNO_3 flow entering the reactor which allows us to conclude that the rate law is first order in $[HNO_3]$. At $T \leq 210$ K no saturation of the rate of uptake on ice has been observed leading to $\gamma_0 = \gamma_{ss}$. Considering a PSC type II surface area of 10^{-7} cm^2 per cm^3 [Turco, 1989] and $\gamma = 0.26$ for HNO_3 adsorption on pure ice at 187 K such as measured in this study , one obtains a lifetime of 1.7 hours for HNO_3. Uptake of HNO_3 on PSC type I clouds, whose surface area is 10 times smaller than for type II, the HNO_3 lifetime would approximately be 1.5 days using an uptake coefficient of the order of 0.1.

Long exposure of the ice sample to gaseous HNO_3 allows one to observe a phase transition during the uptake of nitric acid. At this phase transition between 50 and 500 formal HNO_3 monolayers have been adsorbed on the ice sample, diffusing into a surface layer of 15 nm (180, 190 K) and 70 nm (200 K) thick provided of the condensed phase is crystalline ice. These experiments led us to a mean stoechiometric ratio of the condensate of $HNO_3 \cdot 3H_2O$ at 180 K, and $HNO_3 \cdot nH_2O$ with $0.9 \leq n \leq 1.8$ at 190 and 200 K. These experiments did not allow us to unambiguously confirm the formation of NAM (nitric acid monohydrate) and NAT at the interface at 180 K and 190 or 200 K, respectively. The values of the mean ratio obtained in this study at 180 K are in good agreement with the expected calculated composition of type Ia STS aerosols at 188 K [Zondlo, 1998; Carslaw, 1994; Tabazadeh, 1994].

As has first been suggested by Wofsy *et al.* [1990], HNO_3 is thought to reduce H_2O evaporation rate from ice particles which has been confirmed by others [Peter, 1994; Zondlo, 1997; Livingston, 1998; Warshawsky, 1999] claiming that one HNO_3 monolayer decreases the H_2O partial pressure to a significant, therefore measurable extent. In this study we find that many more than one HNO_3 monolayer is indeed needed to reduce the H_2O evaporation rate. We therefore confirm that the adsorption of HNO_3 influences the evaporation rate of water in contrast to the results obtained by Biermann *et al.* [1998]. This result suggests that for small ice particles HNO_3 may be distributed across the entire bulk at 190 and 200 K. Even at temperature as low as 180 K the penetration depth of HNO_3 in the bulk may be significant.

Kinetic results of the interaction of HNO_3 on frozen H_2SO_4 samples show an abrupt change at 60 wt % H_2SO_4 at 180 and 200 K. At concentrations lower than this threshold the uptake coefficient is constant albeit smaller that on pure ice. Above this concentration the γ values significantly decrease to reach 0.03.

When HNO_3 is added to H_2SO_4 to form solid ternary solutions, the kinetics of the interaction is significantly slower with respect to pure ice and binary solutions at H_2SO_4 concentrations below 60 wt %. We observe a constant value of $\gamma = 0.1$ on all STS compositions studied in this work in the temperature range 185 to 195 K.

Due to the fast uptake kinetics of HNO_3 on the low temperature surfaces studied in this work, nitric acid is continuously removed by sedimentation ultimately leading to denitrification. This results in lower concentrations of available NO_x in the upper troposphere and the lower stratosphere [Wofsy, 1990]. This denitrification is occasionally observed [Kondo, 2000; Dessler, 1999], and this low level of NO_x may contribute to an increase in ozone depletion, because the catalytic cycle of ozone destruction can not be halted by the conversion of the unstable ClO to stable $ClONO_2$.

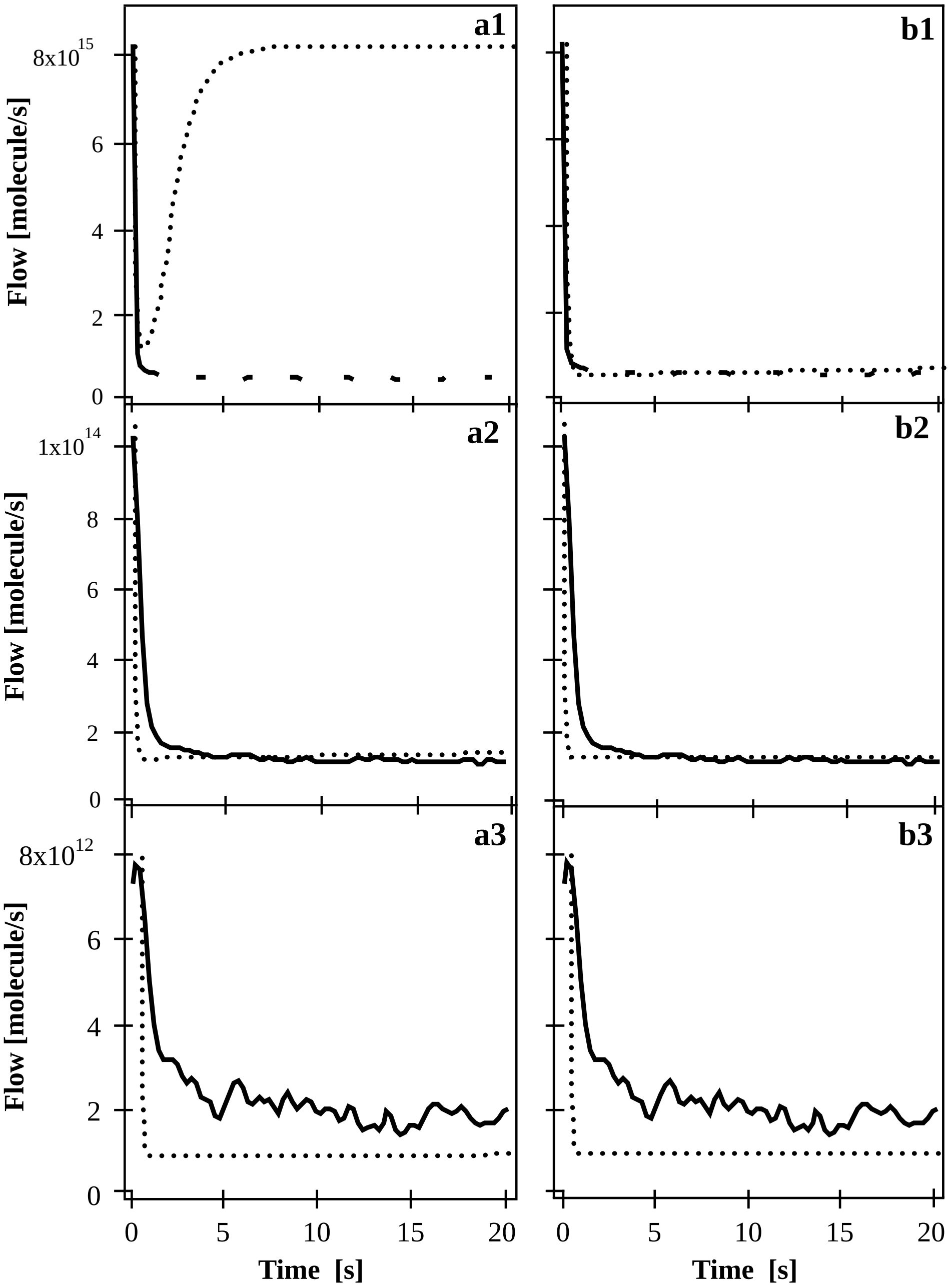

Figure 6.9: Modelling of typical SS experiments. Comparison of experiments at 200 K (solid lines) and models (dotted lines). (a1–3) Simulation results for the adsorption of HNO_3 on ice samples at three different HNO_3 flow rates entering the reactor using the model described in equation (6.11). (b1–3) Simulation results of the same experimental data as in cases (a1–3) using the model described by equations (6.11) and (6.12)

Chapter 7

Interaction of $BrONO_2$ and Br_2O with Ice and Doped-Ice

7.1 Introduction

As described in Chapter 1, stratospheric ozone loss is due to several different catalytic cycles. The main cycle is the chlorine cycle although bromine has also been shown to have a major impact on stratospheric ozone.

The destruction of ozone via bromine radicals is analogous to that of chlorine according to reaction (7.1) [Lary, 1996] where Br atoms are released into the atmosphere by the photolysis of Br_2 and BrCl or by the coupling reaction reaction of ClO/BrO [Anderson, 1989b]:

$$Br + O_3 \rightarrow BrO + O_2 \tag{7.1}$$

Atmospheric bromine chemistry is of particular importance owing to the high instability of the reservoir species $BrONO_2$ and HOBr which results in a large partitioning towards active bromine, namely Br and BrO [Lary, 1996].

In the atmosphere the $BrONO_2$ reservoir is generated by the homogeneous reaction between BrO and NO_2. It may be destroyed by photolysis according to the following reactions [Harwood, 1998]:

$$\begin{aligned} BrONO_2 + h\nu &\rightarrow Br + NO_3 \quad (7.2) \\ &\rightarrow BrO + NO_2 \quad (7.3) \end{aligned}$$

or by hydrolysis [Tie, 1996; Lary, 1996]. Laboratory studies have shown that the hydrolysis of $BrONO_2$ occurs on ice surfaces according to reaction (7.4) with an uptake coefficient of the order of 0.2 at 190 K [Allanic, 1997]:

$$BrONO_2 + H_2O(s) \rightarrow HOBr + HNO_3(s) \tag{7.4}$$

The released gaseous HOBr can then rapidly be converted to active bromine by photolysis (reaction (7.5)) [Orlando, 1995] or by heterogeneous reactions with solvated halide ions (reactions (7.6) and (7.7)) [Abbatt, 1994; Allanic, 1997].

$$HOBr + h\nu \rightarrow Br + OH \tag{7.5}$$

$$HOBr + Br^- + H_3O^+ \rightarrow Br_2 + 2H_2O \tag{7.6}$$

$$HOBr + Cl^- + H_3O^+ \rightarrow BrCl + 2H_2O \tag{7.7}$$

Allanic *et al.* [1997] observed Br_2O as secondary product during $BrONO_2$ uptake on ice according to:

$$BrONO_2 + HOBr \rightarrow Br_2O + HNO_3 \tag{7.8}$$

where $BrONO_2$ may react with adsorbed HOBr. This latter reaction complicates the monitoring of the hydrolysis of $BrONO_2$ on ice since both $BrONO_2$ and Br_2O contribute to the BrO^+ fragment at m/e 95 which we use to monitor $BrONO_2$.

The gas–phase hydrolysis reaction of Br_2O has been observed with an equilibrium constant of 0.02 according to [Orlando, 1995]:

$$Br_2O + H_2O \leftrightarrows 2HOBr \tag{7.9}$$

To date, the analogous hydrolysis reaction occurring on ice surfaces at low temperatures has not been determined. This is the first point that has motivated work described in the following Section, where for the first time the results of Br_2O hydrolysis on ice surfaces as well as the HOBr yield resulting from this interaction are presented. Another motivation for these experiments is that Br_2O is often observed as an impurity in a $BrONO_2$ storage vessel. In Section 7.3, the $BrONO_2$ hydrolysis on different types of ice samples is presented, while Section 7.4 deals with the heterogeneous reaction of $BrONO_2$ on ice doped with HBr.

7.2 Br_2O on Ice: Reference Experiments

Steady–state (SS) experiments on bulk (B) and condensed (C) ice have been performed in the 14 mm escape reactor described in Chapter 2 in the temperature range 180 to

210 K. Br_2O, monitored at its parent peak at m/e 176, can react on fresh ice surfaces to produce hypobromous acid, HOBr monitored at m/e 98, according to the following reaction:

$$Br_2O(g) + H_2O(s) \rightarrow 2HOBr(g) \tag{7.10}$$

Figure 7.1 displays a typical SS experiment performed at 210 K on a (C) ice sample. When the (C) ice is exposed to Br_2O (bold line) with $F^{in}_{Br_2O} = 2 \cdot 10^{15}$ molecule/s in this particular case, a rapid drop of the signal at m/e 176 is observed correlated with a rapid increase of HOBr, monitored at m/e 98 (thin line). One observes right after the opening of the sample compartment, a rapid uptake of Br_2O followed by a slightly smaller steady–state uptake owing to partial surface saturation. In the example displayed in Figure 7.1, the initial uptake rate constant and uptake coefficient were measured as $k_0 = 4.4\ s^{-1}$ and $\gamma_0 = 0.10$, respectively, whereas the corresponding steady–state values were $k_{ss} = 1.8\ s^{-1}$ and $\gamma_{ss} = 0.04$, respectively. Partial saturation of the (B) and (C) ice substrates have been observed for the whole range of temperature and lead to a mean steady state uptake coefficient, γ_{ss}, of 0.04 ± 0.02.

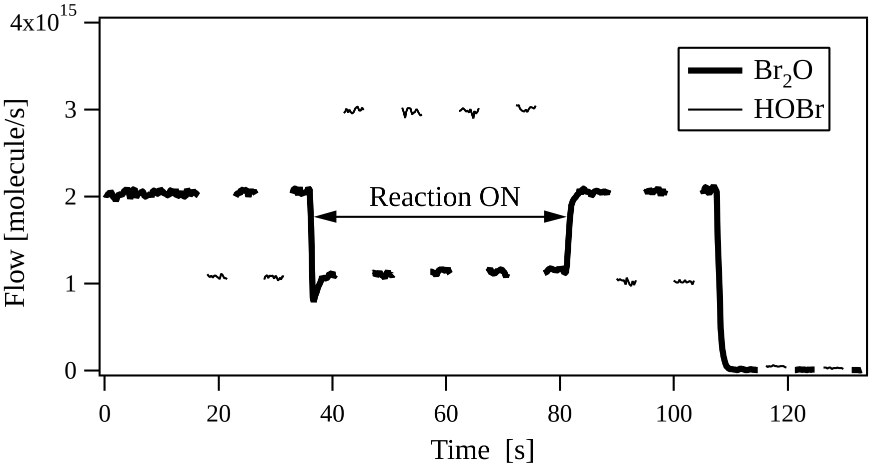

Figure 7.1: Steady–state experiment of Br_2O (m/e 176, bold line) on a (C) ice sample (thickness of approximately 2 μm) at 210 K in the 14 mm orifice reactor. HOBr (m/e 98, thin line), the sole product, appears at a 100 % yield, one Br_2O molecule resulting in two HOBr molecules.

The results on the uptake kinetics of Br_2O on (C) and (B) ice are displayed in Tables E.1 and E.2, respectively in Appendix E. One may note a negative temperature dependence for the initial uptake coefficient γ_0 in the temperature range 180 to 210 K. At a fixed temperature one may conclude that Br_2O follows a first order rate law in $[Br_2O]$. Figure 7.2 displays the Arrhenius representation of the initial uptake rate constant of

Br_2 on (C) (triangles) and (B) (circles) ice. The linear fit gives an adsorption activation energy of $E_a = (-2.3 \pm 0.6)$ kcal/mol.

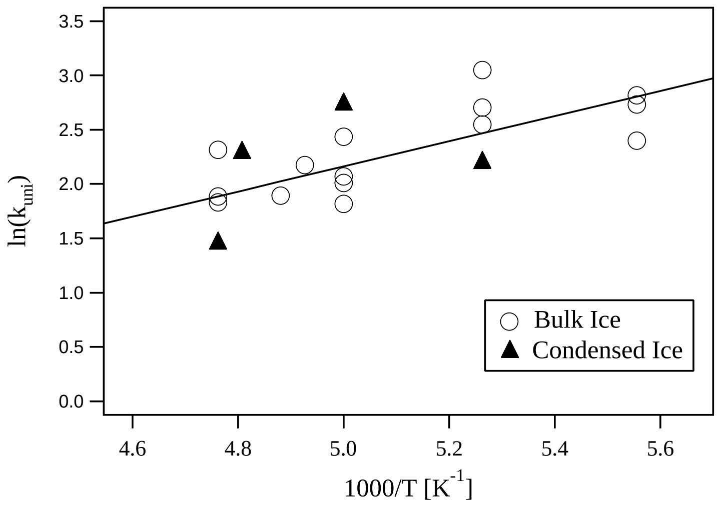

Figure 7.2: Arrhenius representation of the initial uptake rate constant k_{uni} of Br_2O interacting on (C) ice (○) and (C) ice (▲) obtained in steady state experiments using the 14 mm aperture reactor, leading to an adsorption activation energy of $E_a = (-2.3 \pm 0.6)$ kcal/mol.

HOBr has been observed as the only product of the hydrolysis of Br_2O. Figure 7.3 displays the HOBr yield as a function of the temperature. We may see that the product yield increase with temperature from 20–40 % at 180 K to 100 % at 210 K. This is certainly due to the strong interaction of HOBr on ice samples at low temperature [Chu, 1999; Chaix, 2000]. At 180 K, the observed HOBr yield is approximately 30 %. Assuming that the total amount of Br_2O is converted to HOBr during a SS experiment, the observed signal of HOBr is expected to be 3 times higher than the observed one. From this ratio of 3, one may calculate the corresponding γ of HOBr, using $\omega = 61$ s^{-1} and $k_{esc} = 3.1$ s^{-1} [Chaix, 2000], resulting in a γ value of the order of 0.1, which corresponds to the uptake kinetics of HOBr [Chu, 1999; Chaix, 2000]. The assumption that all Br_2O is converted to HOBr in a 100 % yield is confirmed by thermal desorption experiments (TDE) where the missing HOBr is released into the gas–phase at (215 ± 5) K, thus closing the bromine mass balance to an accuracy of ± 20 %. However, during TDE, one can not distinguish between the two following situations: 1) the total amount of Br_2O taken up is converted to HOBr, and during TDE, HOBr is released in the gas phase or 2) a fraction of the total quantity of Br_2O taken up is condensed without being converted to HOBr, and during the increase of the temperature leads to the prompt conversion of Br_2O to HOBr.

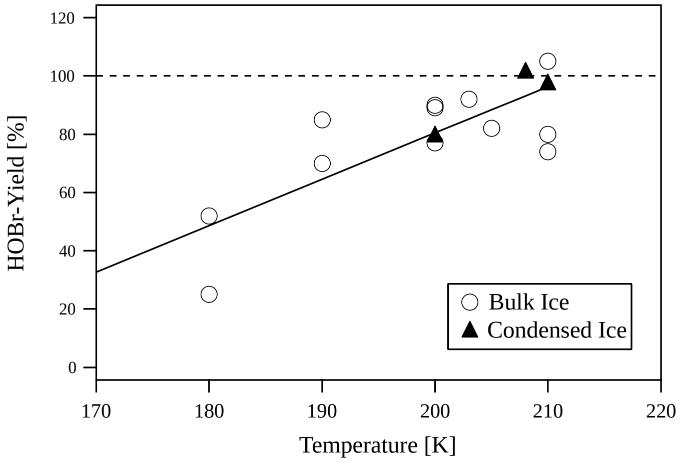

Figure 7.3: HOBr yield during Br_2O hydrolysis on bulk ice (○) and condensed ice (▲) as a function of temperature.

7.3 $BrONO_2$ Uptake on Pure Ice

As mentioned before, $BrONO_2$, monitored at m/e 95 is thought to be one of the main bromine "reservoirs" in the stratosphere. It reacts on pure ice surfaces to produce hypobromous acid, HOBr monitored at m/e 96 (or 98), according to reaction (7.11):

$$BrONO_2 + H_2O \rightarrow HOBr + HNO_3 \tag{7.11}$$

Throughout almost all experiments performed in the reactor, Br_2O monitored at m/e 176 (its molecular peak) was present in the trap as an impurity or was formed as a secondary product according to reaction (7.12):

$$BrONO_2 + HOBr \rightarrow Br_2O + HNO_3 \tag{7.12}$$

As displayed in Figure 3.3 on page 36, Br_2O contributes to the signal at m/e 95 to the extent of 50 % of its molecular ion peak at m/e 176. This ratio has been used to correct the $BrONO_2$ MS signal at m/e 95.

Figure 7.4 shows a typical SS experiment performed on single crystal (SC) ice at 185 K in the 14 mm orifice reactor. Before opening the sample compartment, one should note the low level of contaminants coming out the $BrONO_2$ trap. Right after the opening of the sample compartment, the $BrONO_2$ signal immediately drops and the reaction leads to rapid formation of HOBr and Br_2O. After correction of the $BrONO_2$ MS signal at m/e 95 for the Br_2O contribution, one does not observe saturation of $BrONO_2$ on the ice sample contrary to the situation of $ClONO_2$ interacting with ice [Leu, 1991; Oppliger, 1997].

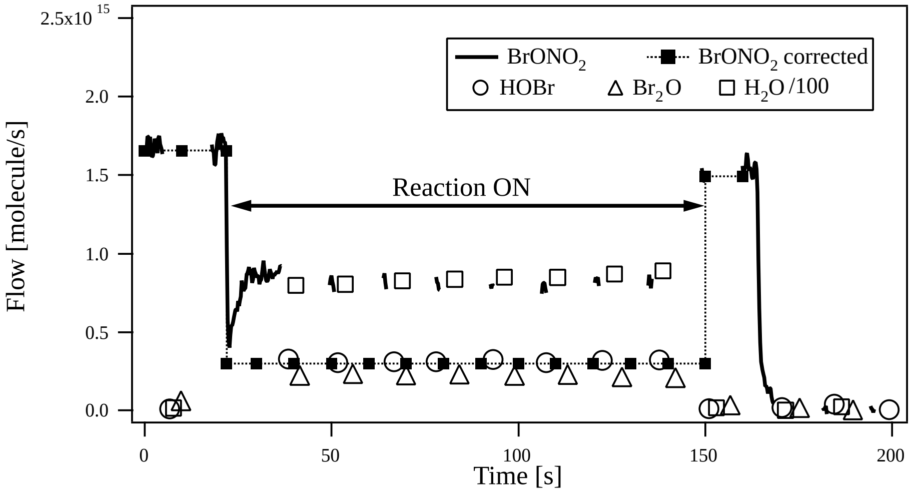

Figure 7.4: Steady–state experiments of $BrONO_2$ (solid line) on single crystal ice at 185 K performed in a 14 mm aperture reactor. $BrONO_2$, monitored at m/e 95, has been corrected according to Br_2O (m/e 176) contribution at m/e 95. HOBr (○), monitored at m/e 98, and Br_2O (△) appear promptly when the plunger is lifted. Note that H_2O signal (□) has been divided by 100.

A pulsed valve (PV) experiment is displayed in Figure 7.5, where panel a) shows the reactant pulses at m/e 95 and panel b) displays the product pulses HOBr and Br_2O. In PV experiment a systematic correction has been applied to the reactive $BrONO_2$ MS signal, whenever Br_2O was observed. The HOBr and Br_2O rise time are 0.08 and 0.18 s, respectively (panel b), clearly indicating that HOBr is the primary product thus confirming the existence of a secondary reaction between $BrONO_2$ and HOBr on the ice surface.

PV and SS experiments did not show any difference in the uptake kinetics of $BrONO_2$ at a fixed temperature and type of ice. All experiments are detailed in Table E.3 in Appendix E. The results are summarized in Table 7.1 and in Figure 7.7. The values are in good agreement with those found in the literature at 190–200 K on (C) ice [Allanic, 1997; Hanson, 1993]. No concentration dependence has been observed in the chosen temperature range, thus confirming a first order rate law in [$BrONO_2$] for all types of ice (Appendix E, Table E.3).

The mean product yields of the heterogeneous hydrolysis of $BrONO_2$ on fresh ice are displayed in Figure 7.6 as a function of the substrate temperature. The uncertainties in the yield have been estimated to be 40 %, primarily resulting from the difficulties to obtain "clean“ sources of HOBr and Br_2O for calibration purposes. HOBr (or Br_2O) sources always contain Br_2O (or HOBr) impurities at different concentrations from batch to batch. While the Br_2O yield appears constant of the order 20 % of for

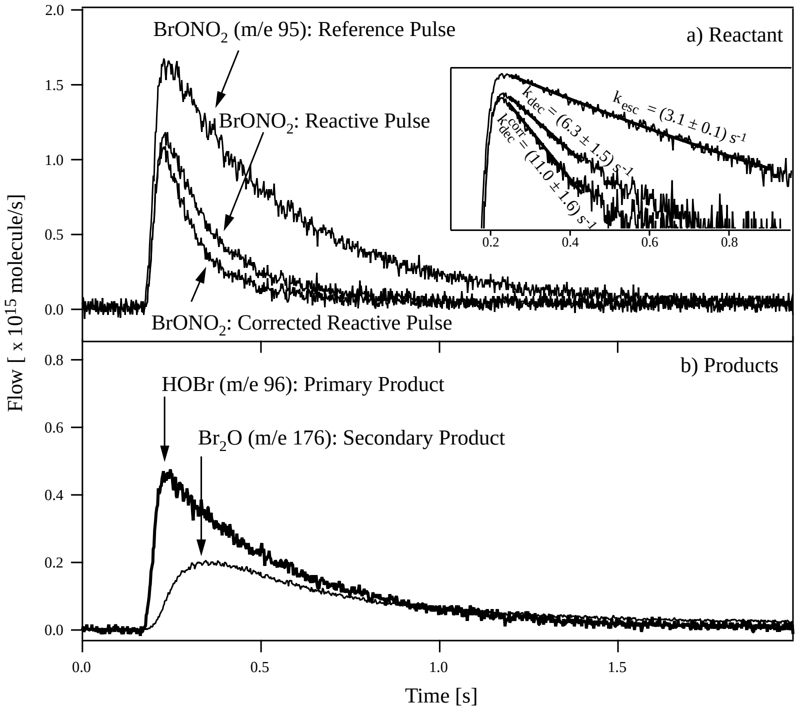

Figure 7.5: Pulsed valve experiment of $BrONO_2$ on condensed ice at 210 K in the 14 mm aperture reactor. Panel a) shows the reactant pulses where the reference pulse corresponds to the decay of the MS signal at m/e 95 in the absence of ice, the reactive pulse corresponds to the same pulse in the presence of the ice sample and the corrected $BrONO_2$ reactive pulse corresponds to the reactive pulse corrected for the Br_2O contribution at m/e 95. The insert in panel a) shows the decays of the different pulses on a logarithmic scale with the corresponding γ value of 0.16 ± 0.03. Panel b) shows the order of appearance of the products in real–time. The bold line shows the primary product HOBr monitored at m/e 96, while the thin line shows the secondary product Br_2O monitored at m/e 176.

all temperatures, the HOBr yield increases with increasing temperature as observed for Br_2O hydrolysis (see Figure 7.3). Thermal desorption experiment (TDE) performed after $BrONO_2$ hydrolysis on (C) ice reveal the missing Br, thus closing the bromine mass balance (Table E.3 in Appendix E). On (B) and (SC) the bromine mass balance appears to be open owing to possible diffusion of bromine species into the bulk of the sample.

The Arrhenius representation displayed in Figure 7.7 clearly shows three different lines each with a negative temperature dependence depending on the three different types if ice used. At 180 K, the uptake kinetics of $BrONO_2$ on (C), (B) and (SC) ice is identical (γ of approximately 0.3) within the experimental uncertainty. At T > 180 K, we observe that the γ values split into three lines and change according to the following sequence for the different types of ice: $\gamma_C > \gamma_B > \gamma_{SC}$ with $\gamma_C \approx 1.4\ \gamma_B$. The uptake

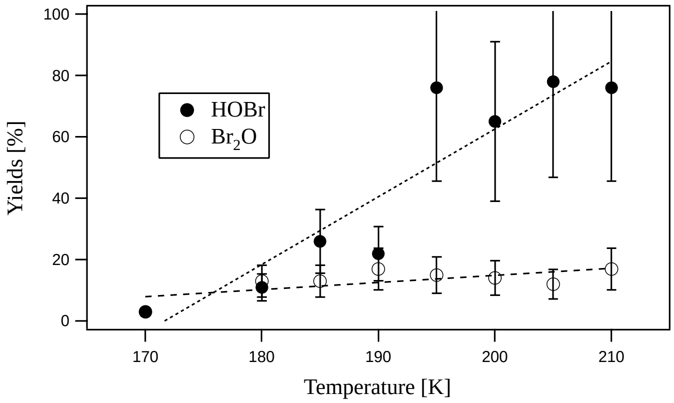

Figure 7.6: HOBr (solid circles) and Br_2O (open circles) yields resulting from the heterogeneous reaction of $BrONO_2$ on pure ice of all types (B, C, SC).

Table 7.1: Initial uptake coefficients for $BrONO_2$ on different types of ice using the 14 mm orifice reactor resulting from SS and PV experiments and adsorption activation energy in kcal/mol.

T [K]	γ_C	γ_B	γ_{SC}
180	0.34 ± 0.03	0.26 ± 0.04	0.35 ± 0.05
190	0.27 ± 0.03	0.20 ± 0.01	0.145 ± 0.005
200	0.22 ± 0.03	0.15 ± 0.01	
210	0.15 ± 0.01	0.11 ± 0.02	0.024 ± 0.001
E_a	–2.0 ± 0.2	–2.1 ± 0.2	–6.6 ± 0.3

using $\omega(BrONO_2) = 34\sqrt{\frac{T}{M}}$ s^{-1} (Table 4.1)

kinetics of $BrONO_2$ on (B) and (C) ice lead to an adsorption activation energy of E_a = –2.0 ± 0.2 kcal/mol. The negative temperature dependence of γ_{SC} is more pronounced than for (B) and (C) ice, leading to E_a = –6.6 ± 0.3 kcal/mol. The uptake coefficient drops from 0.35 at 180 K to 0.02 at 210 K. Because of the slow rate of cooling of H_2O during (SC) generation, it is assumed that the sample surface has very low surface defect densities such as dislocations or cracks [Hobbs, 1974] compared to (B) ice. When the number of defects are important, $BrONO_2$ uptake on ice is apparently faster as is observed in Figure 7.7 because these surface sites strongly interact with the gas–phase. In agreement with these arguments, it is not surprising to observe lower γ values on (SC) than on (C) ice. However, at 180 K the number of the defects stemming from the ice preparation, seems to have no influence on the uptake kinetics of $BrONO_2$ because it already is very fast. The difference observed in the γ values of (C) and (B) ice may be due to the fact that (C) ice is more porous than (B) ice [Chaix, 1998].

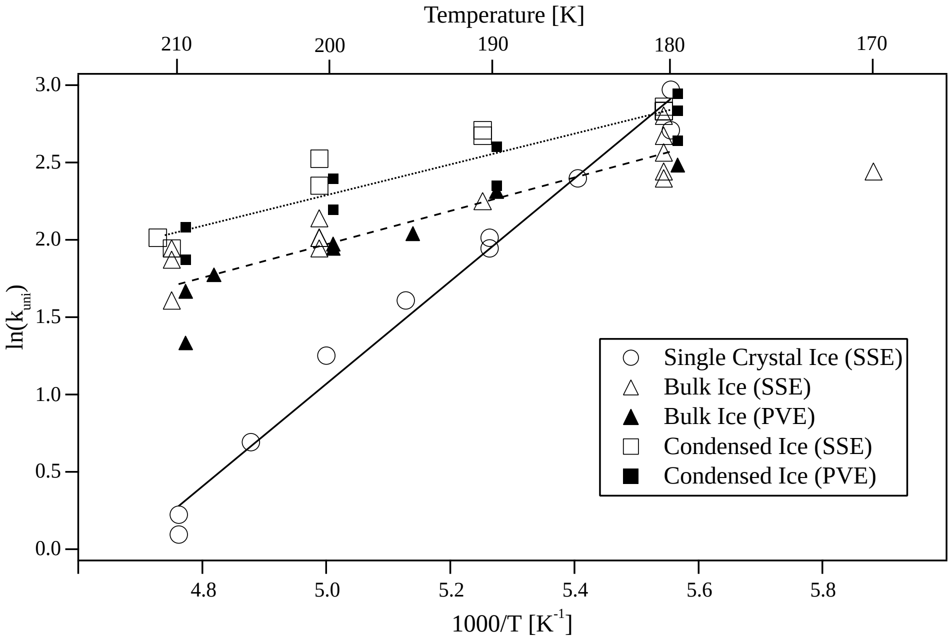

Figure 7.7: Arrhenius representation of the uptake rate constant of the hydrolysis of $BrONO_2$ on (B) ice (triangles), (C) ice (squares) and (SC) ice (circles), obtained in PV (solid symbols) and SS experiments (open symbols).

Similar to $ClONO_2$ hydrolysis leading in HOCl formation [Leu, 1991; Oppliger, 1997], it is thought that the hydrolysis of $BrONO_2$ goes through a precursor formation too. The existence of a precursor in the hydrolysis of $BrONO_2$ is ascertained by the following two observations:

- The negative temperature dependence observed on all types of ice reveals that the hydrolysis of $BrONO_2$ is not an elementary reaction.

- HOBr only begins to appear in the gas–phase after a series of several pulses at doses $< 5 \cdot 10^{14}$ molecules indicating the accumulation of an intermediate species on the surface. At higher doses, both HOBr and Br_2O are released into the gas–phase right after the first pulse (Figure 7.5).

Gane [2000] identified $H_2OBr^+ \cdots NO_3^-$ as a precursor in the hydrolysis of $BrONO_2$ using RAIRS. This precursor corresponds to a complex between protonated hypobromous acid stabilized by nitrate ion. The prompt formation of HOBr suggests that $H_2OBr^+ \cdots NO_3^-$ is less stable than $H_2OCl^+ \cdots NO_3^-$ in the corresponding chlorine system in the same temperature range.

If $BrONO_2$ adsorption occurs on a surface that previously has taken up a few monolayers of HNO_3 from the gas–phase, the rate of uptake is unchanged compared to γ values obtained on clean (B) ice. However, the rate of HOBr production is delayed with respect to a clean ice substrate. It takes approximately 1 minute for HOBr to reach steady–state after the opening of the sample compartment. This shows that the presence of HNO_3 has a marked effect on the rate of production of HOBr by stabilizing the precursor and thus delaying the observation of HOBr in the gas–phase.

7.4 $BrONO_2$ Uptake on Ice doped with HBr

The presence of HBr on the ice sample leads to the competition between the hydrolysis and the following reaction:

$$BrONO_2 + HBr \rightarrow Br_2 + HNO_3 \tag{7.13}$$

Figure 7.8 displays a typical SS experiment on (B) ice performed at 190 K in the 14 mm orifice reactor. When the sample compartment is open, one observes a rapid decrease of $BrONO_2$ (squares) at m/e 95, correlated with a slow production of Br_2 (triangles down) which is the primary product. The $BrONO_2$ signal has been corrected for the contribution of Br_2O at m/e 95. When the production of Br_2 begins to decrease, a slow release of HOBr and Br_2O appears in the gas–phase, confirming the competition between reaction (7.13) and the hydrolysis of $BrONO_2$, reactions (7.11) and (7.12).

In contrast to SS experiments, no HOBr and Br_2O have been observed in PV experiments. The only observed product was Br_2 as displayed in Figure 7.9 (right panel). The reference pulses have been obtained with the sample compartment closed, while reactive pulses correspond to the same pulses with the sample compartment open.

As displayed in Figure 7.8, the production yields of HOBr and Br_2O are small, of the order of 10 % together. However, the contribution of reaction (7.11) to the uptake of $BrONO_2$ might be even more important than observed as HOBr itself reacts with HBr releasing Br_2 [Abbatt, 1994] in the gas–phase according to reaction (7.14). In this case HOBr may be efficiently consumed by HBr leading to the small amount of Br_2O observed.

$$HOBr + HBr \rightarrow Br_2 + H_2O \tag{7.14}$$

The uptake coefficients are summarized in Table 7.2 with all experiments detailed in Table E.4 (Appendix E). No difference between SS and PV experiments have been observed on (C) ice. For a fixed temperature, no difference between (B) and (C) ice has

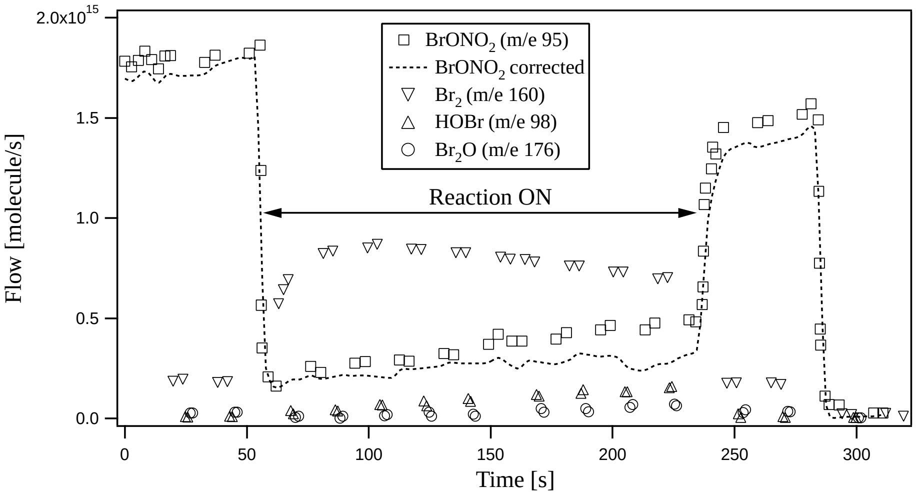

Figure 7.8: SS experiment of $BrONO_2$ on (B) ice doped with $1.1 \cdot 10^{18}$ HBr molecules at 190 K in the 14 mm orifice reactor. The Ms signal of $BrONO_2$ (squares), monitored at m/e 95, has been corrected (dashed line) for the contribution of Br_2O (circles, m/e 176) at m/e 95. The main product, Br_2 (triangles down, m/e 160), appears in a yield of 43 %, the yields of the hydrolysis products, HOBr (triangles up) and Br_2O, are 8 and 4 %, respectively.

been observed as far as the uptake kinetics is concerned. No concentration dependence of the uptake kinetics of $BrONO_2$ has been noted which leads to a first order rate law of the uptake in $[BrONO_2]$.

Table 7.2: Initial uptake coefficients γ^{HBr} for $BrONO_2$ on (C) and (B) ice doped with HBr using the 14 mm orifice reactor resulting from SS and PV experiments (averaged) compared to γ_C^{H2O} on pure ice (Table 7.1). N(HBr) being the amount of HBr taken up prior the uptake experiments.

T [K]	γ^{HBr}	N(HBr) [molecules]	γ_C^{H2O}
180	0.30 ± 0.03	$5.5 \cdot 10^{17} - 4.7 \cdot 10^{18}$	0.34 ± 0.03
190	0.28 ± 0.03	approx. $1.0 \cdot 10^{18}$	0.27 ± 0.03
200	0.23 ± 0.03	$1.0 - 4.5 \cdot 10^{18}$	0.22 ± 0.03
210	0.17 ± 0.02	approx. $1.0 \cdot 10^{18}$	0.15 ± 0.01

In contrast to the $ClONO_2$ + HBr/ice reactive system [Allanic, 2000], one observes a negative temperature dependence in the range 180 to 210 K. The Arrhenius representation displayed in Figure 7.10 reveals a less pronounced dependence as it has been observed for the hydrolysis of $BrONO_2$ on pure ice (Figure 7.7 on page 135). The resulting activation energy for the reaction of $BrONO_2$ with HBr is $E_a = (-1.2 \pm 0.2)$

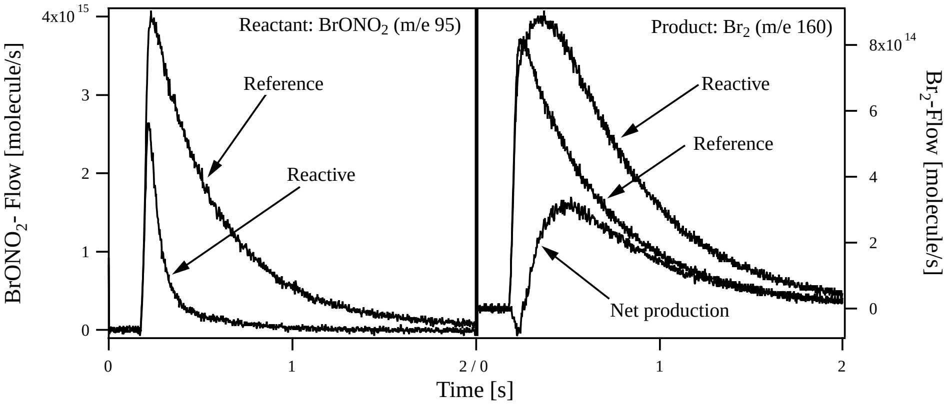

Figure 7.9: PV experiment of $BrONO_2$ on (C) ice doped with $1.1 \cdot 10^{18}$ molecule of HBr at 180 K in the 14 mm orifice reactor. $BrONO_2$ (left panel), monitored at m/e 95, has not been corrected, because no Br_2O has been observed. The main product, Br_2, whose rise time is 0.35 s (right panel, m/e 160), appears in a yield of 17 %, neither HOBr nor Br_2O, have been observed.

kcal/mol which confirms that Br_2 formation in reaction (7.13) does not occur through an elementary reaction.

We will see in the next and last Chapter that using reaction (7.13) in ”*Dope and Probe*“ experiments, we are able to obtain information about the HBr/ice interface. The identical information for the HCl/ice interface has also been obtain from the reaction of $ClONO_2 + HCl \rightarrow Cl_2 + HNO_3$ which has been studied alongside the one involving $BrONO_2$ + HBr.

7.5 Conclusion

Br_2O hydrolysis on ice surfaces occurs rapidly in the chosen temperature range of 180 to 210 K. At a fixed temperature, the uptake kinetic follows an apparent first order rate law in $[Br_2O]$. The observed negative temperature dependence leads to an activation energy E_a for heterogeneous hydrolysis of -2.3 ± 0.6 kcal/mol. These facts point towards a complex reaction mechanism implying that the interaction of Br_2O with ice is not an elementary reaction.

In the gas–phase, the hydrolysis of Br_2O is an equilibrium reaction [Orlando, 1995], however the equilibrium is shifted in favor of HOBr during reaction on ice surfaces at low temperatures (180–210 K), in agreement with the results of Gane [2000]. Due to low atmospheric concentrations, HOBr self reaction to Br_2O will be slow. As only the reverse reaction occurs, one may conclude that there is no significant concentration of Br_2O in the atmosphere.

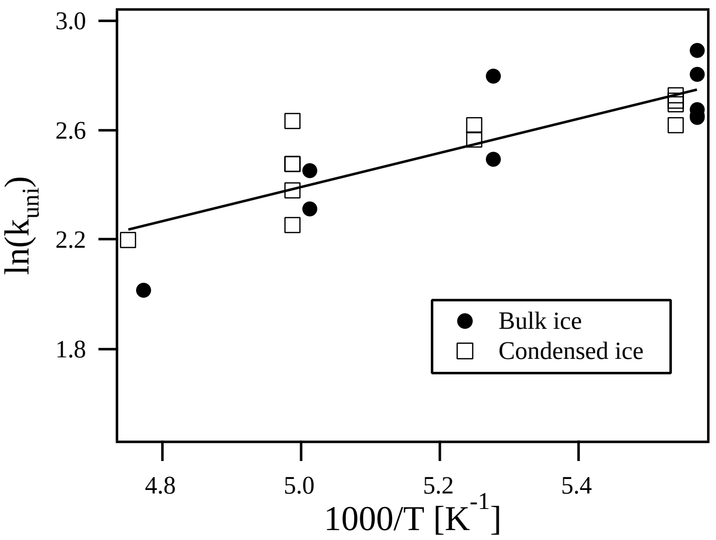

Figure 7.10: Arrhenius representation of the rate constant of the interaction of $BrONO_2$ on (B) and (C) ice doped with HBr. The activation energy for the heterogeneous reaction of $BrONO_2$ with HBr adsorbed on ice is $E_a = -1.2 \pm 0.2$ kcal/mol.

$BrONO_2$ hydrolysis has been measured on (B), (C) and (SC) ice in the temperature range 180–210 K. On all types of ice one observes a prompt HOBr and Br_2O production. At a fixed temperature the rate law is first order in $[BrONO_2]$. The observed negative temperature dependence leads to an activation energy E_a for heterogeneous hydrolysis of $BrONO_2$ on pure ice of (-2.0 ± 0.2), (-2.1 ± 0.2) and (-6.6 ± 0.3) kcal/mol on (C), (B) and (SC) ice, respectively, pointing out different kinetics of $BrONO_2$ on three different types of ice used in this study. The efficiency of the hydrolysis of $BrONO_2$ allows HOBr to become the most important form of night–time bromine in the stratosphere.

The presence of HBr on/in the ice, of the order of 10^{18} molecules condensed prior uptake experiments leads to the rapid formation of Br_2, followed by slow HOBr and Br_2O production. The observed uptake kinetics of the interaction of $BrONO_2$ with HBr is identical as the hydrolysis kinetics of $BrONO_2$ on pure ice (see Table 7.2) suggesting that HBr has no influence on the uptake kinetics. PV experiment show a Br_2 rise time of 0.35 s (Figure 7.9), which is 2 and 4 time larger compared to the rise times of Br_2O and HOBr, respectively observed in PV experiments of $BrONO_2$ on pure ice. This rise time of 0.35 s is relatively large if the reaction occurs directly between $BrONO_2$ and HBr. In agreement with these observations we propose the following reaction scheme for the interaction of $BrONO_2$ on ice doped with HBr:

$$\begin{aligned} BrONO_2(g) + H_2O(s) &\rightarrow HOBr(c) + HNO_3(C) \quad (7.15) \\ HOBr(c) + HBr(c) &\rightarrow Br_2(g) + H_2O(s) \quad (7.16) \end{aligned}$$

The first step consists (reaction (7.15)) of the hydrolysis of BrONO$_2$ leading to the formation of condensed HOBr, which then reacts with HBr to produce gaseous Br$_2$ (reaction (7.16)).

Chapter 8

Properties of HCl/ice and HBr/ice interface

8.1 Introduction

Chlorine and bromine nitrate interacting with frozen PSC particles polluted by HX, with X = Cl or Br, mainly undergo the following competing reactions:

$$XONO_2 + HX \rightarrow X_2 + HNO_3 \tag{8.1}$$

$$XONO_2 + H_2O \rightarrow HOX + HNO_3 \tag{8.2}$$

The properties of the interfacial region, defined as *the near–surface region of the frozen particles in which adsorbed species, such as HCl or HBr are able to directly interact without delay with ClONO$_2$ or BrONO$_2$, respectively,* are deemed to be important in order to establish the branching ratio between hydrolysis (reaction (8.2)) and halogen exchange (reaction (8.1)).

Caloz *et al.* [1997] showed that the heterogeneous reaction of ClONO$_2$ on alkali halide salts displayed a pronounced "sticky" behavior and that the value of its uptake coefficient was independent of the structural characteristics of the substrates. In Chapter 4, the same behavior has been observed for the interaction of BrONO$_2$ on NaCl (Figure 4.4 on page 52). This suggests that XONO$_2$, where X = Cl or Br, interacts with the external surface without diffusion into the bulk. We therefore assume that XONO$_2$ will preferentially probe the gas–solid interface of ice owing to its "sticky" nature. For this reason XONO$_2$ is expected to be the probe molecule of choice to explore the near–surface HX concentrations.

The main goal of this Chapter is to characterize the HX/ice composition (X = Cl

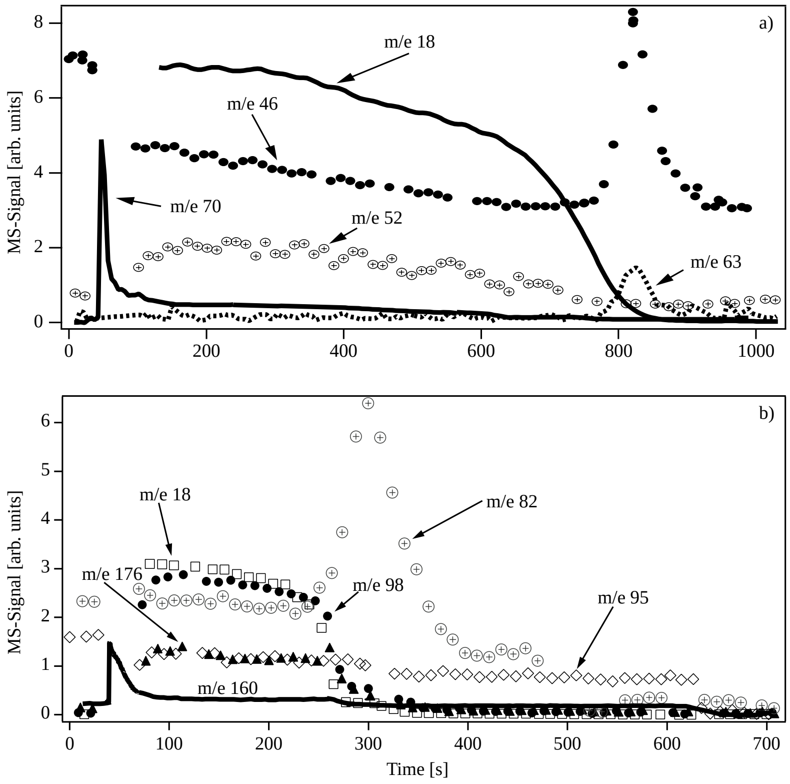

Figure 8.1: ”Dope and probe“ experiments on (C) ice performed in the 14 mm orifice reactor whose total ice thickness is a) 303 nm and b) 440 nm. a) DPE performed at 200 K using the heterogeneous reaction $ClONO_2 + HCl \rightarrow Cl_2 + HNO_3$. $ClONO_2$ is monitored at m/e 46, Cl_2 at m/e 70, HOCl at m/e 52, H_2O at m/e 18 and HNO_3 at m/e 63. b) DPE performed at 205 K using the heterogeneous reaction $BrONO_2 + HBr \rightarrow Br_2 + HNO_3$. The primary product, Br_2 is monitored at m/e 160 (bold solid line); $BrONO_2$ at m/e 95, HOBr at m/e 98, Br_2O at m/e 176, H_2O at m/e 18 and HBr at m/e 82. The delay between the doping and the titration is 2 min leading to a Br_2 yield of 25 % with respect to the amount of HBr condensed.

or Br) in the temperature range 190–205 K through the determination of the diffusion coefficient D of HX in ice. This study is motivated by the experimental observation of a measurable flux F_L of HX as a surface–to–bulk loss, which is a process occurring on the ice on a much longer time scale compared to adsorption and desorption of HX. We will present an indirect way to measure the molecular diffusion coefficient D of HCl and HBr in a solid frozen sample in order to decouple the intrinsic reactivity of $XONO_2$ with HX from the transport properties of HX on/in the ice. The diffusion coefficient D_{HX} of HX has been calculated from measured values of F_L by interpreting them as the flux given in Fick's first law of diffusion to be discussed at the end of this Chapter. Parameters of the interfacial region such as the HX mole fraction and its thickness had to be assessed independently in order to apply Fick's first law.

8.2 "Dope and Probe" Experiments (DPE)

8.2.1 Description of DPE

An ice substrate is doped with HX by exposing it to gas phase HX (X = Cl, Br) and is probed for near–surface HX that is "visible" from the gas phase using the fast titration reaction (8.1). By doping a pure ice substrate with a known amount of HX and varying the time delay between HX condensation ("doping") and titration ("probing") by $XONO_2$, one is able to measure the change of the HX interfacial concentration with time using a mass balance argument. The X_2–yield and its change with the time between the "doping" and the "probing" is an indirect measure of the change with time of the HX concentration at the interface.

Figure 8.1 displays typical "dope and probe" experiments (DPE) performed at 200 K and 205 K, respectively, in the 14 mm diameter orifice reactor. Figure 8.1.a) presents the results from the following titration reaction:

$$ClONO_2 + HCl \rightarrow Cl_2 + HNO_3 \tag{8.3}$$

while Figure 8.1.b) presents the analogous brominated system:

$$BrONO_2 + HBr \rightarrow Br_2 + HNO_3 \tag{8.4}$$

Figure 8.1.a) displays DPE performed with (C) ice at 200 K. After the surface has been doped by a known amount of HCl in the range from 0.2 to 8.4 formal monolayers (ML) with 1 ML corresponding to 10^{15} molecule/cm^2 which is based on approximate Lennard-Jones parameters, a continuous $ClONO_2$ flow of approximately 10^{15} molecule/s enters the reactor. When the sample compartment is opened at t = 20 s, $ClONO_2$ reacts with the HCl/ice sample according to reaction (8.3). The MS signal at m/e 46 (NO_2^+) rapidly drops correlated with a prompt Cl_2 (m/e 70) production. The Cl_2 signal decreases on a time scale of 5–20 s to a low and slowly decreasing level lasting for a few minutes. HOCl (m/e 52) gradually appears in the gas phase when low Cl_2 levels are observed. At t = 800 s, the H_2O signal (m/e 18) suddenly drops, indicating the end of the H_2O supply for hydrolysis, reaction (8.2). At that moment the HNO_3 (m/e 63) produced in reactions (8.1) and (8.2) in the condensed phase is released into the gas phase. In the following sections, we will focus our attention on the rapid molecular halogen (Cl_2 or Br_2) production just after the opening of the sample compartment. This large rate of X_2 production will be called in the following the "*main Burst*".

The same general behavior has been observed for the $BrONO_2$/HBr system displayed in Figure 8.1.b). Once the plunger has been lifted at t = 30 s, $BrONO_2$ (m/e 95) reacts on the ice doped with HBr to produce Br_2 (m/e 160) as a primary product as described in Chapter 7. The prompt Br_2 release is followed by desorption of the hydrolysis products, namely HOBr (m/e 98) and Br_2O (m/e 176). The main burst of Br_2 is observed on a time scale of 10–50 s, twice as long as in the $ClONO_2$/HCl system. At t = 270 s the H_2O signal (m/e 18) drops indicating the end of the $BrONO_2$ hydrolysis which coincides with the sudden appearance of HBr (m/e 82). The release of HBr at the end of the hydrolysis reaction underlines an important point, which is that, in contrast to HCl, not all HBr adsorbed on the ice is available for reaction (8.4). This fact has already been observed by Seisel *et al.* in the studies of the heterogeneous reactions of N_2O_5 [Seisel, 1998] and HONO [Seisel, 1997] on ice doped with HBr, where they observed Br_2 and BrNO yields of only 50 and 50–70 % of the total HBr condensed, respectively.

We performed DPE of $BrONO_2$ on HBr incorporated into sandwich ice samples (S) at 205 K. A sandwich ice sample is prepared according to the three following sequential deposition processes: (1) a thin H_2O–ice (C) film of approximately 80 nm, (2) approximately $4 \cdot 10^{17}$ HBr molecules have subsequently been condensed on this thin (C) ice layer, and (3) finally H_2O vapor is condensed on top of these layers in order to obtain an ice substrate of total thickness of approximately 800 nm. These DPE on (S) ice show the same behavior as described for (C) ice.

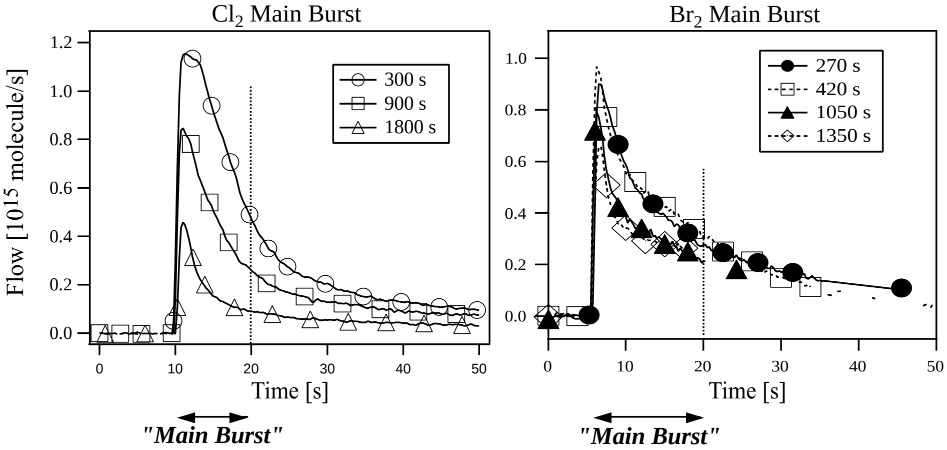

Figure 8.2: Left panel: Main burst of Cl_2 (monitored at m/e 70) at 190 K for increasing time delays ranging from 300 to 1800 s between doping and probing. The experiments were performed on (B) ice samples using a probing $ClONO_2$ flow rate of $1.0 \cdot 10^{15}$ molecule/s. Right panel: Main burst of Br_2 (monitored at m/e 160) at 205 K for increasing time delays ranging from 270 to 1350 s between doping and probing. The experiments were performed on (C) ice samples using a probing $BrONO_2$ flow rate of $1.5 \cdot 10^{15}$ molecule/s. All experiments have been performed in the 14 mm aperture reactor.

The main burst of X_2 production, where X = Cl, Br, (Figure 8.2) is interpreted as the result of the reaction of $XONO_2$ with HX in the interface region. The shape as well as the duration of the rapid initial rate of halogen production indicate that the interfacial region is a well-defined HX reservoir of thickness I and an associated HX mole fraction X_{HX}. When the interface is sufficiently depleted in HX, back–diffusion of HX from the bulk to the interface region leads to the low rate of X_2 production observed in the tail of the MS signal.

8.2.2 Analysis of the Main Burst Production of X_2

Main Burst of X_2

Figure 8.2 shows raw MS signals of Cl_2 (left panel) and Br_2 (right panel) monitored at m/e 70 and 160, respectively, for various time delays ranging from 4.5 to 30 minutes between HX doping and $XONO_2$ probing. The experiments performed on (B) ice have been performed on the same ice sample after regeneration of the sample by thermal desorption of HNO_3 between each measurement. Each experiment on (C) ice samples has been performed on a fresh sample without adding an external flow of H_2O vapor (desorbing ice) which usually compensates the rate of H_2O evaporation of the ice sample. The motivation of performing experiments on desorbing ice samples is to enable the determination the hydrolysis time t_{hyd} which is one of the parameters needed to calculate the thickness of the interface region I (equation (8.10)). Some DPE's of $BrONO_2$ on (C) ice have been performed by adding an external flow of H_2O, however, no difference has been observed in the rate of Br_2 main burst production with respect to DPE performed without external H_2O flow. However, t_{hyd} is not measurable because of the constant thickness of the sample.

As may be seen in Figure 8.2, Cl_2 and Br_2 display the same trend concerning both the shape as well as the decreasing rate of X_2 formation as a function of the time delay between doping and probing. The duration of the main burst of chlorine and bromine, t_{MB} is roughly equal to 10 and 15 s, respectively, at a given flow rate $F^{in}_{ClONO_2}$ of $1.0 \cdot 10^{15}$ and $F^{in}_{BrONO_2}$ of $1.5 \cdot 10^{15}$ molecule/s. However, due to the sticky nature of Br_2 on HBr/ice, the main burst of Br_2 is less prompt than the release of Cl_2. For instance, the main burst of Br_2 observed at a delay of 270 s is almost the same as the one observed at 420 s due to the secondary interaction of Br_2 with HBr on ice (Figure 8.4).

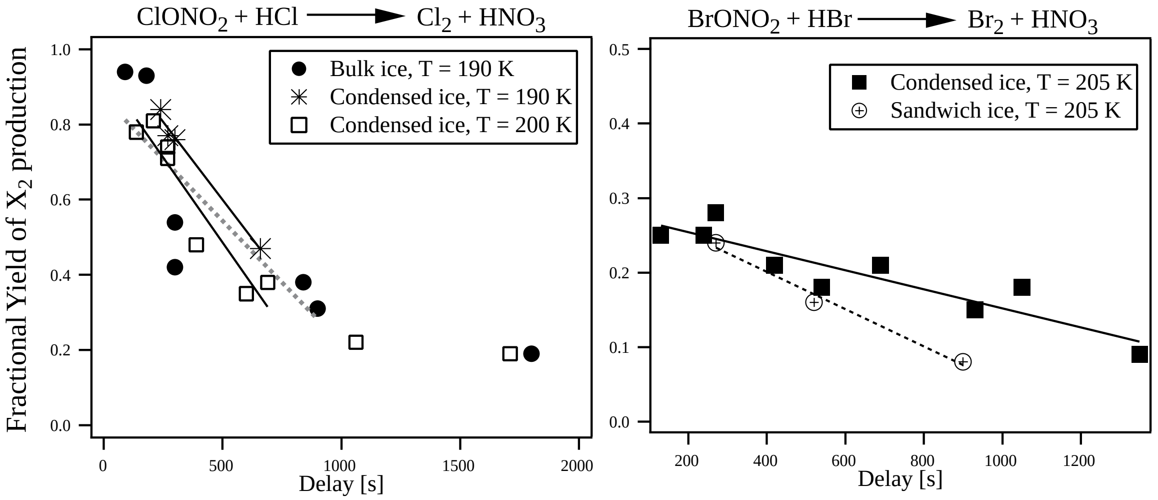

Figure 8.3: Left panel: Fractional yield of Cl_2, η_{Cl_2}, as a function of the time delay between HCl doping and $ClONO_2$ probing on (B) ice at 190 K (solid circles), on (C) ice at 190 K (stars) and 200 K (open squares). Right panel: Fractional yield of Br_2, η_{Br_2}, as a function of the time delay between HBr doping and $BrONO_2$ probing on (C) (solid squares) and (S) (open circles) ice at 205 K.

Fractional Yield of X_2

The fractional yield of X_2 production, η_{X_2} where X = Cl, Br, during a DPE is defined as $N(X_2)/N(HX)$ where $N(X_2)$ is the integral of the Cl_2 and Br_2 main burst during the first 10 and 15 seconds, respectively, and N(HX) is the total amount of HX previously taken up. As displayed in Figures 8.2 and 8.3, η_{X_2} decreases with increasing delay between doping and probing. η_{Cl_2} and η_{Br_2} are displayed in Tables 8.3 and 8.4 on pages 159 and 160, respectively. In the $ClONO_2$/HCl system, the total chlorine yield is the sum of the initial main burst (high rate of Cl_2 formation) and the subsequent yield corresponding to the Cl_2 molecules forming the tail of the MS signal corresponding to a low rate of Cl_2 formation. The mass balance indicates a 1:1 correspondence between Cl–atoms lost in HCl and chlorine generated in Cl_2 for all experiments leading to a closed chlorine mass balance. This means that all the condensed HCl is titrated by the probing $ClONO_2$ in contrast to the $BrONO_2$/HBr system. As displayed in Figure 8.3 (right panel), the amount of Br_2 released into the gas phase at short delay times is approximately 25 % in comparison to released Cl_2 which is close to 100 % at short delay times. The low rate of Br_2 production after the main burst between 80 and 280 s as displayed in Figure 8.1 reveals a mass balance of total bromine of between 20 and 40 % indicating that not all HBr is consumed during the experiment. As displayed in Figure 8.1.b) one may observe an increase in the HBr MS signal, monitored at m/e 82 at t = 250 s leading to a release into the gas phase of approximately 50 % of the total amount of HBr previously taken up so that the bromine mass balance is closed.

Figure 8.4 displays the interaction of Br_2 on ice (circles) compared to the interaction of Br_2 on ice doped with HBr (triangles) at 200 K leading to a value of γ_0 of $7 \cdot 10^{-2}$ in good agreement with values reported by Seisel *et al.* [1998]. Figure 8.4 shows that Br_2 condenses on an ice sample doped with HBr which may be one of the reasons that not all the HBr is available for the titration reaction.

Except that we did not have a 1:1 correspondence between the amount of Br_2 released and the amount of HBr taken up prior to the experiments, the uptake of Br_2 on ice doped with HBr will not influence the determination of the flux F_L corresponding to the surface–to-bulk loss, because our methodology is sensitive only to the change in Br_2 rate of formation regardless of the absolute amount released (fit to the slope in Figure 8.3).

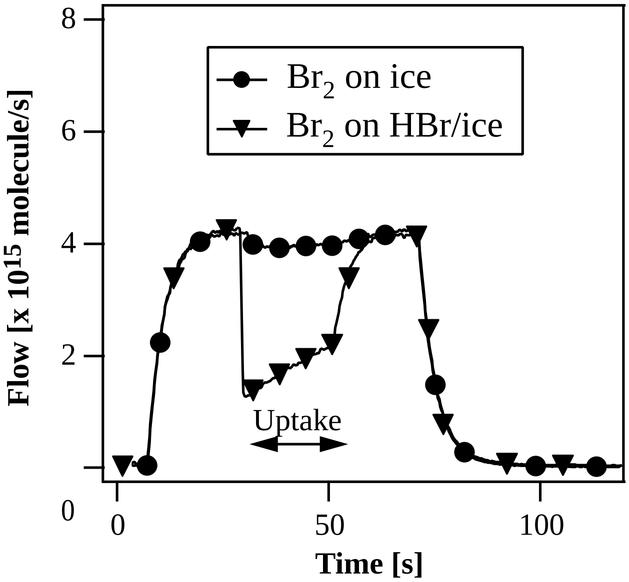

Figure 8.4: Uptake of Br_2 on pure (B) ice (circles) compared to the uptake on (B) ice doped with HBr (triangles) at 200 K using the 8 mm diameter escape reactor and $F^{in}_{Br_2} = 4.2 \cdot 10^{15}$ molecule/s, where the amount of HBr taken up prior the uptake experiment is approximately $2 \cdot 10^{16}$ molecules. The uptake coefficient of Br_2 on pure ice is less than 10^{-5} (detection limit), while the uptake coefficient of Br_2 on ice doped with HBr leads to $\gamma_0 = 7.5 \cdot 10^{-2}$, with $k^{8mm}_{esc} = 1.0\ s^{-1}$ and $\omega = 38\ s^{-1}$.

The time dependence of η_{X_2} is the manifestation of the decrease of the HX concentration in the interface region owing to diffusion of HX into the bulk of the ice substrate. The rate of surface–to–bulk loss is $R_L = F_L \cdot A_s$, where F_L is the flux of the

HX surface–to–bulk loss rate in units of molecule/s·cm^2 and A_s is the geometric sample area [Fluckiger, 2000]. We will focus our attention on the linear time dependence of η_{X_2}, which means on the time scale 0–700 s for η_{Cl_2} and 0–1200 s for η_{Br_2} (see Figure 8.3). The linear fits displayed in Figure 8.3 are equivalent to the assumption that F_L is constant independent of time over the decay range given above.

The amount of Cl_2, $N(Cl_2)$, produced in a DPE may be described as a function of the time delay t according to the following equation:

$$N(Cl_2)(t) = N(HCl) - F_L^{HCl} A_s t \tag{8.5}$$

where N(HCl) is the amount of HCl taken up prior to titration by the $ClONO_2$ probing phase of the experiment. For the bromine system we may express the amount of Br_2, $N(Br_2)$, produced in a DPE according to:

$$N(Br_2)(t) = 0.3N(HBr) - F_L^{HBr} A_s t \tag{8.6}$$

The introduction of the factor 0.3 in equation (8.6) is justified by the fact that $N(Br_2)(t)$, resulting from the integration over the main burst of Br_2 production starting at $t = 0$, which corresponds to the maximum value of η_{Br_2}, is 30 % on average (Figure 8.3). This then means that only 30 % of all adsorbed HBr molecules may contribute to Br_2 according to reaction (8.4). The flux of the surface–to–bulk loss, F_L^{HCl}, is then determined by the slope of the least squares fit displayed in Figure 8.3, and values are displayed in Table 8.5 for HCl interacting with three types of ice ((SC), (C), (B)) at 190 K and for (B) ice at 200 K. Table 8.6 displays F_L^{HBr} for HBr adsorbed on (B) and (S) ice. The values of F_L^{HCl} at 190 K for HCl are found to be equal to $(2.6 \pm 0.6) \cdot 10^{11}$, $(8.1{\pm}2.0){\cdot}10^{11}$ and $(1.6{\pm}0.4){\cdot}10^{12}$ molecule/s·cm^2 for (SC), (B) and (C) ice, respectively. The difference may certainly be attributed to the structural properties of the ice matrix which influences pathways for diffusion of HX. The values of F_L^{HBr} at 205 K for HBr have been measured to be $(1.2 \pm 0.3) \cdot 10^{11}$ and $(3.4 \pm 0.8) \cdot 10^{11}$ molecule/s·cm^2 for (C) and (S) ice samples, where (S) ice means a sandwich ice sample which is obtained by deposition of gaseous HBr on a thin (C) film, finally followed by deposition of a large amount of water vapor.

As displayed in Figure 8.3, the fractional yield of Br_2, η_{Br_2}, has been calculated for a main burst duration of 15 s for the (C) ice sample. Br_2 yield calculations performed at $t = 25$ s, which corresponds to a main burst duration of 20 s, did not show any difference in the F_L^{HBr} value compared to a 15 s main burst duration. However, yield calculations performed for a main burst duration of 10 s lead to a F_L^{HBr} value of $0.9 \cdot 10^{11}$

molecule/s·cm^2 compared to $F_L^{HBr} = (1.2 \pm 0.3) \cdot 10^{11}$ molecule/s·cm^2 for a main burst duration of 15 s. Therefore an uncertainty of 25 % on the F_L value has been assumed.

8.2.3 The HX Concentration in the Interface Region in Terms of its Mole Fraction

Whereas the solubility of HCl in pure ice has been the subject of many studies [Molina, 1987; Wofsy, 1988, Hanson, 1990; Thibert, 1997], the solubility of HBr in pure ice does not seem to be known. In their study of the thermodynamics and kinetics of HCl in ice Thibert and Dominé [1997] proposed the following equation for the calculation of HCl solubility in the temperature range 238–265 K:

$$X_{HCl} = 6.13 \cdot 10^{-10} e^{2806.5/T} P_{HCl}^{1/2.73} \tag{8.7}$$

where T is expressed in K and P_{HCl} in Pa. If the incorporation of HCl into ice is controlled by condensation kinetics the HCl mole fraction is given by equation (8.8):

$$X_{HCl} = \frac{P_{HCl}}{P_{H_2O}} \frac{\alpha_{HCl}}{\alpha_{H_2O}} \sqrt{\frac{M_{H_2O}}{M_{HCl}}} \tag{8.8}$$

where α is the mass accommodation coefficient, P the partial pressure of HCl and H_2O and M the molecular weight. Calculated HCl mole fractions are displayed in Table 8.1. Equation (8.8) has also been proposed by the authors to describe the HNO_3 mole fraction in ice [Thibert, 1998]. Thus it seems to be reasonable to apply this equation also to the HBr/ice system, with $\alpha_{HBr} = \gamma_0$ where γ_0 is the initial uptake coefficient of HBr on ice. The calculated X_{HCl} and X_{HBr} are displayed in Table 8.1.

Because our experimental conditions were different from those of to Thibert and Dominé [1997] we performed HX/H_2O co–deposition experiments in order to obtain a value of X_{HX} for our experimental conditions. We have simultaneously condensed gaseous H_2O and HCl or HBr for 5 minutes in the low temperature support at typical flow rates of 10^{17} and $4 \cdot 10^{14}$ or $1 \cdot 10^{15}$ molecule/s, respectively, at temperatures at which "Dope and Probe“ experiments have been performed. The composition of such co–condensed samples ($C^\star$), whose thickness is at least 1 μm, has been assumed to be homogeneous. By measuring the flow rates of the gaseous species and the duration of the co–deposition, we were able to determine the HX mole fraction, X_{exp}, whose values are displayed in Table 8.1. We stress that equation (8.8) describes our HX/ice system very well for our experimental conditions.

Figure 8.5 displays the Cl_2 (●) and Br_2 (■) production on co–condensed ice ($C^\star$) resulting from the uptake of $ClONO_2$ on HCl/H_2O at 190 K and $BrONO_2$ on HBr/H_2O

Table 8.1: Experimental a) HCl and b) HBr mole fractions X_{exp} determined by co–deposition experiments of HCl/H_2O and HBr/H_2O, respectively. The calculated HCl and HBr mole fractions are compared to experimental values.

T [K]	P_{HX} [Torr]	P_{H_2O} [Torr]	X_{exp}	X_{HCl} (c)	X_{HX} (d)
	a) HCl				
190	$1.6 \cdot 10^{-6}$	$6.1 \cdot 10^{-4}$	$1.6 \cdot 10^{-3}$	$1.1 \cdot 10^{-5}$	$1.1 \cdot 10^{-3}$
200	$6.4 \cdot 10^{-7}$	$5.7 \cdot 10^{-4}$	$6.1 \cdot 10^{-4}$	$7.8 \cdot 10^{-6}$	$4.8 \cdot 10^{-4}$
	b) HBr				
205	$6.4 \cdot 10^{-6}$	$3.0 \cdot 10^{-4}$	$9.6 \cdot 10^{-3}$		$8.1 \cdot 10^{-3}$
205	$7.6 \cdot 10^{-6}$	$2.7 \cdot 10^{-4}$	$1.3 \cdot 10^{-2}$		$1.1 \cdot 10^{-2}$

(c) Calculated according to equation (8.7). (d) Calculated according to equation (8.8) with $\alpha_{H_2O} = 0.50$, $\alpha_{HCl} = 0.30$ and $\alpha_{HBr} = 0.27$.

at 205 K, respectively. The $ClONO_2$ and $BrONO_2$ flow rates were $6 \cdot 10^{15}$ and $2 \cdot 10^{15}$ molecule/s, respectively. The duration of the main burst for both molecular halogen production processes is equal to approximately 20 s. Following the X_2 main burst a steady state is observed whose levels are higher than the one on pure (B) and (C) ice doped with HX (Figure 8.2) where bulk ice was essentially free of HX (X = Cl or Br). We may note, that even on ($C^\star$) ice which is assumed to be a homogeneous substrate by virtue of the co-condensation procedure, the DPE reveals an interface region where the rate of the probing reactions are significantly higher. To date no explanation is proposed to understand this behavior. However, FTIR studies are in progress in our laboratory.

8.3 The Extent of the Interface Region in Terms of its Thickness

The determination of the interface thickness I is motivated by the fact that this parameter is crucial for the determination of the bulk diffusion coefficient D_{HX} of HX (equation 8.14). The interface is the region over which the HX concentration is well defined and acts as a HX reservoir leading to diffusion of HX molecules into the bulk of the ice sample.

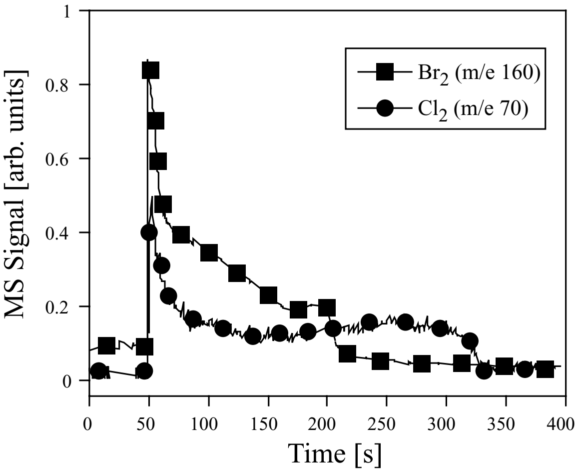

Figure 8.5: Cl_2 (●) and Br_2 (■) production from the heterogeneous reaction of $XONO_2$ on a HX/H_2O co–condensed sample ($C^\star$) at 190 K for X = Cl and at 205 K for X = Br.

8.3.1 Determination of the Interface Thickness I

The thickness of the interface region, I, has been calculated according to two different methods described in detail in Fluckiger *et al.* [2000]. The first method is based on the rate of H_2O consumption and yields to the following expression for the interface thickness I_1 (which is assumed to be identical for both the interface region and the (B) or (C) ice sample):

$$I_1 = (k_{MB} \cdot [ClONO_2] \cdot V + R_{evap}) \cdot \left(\frac{k_{hyd}}{k_{MB}}\right) \cdot t_{MB} \cdot \frac{d}{1.6 \cdot 10^{16}} \tag{8.9}$$

where I_1 is the interface thickness in nm, k_{MB} the pseudo first–order rate constant for the titration (probing) reaction, k_{hyd} the pseudo first–order rate constant for hydrolysis, V the reactor volume, R_{evap} the rate of evaporation of H_2O, t_{MB} the duration of the main burst and d the thickness of one nominal layer of H_2O ice estimated to be equal to 0.4 nm [Hobbs, 1974]. The values k_{MB} and k_{hyd} were determined at 3.5 s^{-1} and 0.6 s^{-1}, respectively for the DPE of $ClONO_2$ with HCl/ice. Because no saturation of the surface has been observed in the interaction of $BrONO_2$ with HBr/ice (Figure 7.8 on page 137), the ratio k_{MB}/k_{hyd} is equal to 1. The rates of evaporation R_{evap} of water used are the values reported by Chaix *et al.* [1998] and are displayed in Table 8.2.

The second method is based on the comparison of the time for hydrolysis t_{hyd} of the whole ice substrate and the hypothetical time for hydrolysis during the main burst for molecular halogen production. A good correlation has been obtained between the total duration of the hydrolysis and the number of H_2O constituting the thin ice film sample. The hydrolysis time, t_{hyd}, is equal to the ratio of the total thickness h and the rate

Table 8.2: Rate of evaporation of H_2O in molecule/s·cm^2 used in the calculation of the interface thickness. Values from Chaix *et al.* [1998].

T [K]	(C)	(B)	(SC)
190	$1.6 \cdot 10^{16}$	$3.5 \cdot 10^{16}$	$8.0 \cdot 10^{15}$
200	$3.5 \cdot 10^{16}$	$1.0 \cdot 10^{17}$	
205	$5.0 \cdot 10^{16}$		

constant for the hydrolysis k_{hyd}, expressed in monolayers per unit time. The hydrolysis time for the duration of the main burst is given by $(k_{MB}/k_{hyd})\cdot t_{MB}$ which is equal to the interface thickness I divided by the rate of hydrolysis. We may therefore write the following expression for the interface thickness I_2:

$$\frac{I_2}{h} = \frac{t_{MB}\left(\frac{k_{MB}}{k_{hyd}}\right)}{t_{hyd}} \quad or \quad I_2 = h\left(\frac{t_{MB}}{t_{hyd}}\right)\left(\frac{k_{MB}}{k_{hyd}}\right) \tag{8.10}$$

assuming that the rate of hydrolysis is identical for H_2O molecules making up the interface region compared to H_2O molecules present throughout the bulk of the sample of thickness h. Equation (8.10) has not been used to calculate the interface thickness for DPE performed on (B) and (SC) ice due to the large value of h compared to I.

8.3.2 Results

The values for I calculated according to equations (8.9) and (8.10) are displayed in Tables 8.3 and 8.4 for HCl and HBr interfaces, respectively. Figure 8.6 displays the values for the thickness I_2 of the HCl interface calculated according to equation (8.10) for (C) ice at different conditions obtained in this work which are compared to the values reported by Fluckiger *et al.* [2000]. Values for the interface thickness resulting from DPE performed on (B) or (SC) have been calculated according to equation (8.9) and are called I_1.

From Tables 8.3 and 8.4, one notices a systematically higher value for I_1 than for I_2 for all experiments. Equation (8.9) seems to overestimate the values of the interface thickness I_1 owing to an overestimation of the rate of evaporation of H_2O. In equation (8.9), we may note that:

$$k_{MB}[ClONO_2]V \ll R_{evap} \tag{8.11}$$

The term $(k_{MB}[ClONO_2]V)$ may therefore be neglected if R_{evap} is as large as given

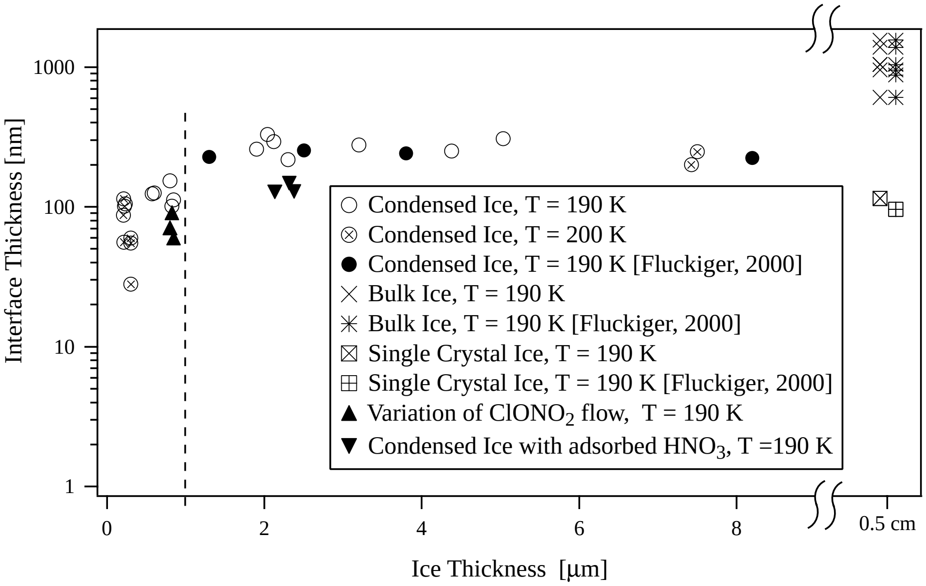

Figure 8.6: Values for the thickness I_2 for the interface of HCl/ice for (C) ice as a function of the total thickness of the ice sample. Values of the interface thickness I_1 of the interface of HCl/ice for (B) and (SC) ice sample. The present results are compared to the results obtained by Fluckiger *et al.* [2000].

in Table 8.2. Calculations of I_2 with and without the term ($k_{MB}[ClONO_2]V$) effectively lead to identical results using equation (8.9). The H_2O rates of evaporation used for the determination of I_1 (Table 8.2) are rates of evaporation of H_2O from pure ice samples [Chaix, 1998]. However, in our case ice samples are doped with HX, which significantly reduces the rate of evaporation of H_2O from the sample surface [Diehl, 1998]. Therefore, equation (8.9) gives an upper limit for the thickness of the interfacial region. A decrease by a factor of 3 in the evaporation rate adjusts the values for I_1 to those for I_2. In the following, we will focus our attention on results obtained by the second method (I_2), especially for the determination of the diffusion coefficient D_{HX} of HX in bulk ice.

We may note that the I_1 values obtained for the HCl/ice interface for (C) and (B) ice are of the order of 300 nm and 1200 nm, respectively (see Table 8.3). This discrepancy may in part be due to the structural term $\frac{d}{1.6 \cdot 10^{16}}$ in equation (8.9) where d is the thickness of one nominal monolayer of water ice and is estimated to be equal to 0.4 nm obtained for crystalline ice [Hobbs, 1974]. It is very likely that this term does not apply to (B) ice owing to its production, d addresses to a near perfect single crystal which clearly bulk ice is not. As discussed above, a systematically higher value of the interface thickness I_1 is obtained compared to I_2 for (C) ice samples where I could be assessed using both methods. The mean ratio for the HCl/ice system $I_2/I_1 = 0.37$ calculated for (C) ice can be used to scale down the mean value of $I_1 = 1200$, 115 nm for (B), (SC) ice, respectively, to a corrected value of 444, 43 nm, respectively, which are significantly smaller than the original I_1 value obtained for (C) ice. These values of I of 444 ± 120 nm and 43 ± 16 nm will be used in the determination of the diffusion coefficient D_{HCl} of HCl in (B) and (SC) ice at 190 K, respectively. We may note that the ratio of $I_2/I_1 = 0.37$ may be an indication of the decrease of R_{evap} when HX is condensed on pure ice.

For (C) ice no temperature dependence of the interface thickness I_2 has been observed between 190 and 200 K, and for samples thicker than h = 1 μm a constant value of approximately 250 nm is observed. However, the interface thickness decreases down to 30 nm when the total ice thickness is of the order of 200–300 nm. Results obtained by Fluckiger *et al.* [2000] and the present results are in good agreement as displayed in Figure 8.6.

Table 8.4 displays the results for I_2 obtained for HBr/ice at 205 K on (C) and (S) ice. For the thickness I_2 of the HBr interface, one obtains a value of $I_2 = 104 \pm 38$ nm on (C) ice and $I_2 = 120 \pm 30$ nm on (S) ice.

8.3.3 The Cl_2 Main Burst as a Function of the Flow Rate of $ClONO_2$ and its Influence on the Thickness I of the Interface Region

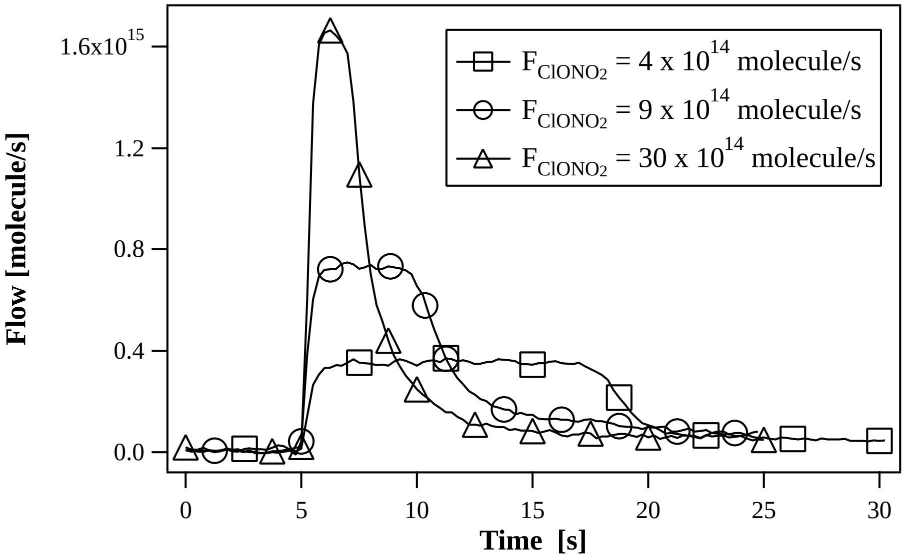

Figure 8.7: Main burst of Cl_2 (m/e 70) at different $ClONO_2$ probing flow rates at 190 K in the 14 mm aperture reactor on (C) ice samples. The amount of HCl deposited on the ice surface is $8{\cdot}10^{15}$ molecules, corresponding to 0.5 HCl ML and the delay between the doping and the probing is 4 minutes.

Figure 8.7 displays the main burst of Cl_2 (m/e 70) at 190 K resulting from DPE on (C) ice at different $ClONO_2$ flow rates in the range 4–30·10^{14} molecule/s. The amount of HCl taken up prior to the probe with $ClONO_2$ has been held constant at N(HCl) = $8 \cdot 10^{15}$ molecules corresponding to 0.5 of a formal monolayer (ML) of HCl and the delay time between the HCl deposition (doping) and the titration with $ClONO_2$ (probing) is 4 minutes. The higher the $ClONO_2$ flow rate is, the shorter is the duration of the main burst, t_{MB}. As expected, the Cl_2–yield is constant for this delay and amounts to (75 ± 5) %. With increasing [$ClONO_2$], the rate of hydrolysis is accelerating thus leading to a shorter hydrolysis time, t_{hyd}. The ratio $\frac{t_{MB}}{t_{hyd}}$ remains thus constant and therefore does not influence the value of the interface thickness I_2 calculated according to equation (8.10).

8.3.4 Influence of the Quantity of Adsorbed HCl, N(HCl), on the Interface Thickness I

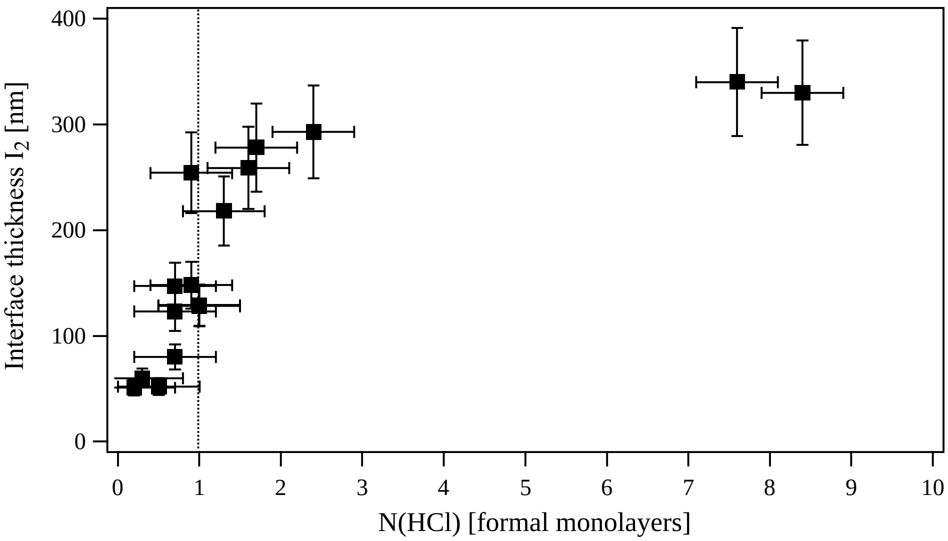

Figure 8.8: The interface thickness I_2 of HCl/ice as a function of the number of HCl condensed N(HCl) on (C) ice samples at 190 K. The total ice thickness is of the order of 2 μm and the probing $ClONO_2$ flow rate is 1·10^{15} molecule/s with one HCl formal monolayer corresponding to 1·10^{15} molecule/cm^2.

The measured thickness I_2 of the interface strongly depends on the amount of HCl (N(HCl)) in the range 0 to 1 ML as displayed in Figure 8.8. For a higher surface concentration, the value of I_2 reaches a limiting value of approximately 300 nm characteristic of (C) ice. Apparently, for [HCl] $<$ 1 ML, the HCl molecules occupy the interfacial region to such an extent, that the mole fraction X_{HCl} is preserved and equal to about

10^{-3} at 190 K (Table 8.1). The occupation of the interfacial region I_2 does not seem to be the rate limiting step for diffusion into the bulk. For a coverage greater than 1 ML of HCl, the diffusion of HCl into the bulk ice becomes the rate limiting step and, thus limits the possible increase of the value I_2. It is interesting to note that the limiting value for N(HCl) of 1 ML corresponds to the dose giving rise to the "liquid" state of HCl on ice, as observed by Fluckiger *et al.* [1998] and in agreement with the HCl/ice phase diagram [Shen, 1995].

Table 8.3: Cl_2-yield η_{Cl_2} observed from DPE on (C), (B), (SC) and (C*) ice as a function of the time delay between HCl doping and $ClONO_2$ probing and the corresponding value for the interfacial thickness I_1, I_2 calculated according to equations (8.9) and (8.10), respectively, with h being the total ice thickness.

N(HCl) (e) [molecules]	Cl_2(g) (f) [molecules]	Delay [s]	η_{Cl_2} [%]	I_1 [nm]	I_2 [nm]	h [nm]
(C) 190 K						
$3.8 \cdot 10^{16}$	$2.0 \cdot 10^{16}$	240	84	420	126	810
$1.6 \cdot 10^{16}$	$1.2 \cdot 10^{16}$	270	77	333	129	710
$3.8 \cdot 10^{16}$	$2.9 \cdot 10^{16}$	300	76	475	193	820
$3.2 \cdot 10^{16}$	$1.5 \cdot 10^{16}$	660	47	455	105	795
(C) 200 K						
$1.8 \cdot 10^{16}$	$1.4 \cdot 10^{16}$	138	78	201	102	221
$1.9 \cdot 10^{16}$	$1.5 \cdot 10^{16}$	210	81	280	69	300
$1.7 \cdot 10^{16}$	$1.2 \cdot 10^{16}$	270	71	184	56	213
$2.7 \cdot 10^{16}$	$2.0 \cdot 10^{16}$	270	74	438	248	7500
$1.8 \cdot 10^{16}$	$8.5 \cdot 10^{15}$	390	48	263	55	302
$2.0 \cdot 10^{16}$	$7.0 \cdot 10^{15}$	600	35	228	200	7425
$1.8 \cdot 10^{16}$	$6.9 \cdot 10^{15}$	690	38	210	102	212
$1.8 \cdot 10^{16}$	$4.0 \cdot 10^{15}$	1062	22	175	28	303
$1.6 \cdot 10^{16}$	$3.0 \cdot 10^{15}$	1710	19	175	87	207
(B) 190 K						
$1.6 \cdot 10^{16}$	$1.5 \cdot 10^{16}$	90	94	1041		
$2.4 \cdot 10^{16}$	$2.0 \cdot 10^{16}$	180	83	1735		
$2.0 \cdot 10^{16}$	$1.1 \cdot 10^{16}$	300	54	1388		
$2.6 \cdot 10^{16}$	$1.1 \cdot 10^{16}$	300	42	954		
$3.3 \cdot 10^{16}$	$1.3 \cdot 10^{16}$	840	38	1562		
$2.6 \cdot 10^{16}$	$7.8 \cdot 10^{15}$	900	31	1040		
$2.2 \cdot 10^{16}$	$4.2 \cdot 10^{15}$	1800	19	607		
(SC) 190 K						
$1.6 \cdot 10^{16}$	$1.5 \cdot 10^{16}$	180	95	115		
(C*) 190 K						
$1.3 \cdot 10^{17}$	$2.1 \cdot 10^{16}$	–	16	404	173	1830
(C*) 200 K						
$5.0 \cdot 10^{16}$	$1.5 \cdot 10^{16}$	–	30	323	131	1930

(e) N(HCl) is the total number of HCl molecules adsorbed on the ice sample. (f) Cl_2(g) is the number of Cl_2 molecules released during the "main burst" into the gas phase.

Table 8.4: Br_2-yield η_{Br_2} observed from DPE experiments on (C), (S) and ($C^\bigstar$) ice at 205 K as a function of the time delay between HBr doping and $BrONO_2$ ($F^{in} \approx 1.5 \cdot 10^{15}$ molecule/s) probing and the corresponding value for the interfacial thickness I_1, I_2 calculated according to equations (8.9) and (8.10), respectively, with h being the total ice thickness.

N(HBr) [a] [molecules]	Br_2(g) [b] [molecules]	Delay [s]	η_{Br_2} [%]	I_1 [nm]	I_2 [nm]	h [nm]
(C)						
$5.6 \cdot 10^{16}$	$1.4 \cdot 10^{16}$	130	25	394	127	633
$5.5 \cdot 10^{16}$	$1.4 \cdot 10^{16}$	240	25	638	128	678
$5.4 \cdot 10^{16}$	$1.5 \cdot 10^{16}$	270	28	375	73	452
$5.7 \cdot 10^{16}$	$1.2 \cdot 10^{16}$	420	21	600	108	673
$5.4 \cdot 10^{16}$	$9.7 \cdot 10^{15}$	540	18	413	65	440
$5.2 \cdot 10^{16}$	$1.0 \cdot 10^{16}$	690	21	450	142	656
$5.2 \cdot 10^{16}$	$7.5 \cdot 10^{15}$	930	15	469	64	483
$5.2 \cdot 10^{16}$	$9.1 \cdot 10^{15}$	1050	18	544	149	690
$5.7 \cdot 10^{16}$	$4.8 \cdot 10^{15}$	1350	9	206	34	409
(S)[c]						
$6.7 \cdot 10^{16}$	$1.6 \cdot 10^{16}$	270	24	769	113	808
$5.5 \cdot 10^{16}$	$9.0 \cdot 10^{15}$	520	16	413	156	864
$1.1 \cdot 10^{17}$	$9.2 \cdot 10^{15}$	900	8	788	73	753
($C^\bigstar$)						
$3.4 \cdot 10^{17}$	$4.6 \cdot 10^{16}$	–	14	488	61	824
$4.0 \cdot 10^{17}$	$1.4 \cdot 10^{17}$	–	35	750	70	729

[a] N(HBr) is the total number of HBr molecules adsorbed on the ice sample.

[b] Br_2(g) is the number of Br_2 molecules released during the "main burst" into the gas phase.

[c] (S) = Sandwich ice: A thin (C) sample ice is prepared by first depositing an ice layer on the order of approximately 80 nm. We subsequently condense HBr on this thin (C) ice sample and finally gaseous water is deposited on top of the condensate in order to obtain a sample thickness of approximately 800 nm.

8.4 Diffusion Coefficient D for HCl and HBr in Ice

This Section describes the method for the determination of the diffusion coefficient D_{HX} of HX in ice. The flux of HX surface–to–bulk loss F_L^{HX} resulting from the measurements of the concentration change of HX at the interface, the value of the thickness of the interface and the concentration of HX will be used for the calculation of the D_{HX} for X = Cl and Br in ice.

8.4.1 Determination of the Diffusion Coefficient

Fick's First Law

We will use Fick's first law of diffusion, equation (8.12), to interpret our data displayed in Figure 8.3 and Tables 8.3 and 8.4 in order to determine the HX diffusion coefficient in the bulk phase of the ice. As already seen in Chapter 6, Fick's first law of diffusion may be used to describe a stationary process of molecular diffusion.

$$J = -D\frac{\partial C(x,t)}{\partial x} \tag{8.12}$$

where the flux J is the flux of HX from the interface region to the bulk of the sample and has been set equal to F_L^{HX}, the flux of HX surface–to–bulk loss, D is the diffusion coefficient of HX in the ice. The concentration gradient, $\frac{\partial C(x,t)}{\partial x}$, may be approximated by the linear differential relationship displayed in (8.13) using the known amount of HX, N(HX) taken up into the unknown volume $V_{IR} = A_s \cdot I$, where $A_s = 15$ cm^2 is the geometrical area of the ice sample and I the thickness or depth of the interfacial region. The gradient of HX in the ice substrate may therefore be expressed using the following expression:

$$-\frac{\partial C(x,t)}{\partial x} = \frac{C(I,t) - C(x,t)}{I} \approx \frac{N(HX)}{V_{IR}I} \tag{8.13}$$

where C(I,t) is the initial concentration of HX throughout the interfacial region and where C(x,t) has been set to zero because we only consider the initial situation close to t = 0. By setting C(I,t) = N(HX)/V_{IR} and C(x,t) = 0 in equation (8.13) we obtain for equation (8.12) the diffusion coefficient D_{HX} expressed in equation (8.14):

$$D_{HX} = F_L\frac{I}{N(HX)}V_{IR} = F_L\frac{A_s I^2}{N(HX)} \tag{8.14}$$

Equation (8.14) establishes the relationship between the measured flux of surface–to-bulk loss F_L and the diffusion coefficient D_{HX} of HX in ice, where X = Cl or Br based on the assumption that for short times in the proximity of t = 0 the initial HX concentration is constant in the interface region and C(x,t) = 0 as displayed in Figure 8.9.

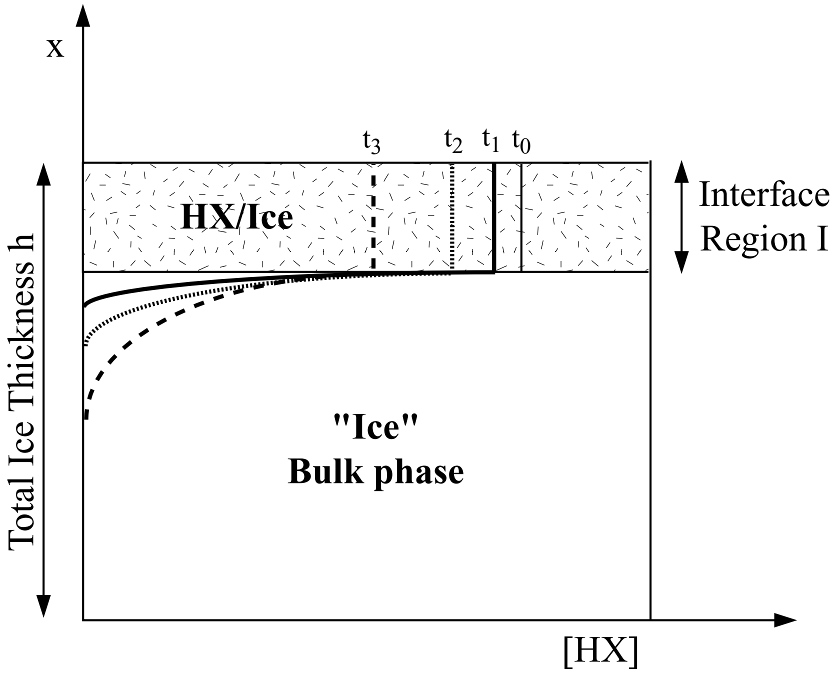

Figure 8.9: Schematic HX concentration at different delay times with $t_1 < t_2 < t_3$. The concentration in the interface region corresponding to the HX reservoir is assumed to be constant at a short time delay between doping and probing.

8.4.2 Results and Discussion

The diffusion coefficient D_{HX} of HX, with X = Cl or Br calculated according to equation (8.14) are displayed in Tables 8.5 and 8.6 for D_{HCl} and D_{HBr}, respectively. These values have been obtained with $A_s = 15$ cm^2 and N(HX) being the amount of HX taken up prior to a DPE whose data are presented in Tables 8.3 and 8.4 for HCl/ice and HBr/ice, respectively. The flux F_L of HX surface–to–bulk loss displayed in Tables 8.5 and 8.6 for X = Cl and Br, respectively have been obtained from the decrease of the main burst with increasing the delay time between "dope“ and "probe“ (Figures 8.2 and 8.3).

The diffusion coefficient D_{HCl} of HCl appears to be dependent on the nature of the ice substrates. One observes that there is a difference of two orders of magnitude between $D^{(SC)}_{HCl}$, the lowest value, and $D^{(B)}_{HCl}$ using the interface thickness scaled for I_2. The values of $D^{(C)}_{HCl}$ obtained on (C) ice at 190 and 200 K are $(1.5 \pm 0.4) \cdot 10^{-13}$ and $(1.1 \pm 0.3) \cdot 10^{-13}$ cm^2/s, respectively, indicating no temperature dependence of the diffusion coefficient in

Table 8.5: Flux of HCl surface-to-bulk loss F_L^{HCl}, N(HCl) mean values and HCl diffusion coefficients D_{HCl} calculated according to equation (8.14).

Ice Type	T [K]	I_2 [nm]	F_L^{HCl} [molecule/s·cm^2]	N(HCl) [molecules]	D_{HCl} [cm^2/s]
(SC)	190	43 ± 16 [(a)]	$(2.6 \pm 0.6) \cdot 10^{11}$	$(1.6 \pm 0.2) \cdot 10^{16}$	$(4.5 \pm 1.1) \cdot 10^{-15}$
(C)	190	140 ± 60	$(1.6 \pm 0.4) \cdot 10^{12}$	$(3.1 \pm 0.9) \cdot 10^{16}$	$(1.5 \pm 0.4) \cdot 10^{-13}$
(C)	200	105 ± 70	$(1.2 \pm 0.3) \cdot 10^{12}$	$(1.9 \pm 0.3) \cdot 10^{16}$	$(1.1 \pm 0.3) \cdot 10^{-13}$
(B)	190	444 ± 120 [(a)]	$(8.1 \pm 2.0) \cdot 10^{11}$	$(2.4 \pm 0.5) \cdot 10^{16}$	$(1.0 \pm 0.6) \cdot 10^{-12}$

[(a)] Interface thickness corrected according to the ratio $I_2/I_1 = 0.37$.

(C) ice. This was expected owing to the absence of a temperature dependence in the values of I_2 and F_L^{HCl} between 190 and 200 K.

The values we obtain for D_{HBr} at 205 K are $(3.6 \pm 1.2) \cdot 10^{-15}$ and $(9.5 \pm 0.7) \cdot 10^{-15}$ cm^2/s for (C) and (S) ice, respectively. The two different methods to produce doped condensed ice samples ((C) and (S)) lead to diffusion coefficients differing by a factor of 2.5 which measures the experimental uncertainty, because a (S) ice sample is in fact nothing else than a doped (C) ice sample.

D_{HBr} in (C) ice at 205 K is smaller by a factor of 20 compared to D_{HCl} in (C) ice at 200 K. The diffusion of HBr in (C) ice is slower than HCl in (C) ice. As pointed out by Barnaal and Slotfeldt-Ellingsen [1983] this may be due to the larger ionic radius and lower mobility of HBr compared to HCl. Our measurements of F_L for HCl/ice and HBr/ice show that F_L^{HCl} is one order of magnitude higher than F_L^{HBr} in agreement with our expectation that D_{HBr} would be smaller than D_{HCl} in ice at a given temperature and ice sample.

Table 8.6: Flux of HBr surface-to-bulk loss F_L^{HBr}, N(HBr) mean values and HBr diffusion coefficients D_{HBr} calculated according to equation (8.14).

Ice Type	T [K]	I_2 [nm]	F_L [molecule/s·cm^2]	N(HBr) [molecules]	D_{HBr} [cm^2/s]
(C)	205	104 ± 38	$(1.2 \pm 0.3) \cdot 10^{11}$	$(5.4 \pm 0.2) \cdot 10^{16}$	$(3.6 \pm 1.2) \cdot 10^{-15}$
(S)	205	120 ± 30	$(3.4 \pm 0.8) \cdot 10^{11}$	$(7.7 \pm 0.5) \cdot 10^{16}$	$(9.5 \pm 0.7) \cdot 10^{-15}$

As displayed in Figure 8.10, the diffusion of HCl in ice has been studied by numerous research laboratories in an atmospheric context. Owing to the large number of studies, a wide variety of different methods have been used leading to different values for D_{HCl} owing to the different types of ice and HCl partial pressures used. A summary of some selected values of D_{HCl} is displayed in Figure 8.10 which shows a constant value of D_{HCl} obtained by Thibert and Dominé [2000] of approximately $5 \cdot 10^{-12}$ cm^2/s on hexagonal ice. They did not observed any temperature dependence of D_{HCl} in the range 238–265 K using depth profiling. Using ATR–FTIR spectroscopy on ice films 1–2 μm thick, Horn *et al.* [1997] found a diffusion coefficient of $D_{HCl} = 1.5 \cdot 10^{-11}$ cm^2/s at 150 K. D_{HCl} values between 10^{-12} and 10^{-10} cm^2/s have been measured by Wolff *et al.* [1989] at 185 K. We may observe that the diffusion coefficient from the present work is in good agreement with values reported by Fluckiger *et al.* [2000] using the same methodology. Moreover, we were able to narrow the uncertainties for D_{HCl} for our specific types of ice sample.

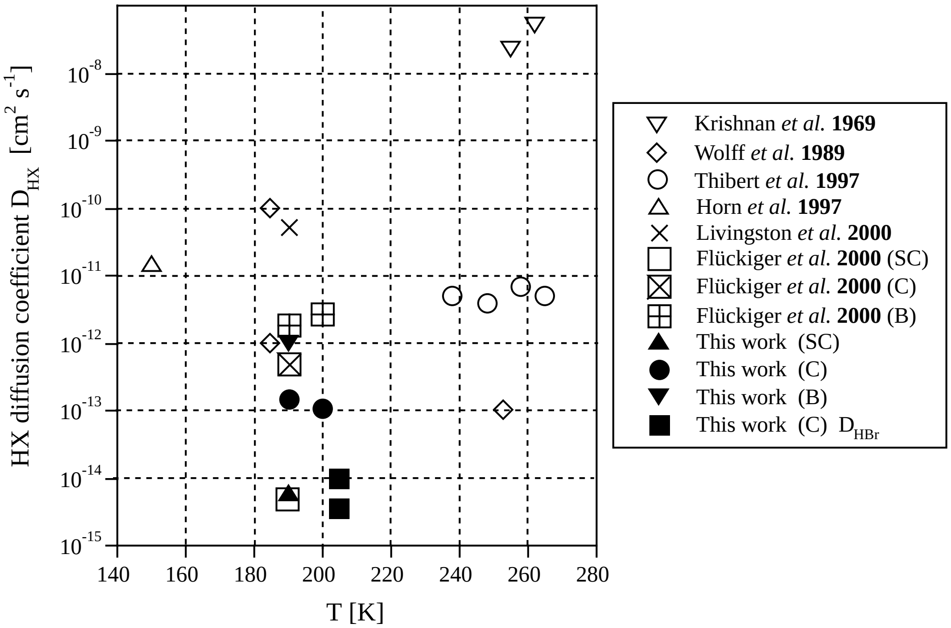

Figure 8.10: Comparison of the diffusion coefficient D_{HCl} of HCl in ice measured in this work for different types of ice (full symbols) with values obtained from the literature: (▽) Krishnan [1969], (◊) Wolff [1989], (○) Thibert [1997], (△) Horn [1997], (×) Livingston, [2000], (□), (⊠) and (⊞) Fluckiger [2000] for (SC), (C) and (B), respectively. Diffusion coefficient D_{HBr} (■) of HBr in (C) ice samples obtained in the present work.

The range of results obtained for D_{HCl} suggests that the values reported in Figure 8.10 correspond to results obtained for different types of ice. The preparation and characterization of ice samples seem to be an open question and worthy of pursuit in the future.

8.5 Conclusion

In this Chapter, an indirect method has been presented in order to measure the bulk diffusion coefficient D_{HCl} of HCl and for the first time D_{HBr} of HBr in ice.

"Dope and probe" experiments (DPE) have been performed in order to probe the gas–solid interface of ice. $ClONO_2$ and $BrONO_2$ have been chosen to interrogate the HCl/ice and HBr/ice interface, respectively. We have assumed that $XONO_2$ (X = Cl or Br) will preferentialy probe the gas–solid interface of ice owing to its "sticky" nature. For this reason $XONO_2$ has been chosen to be the probe molecule to explore the near–surface HX concentrations. The gaseous reaction products, X_2 of the heterogeneous reaction $XONO_2 + HX \rightarrow X_2 + HNO_3$ have been followed as a function of time in order to obtain information on the flux of the surface–to–bulk loss of HX. DPE reveal a fast molecular halogen production ("main burst"), followed by a low rate of X_2 production. The main burst of X_2 production has been interpreted as a result of the reaction of $XONO_2$ with HX in a well defined region: the interface which is characterized by a thickness I and a HX mole fraction X_{HX}.

The thickness I of the interfacial region has been determined to be substrate dependent for the HCl/ice interface: I = 43 ± 16 nm for (SC) ice, I = 444 ± 120 nm for (B) ice at 190 K and I = 250 ± 50 nm for (C) ice whose total thickness exceeds 1 μm. The HBr/ice interface for (C) ice is I = 110 ± 15 nm at 205 K. The interface thickness obtained at 200 K on (C) for HCl ice is identical to the one measured at 190 K within experimental accuracy. No temperature dependence has been experimentally observed for the thickness I of the interface. This trend in I with respect to the type of ice may be correlated with increasing structural defects in the ice, such as grain boundaries and dislocations.

No influence of the probing flow rate of $ClONO_2$ has been observed resulting in a constant value for the interface. The higher the $ClONO_2$ flow rate, the shorter is the duration of the main burst of Cl_2 production. This dependence shows that the response to the titration reaction is linear, giving an additional validation to the method of "Dope and Probe" experiments in the determination of the diffusion coefficient D_{HX}.

It has been shown that the thickness of the HCl interface is strongly influenced by the amount of HCl incorporated in the (C) ice sample. For a coverage greater than 1 ML, the diffusion of HCl into the bulk becomes rate limiting leading to a constant value of the interface. To maintain a constant concentration in the interface of the order of a mole fraction of 10^{-3} at 190 K, HCl will diffuse throughout the interface region until it reaches this concentration. We insist that the large values obtained in the present work for the interface thickness I are a consequence of the constant HX concentration in the interface region. Using Lennard-Jones parameters for H_2O ($\sigma_{H_2O} = 2.64$ Å) and HCl ($\sigma_{HCl} = 3.34$ Å) one may for instance calculate the average concentration of 2 monolayers of HCl adsorbed in a 250 nm thick slab of water. The total amounts of H_2O and HCl are $1.4 \cdot 10^{18}$ and $1.8 \cdot 10^{15}$ molecules, respectively, leading to a HCl mole fraction of $1.3 \cdot 10^{-3}$. The smaller the HCl partial pressure while doping the ice sample, the shorter will be the penetration depth of HCl in the ice, because the mole fraction of 10^{-3} is reached for a smaller I. For a sample with a high coverage of HCl, we will have the formation of a liquid atop the ice sample whose concentration remains constant.

The diffusion coefficient D_{HCl} of HCl in ice has been determined to lie in the range $4.0 \cdot 10^{-15} - 1.0 \cdot 10^{-12}$ cm^2/s at 190 K, which is in good agreement with values reported by Fluckiger *et al.* [2000] and by Thibert and Dominé [1997]. The diffusion coefficient D_{HBr} of HBr in (C) ice at 205 K has been found to be $6.5 \pm 3.0 \cdot 10^{-15}$ cm^2/s. To date no known measurements of HBr diffusion in ice exists, however as mentioned by Barnaal and Slotfeldt-Ellingsen [1983] due to the larger ionic radius and lower mobility of HBr compared to HCl, D_{HBr} is expected to be smaller than D_{HCl}. We insist on the fact that the diffusion coefficient determination has been performed only by the detection of the gas–phase whose results shows that this method is sensitive to ice morphology.

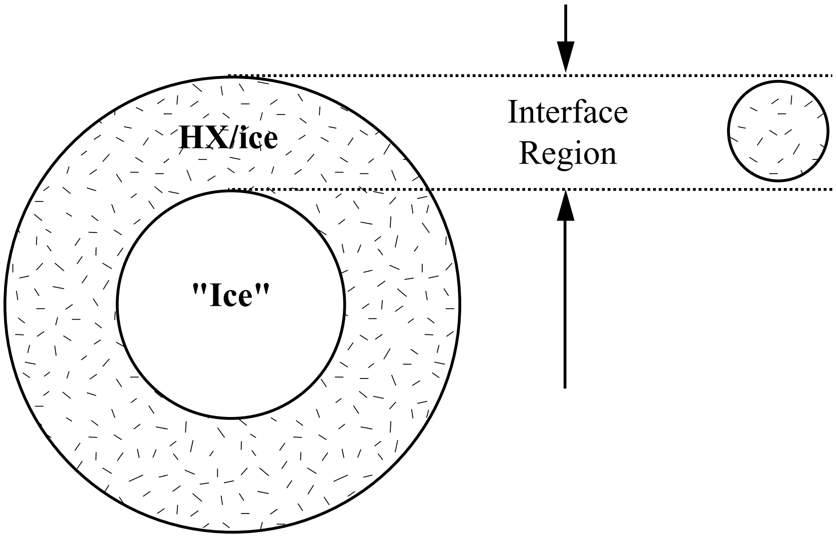

Figure 8.11: Schematic view of the composition of ice particles according to "Dope and Probe" experiments. The left particle whose diameter is larger than the interface region presents an external layer in which HX is present leaving the core of the particle "free" of HX. The right particle has a diameter smaller than the interfacial region suggesting that the whole particle constitutes the interface.

This large value measured for the HX/ice interface may be important for the branching ratio between heterogeneous hydrolysis on ice or reactions with HX. For particles of the size on the order of I (or less), the main process occurring during the particle lifetime will be the reaction with HX, thus liberating volatile halogen which may then photolysize leading to an increase of halogen atom concentrations. On the other hand, if the particle size is much larger than the interface thickness (such as in PSC type II [Turco, 1989]), heterogeneous hydrolysis may compete with halogen exchange reaction once the interface has been depleted in HX (Figure 8.11).

Outlook

The work presented in the former Chapters has been performed using the Knudsen flow reactor technique, which is a very well adapted technique for the study of fast heterogeneous reactions. This technique is based only on the gas phase detection with the use of a quadrupole mass spectrometer. However, the Knudsen cell apparatus should be coupled to FTIR detection, for instance, to obtain information on the behavior of the condensed phase during an uptake experiment in order to acquire a more complete understanding of the reaction mechanism. The coupled techniques would be of a great interest specially in regards to heterogeneous reactions taking place on ice surfaces where the exact composition of the condensed phase substrate should be determined in real–time.

As described in Chapter 4, the experiments performed involving $BrONO_2$ and $ClONO_2$ took place on dry salt substrates. However, in the marine environment salts are seldom dry. It would certainly be important to develop a new experiment in order to study heterogeneous reactions on deliquescent sea salts from the point of view of atmospheric implications. All the studies concerning heterogeneous reactions on salts have been obtained using bulk model surfaces under dry conditions. However, uptake experiments on aerosol particles with realistic relative humidity conditions should be more relevant to salt surfaces encountered in the marine boundary layer. The build up of a new experiment in which relative humidity, aerosol sizes and gaseous species could be controlled would be more representative of the conditions of the marine troposphere.

For a more realistic representation of marine tropospheric chemistry, one should perhaps performed additional runs by including more bromine reactions. For instance the fast heterogeneous reaction of NO_3 with KBr according to [Seisel, 1999]:

$$NO_3 + KBr \xrightarrow{\gamma = 0.2} Br + KNO_3 \tag{8.15}$$

should be adding.

To be able to better characterize the reaction mechanism of the heterogeneous reaction of $BrONO_2$ on ice doped with HBr, additional experiments need to be performed, especially a more systematic study of the dependence of the uptake kinetics of $BrONO_2$ as a function of the amount of HBr previously condensed on the ice substrate. More specifically, experiments performed with concurrent flows of $BrONO_2$ and HBr would be necessary to determine whether the reaction mechanism occurs through the direct halogen exchange reaction or whether the mechanism first goes through the hydrolysis of $BrONO_2$ leading to the formation of HOBr which may then react with HBr to produce Br_2 according to:

$$BrONO_2 + H_2O \rightarrow HOBr + HNO_3$$

$$HOBr + HBr \rightarrow Br_2 + H_2O$$

On the other hand, more work need to be done concerning the behavior of HBr in bulk ice, for instance in determining HBr diffusion coefficients in different types of ice which to date are not available.

To have a complete understanding of halogen release in the atmosphere, one should not forget iodine chemistry. Recent measurements of IO up to 6.6 ppt within the marine boundary layer at Mace Head (Ireland) [Stutz, 1999] and greater than 3.5 ppt at Tenerife (Canary Islands) [Allan, 2000] lead to a new interest in the role of iodine chemistry in the atmosphere. The study of iodine has already started in our laboratory with the study of the the interaction of HOI on substrates of atmospheric importance [Allanic, 2000b], but it should be important enough to study the behavior of $IONO_2$ on ice as well as on salt substrates to complete the halogen nitrate series ($ClONO_2$, $BrONO_2$). However, the challenge of the production of the gaseous reactant, $IONO_2$, still remains.

Appendix A

Methane Oxidation by OH-Radical

The oxidation of methane (CH_4) is of great importance for tropospheric photochemistry. Following the initial attack of OH on CH_4, the prevailing concentration of NO determines which oxidation pathway dominates.

In NO–rich environments, rapid formation of ozone (O_3) and formaldehyde (CH_2O) occurs.

$$CH_4 + OH \rightarrow CH_3 + H_2O \tag{A.1}$$

$$CH_3 + O_2 + M \rightarrow CH_3O_2 + M \tag{A.2}$$

$$CH_3O_2 + NO \rightarrow CH_3O + NO_2 \tag{A.3}$$

$$CH_3O + O_2 \rightarrow CH_2O + HO_2 \tag{A.4}$$

$$HO_2 + NO \rightarrow OH + NO_2 \tag{A.5}$$

$$2[NO_2 + h\nu(\lambda < 420nm) \rightarrow NO + O] \tag{A.6}$$

$$2[O + O_2 + M \rightarrow O_3 + M] \tag{A.7}$$

This reaction scheme leads to the following net reaction:

$$CH_4 + 4O_2 \rightarrow CH_2O + H_2O + O_3 \tag{A.8}$$

In NO–poor environments, CH_4 is oxidized to CH_2O by either of the following pathways:

Pathway 1:

$$CH_4 + OH \rightarrow CH_3 + H_2O \tag{A.9}$$

$$CH_3 + O_2 + M \rightarrow CH_3O_2 + M \tag{A.10}$$

$$CH_3O_2 + HO_2 \rightarrow CH_3O_2H + O_2 \tag{A.11}$$

$$CH_3O_2H + h\nu(\lambda < 330nm) \rightarrow CH_3O + OH \tag{A.12}$$

$$CH_3O + O_2 \rightarrow CH_2O + HO_2 \tag{A.13}$$

This pathway leads to the following net reaction:

$$CH_4 + O_2 \rightarrow CH_2O + H_2O \tag{A.14}$$

Pathway 2:

$$CH_4 + OH \rightarrow CH_3 + H_2O \tag{A.15}$$

$$CH_3 + O_2 + M \rightarrow CH_3O_2 + M \tag{A.16}$$

$$CH_3O_2 + HO_2 \rightarrow CH_3O_2H + O_2 \tag{A.17}$$

$$CH_3O_2H + OH \rightarrow CH_2O + H_2O + OH \tag{A.18}$$

This last pathway leads to the following net reaction:

$$CH_4 + OH + HO_2 \rightarrow CH_2O + 2H_2O \tag{A.19}$$

The oxidation pathways in NO–poor environment are therefore, more complex than in NO–rich environment, but it is clear that OH radical is being lost.

Appendix B

Kinetic Results of $BrONO_2$ and $ClONO_2$ on Salt Surfaces

This Appendix presents the details of all the different experiments performed in the Knudsen cell reactor in the study of the heterogeneous reactions of $BrONO_2$ and $ClONO_2$ as gaseous reactants and salt samples.

Table B.1: Kinetics (Section a), product yields (Section b) and hydrolysis yields (Section c) of $BrONO_2$/NaCl system.

Salt	Mass	Flow	Concentration	Dose	Orifice	k_{uni}	γ_0		Yields	
Type	[g]	[molec. s^{-1}]	[molec. cm^{-3}]	[molec.]	[mm]	[s^{-1}]		BrCl	Br_2	HCl
Section a										
Grain	6.1	$9.1 \cdot 10^{14}$	$2.0 \cdot 10^{11}$		14	20	0.40			
Grain	6.1	$1.1 \cdot 10^{15}$	$2.4 \cdot 10^{11}$		14	13	0.26			
Grain	6.1	$1.2 \cdot 10^{15}$	$2.7 \cdot 10^{11}$		14	30	0.59			
Grain	12.0	$1.2 \cdot 10^{15}$	$2.7 \cdot 10^{11}$		14	24	0.47			
Grain	1.5	$1.3 \cdot 10^{15}$	$2.9 \cdot 10^{11}$		14	21	0.42			
Grain	2.0	$1.3 \cdot 10^{15}$	$2.9 \cdot 10^{11}$		14	16	0.31			
Grain	6.1	$1.3 \cdot 10^{15}$	$2.9 \cdot 10^{11}$		14	18	0.35			
Grain	4.0	$1.4 \cdot 10^{11}$	$3.1 \cdot 10^{11}$		14	22	0.43			
Grain	6.0		$4.4 \cdot 10^{11}$	$8.0 \cdot 10^{14}$	14	7	0.14			
Grain	6.1	$2.4 \cdot 10^{15}$	$5.3 \cdot 10^{11}$		14	19	0.37			
Grain	6.0	$2.5 \cdot 10^{15}$	$5.6 \cdot 10^{11}$		14	20	0.40			
Grain	6.1	$2.6 \cdot 10^{15}$	$5.8 \cdot 10^{11}$		14	16	0.32			
Grain	6.1	$3.0 \cdot 10^{15}$	$6.7 \cdot 10^{11}$		14	17	0.34			
Grain	6.1	$3.7 \cdot 10^{15}$	$8.2 \cdot 10^{11}$		14	14	0.28			
Grain	8.1	-	-		4	8.5	0.17			
Grain	6.0	-	-		14	13	0.26			
Grain	8.1	-	-		14	13	0.26			
Powder (a)	5.0	$1.4 \cdot 10^{15}$	$3.1 \cdot 10^{11}$		14	15	0.30			
Powder (a)	10.0	-	-		14	16.5	0.33			
Powder (a)	10.0	-	-		14	16	0.32			
Powder (b)	5.0	$1.5 \cdot 10^{15}$	$3.3 \cdot 10^{11}$		14	25	0.50			

to be continued

Salt Type	Mass [g]	Flow [molec. s^{-1}]	Concentration [molec. cm^{-3}]	Dose [molec.]	Orifice [mm]	k_{uni} [s^{-1}]	γ_0	Yields BrCl	Br_2	HCl
Film	0.004	$7.0 \cdot 10^{14}$	$1.6 \cdot 10^{11}$		14	16	0.31			
Film	0.003	$1.4 \cdot 10^{15}$	$3.1 \cdot 10^{11}$		14	18	0.36			
Film	0.007	-	-		14	10.5	0.21			
Film	0.005	-	-		14	23	0.46			
Film	0.003	-	-		14	13.5	0.27			
Film	0.004	-	-		14	15.5	0.31			
Film (c)	0.008	$9.5 \cdot 10^{14}$	$2.1 \cdot 10^{11}$		14	20	0.40			
Section b										
Grain	6.0	$1.1 \cdot 10^{15}$	$5.1 \cdot 10^{11}$		8	14.5	0.29	1.10	0.03	
Grain	6.0	$4.5 \cdot 10^{15}$	$2.1 \cdot 10^{11}$		8	19	0.38	0.92	0.08	
Grain	6.0	$1.4 \cdot 10^{15}$	$2.6 \cdot 10^{11}$		4	9.5	0.19	0.50	0.11	
Grain	6.0	$2.5 \cdot 10^{15}$	$4.6 \cdot 10^{11}$		4	8.5	0.17	0.45	0.05	
Film	0.002	$1.7 \cdot 10^{15}$	$3.8 \cdot 10^{11}$		14	14	0.28	0.61	0.10	
Film (c)	0.003	$6.0 \cdot 10^{14}$	$1.3 \cdot 10^{11}$		14	26	0.52	0.60	0.14	
Film (c)	0.003	$1.7 \cdot 10^{15}$	$3.8 \cdot 10^{11}$		14	9	0.18	0.65	0.20	
Film (c)	0.003	$1.9 \cdot 10^{15}$	$4.2 \cdot 10^{11}$		14	13	0.26	0.67	0.15	
Section c										
Grain	7.5	$1.0 \cdot 10^{15}$	$2.2 \cdot 10^{11}$		14	15	0.30	0.75	0.09	0.20
Grain	8.0	$1.2 \cdot 10^{15}$	$2.7 \cdot 10^{11}$		14	10	0.20	0.84	0.03	0.20
Grain	8.0	$2.0 \cdot 10^{15}$	$4.4 \cdot 10^{11}$		14	12.5	0.25	0.88	0.04	0.18
Grain	7.5	$1.1 \cdot 10^{15}$	$5.1 \cdot 10^{11}$		8	10	0.20	1.10	0.03	0.21
Grain	8.0	$1.5 \cdot 10^{15}$	$6.9 \cdot 10^{11}$		8	17	0.34	0.93	0.04	0.21
Grain	8.0	$1.9 \cdot 10^{15}$	$8.8 \cdot 10^{11}$		8	14	0.28	1.00	0.03	0.25
Powder (a)	6.0		$2.6 \cdot 10^{11}$	$4.7 \cdot 10^{14}$	14	15	0.30	0.45	0.06	0.22
Powder (a)	6.0		$6.1 \cdot 10^{11}$	$1.1 \cdot 10^{15}$	8	11	0.22	0.25	0.08	0.40
Window		$1.3 \cdot 10^{15}$	$2.9 \cdot 10^{11}$		14	12.5	0.25	0.48	0.08	0.13
Window		$1.3 \cdot 10^{15}$	$6.0 \cdot 10^{11}$		8	9.5	0.19	0.38	0.19	0.13
Window		$2.9 \cdot 10^{15}$	$6.4 \cdot 10^{11}$		14	7.5	0.15	0.40	0.02	0.10

(a) NaCl-particle size between 36 and 100 μm.

(b) NaCl-particle size $\leq$ 36 μm.

(c) After heating to 550 K.

Table B.2: Kinetics (Section a), product yields (Section b) and hydrolysis yields (Section c) of $BrONO_2$/KBr system.

Salt	Mass	Flow	Concentration	Dose	Orifice	k_{uni}	γ_0	Yields	
Type	[g]	[molec. s^{-1}]	[molec. cm^{-3}]	[molec.]	[mm]	[s^{-1}]		Br_2	HBr
Section a									
Grain	6.0	$2.3 \cdot 10^{14}$	$5.1 \cdot 10^{10}$		14	17	0.34		
Grain	-	$2.7 \cdot 10^{14}$	$6.0 \cdot 10^{10}$		14	12.5	0.25		
Grain	8.0	-	-		14	25	0.50		
Grain	7.0	-	-		14	15.5	0.31		
Window		$1.3 \cdot 10^{15}$	$2.9 \cdot 10^{11}$		14	10	0.20		
Section b									
Grain	6.0	$4.0 \cdot 10^{14}$	$8.9 \cdot 10^{10}$		14	16	0.32	0.70	
Grain	6.0	$5.4 \cdot 10^{14}$	$1.2 \cdot 10^{11}$		14	20	0.40	0.72	
Grain	6.0	$6.4 \cdot 10^{14}$	$1.4 \cdot 10^{11}$		14	24	0.48	0.66	
Grain	6.0	$1.1 \cdot 10^{15}$	$2.4 \cdot 10^{11}$		14	21	0.42	0.47	
Grain	6.0	$6.5 \cdot 10^{14}$	$3.0 \cdot 10^{11}$		8	13	0.25	0.59	
Grain	6.0	$1.5 \cdot 10^{15}$	$3.3 \cdot 10^{11}$		14	19	0.38	0.60	
Grain	6.0	$1.7 \cdot 10^{15}$	$3.8 \cdot 10^{11}$		14	25	0.50	0.56	
Grain	6.0	$1.2 \cdot 10^{15}$	$5.3 \cdot 10^{11}$		8	15	0.30	0.56	
Grain	6.0	$1.9 \cdot 10^{15}$	$8.8 \cdot 10^{11}$		8	22	0.44	0.50	
Grain	6.0		$4.1 \cdot 10^{12}$	$7.3 \cdot 10^{15}$	14	13.5	0.27	0.50	
Grain	6.0		$6.1 \cdot 10^{12}$	$1.1 \cdot 10^{16}$	14	18	0.36	0.51	
Grain	6.0		$6.7 \cdot 10^{12}$	$1.2 \cdot 10^{16}$	14	19	0.38	0.52	
Grain	6.0		$7.8 \cdot 10^{12}$	$1.4 \cdot 10^{16}$	8	21.5	0.43	0.45	
Grain	6.0		$1.3 \cdot 10^{13}$	$2.4 \cdot 10^{16}$	8	14.5	0.29	0.40	
Grain	6.0		$1.7 \cdot 10^{13}$	$3.0 \cdot 10^{16}$	8	12.5	0.25	0.61	
Grain	6.0		$1.7 \cdot 10^{13}$	$3.0 \cdot 10^{16}$	8	11.5	0.23	0.50	
Film	0.006	$6.2 \cdot 10^{14}$	$1.4 \cdot 10^{11}$		14	15	0.30	0.75	
Film	0.003		$2.0 \cdot 10^{12}$	$3.6 \cdot 10^{15}$	14	12	0.24	0.30	
Film (a)	0.006	$6.6 \cdot 10^{14}$	$1.5 \cdot 10^{11}$		14	17.5	0.35	0.30	
Section c									
Grain	10.0	$9.0 \cdot 10^{14}$	$2.0 \cdot 10^{11}$		14	15	0.30	0.70	0.11
Grain	8.1		$2.9 \cdot 10^{11}$	$5.3 \cdot 10^{14}$	14	8	0.16	0.40	n. o. (b)
Grain	10.0	$1.5 \cdot 10^{15}$	$3.3 \cdot 10^{11}$		14	20.5	0.41	0.66	0.10
Grain	7.0	$2.2 \cdot 10^{15}$	$4.9 \cdot 10^{11}$		14	18.5	0.37	0.50	0.04
Grain	10.0	$2.6 \cdot 10^{15}$	$5.8 \cdot 10^{11}$		14	14	0.28	0.60	0.06
Grain	7.0	$1.4 \cdot 10^{15}$	$6.5 \cdot 10^{11}$		8	10.5	0.21	0.84	0.11
Grain	10.0	$2.1 \cdot 10^{15}$	$1.6 \cdot 10^{12}$		14	10	0.20	0.52	0.05
Film	0.007	$1.6 \cdot 10^{15}$	$3.6 \cdot 10^{11}$		14	14	0.28	0.50	0.10
Film (a)	0.006	$1.6 \cdot 10^{15}$	$3.6 \cdot 10^{11}$		14	11	0.22	0.52	0.11

(a) After heating to 550 K.

(b) n. o. = not observed.

Table B.3: Experimental Results of $ClONO_2$ interacting with NaCl (section a) and KBr (section b).

Salt Type	Mass [g]	Flow [molec. s^{-1}]	Concentration [molec. cm^{-3}]	Dose [molec.]	Orifice [mm]	k_{uni} [s^{-1}]	γ_0	Yields		
								Cl_2	HCl	
				Section a						
Grain	10		$2.0 \cdot 10^{11}$	$3.6 \cdot 10^{14}$	4	2.6	0.04	120%	21%	
Grain	7	$2.4 \cdot 10^{14}$	$2.7 \cdot 10^{11}$		4	2.8	0.04	90%	n.d	
Grain	10		$2.7 \cdot 10^{11}$	$4.9 \cdot 10^{14}$	4	7.2	0.11	114%	20%	
Powder (a)	6	$6.8 \cdot 10^{14}$	$7.6 \cdot 10^{11}$		4	6.8	0.10	95%	n.d.	
Grain	10		$9.0 \cdot 10^{11}$	$1.6 \cdot 10^{15}$	4	2.6	0.04	115%	24%	
Grain	7	$8.8 \cdot 10^{14}$	$9.8 \cdot 10^{11}$		4	4.1	0.06	105%	n.d.	
Grain	7	$1.3 \cdot 10^{15}$	$1.4 \cdot 10^{12}$		4	3.4	0.05	100%	n.d.	
Powder (a)	6	$3.5 \cdot 10^{14}$	$1.3 \cdot 10^{11}$		8	10.2	0.15	110%	n.d.	
Powder (a)	6	$5.0 \cdot 10^{14}$	$9.2 \cdot 10^{10}$		14	20.4	0.30	80%	n.d.	
								Br_2	Cl_2	BrCl
				Section b						
Powder (b)	4.5	$1.4 \cdot 10^{14}$	$1.6 \cdot 10^{11}$		4	5.1	0.08	105%	n.o.	n.o.
Powder (b)	5.5	$2.6 \cdot 10^{14}$	$2.9 \cdot 10^{11}$		4	6.5	0.10	110%	n.o.	n.o.
Powder (b)	5.5	$4.4 \cdot 10^{14}$	$4.9 \cdot 10^{11}$		4	5.4	0.08	80%	n.o.	n.o.
Powder (b)	5.5	$8.5 \cdot 10^{14}$	$9.4 \cdot 10^{11}$		4	8.2	0.12	71%	n.o.	6%
Powder (b)	5.5	$2.1 \cdot 10^{15}$	$2.3 \cdot 10^{12}$		4	7.5	0.11	50%	20%	6%
Powder (b)	5.5	$2.5 \cdot 10^{15}$	$2.8 \cdot 10^{12}$		4	8.8	0.13	35%	40%	15%
Powder (b)	5.5	$2.6 \cdot 10^{15}$	$2.9 \cdot 10^{12}$		4	8.8	0.13	44%	34%	14%
Powder (b)	5.5	$2.2 \cdot 10^{14}$	$8.2 \cdot 10^{10}$		8	12.2	0.18	64%	19%	8%
Powder (b)	5.5	$3.1 \cdot 10^{14}$	$1.2 \cdot 10^{11}$		8	17.4	0.26	66%	n.o.	12%
Powder (b)	8.0	$2.2 \cdot 10^{14}$	$3.0 \cdot 10^{11}$		8	15.0	0.22	50%	22%	15%
Powder (b)	5.5	$1.9 \cdot 10^{15}$	$6.9 \cdot 10^{11}$		8	11.6	0.17	40%	48%	24%
Powder (b)	5.5	$2.3 \cdot 10^{15}$	$8.5 \cdot 10^{11}$		8	14.3	0.21	37%	40%	21%
Powder (b)	5.5	$8.4 \cdot 10^{13}$	$1.6 \cdot 10^{10}$		14	12.2	0.18	60%	15%	17%
Powder (b)	5.5	$4.1 \cdot 10^{14}$	$7.6 \cdot 10^{10}$		14	15.6	0.23	52%	18%	24%
Powder (b)	5.5	$4.4 \cdot 10^{14}$	$8.1 \cdot 10^{10}$		14	21.1	0.31	46%	n.o.	13%
Powder (b)	5.5	$1.0 \cdot 10^{15}$	$1.9 \cdot 10^{11}$		14	19.7	0.29	44%	18%	20%
Powder (b)	5.5	$1.5 \cdot 10^{15}$	$2.7 \cdot 10^{11}$		14	15.0	0.22	37%	17%	28%
Powder (b)	5.5	$2.8 \cdot 10^{15}$	$5.1 \cdot 10^{11}$		14	17.0	0.25	35%	20%	26%

(a) NaCl-powder of average size range 35–160 μm.

(b) KBr-powder of average size range 160–250 μm.

n.d. = not determined.

n.o. = not observed.

Table B.4: Results of steady state experiments of $ClONO_2$ interacting with Na_2SO_4 (section a) and $NaNO_3$ (section b).

Salt Type	Mass [g]	Flow [molec. s^{-1}]	Concentration [molec. cm^{-3}]	Orifice [mm]	k_{uni} [s^{-1}]	γ_0	Product Cl_2	Yields HOCl
			Section a					
Grain	7	$5.0 \cdot 10^{14}$	$5.6 \cdot 10^{11}$	4	4.8	0.07	22%	n.o.
Grain	7	$8.0 \cdot 10^{14}$	$1.5 \cdot 10^{11}$	14	19.7	0.29	25%	n.o.
Grain (a)	6	$9.6 \cdot 10^{14}$	$1.1 \cdot 10^{12}$	4	6.8	0.10	33%	12%
Grain (a)	10	$1.0 \cdot 10^{14}$	$1.9 \cdot 10^{10}$	14	24.5	0.36	25%	n.d.
Grain (a)	8	$5.8 \cdot 10^{14}$	$1.1 \cdot 10^{11}$	14	16.3	0.24	24%	n.d.
Grain (a)	8	$7.4 \cdot 10^{14}$	$1.4 \cdot 10^{11}$	14	12.2	0.18	30%	n.d.
Grain (a)	6	$8.0 \cdot 10^{14}$	$1.5 \cdot 10^{11}$	14	25.8	0.38	35%	10%
			Section b					
Powder	6	$1.8 \cdot 10^{14}$	$3.3 \cdot 10^{10}$	14	25.2	0.37	n.o.	n.o.
Powder	15	$3.2 \cdot 10^{14}$	$5.9 \cdot 10^{10}$	14	11.6	0.17	n.o.	n.o.
Powder (a)	7	$1.2 \cdot 10^{15}$	$1.3 \cdot 10^{12}$	4	1.4	0.02	30%	n.o.
Powder (a)	12	$4.5 \cdot 10^{14}$	$8.3 \cdot 10^{10}$	14	16.3	0.24	21%	n.o.

(a) Salt has been pumped for 5minutes prior to experiment.

n.d. = not determined, n.o. = not observed.

Appendix C

Parameters Used in the Tropospheric Box Model

This Appendix presents the different reactions taken into account in the tropospheric box model presented in Chapter 5 and their rate constant or γ value.

Table C.1: Forward rate constants, k, used in the model calculated at 300 K [NASA, 1997]. The units for bimolecular and termolecular reactions are cm^3 s^{-1} and cm^6 s^{-1}, respectively. The backward rate constant is defined by the thermodynamics.

Reaction	k
$O_2 + O^1(D) \rightleftarrows O_2 + O$	$4.0 \cdot 10^{-11}$
$O^1(D) + N_2 \rightleftarrows O + N_2$	$2.6 \cdot 10^{-11}$
$O_2 + O + M \rightleftarrows O_3 + M$	$6.0 \cdot 10^{-34}$
$O^1(D) + H_2O \rightleftarrows 2OH$	$2.2 \cdot 10^{-10}$
$O + O_3 \rightleftarrows 2O_2$	$8.0 \cdot 10^{-15}$
$OH + O_3 \rightleftarrows HO_2 + O_2$	$6.8 \cdot 10^{-14}$
$HO_2 + O_3 \rightleftarrows OH + 2O_2$	$2.0 \cdot 10^{-15}$
$HO_2 + NO \rightleftarrows OH + NO_2$	$8.1 \cdot 10^{-12}$
$NO_2 + O \rightleftarrows NO + O_2$	$9.7 \cdot 10^{-12}$
$NO_2 + NO_3 + M \rightleftarrows N_2O_5 + M$	$5.0 \cdot 10^{-32}$
$NO + O_3 \rightleftarrows NO_2 + O_2$	$1.8 \cdot 10^{-14}$
$OH + NO + M \rightleftarrows HONO + M$	$4.9 \cdot 10^{-12}$
$OH + HO_2 \rightleftarrows H_2O + O_2$	$1.1 \cdot 10^{-10}$

continued

Reaction	k
$OH + NO_2 + M \rightleftarrows HNO_3 + M$	$3.3 \cdot 10^{-31}$
$NO_3 + NO \rightleftarrows 2NO_2$	$2.6 \cdot 10^{-11}$
$H_2O_2 + OH \rightleftarrows H_2O + HO_2$	$1.7 \cdot 10^{-12}$
$O + NO + M \rightleftarrows NO_2 + M$	$1.7 \cdot 10^{-12}$
$O + NO_2 + M \rightleftarrows NO_3 + M$	$1.6 \cdot 10^{-12}$
$O_3 + NO_2 \rightleftarrows NO_3 + O_2$	$3.2 \cdot 10^{-17}$
$OH + NO_3 \rightleftarrows NO_2 + HO_2$	$2.2 \cdot 10^{-12}$
$N_2O_5 \rightleftarrows NO_2 + NO_3$	$4.4 \cdot 10^{-2}$
$CO + OH \rightleftarrows CO_2 + H$	$2.4 \cdot 10^{-13}$
$H + O_2 + M \rightleftarrows HO_2 + M$	$1.4 \cdot 10^{-12}$
$HCO + O_2 \rightleftarrows HO_2 + CO$	$5.5 \cdot 10^{-12}$
$CH_4 + OH \rightleftarrows CH_3 + H_2O$	$6.3 \cdot 10^{-15}$
$CH_3 + O_2 + M \rightleftarrows CH_3O_2 + M$	$4.3 \cdot 10^{-32}$
$CH_3O_2 + NO \rightleftarrows CH_3O + NO_2$	$7.7 \cdot 10^{-12}$
$CH_3O + NO_2 \rightleftarrows CH_2O + HONO$	$2.0 \cdot 10^{-13}$
$CH_3O_2 + NO_2 + M \rightleftarrows CH_3O_2NO_2 + M$	$8.5 \cdot 10^{-12}$
$CH_3O + O_2 \rightleftarrows HO_2 + CH_2O$	$1.9 \cdot 10^{-15}$
$CH_2O + OH \rightleftarrows H_2O + HCO$	$1.1 \cdot 10^{-11}$
$C_2H_6 + OH \rightleftarrows C_2H_5 + H_2O$	$2.4 \cdot 10^{-13}$
$C_2H_5 + O_2 + M \rightleftarrows C_2H_5O_2 + M$	$7.5 \cdot 10^{-12}$
$C_2H_5O_2 + HO_2 \rightleftarrows C_2H_5OOH + O_2$	$7.7 \cdot 10^{-12}$
$C_2H_5O_2 + NO \rightleftarrows C_2H_5O + NO_2$	$8.7 \cdot 10^{-12}$
$C_2H_5O + NO_2 + M \rightleftarrows C_2H_5ONO_2 + M$	$2.7 \cdot 10^{-11}$
$C_2H_5O + O_2 \rightleftarrows CH_3HCO + HO_2$	$9.5 \cdot 10^{-15}$
$CH_3HCO + OH \rightleftarrows CH_3CO + H_2O$	$1.4 \cdot 10^{-11}$
$CH_3CO + O_2 \rightleftarrows CH_3COO_2$	$5.0 \cdot 10^{-12}$
$CH_3COO_2 + NO \rightleftarrows CH_3 + CO_2 + NO_2$	$1.8 \cdot 10^{-11}$
$CH_3COO_2 + NO_2 + M \rightleftarrows CH_3CO_3NO_2 + M$	$8.5 \cdot 10^{-12}$
Chlorine chemistry	
$ClO + O \rightleftarrows Cl + O_2$	$3.8 \cdot 10^{-11}$
$ClO + NO_2 + M \rightleftarrows ClONO_2 + M$	$2.0 \cdot 10^{-12}$
$ClO + HO_2 \rightleftarrows HOCl + O_2$	$5.0 \cdot 10^{-12}$
$ClO + NO \rightleftarrows Cl + NO_2$	$1.7 \cdot 10^{-11}$

continued

Reaction	k
$ClO + ClO + M \rightleftarrows Cl_2O_2 + M$	$2.9 \cdot 10^{-13}$
$ClO + ClO \rightleftarrows Cl_2 + O_2$	$4.8 \cdot 10^{-15}$
$ClO + ClO \rightleftarrows OClO + Cl$	$3.5 \cdot 10^{-15}$
$ClO + ClO \rightleftarrows ClOO + Cl$	$8.0 \cdot 10^{-15}$
$OClO + O \rightleftarrows ClO + O_2$	$1.0 \cdot 10^{-13}$
$OClO + OH \rightleftarrows HOCl + O_2$	$6.8 \cdot 10^{-12}$
$HOCl + OH \rightleftarrows H_2O + ClO$	$5.0 \cdot 10^{-13}$
$ClNO_2 + OH \rightleftarrows HOCl + NO_2$	$3.6 \cdot 10^{-14}$
$HCl + OH \rightleftarrows Cl + H_2O$	$8.0 \cdot 10^{-13}$
$Cl + O_3 \rightleftarrows ClO + O_2$	$1.2 \cdot 10^{-11}$
$Cl + HO_2 \rightleftarrows HCl + O_2$	$3.2 \cdot 10^{-11}$
$Cl + HO_2 \rightleftarrows ClO + OH$	$9.1 \cdot 10^{-12}$
$Cl + H_2 \rightleftarrows HCl + H$	$1.6 \cdot 10^{-14}$
$Cl + O_2 + M \rightleftarrows ClOO + M$	$2.7 \cdot 10^{-33}$
$Cl + CH_4 \rightleftarrows HCl + CH_3$	$1.0 \cdot 10^{-13}$
$Cl + C_2H_6 \rightleftarrows HCl + C_2H_5$	$5.7 \cdot 10^{-11}$
$Cl + CH_2O \rightleftarrows HCl + HCO$	$7.3 \cdot 10^{-11}$
$Cl + NO_2 + M \rightleftarrows ClNO_2 + M$	$2.9 \cdot 10^{-12}$
$Cl + NO_3 \rightleftarrows ClO + NO_2$	$2.4 \cdot 10^{-11}$
$Cl + CH_3O_2 \rightleftarrows ClO + CH_3O$	$1.6 \cdot 10^{-10}$
$Cl + C_2H_5O_2 \rightleftarrows ClO + C_2H_5O$	$7.4 \cdot 10^{-11}$
$Cl + C_2H_5O_2 \rightleftarrows HCl + C_2H_4O_2$	$7.7 \cdot 10^{-11}$
$Cl + H_2O_2 \rightleftarrows HCl + HO_2$	$4.1 \cdot 10^{-13}$
Bromine Chemistry	
$Br + O_3 \rightleftarrows BrO + O_2$	$1.2 \cdot 10^{-12}$
$Br + HO_2 \rightleftarrows HBr + O_2$	$2.0 \cdot 10^{-12}$
$HBr + OH \rightleftarrows Br + H_2O$	$1.1 \cdot 10^{-11}$
$HBr + O \rightleftarrows Br + OH$	$3.8 \cdot 10^{-14}$
$Br_2 + OH \rightleftarrows HOBr + Br$	$4.2 \cdot 10^{-11}$
$HOBr + O \rightleftarrows OH + BrO$	$2.8 \cdot 10^{-11}$
$BrO + NO \rightleftarrows Br + NO_2$	$2.1 \cdot 10^{-11}$
$BrO + O \rightleftarrows Br + O_2$	$4.1 \cdot 10^{-11}$
$BrO + BrO \rightleftarrows 2Br + O_2$	$2.7 \cdot 10^{-12}$

continued

Reaction	k
$BrO + BrO \rightleftarrows Br_2 + O_2$	$5.0 \cdot 10^{-13}$
$BrO + ClO \rightleftarrows BrCl + O_2$	$1.0 \cdot 10^{-12}$
$BrO + ClO \rightleftarrows Br + OClO$	$6.8 \cdot 10^{-12}$
$BrO + ClO \rightleftarrows Br + ClOO$	$6.1 \cdot 10^{-12}$
$BrO + NO_2 + M \rightleftarrows BrONO_2 + M$	$4.3 \cdot 10^{-12}$
$BrO + HO_2 \rightleftarrows HOBr + O_2$	$2.1 \cdot 10^{-11}$
$BrO + O_3 \rightleftarrows Br + 2O_2$	$2.0 \cdot 10^{-17}$
$BrO + OH \rightleftarrows Br + HO_2$	$7.5 \cdot 10^{-11}$
Additional reactions	
$OH + HNO_3 + M \rightleftarrows NO_3 + H_2O + M$	$1.0 \cdot 10^{-13}$
$Br + CH_2O \rightleftarrows HBr + HCO$	$1.1 \cdot 10^{-12}$

Table C.2: Photolysis rate constants, J, used in the model. The values refer to ground level, 30°N on the first of January calculated at local noon.

Reaction	J [s^{-1}]	Reaction	J [s^{-1}]
$O_3 \rightarrow O + O_2$	$5.0 \cdot 10^{-4}$	$O_3 \rightarrow O^1(D) + O_2$	$2.0 \cdot 10^{-5}$
$NO_2 \rightarrow NO + O$	$1.0 \cdot 10^{-2}$	$NO_3 \rightarrow NO_2 + O$	$1.8 \cdot 10^{-1}$
$NO_3 \rightarrow NO + O_2$	$2.0 \cdot 10^{-2}$	$N_2O_5 \rightarrow NO_3 + NO_2$	$2.0 \cdot 10^{-5}$
$HONO \rightarrow OH + NO$	$3.2 \cdot 10^{-3}$	$HNO_3 \rightarrow NO_2 + OH$	$7.0 \cdot 10^{-7}$
$HCl \rightarrow Cl + H$	$4.9 \cdot 10^{-8}$	$Cl_2 \rightarrow 2Cl$	$1.2 \cdot 10^{-3}$
$ClO \rightarrow Cl + O$	$6.2 \cdot 10^{-5}$	$Cl_2O_2 \rightarrow Cl + OClO$	$1.5 \cdot 10^{-3}$
$HOCl \rightarrow Cl + OH$	$2.0 \cdot 10^{-4}$	$ClNO_2 \rightarrow Cl + NO_2$	$6.2 \cdot 10^{-4}$
$ClONO_2 \rightarrow Cl + NO_3$	$8.8 \cdot 10^{-5}$	$BrCl \rightarrow Cl + Br$	$1.7 \cdot 10^{-2}$
$HBr \rightarrow H + Br$	$4.9 \cdot 10^{-6}$	$Br_2 \rightarrow 2Br$	$1.5 \cdot 10^{-2}$
$BrO \rightarrow Br + O$	$5.0 \cdot 10^{-2}$	$HOBr \rightarrow Br + OH$	$1.3 \cdot 10^{-3}$
$BrNO_2 \rightarrow Br + NO_2$	$9.4 \cdot 10^{-3}$	$BrONO_2 \rightarrow Br + NO_3$	$1.1 \cdot 10^{-3}$
$H_2O_2 \rightarrow 2OH$	$1.9 \cdot 10^{-5}$	$CH_2O \rightarrow H_2 + CO$	$7.9 \cdot 10^{-5}$
$CH_2O \rightarrow H + HCO$	$6.1 \cdot 10^{-5}$		

C.1 Program Listing without Surface Saturation

```
      PROGRAM CALCUL

C     Application du programme chemkin à la chimie hétérogène sur les sels
C
C                                            François CALOZ, 1999
C                                            Arnaud AGUZZI,  1999
C
      IMPLICIT DOUBLE PRECISION (A-H,O-Z), INTEGER(I-N)
C
C ====================================================================
C
C     ==============
C     1 DECLARATIONS
C     ==============
c     PARAMETER (LENIWK=5000, LENRWK=5000, LENCWK=500, NK=5, NLMAX=55,
c     1   LRW=5000, LIW=100, LIN=5, LOUT=6, LINCK=25, FOUT=26,AOUT=27
c     2         , KMAX=50,LOUT2=10)
      PARAMETER (LENIWK=10000, LENRWK=10000, LENCWK=500, NK=5, NLMAX=55,
      1   LRW=10000, LIW=100, LIN=5, LOUT=6, LINCK=25, FOUT=26,AOUT=27
      2         , KMAX=65,LOUT2=10)
      DOUBLE PRECISION ATOL, RPAR, RTOL, RWORK, T, TOUT, Y
      DIMENSION Z(KMAX), ELWRK(LRW), IELWRK(LIW)
      COMMON /PARAMR/ RCKWRK(10000), P,RU,WT(65),WDOT(65),H(65),X(65), T
      1   ,ANGLE, PHOTO(30), HET(30), HET2(30), ANA(200,65,10),CST(100),
      2    ALAT,ALONG
      3  ,XTOT, ChHet(12), VarJ(40,4),Surface
      COMMON /PARAMI/ ICKWRK(10000), KK, MM,NbrPhoto,NbrHet, MONAT(12)
      CHARACTER  CCKWRK(LENCWK)*16,KSYM(KMAX)*16, LIGNE*20, SPEC*16,
      1         REACTION*24
      LOGICAL KERR, IERR
      EXTERNAL FUN
      DATA KERR/.FALSE./, X/KMAX*0.0/, KSYM/KMAX*' '/
      DATA (MONAT(I),I=1,12) /31,28,31,30,31,30,31,31,30,31,30,31/
      REAL batman
```

```
C     ===================================================
C     2 OUVERTURE DU FICHIER PROVENANT DE L'INTERPRETEUR
C     ===================================================

      OPEN (LINCK, FORM='UNFORMATTED', file='cklink')

C     ===========================
C     3 INITIALISATION DE CHEMKIN
C     ===========================
C MM est le nombre d'élements formant les différentes espèces
C KK est le nombre d'espèces différentes
C II est le nombre total de réactions dans le modèle
C -------------------------------------------------------------
      CALL CKINIT (LENIWK, LENRWK, LENCWK, LINCK, LOUT, ICKWRK,
     1             RCKWRK, CCKWRK)
      CALL CKINDX (ICKWRK, RCKWRK, MM, KK, II, NFIT)
      IF (KK .GT. KMAX) THEN
         WRITE (LOUT, *)
     1   ' Species dimension too small...must be at least ',KK
         STOP
      ENDIF
      CALL CKSYMS (CCKWRK, LOUT, KSYM, IERR)
      IF (IERR) KERR = .TRUE.
      CALL CKWT   (ICKWRK, RCKWRK, WT)
      CALL CKRP   (ICKWRK, RCKWRK, RU, RUC, PATM)

C     =========================
C     4 LECTURE DU FICHIER INIT
C     =========================
        OPEN (1, FORM='FORMATTED', file='init')
C       4.1  Lecture des conditions générales
C       --------------------------------------
          READ (1,7216) Ligne
          READ (1,7216) Ligne
C         Nbr de reaction photochimiques et hétérogènes
```

```
C         ---------------------------------------------
            READ (1,7216) Ligne
            READ (1,7217) NbrPhoto,NbrHet
C           Enregistrement des constantes photochimiques
C       WRITE (28, 7217) NbrPhoto,NbrHet
            DO 18 i=1,NbrPhoto
               PHOTO(i)=RCKWRK(1+MM+KK*18+(i-1)*4)
18          CONTINUE
C           Enregistrement des constantes hétérogènes
C     ---------------------------------------------------
C     HET(I) : constante de vitesse de la reaction het I
C     HET2(I)/Nombre Avogadro : gamma de la reaction het I
C     ---------------------------------------------------
            DO 19 I=1,NbrHet
            HET(I)=RCKWRK(1+MM+KK*18+NbrPhoto*4+(I-1)*4)
      HET2(I)=RCKWRK(1+MM+KK*18+NbrPhoto*4+(I-1)*4)
               RCKWRK(1+MM+KK*18+NbrPhoto*4+(I-1)*4)=0
C     WRITE (31, 7251) HET(I),HET2(I)/6.023E+23
19          CONTINUE
C         Pression et temperature
C         -----------------------
            READ (1,7216) Ligne
            READ  (1,7249) PA, T
            P = PA*PATM
C       WRITE (28, 7250) PA, T, P
C         Latitude  Longitude
C         --------------------
            READ (1,7216) Ligne
            READ  (1,*) ALAT,ALONG
C         Concentrations initiales
C         -----------------------
            READ (1,7216) Ligne
C           Initialisation à zéro
        DO 44 K = 1, KK
          X(K)=0
                IF (CCKWRK(MM+K) .EQ. "NACL") THEN
```

```
                  ChHet(6)=K
                ENDIF
                IF (CCKWRK(MM+K) .EQ. "KBR") THEN
                  ChHet(8)=K
                ENDIF
44            CONTINUE
C           Valeurs initiales des concentrations
              DO 46 K = 1, KK
                READ  (1,7230,ERR=47) SPEC, Concentration
          DO 45 I=MM+1,MM+KK
            IF (SPEC .EQ. CCKWRK(I)) THEN
              X(I-MM)=Concentration
C               WRITE (28, 7230) SPEC,Concentration
            ENDIF
45           CONTINUE
46            CONTINUE
C       4.2  Lecture des conditions de simulation
C       ------------------------------------------
            READ (1,7216) Ligne
47          READ (1,7216) Ligne
            READ (1,7216) Ligne
C         Debut et fin de la simulation
C         -----------------------------
            READ (1,7216) Ligne
            READ (1,7216) Ligne
            READ (1,*) NbrMoisD,NbrJourD,NbrMoisF,NbrJourF
C           WRITE (28, 7217) NbrMoisD,NbrJourD
C           WRITE (28,7217)  NbrMoisF,NbrJourF
C         Pas de temps:  calcul et impression
C         ----------------------------------
            READ (1,7216) Ligne
            READ (1,7216) Ligne
            READ  (1,*) DT,DTPRINT
C           WRITE (28, 7250) DT, DTPRINT
C       4.3  Lecture des conditions pour la chimie hétérogène
C       -----------------------------------------------------
```

```
           READ (1,7216) Ligne
           READ (1,7216) Ligne
C        Surface et volume
C        ------------------
           READ (1,7216) Ligne
           READ (1,7216) Ligne
           READ  (1,*) Surface,ChHet(10)
C          WRITE (28, 7250) Surface,ChHet(10)
           ChHet(1)=0.0
C          ChHet(1) Scf en micromètre carré
C          ChHet(10) Volume en cc
           READ (1,7216) Ligne
           READ (1,7216) Ligne
           READ (1,7216) Ligne
C        Début et fin (Mois et Jour de la chimie hétérogène)
C        ---------------------------------------------------
           READ  (1,*) ChHet(2),ChHet(3),ChHet(4),ChHet(5)
C          WRITE (28, 7250) ChHet(2),ChHet(3),ChHet(4),ChHet(5)
C          ChHet(2) Mois du début de l'activation de la chimie hétérogène
C          ChHet(3) Jour du début de l'activation de la chimie hétérogène
C          ChHet(4) Mois de la fin de l'activation de la chimie hétérogène
C          ChHet(5) Jour de la fin de l'activation de la chimie hétérogène

      IF (KERR) STOP

C     ======================================================================
C     5 Modification des taux de photolyse en fonction de l'espèce et de la
C       latitude
C     ======================================================================

C     Le taux de photolyse de l'espèce i varie selon la loi:
C     phorat(i) = coef(i,1)  * cosz**coef(i,2) * exp(-coef(i,3)/cosz)

C     Les paramètres coeff(i,j) sont déterminés par le programme extraction.exe
C     qui construit un fichier contenant ces valeurs pour toutes les altitudes
C     et latitudes.
```

```
      OPEN (UNIT=2, NAME='f:\CHEMKIN\EXTRACTION\ESSAI1', STATUS='OLD')
READ (2,*) Ligne
READ (2,*) Ligne
READ (2,*) Ligne
      DO 60 i=1,NbrPhoto
  READ (2,7300) Reaction,VarJ(i,1),VarJ(i,2),VarJ(i,3)
  VarJ(i,4)=i

60    CONTINUE

      K=1+3*KK+KK*MM+6*II
      ChHet(11)=0.0
      ChHet(12)=0.0

C     ======================================
C     6 NORMALISATION DES FRACTIONS MOLAIRES
C     ======================================
C     Calcul de XTOT : nombre total de molécules dans le système

        XTOT = 0.00
        DO 50 K = 1, KK
          XTOT = XTOT + X(K)*ChHet(10)
          WRITE (83, 7270) K,X(K),XTOT
50      CONTINUE

C     Normalisation des fractions molaires

        DO 55 K = 1, KK
          X(K) = X(K) / XTOT*ChHet(10)
55      CONTINUE

C     ======================
C     7 CONDITIONS INITIALES
C     ======================
```

```
        CALL CalculJour(1,NbrMoisD,NbrJourD,0,NumJour)
        TT1  = (NumJour-1)*24*3600
        CALL CalculJour(1,NbrMoisF,NbrJourF,0,NumJour)
        T2  = NumJour*24*3600
        Z(1) = T
        CALL CKXTY (X, ICKWRK, RCKWRK, Z(2))

C     ===================================
C     8 PARAMETRES D'INTEGRATION DE DVODE
C     ===================================

        TT2   = TT1
        NEQ   = KK + 1
        MF    = 22
        ITOL  = 1
        IOPT  = 0
        RTOL =  1.0E-6
        ITASK = 1
        ATOL  = 1.0E-15
        ISTATE= 1
        NLINES=NLMAX + 1
        TPrint=TT2
        K=1+3*KK+KK*MM+6*II

C do 71 i=I,NbrHet
C write (29, 7269) KK,MM,II,K
C71 continue

C ===========================================
C CALCUL DE kuni DES REACTIONS HETEROGENES
C ===========================================

DO 82 I=1,NbrHet
ChHet(12)=ICKWRK(K+(I-1)*6+2+6*NbrPhoto-1)+MM
batman=(8*8.32*300*1.0E+7/3.14/
1    RCKWRK(ChHet(12)))**0.5
```

```
     2    *HET2(I)/4*Surface*1E-8/(ChHet(10))/6.023e+23
WRITE (82,7270) I,batman,HET2(I)
82 CONTINUE

C     =====================
C     9 BOUCLE D'INTEGRATION
C     =====================

        DO  1000 TT2=TT1,T2,DT

C         9.1 Calcul de l'angle zenithal
C         ===============================
          NJour=1+INT(TT2/3600/24)
          IZEIT=INT(TT2/60-(NJour-1)*24*60)
          CALL CalculJour(3,IMONAT,ITAG,NbrSec,NJour)
          IZTYP=1
          ALAT2=ALAT
          ALONG2=ALONG
          CALL ZENANG (ALAT2,ALONG2,ITAG,IMONAT,IZEIT,IZTYP,COSZ)
          ANGLE=COSZ
          CST(1)=ALAT
          CST(2)=ALONG
          CST(3)=ITAG
          CST(4)=IMONAT
          CST(5)=IZEIT
C
C         9.2 Calcul des constantes photochimiques en fct de cosZ
C         ========================================================
C     Le taux de photolyse de l'espèce i varie selon la loi
C     phorat(i) = coef(i,1)  * cosz**coef(i,2) * exp(-coef(i,3)/cosz)
C
          do 66 i=1,NbrPhoto
      IF (ANGLE .LE. 0.0667) THEN
        RCKWRK(1+MM+KK*18+(i-1)*4)=PHOTO(i)*ANGLE
C             WRITE (28, 7250) PHOTO(i)*ANGLE, ANGLE, TT2
              ELSE
```

```
             RCKWRK(1+MM+KK*18+(i-1)*4)=VarJ(i,1)*
     1          ANGLE**VarJ(i,2)
     2          *exp(-VarJ(i,3)/ANGLE)
C            WRITE (28, 7250) RCKWRK(1+MM+KK*18+(i-1)*4), ANGLE, TT2
             ENDIF
             ANA(1,1,1)=RCKWRK(1+MM+KK*18+(i-1)*4)
66       CONTINUE

C      goto 156

C        =================================================================
C        9.3 Transformation des constantes 1°ordre en pseudo second ordre
C        =================================================================
         CALL CKYTX (Z(2), ICKWRK, RCKWRK, X)
         CALL CalculJour(1,int(ChHet(2)),int(ChHet(3)),0,JourDebut)
         CALL CalculJour(1,int(ChHet(4)),int(ChHet(5)),0,JourFin)
         CALL CalculJour(2,0,0,TT2,Jour)

C        =====================================================================
C        9.4 Début du calcul des vitesses impliquant les réactions hétérogènes
C        =====================================================================
         IF ((Jour .GE. JourDebut) .AND. (Jour .LE. JourFin)) THEN
           K=1+3*KK+KK*MM+6*II
           ChHet(1) = Surface

C           do 69 I=1,NbrHet
C               write (29, 7269) I, ICKWRK(K+(I-1)*6+6*NbrPhoto+1),
C       1       ICKWRK(K+(I-1)*6+6*NbrPhoto+2),
C       2       ICKWRK(K+(I-1)*6+6*NbrPhoto+3),
C       3       ICKWRK(K+(I-1)*6+6*NbrPhoto+4),
C       4       ICKWRK(K+(I-1)*6+6*NbrPhoto+5),
C       5       ICKWRK(K+(I-1)*6+6*NbrPhoto+6)
C69         continue

            DO 167 I=1,NbrHet
C             WRITE (31,7301) Jour, JourDebut, JourFin, int(TT2/86400),
```

```
C       1       TT2/86400

C             WRITE (29,7301) ICKWRK(K+(I-1)*6+1+6*NbrPhoto),
C       1       ICKWRK(K+(I-1)*6+2+6*NbrPhoto),
C       2       ICKWRK(K+(I-1)*6+3+6*NbrPhoto),K, ChHet(6)

C            ---------------------------------------------
C            Réactions dépendant de la concentration NACL
C            ---------------------------------------------
             IF (ICKWRK(K+(I-1)*6+2+6*NbrPhoto) .EQ. ChHet(6)) THEN

          IF (X(ChHet(6)) .GE. 1.0E-14) THEN

                    ChHet(12)=ICKWRK(K+(I-1)*6+2+6*NbrPhoto-1)+MM
                    HET(I)=(8*8.32*300*1.0E+7/3.14/
        1                 RCKWRK(ChHet(12)))**0.5
        2                 *HET2(I)/4*ChHet(1)*1E-8/(ChHet(10))
                    RCKWRK(1+MM+KK*18+NbrPhoto*4+(I-1)*4)=Het(I)
        1                 /(X(ChHet(6))*XTOT)
                  ELSE
                    RCKWRK(1+MM+KK*18+NbrPhoto*4+(I-1)*4)=0
                  ENDIF
              ENDIF

C             --------------------------------------------
C             Réactions dépendant de la concentration KBR
C             --------------------------------------------
              IF (ICKWRK(K+(I-1)*6+2+6*NbrPhoto) .EQ. ChHet(8)) THEN

                   IF (X(ChHet(8)) .GE. 1.0E-14) THEN

                     ChHet(12)=ICKWRK(K+(I-1)*6+2+6*NbrPhoto-1)+MM
                     HET(I)=(8*8.32*300*1.0E+7/3.14/
        1                  RCKWRK(ChHet(12)))**0.5
        2                  *HET2(I)/4*ChHet(1)/71.1*1E-8/(ChHet(10))
                     RCKWRK(1+MM+KK*18+NbrPhoto*4+(I-1)*4)=Het(I)
```

```
        1                  /(X(ChHet(8))*XTOT)
                   ELSE
                     RCKWRK(1+MM+KK*18+NbrPhoto*4+(I-1)*4)=0
                   ENDIF
               ENDIF
167        CONTINUE
         ENDIF
156      I=1
C       ================================
C       9.5 Fin de la chimie hétérogène
C       ================================
        IF (Jour .GT. JourFin) THEN
         DO 68 i=1,NbrHet
           RCKWRK(1+MM+KK*18+NbrPhoto*4+(i-1)*4)=0
              ChHet(1) = 0.0
68       CONTINUE
        ENDIF
C       ===========================
C       9.6 Affichage des résultats
C       ===========================
        IF (TPRINT .LE. TT2) THEN
          write(LOUT2,7250) CST(3),CST(4),CST(5),TT2,ANGLE,CST(1)
          TPRINT=TPRINT+DTPRINT
C         Pages d'entête
C         ------------------
          IF (NLINES .EQ. NLMAX + 1) THEN
            WRITE (LOUT, 7003)
            WRITE (LOUT, 7100) (KSYM(K)(:10), K=1,MIN(NK,KK))
            WRITE (FOUT, 7100) (KSYM(K)(:10), K=1,MIN(NK,KK))
            NLINES = 1
            DO 200 K1 = NK+1, KK, NK
              WRITE (LOUT, 7110) (KSYM(K)(:10), K=K1, MIN(K1+NK-1, KK))
              WRITE (FOUT, 7110) (KSYM(K)(:10), K=K1, MIN(K1+NK-1, KK))
              NLINES = NLINES + 1
200         CONTINUE
          ENDIF
```

```
C         Expression de la fraction molaire en fct de la fraction massique
C         ----------------------------------------------------------------
          CALL CKYTX (Z(2), ICKWRK, RCKWRK, X)

C         Affichage du nombre de molécules
C         --------------------------------
          T=Z(1)
          WRITE (LOUT, 7105) TT1, T, (X(K)*XTOT, K=1,MIN(NK,KK))
          WRITE (FOUT, 7105) TT1, T, (X(K)*XTOT, K=1,MIN(NK,KK))
          NLINES = NLINES + 1
          DO 300 K1 = NK+1, KK, NK
            WRITE (LOUT, 7115) (X(K)*XTOT, K=K1, MIN(K1+NK-1,KK))
            WRITE (FOUT, 7115) (X(K)*XTOT, K=K1, MIN(K1+NK-1,KK))
            NLINES = NLINES + 1
300       CONTINUE
C         Calcul du nbr d'itérations restant à effectuer
C         ---------------------------------------------
          IF (T2 .EQ. TT2) THEN
            Nbr=0
          ELSE
            Nbr=INT((T2-TT2)/DTPRINT)
          ENDIF

          WRITE (6,*) 'Nbr d iterations a effectuer:',Nbr
        ENDIF
C       Call the differential equation solver
C       -------------------------------------
        CST(61)=TT2
        Tlim=TT2
        ISTATE=1
350     CALL DVODE (FUN, NEQ, Z, TT1, TT2, ITOL, RTOL, ATOL, ITASK,
     1            ISTATE, IOPT, ELWRK, LRW, IELWRK, LIW, JAC, MF,
     2            RPAR, IPAR)
C       Analyse de ISTATE
C       -----------------
        IF (ISTATE .LE. -1) THEN
```

```
          IF (ISTATE .EQ. -1) THEN
            ISTATE = 2
            GOTO 350
          ELSE
            WRITE (LOUT,*) ' ISTATE=',ISTATE
            STOP
          ENDIF
        ENDIF
1000    CONTINUE

C     Formats
C     -------
 7003 FORMAT (1H1)
 7100 FORMAT (2X, 'T(SEC)', 6X, 'TMP(K)', 6X, 5(1X,A10))
 7105 FORMAT (E11.4,11E11.3E3)
 7110 FORMAT (26X, 5(1X,A10))
 7115 FORMAT (22X, 10E11.3E3)
 7121 FORMAT (1x,I5,3(1X,E11.4),1X,I5,1X,I5)
 7200 FORMAT (1X,A35,E11.4)
 7216 FORMAT (1x,A30)
 7217 FORMAT (1x,2I5)
 7230 FORMAT (A16,E10.2)
 7249 FORMAT (2E10.2)
 7250 FORMAT (I5,1X, 6(1X,E12.6))
 7251 FORMAT (2(X,1E12.6))
 7269 FORMAT (I5,3(X,1E12.6))
 7270 FORMAT (I5,X,1E12.6,X,1E12.6)
 7271 FORMAT (2(I5),4(X,1E12.6))
 7300 FORMAT (2X,a24,1p,3e15.6)
 7301 FORMAT (1X,I5,1X,I5,1X,I5,1X,I5,1X,E12.6)
 7302 FORMAT (1X,I5,1X,I5,1X,I5,1X,E12.6)
       END
C
       SUBROUTINE FUN (N, TIME, Z, ZP)
C
C     double precision
```

```
      IMPLICIT DOUBLE PRECISION(A-H,O-Z), INTEGER(I-N)
      COMMON /PARAMR/ RCKWRK(10000), P,RU,WT(65),WDOT(65),H(65),X(65), T
     1   ,ANGLE, PHOTO(30), HET(30), HET2(30), ANA(200,65,10),CST(100),
     2   ALAT,ALONG
     3   ,XTOT, ChHet(12) , VarJ(40,4),Surface
      COMMON /PARAMI/ ICKWRK(10000), KK, MM,NbrPhoto,NbrHet, MONAT(12)
       DIMENSION Z(N), ZP(N)
C
C     Variables in Z are:  Z(1)   = T
C                          Z(K+1) = Y(K)
C     ========================
C     Call CHEMKIN subroutines
C     ========================
      CALL CKRHOY (P, Z(1), Z(2), ICKWRK, RCKWRK, RHO)
      CALL CKCPBS (Z(1), Z(2), ICKWRK, RCKWRK, CPB)
C     ChHet(1) Surface des particules   ChHet(7) N°élément HClc
      CALL CKWYP (P,Z(1),Z(2),ICKWRK,RCKWRK,WDOT,ChHet(1),ChHet(7))
      CALL CKHMS (Z(1), ICKWRK, RCKWRK, H)

C     =======================
C     Form governing equation
C     =======================

      SUM = 0.0
      DO 100 K = 1, KK
         ZP(K+1) = WDOT(K) * WT(K) / RHO
         SUM = SUM + H(K) * WDOT(K) * WT(K)
100   CONTINUE
      ZP(1) = -SUM / (RHO*CPB)
      RETURN
      END

      SUBROUTINE ZENANG (PHI,PSI,ITAG,IMONAT,IZEIT,IZTYP,COSZ)
C     ===============================================================
C     CALCULATES THE SOLAR ZENITH ANGLE FOR A CHOOSEN PLACE AND TIME
C     CREATED 1991 BY ANSGAR RUGGABER, UNIVERSITY OF MUNICH, FRG
```

```
C     FUNDED BY THE GERMAN MINISTER OF RESEARCH AND TECHNOLOGY (BMFT)
C     UNDER CONTRACT NO. 521-4007-07EU-738 8
C     ===============================================================

      IMPLICIT DOUBLE PRECISION (A-H,O-Z), INTEGER(I-N)
      COMMON /PARAMR/ RCKWRK(10000), P,RU,WT(65),WDOT(65),H(65),X(65), T
     1   ,ANGLE, PHOTO(30), HET(30), HET2(30), ANA(200,65,10),CST(100)
     2  ,ALAT,ALONG
     3   ,XTOT, ChHet(10) , VarJ(40,4),Surface
      COMMON /PARAMI/ ICKWRK(10000), KK, MM,NbrPhoto,NbrHet, MONAT(12)
         PARAMETER (PI=3.141592653,RAD=PI/180.0)
C      WRITE (6,*) PHI,PSI,ITAG,IMONAT,IZEIT
      IF (IZEIT.LT.0) THEN
        JAHRTA=-1
        IZEIT=24*60+IZEIT
      ELSE
        JAHRTA=0
      ENDIF
      IF (IZEIT.GT.24*60) THEN
        PRINT*,'Problem in subroutine ZENANG'
        STOP
      ENDIF

      DO 10 NM=1,IMONAT-1
10    JAHRTA=MONAT(NM)+JAHRTA
      JAHRTA=JAHRTA+ITAG

      IF (JAHRTA.LE.0) JAHRTA=365+JAHRTA

      PHI=PHI*RAD
      ZETT=-7.7*SIN(((0.9856*JAHRTA-2.72)*RAD))
     1     -9.9*SIN(((1.9712*JAHRTA+19.55)*RAD))
      A=SIN(((0.9856*JAHRTA-2.72)*RAD))
      DELTA=ASIN(0.3978*SIN((0.9856*JAHRTA+1.92*A-80.23)*RAD))
      IF(IZTYP.EQ.1) THEN
        OMEGA=(IZEIT+60+((PSI-15.)*4)+ZETT-720.)/4.*RAD
```

```
      ELSE
        OMEGA=(IZEIT-720.)/4.*RAD
      ENDIF
      COSZET=SIN(PHI)*SIN(DELTA)+COS(PHI)*COS(DELTA)*COS(OMEGA)
      AM0=90.-(ASIN(COSZET))/RAD

      COSZ=MAX(0.,COS(AM0*RAD))
      CST(40)=IZEIT
      CST(41)=ZETT
      CST(42)=A
      CST(43)=DELTA
      CST(44)=OMEGA
      CST(45)=COSZET
      CST(46)=AM0
      CST(47)=COSZ
      RETURN
      END

      SUBROUTINE CalculJour(IType,IMois,IJour,Seconde,NumJour)
C     ===============================================================
C     routine permettant de calculer le nombre de jour en fonction de
C     deux types de données
C     Type 1 : en fonction du numero du mois et du jour
C     Type 2 : en fonction du nombre de secondes
C     ===============================================================

      IMPLICIT DOUBLE PRECISION (A-H,O-Z), INTEGER(I-N)
      COMMON /PARAMR/ RCKWRK(10000), P,RU,WT(65),WDOT(65),H(65),X(65), T
     1   ,ANGLE, PHOTO(30), HET(30), HET2(30), ANA(200,65,10),CST(100),
     2   ALAT,ALONG
     3   ,XTOT, ChHet(12) , VarJ(40,4),Surface
      COMMON /PARAMI/ ICKWRK(10000), KK, MM,NbrPhoto,NbrHet, MONAT(12)
      IF (IType .EQ. 1) THEN
        NumJour=0
        DO 10 I=1,IMois-1
           NumJour=NumJour+MONAT(I)
```

```
10       CONTINUE
         NumJour=NumJour+IJour
       ENDIF
       IF (IType .EQ. 2) THEN
         NumJour=1+INT(Seconde/3600/24)
       ENDIF
       IF (IType .EQ. 3) THEN
         DO 20 I=1,12
            NumJour=NumJour-MONAT(I)
            IF (NumJour .LE. 0) THEN
              IMois=I
              IJour=NumJour+MONAT(I)
              GOTO 30
            ENDIF
20       CONTINUE
30     ENDIF
       RETURN
       END
```

C.2 Example of an "Init" File

We present here an example of a calculation using the code described above. First, we show the "Init" file, which contains all initial conditions. A display of all the 64 species involved in the simulations is presented below.

```
         CONDITIONS  GENERALES
=============================================
 Nbr de reactions photochimiques et hetero
 25     15
 Pression et temperature
1.0E+00   3.0E+02
 Latitude  Longitude
    30.0    0.0
 Concentrations initiales
NACL                 1.0E+15
KBR                  1.0E+15
N2                   2.0E+19
```

```
NO                  2.4E+10

NO2                 2.4E+10

NO3                 1.8E+08

N2O5                2.0E+08

O2                  4.5E+18

H2O                 6.0E+17

CH4                 1.0E+13

C2H6                1.0E+11

O3                  1.0E+12

CO2                 7.0E+15

CO                  3.0E+10

HNO3                4.8E+10

==============================================

CONDITIONS  DE SIMULATION

==============================================

Simulation depuis     jusqu'au

  Mois   Jour      Mois   Jour

    1       1        1     10

Pas de temps

 simulation  impression

  3.60E+3    3.60E+3

==============================================

CHIMIE HETEROGENE

==============================================

 Surface des particules: Nbr de micrometre carre pour un volume de x cc

  1.0E+01     1

 Chimie hétérogène en activité

   Depuis le      jusqu'au

  Mois   Jour    Mois   Jour

    1     3        1     8

==============================================
```

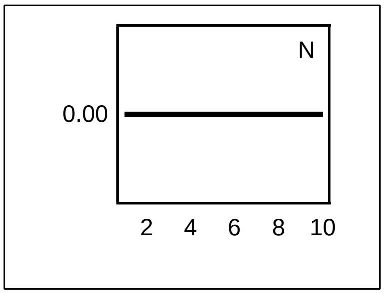
N
0.00
2
4
6
8
10

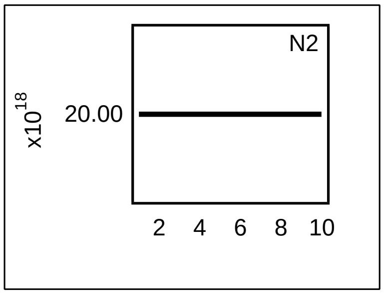
N2
x10^18
20.00
2
4
6
8
10

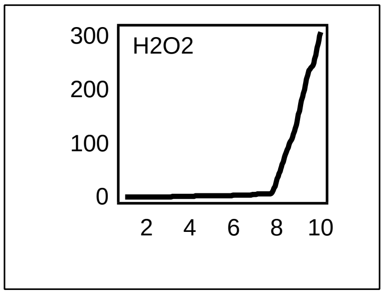
H2O2
300
200
100
0
2
4
6
8
10

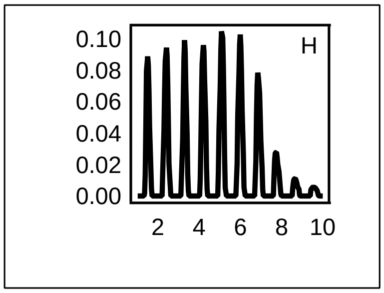
H
0.10
0.08
0.06
0.04
0.02
0.00
2
4
6
8
10

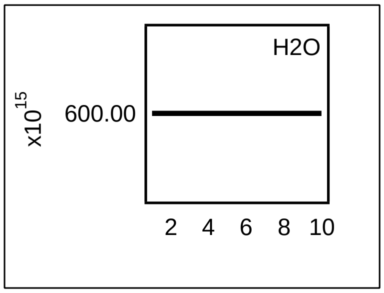
H2O
x10^15
600.00
2
4
6
8
10

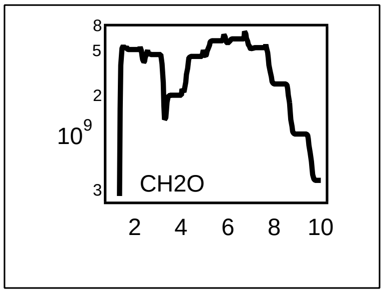
CH2O
8
5
2
10^9
3
2
4
6
8
10

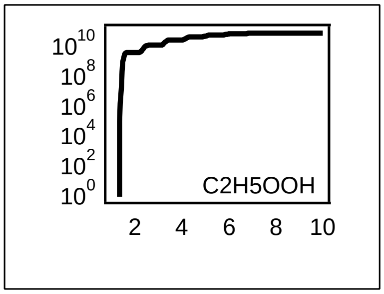
C2H5OOH
10^10
10^8
10^6
10^4
10^2
10^0
2
4
6
8
10

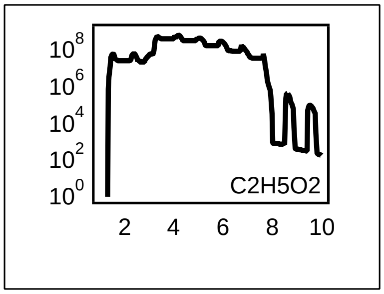
C2H5O2
10^8
10^6
10^4
10^2
10^0
2
4
6
8
10

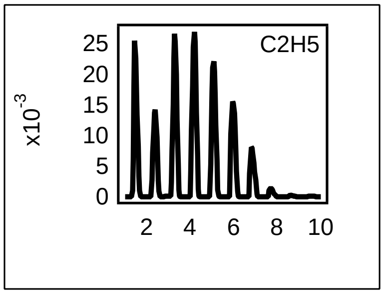
C2H5
x10^-3
25
20
15
10
5
0
2
4
6
8
10

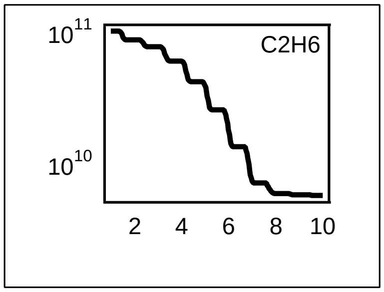
C2H6
10^11
10^10
2
4
6
8
10

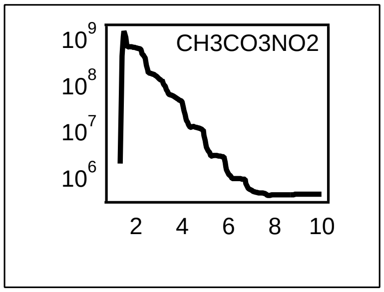
CH3CO3NO2
10^9
10^8
10^7
10^6
2
4
6
8
10

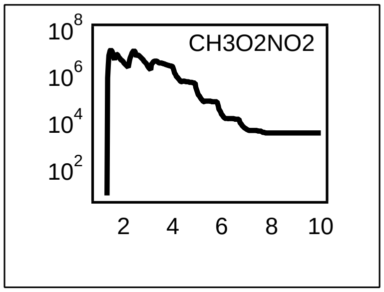
CH3O2NO2
10^8
10^6
10^4
10^2
2
4
6
8
10

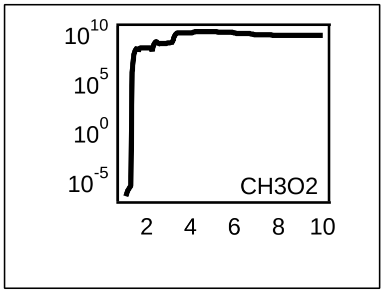
CH3O2
10^10
10^5
10^0
10^-5
2
4
6
8
10

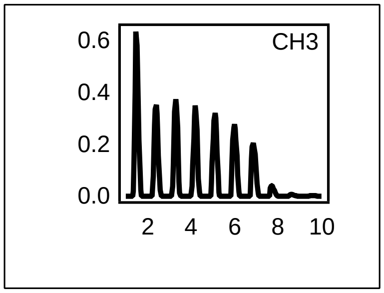
CH3
0.6
0.4
0.2
0.0
2
4
6
8
10

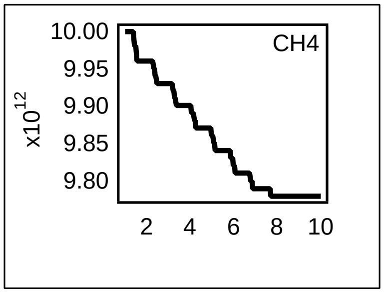
CH4
x10^12
10.00
9.95
9.90
9.85
9.80
2
4
6
8
10

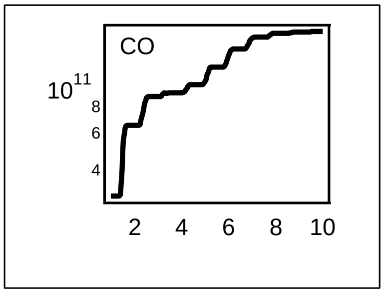
CO
10^11
8
6
4
2
4
6
8
10

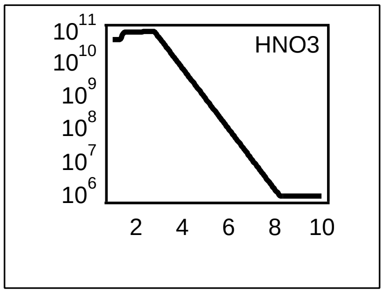
HNO3
10^11
10^10
10^9
10^8
10^7
10^6
2
4
6
8
10

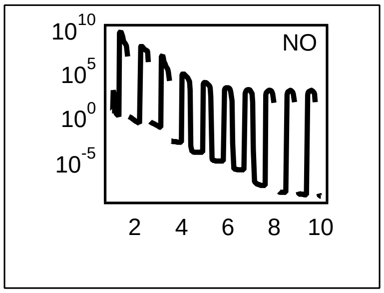
NO
10^10
10^5
10^0
10^-5
2
4
6
8
10

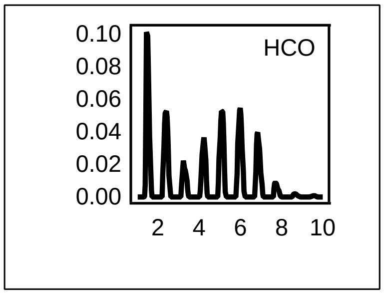
HCO
0.10
0.08
0.06
0.04
0.02
0.00
2 4 6 8 10

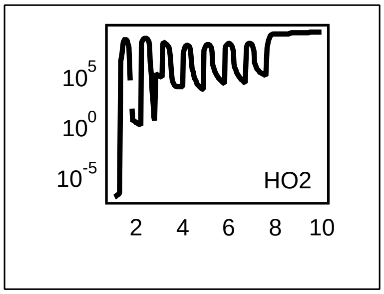
HO2
10^{5}
10^{0}
10^{-5}
2 4 6 8 10

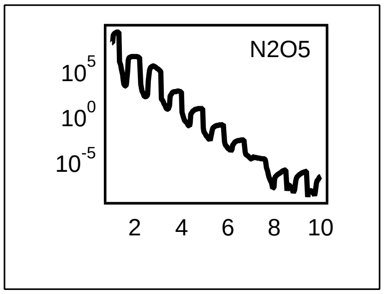
N2O5
10^{5}
10^{0}
10^{-5}
2 4 6 8 10

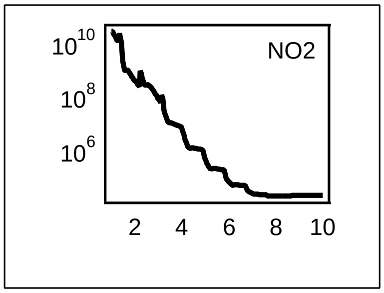
NO2
10^{10}
10^{8}
10^{6}
2 4 6 8 10

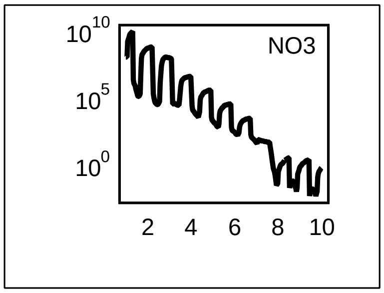
NO3
10^{10}
10^{5}
10^{0}
2 4 6 8 10

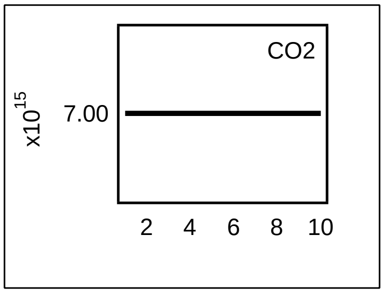
CO2
$x10^{15}$
7.00
2 4 6 8 10

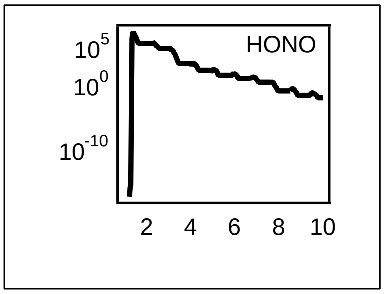
HONO
10^{5}
10^{0}
10^{-10}
2 4 6 8 10

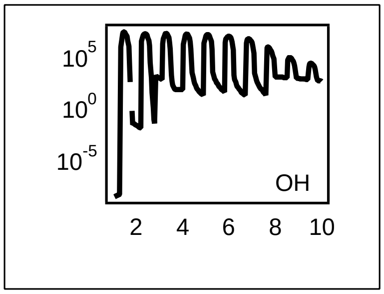
OH
10^{5}
10^{0}
10^{-5}
2 4 6 8 10

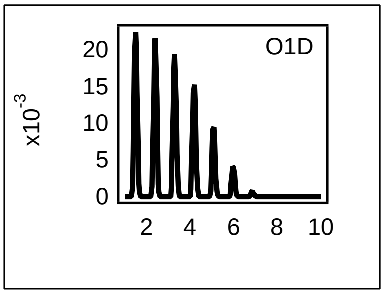
O1D
$x10^{-3}$
20
15
10
5
0
2 4 6 8 10

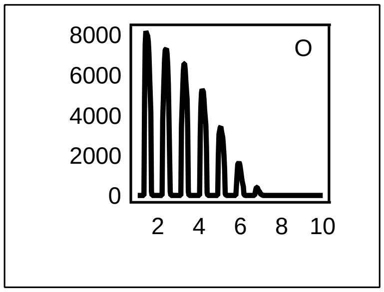
O
8000
6000
4000
2000
0
2 4 6 8 10

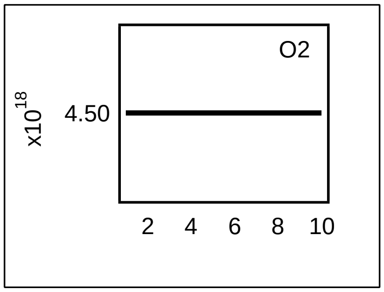
O2
$x10^{18}$
4.50
2 4 6 8 10

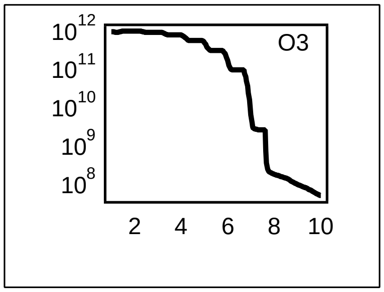
O3
10^{12}
10^{11}
10^{10}
10^{9}
10^{8}
2 4 6 8 10

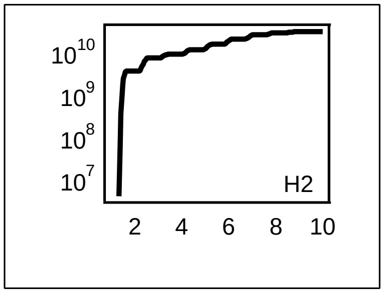
H2
10^{10}
10^{9}
10^{8}
10^{7}
2 4 6 8 10

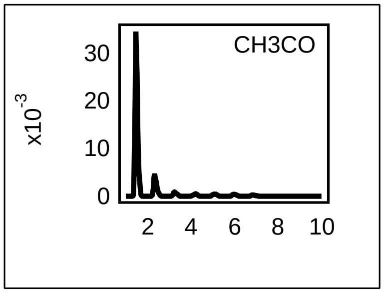
CH3CO
$x10^{-3}$
30
20
10
0
2 4 6 8 10

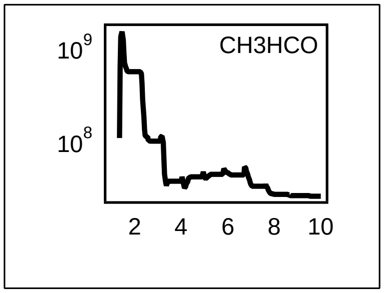
CH3HCO
10^{9}
10^{8}
2 4 6 8 10

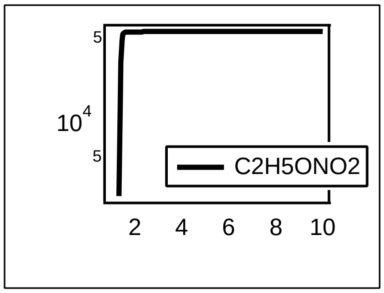
C2H5ONO2
5
10^{4}
5
2 4 6 8 10

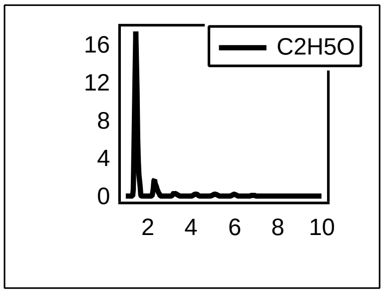
C2H5O
16
12
8
4
0
2 4 6 8 10

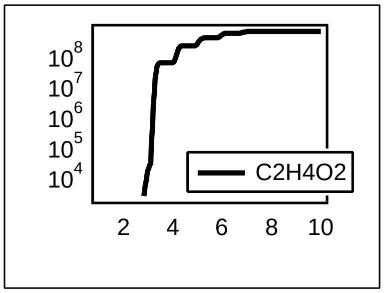
C2H4O2
10^{8}
10^{7}
10^{6}
10^{5}
10^{4}
2 4 6 8 10

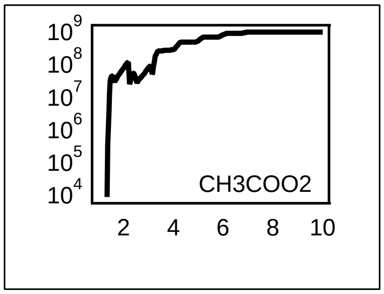
CH3COO2
10^9
10^8
10^7
10^6
10^5
10^4
2
4
6
8
10

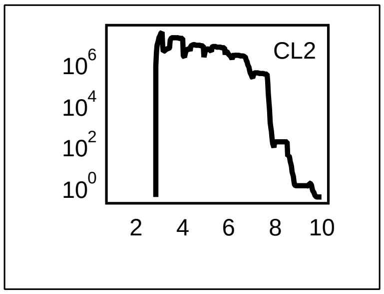
CL2
10^6
10^4
10^2
10^0
2
4
6
8
10

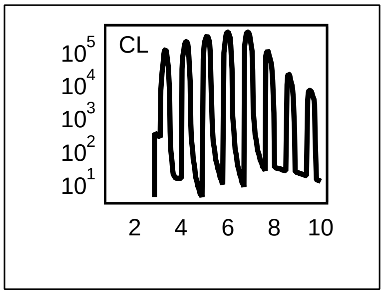
CL
10^5
10^4
10^3
10^2
10^1
2
4
6
8
10

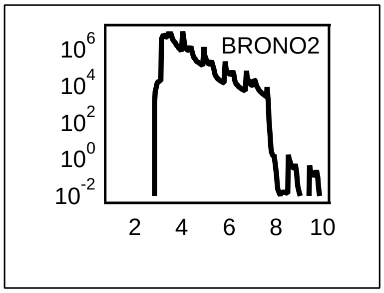
BRONO2
10^6
10^4
10^2
10^0
10^{-2}
2
4
6
8
10

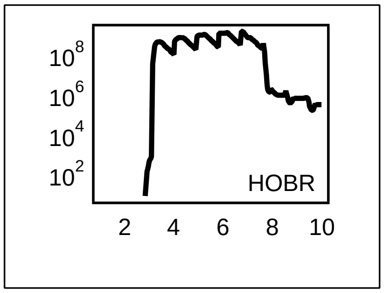
HOBR
10^8
10^6
10^4
10^2
2
4
6
8
10

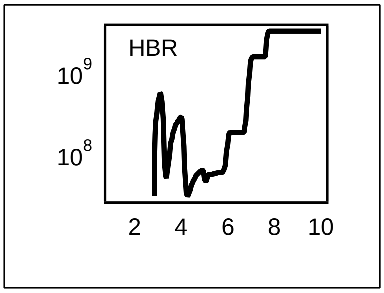
HBR
10^9
10^8
2
4
6
8
10

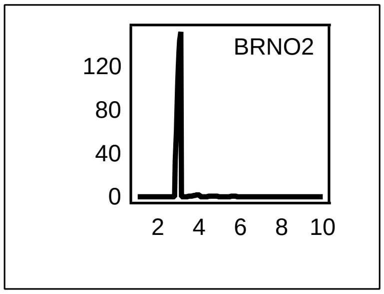
BRNO2
120
80
40
0
2
4
6
8
10

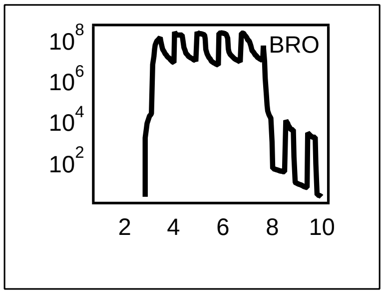
BRO
10^8
10^6
10^4
10^2
2
4
6
8
10

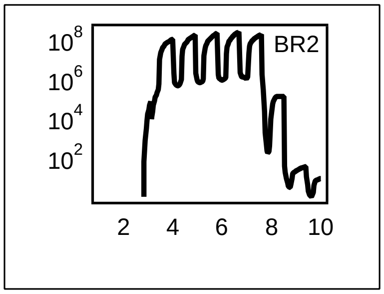
BR2
10^8
10^6
10^4
10^2
2
4
6
8
10

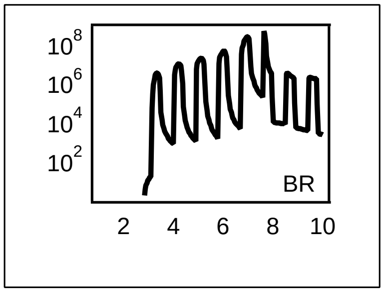
BR
10^8
10^6
10^4
10^2
2
4
6
8
10

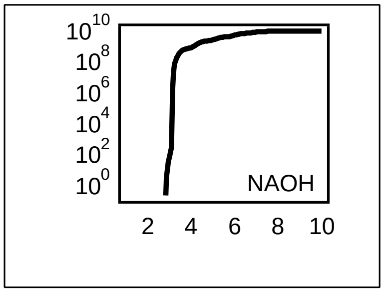
NAOH
10^{10}
10^8
10^6
10^4
10^2
10^0
2
4
6
8
10

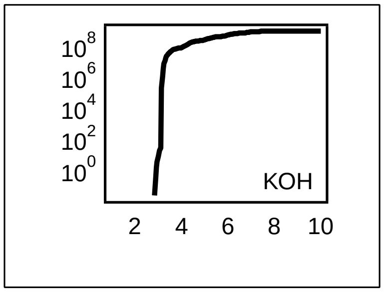
KOH
10^8
10^6
10^4
10^2
10^0
2
4
6
8
10

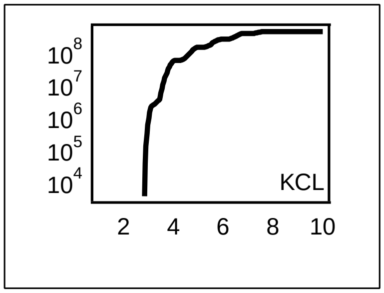
KCL
10^8
10^7
10^6
10^5
10^4
2
4
6
8
10

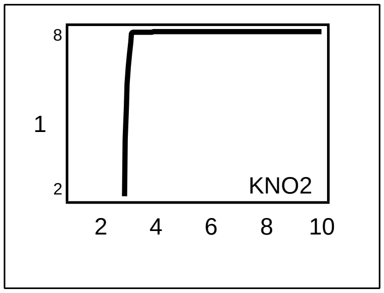
KNO2
8
1
2
2
4
6
8
10

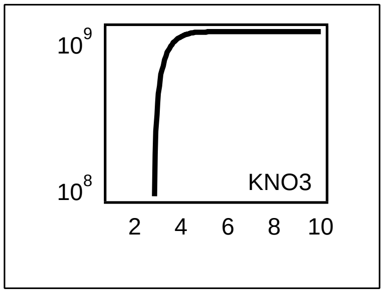
KNO3
10^9
10^8
2
4
6
8
10

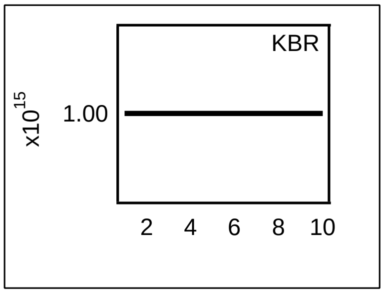
KBR
$x10^{15}$
1.00
2
4
6
8
10

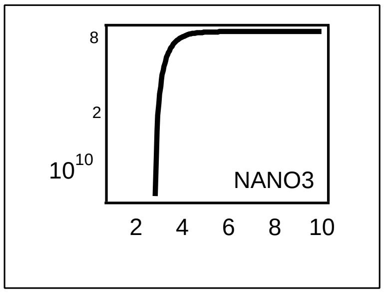
NANO3
8
2
10^{10}
2
4
6
8
10

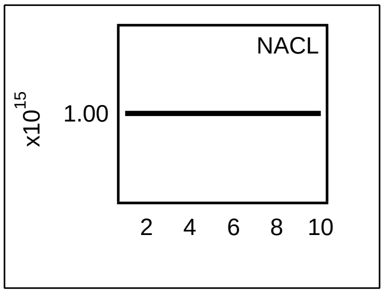
NACL
$x10^{15}$
1.00
2
4
6
8
10

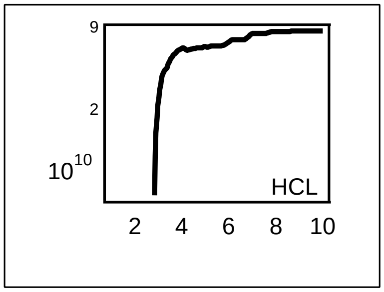
9
2
10^{10}
HCL
2
4
6
8
10

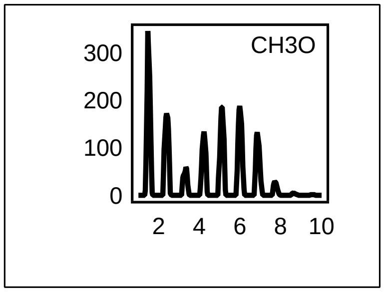
300
200
100
0
CH3O
2
4
6
8
10

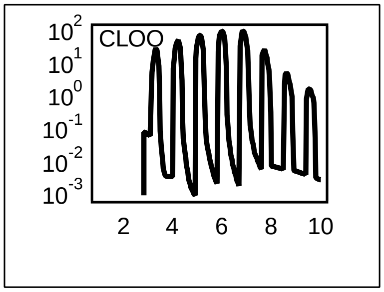
10^{2}
10^{1}
10^{0}
10^{-1}
10^{-2}
10^{-3}
CLOO
2
4
6
8
10

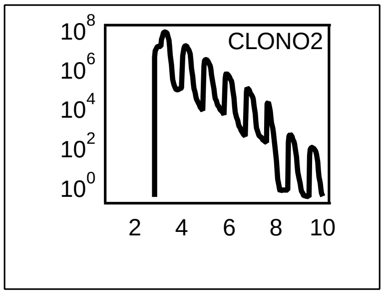
10^{8}
10^{6}
10^{4}
10^{2}
10^{0}
CLONO2
2
4
6
8
10

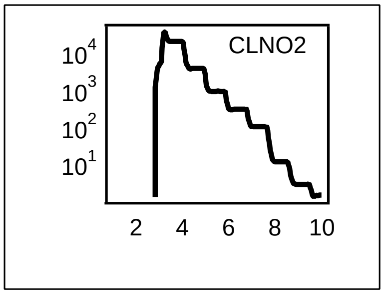
10^{4}
10^{3}
10^{2}
10^{1}
CLNO2
2
4
6
8
10

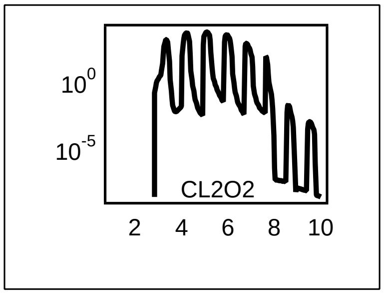
10^{0}
10^{-5}
CL2O2
2
4
6
8
10

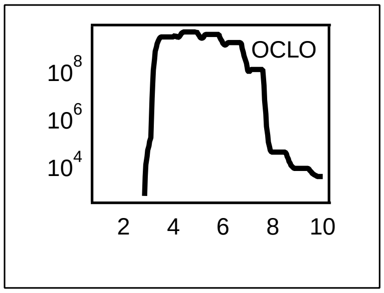
10^{8}
10^{6}
10^{4}
OCLO
2
4
6
8
10

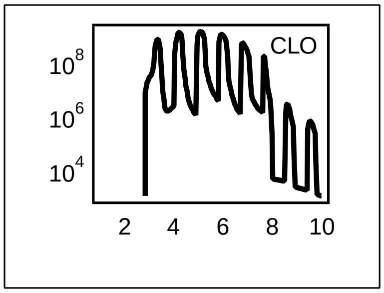
10^{8}
10^{6}
10^{4}
CLO
2
4
6
8
10

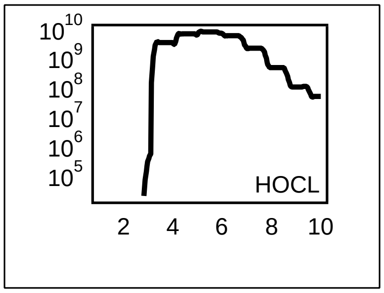
10^{10}
10^{9}
10^{8}
10^{7}
10^{6}
10^{5}
HOCL
2
4
6
8
10

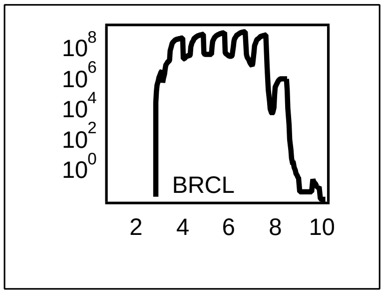
10^{8}
10^{6}
10^{4}
10^{2}
10^{0}
BRCL
2
4
6
8
10

Appendix D

Kinetic Results of HNO_3 on Ice

Table D.1: Uptake coefficient of HNO_3 at T = 180 K

Ice $^{(a)}$	Flow [molec. s^{-1}]	Dose [molec.]	Concentration [molec. cm^{-3}]	k_{esc} [s^{-1}]	k_{uni} [s^{-1}]	γ_{obs}	γ_{corr} $^{(b)}$
			PV experiments				
B		$2.8 \cdot 10^{12}$	$1.4 \cdot 10^{9}$	5.1	16.8	0.24	
B		$3.6 \cdot 10^{12}$	$1.8 \cdot 10^{9}$	4.8	22.4	0.32	
B		$5.9 \cdot 10^{12}$	$3.0 \cdot 10^{9}$	5.1	18.9	0.27	
B		$1.0 \cdot 10^{13}$	$5.0 \cdot 10^{9}$	5.2	18.9	0.27	
B		$1.1 \cdot 10^{13}$	$5.5 \cdot 10^{9}$	4.9	15.4	0.22	
B		$1.6 \cdot 10^{13}$	$8.0 \cdot 10^{9}$	4.6	21.7	0.31	
B		$1.9 \cdot 10^{13}$	$9.5 \cdot 10^{9}$	4.9	20.3	0.29	
B		$2.2 \cdot 10^{13}$	$1.1 \cdot 10^{10}$	4.3	19.6	0.28	
B		$3.5 \cdot 10^{13}$	$1.8 \cdot 10^{10}$	4.3	19.6	0.28	
B		$4.5 \cdot 10^{13}$	$2.3 \cdot 10^{10}$	4.2	18.2	0.26	
B		$1.0 \cdot 10^{14}$	$5.0 \cdot 10^{10}$	4.0	20.3	0.29	
			SS experiments				
C	$9.9 \cdot 10^{12}$		$2.1 \cdot 10^{9}$	2.4	14.0	0.20	0.27
B	$7.6 \cdot 10^{12}$		$2.7 \cdot 10^{9}$	1.4	16.1	0.23	0.28
B	$1.5 \cdot 10^{13}$		$3.7 \cdot 10^{9}$	2.0	18.9	0.27	0.32
C	$1.6 \cdot 10^{13}$		$4.4 \cdot 10^{9}$	1.8	16.8	0.24	0.29
B	$3.1 \cdot 10^{13}$		$6.5 \cdot 10^{9}$	2.4	20.3	0.29	0.31
B	$2.3 \cdot 10^{13}$		$6.7 \cdot 10^{9}$	1.7	16.1	0.23	-
B	$3.4 \cdot 10^{13}$		$7.0 \cdot 10^{9}$	2.4	20.3	0.29	-

to be continued

Ice [(a)]	Flow [molec. s^{-1}]	Dose [molec.]	Concentration [molec. cm^{-3}]	k_{esc} [s^{-1}]	k_{uni} [s^{-1}]	γ_{obs}	γ_{corr} [(b)]
B	$1.6 \cdot 10^{14}$		$4.0 \cdot 10^{10}$	2.0	20.3	0.29	0.30
C	$1.7 \cdot 10^{14}$		$4.4 \cdot 10^{10}$	2.0	18.9	0.27	0.31
C [(c)]	$1.1 \cdot 10^{14}$		$4.6 \cdot 10^{10}$	1.2	18.9	0.27	0.32
C	$5.0 \cdot 10^{15}$		$1.0 \cdot 10^{12}$	2.4	20.3	0.29	-
C	$5.1 \cdot 10^{15}$		$1.1 \cdot 10^{12}$	2.3	21.7	0.31	-

Table D.2: Uptake coefficient of HNO_3 at T = 190 K.

Ice [(a)]	Flow [molec. s^{-1}]	Dose [molec.]	Concentration [molec. cm^{-3}]	k_{esc} [s^{-1}]	k_{uni} [s^{-1}]	γ_{obs}	γ_{corr} [(b)]
			PV experiments				
B		$3.1 \cdot 10^{12}$	$1.6 \cdot 10^{9}$	5.9	18.9	0.27	
B		$1.3 \cdot 10^{13}$	$6.5 \cdot 10^{9}$	5.5	17.5	0.25	
B		$1.6 \cdot 10^{13}$	$8.0 \cdot 10^{9}$	5.0	17.5	0.25	
			SS experiments				
B	$9.5 \cdot 10^{12}$		$2.3 \cdot 10^{9}$	2.1	18.9	0.27	-
B	$9.4 \cdot 10^{12}$		$2.6 \cdot 10^{9}$	1.8	16.1	0.23	0.27
C	$1.0 \cdot 10^{14}$		$3.1 \cdot 10^{10}$	1.6	18.2	0.26	0.30
B	$1.5 \cdot 10^{14}$		$3.3 \cdot 10^{10}$	2.2	14.0	0.20	0.21
C	$4.9 \cdot 10^{14}$		$1.1 \cdot 10^{11}$	2.2	18.9	0.27	-
C	$5.3 \cdot 10^{15}$		$1.3 \cdot 10^{12}$	2.1	16.8	0.25	-

Table D.3: Uptake coefficient of HNO_3 at T = 200 K.

Ice [a]	Flow [molec. s^{-1}]	Dose [molec.]	Concentration [molec. cm^{-3}]	k_{esc} [s^{-1}]	k_{uni} [s^{-1}]	γ_{obs}	γ_{corr} [b]
			PV experiments				
B		$3.3 \cdot 10^{12}$	$1.7 \cdot 10^{9}$	5.5	11.9	0.17	
B		$6.2 \cdot 10^{12}$	$3.1 \cdot 10^{9}$	4.4	13.3	0.19	
B		$8.6 \cdot 10^{12}$	$4.3 \cdot 10^{9}$	5.6	11.9	0.17	
B		$1.3 \cdot 10^{13}$	$6.5 \cdot 10^{9}$	4.3	14.0	0.20	
B		$2.6 \cdot 10^{13}$	$1.3 \cdot 10^{10}$	4.4	12.6	0.18	
B		$3.7 \cdot 10^{13}$	$1.9 \cdot 10^{10}$	4.4	14.7	0.21	
B		$3.8 \cdot 10^{13}$	$1.9 \cdot 10^{10}$	4.0	12.6	0.18	
B		$1.0 \cdot 10^{14}$	$5.0 \cdot 10^{10}$	4.0	13.3	0.19	
			SS experiments				
B	$8.0 \cdot 10^{12}$		$1.6 \cdot 10^{9}$	2.5	10.5	0.15	0.18
C	$1.1 \cdot 10^{13}$		$1.8 \cdot 10^{9}$	3.0	11.9	0.17	-
B	$8.8 \cdot 10^{12}$		$1.8 \cdot 10^{9}$	2.5	10.5	0.15	0.20
C	$2.0 \cdot 10^{13}$		$3.7 \cdot 10^{9}$	2.7	10.5	0.15	0.16
B	$1.7 \cdot 10^{13}$		$4.3 \cdot 10^{9}$	2.0	12.6	0.18	0.23
B	$3.4 \cdot 10^{13}$		$1.1 \cdot 10^{10}$	1.6	12.6	0.18	0.23
B	$3.0 \cdot 10^{13}$		$1.2 \cdot 10^{10}$	1.3	9.8	0.14	0.15
C	$5.3 \cdot 10^{13}$		$1.2 \cdot 10^{10}$	2.2	11.9	0.17	-
B	$3.8 \cdot 10^{13}$		$1.4 \cdot 10^{10}$	1.4	10.5	0.15	0.18
B	$1.2 \cdot 10^{14}$		$2.3 \cdot 10^{10}$	2.2	11.2	0.16	0.16
B [c]	$8.7 \cdot 10^{14}$		$3.4 \cdot 10^{10}$	1.3	11.9	0.17	-
C	$1.1 \cdot 10^{14}$		$3.8 \cdot 10^{10}$	1.4	11.2	0.16	0.17
B	$1.9 \cdot 10^{14}$		$4.3 \cdot 10^{10}$	2.2	14.0	0.20	-
C [c]	$1.3 \cdot 10^{15}$		$5.9 \cdot 10^{11}$	1.1	9.8	0.15	-
C	$3.9 \cdot 10^{15}$		$9.3 \cdot 10^{11}$	2.1	11.2	0.16	-
C	$4.8 \cdot 10^{15}$		$1.2 \cdot 10^{12}$	2.0	12.6	0.18	-
C	$5.6 \cdot 10^{15}$		$1.8 \cdot 10^{12}$	1.6	13.3	0.19	-
C [c]	$8.3 \cdot 10^{15}$		$4.6 \cdot 10^{12}$	0.9	11.2	0.16	-

Table D.4: Uptake coefficient of HNO_3 at T = 210 K.

Ice [(a)]	Flow [molec. s^{-1}]	Dose [molec.]	Concentration [molec. cm^{-3}]	k_{esc} [s^{-1}]	k_{uni} [s^{-1}]	γ_{obs}	γ_{corr} [(b)]
			PV experiments				
B		$4.7 \cdot 10^{12}$	$2.4 \cdot 10^{9}$	5.6	5.6	0.08	
B		$1.0 \cdot 10^{13}$	$5.0 \cdot 10^{9}$	5.7	5.6	0.08	
B		$2.9 \cdot 10^{13}$	$1.5 \cdot 10^{10}$	4.7	7.7	0.11	
B		$7.6 \cdot 10^{13}$	$3.8 \cdot 10^{10}$	4.2	7.0	0.10	
			SS experiments				
B	$1.8 \cdot 10^{13}$		$3.6 \cdot 10^{9}$	2.5	4.9	0.07	0.08
B	$2.5 \cdot 10^{13}$		$5.2 \cdot 10^{9}$	2.4	3.5	0.05	0.06
B	$9.8 \cdot 10^{13}$		$2.0 \cdot 10^{10}$	2.4	4.8	0.07	-

Table D.5: Uptake coefficient of HNO_3 at T = 211 K.

Ice [(a)]	Flow [molec. s^{-1}]	Concentration [molec. cm^{-3}]	k_{esc} [s^{-1}]	k_{uni} [s^{-1}]	γ_{obs}	γ_{corr} [(b)]
B	$9.4 \cdot 10^{12}$	$3.6 \cdot 10^{9}$	1.3	5.6	0.08	0.09
C	$1.5 \cdot 10^{14}$	$2.9 \cdot 10^{10}$	2.5	4.2	0.06 [(d)]	-
C	$2.1 \cdot 10^{14}$	$4.4 \cdot 10^{10}$	2.4	3.5	0.05 [(d)]	-

[(a)] Symbols are explained in the text.

[(b)] The corrected uptake coefficient has been obtained using equation (6.6).

[(c)] Performed in the 8 mm orifice reactor.

[(d)] Partial saturation of the ice sample has been observed.

Appendix E

Kinetic Results of Br_2O and $BrONO_2$ on Ice

This Appendix presents the details of the different experiments performed in the Knudsen cell reactor in the study of the heterogeneous reactions of Br_2O and $BrONO_2$ on different types of ice.

Table E.1: Steady state experiments of Br_2O performed on condensed ice samples in the 14 mm orifice reactor.

T [K]	Flow [molecule/s]	γ_0	γ_{ss}	HOBr–Yield [%]
190	$4.8 \cdot 10^{14}$	0.21	0.05	n.d.(a)
200	$1.5 \cdot 10^{15}$	0.36	0.02	80
208	$3.6 \cdot 10^{14}$	0.23	0.06	102
210	$2.0 \cdot 10^{15}$	0.10	0.04	98

(a) n.d. = not determined.

Table E.2: Steady state experiments of Br_2O performed on bulk ice samples in the 14 mm orifice reactor.

T [K]	Flow [molecule/s]	γ_0	γ_{ss}	HOBr–Yield [%]
180	$5.5 \cdot 10^{14}$	0.38	0.01	52
180	$8.6 \cdot 10^{14}$	0.35	0.02	25
180	$8.7 \cdot 10^{14}$	0.25	0.03	n.d.(a)
190	$8.1 \cdot 10^{14}$	0.29	0.03	85
190	$1.3 \cdot 10^{15}$	0.34	0.04	70
190	$1.5 \cdot 10^{15}$	0.48	0.03	n.d.
200	$6.2 \cdot 10^{14}$	0.26	0.02	77
200	$1.1 \cdot 10^{15}$	0.17	0.05	89
200	$1.3 \cdot 10^{15}$	0.14	0.03	90
200	$4.4 \cdot 10^{15}$	0.18	0.02	n.d.
203	$1.9 \cdot 10^{15}$	0.20	0.03	92
205	$2.5 \cdot 10^{15}$	0.15	0.03	82
210	$1.5 \cdot 10^{15}$	0.15	n.o.(b)	80
210	$1.6 \cdot 10^{15}$	0.14	n.o.	74
210	$1.8 \cdot 10^{15}$	0.23	0.07	105
210	$2.0 \cdot 10^{15}$	0.14	0.06	105

(a) n.d. = not determined. (b) n.o. = not observed.

Table E.3: Results of the interaction of $BrONO_2$ on different types of ice performed in the 14 mm escape orifice reactor: a) Bulk (B) ice, b) Condensed (C) ice and c) Single crystal (SC) ice.

T [K]	γ_0	k_{uni} [s^{-1}]	Flow$^{(a)}$ [molecule/s]	Dose$^{(b)}$ [molecules]	η_{HOBr} $^{(c)}$ [%]	η_{Br_2O} $^{(c)}$ [%]	η_{HOBr} $^{(d)}$ [%]	η_{Br_2O} $^{(d)}$ [%]
				a) Bulk (B)				
170	0.23	11.5	$1.2 \cdot 10^{15}$		3	3	42	16
180	0.29	14.5	$1.2 \cdot 10^{15}$		6	7		
180	0.26	13.0	$1.2 \cdot 10^{15}$		9	9	35	45
180	0.33	16.5	$1.4 \cdot 10^{15}$		8	17		
180	0.23	11.5	$2.2 \cdot 10^{15}$		12	11	35	13
180	0.22	11.0	$3.6 \cdot 10^{15}$		12	n.o.$^{(e)}$		
190	0.19	9.5	$1.8 \cdot 10^{15}$		6	n.o.		
200	0.14	7.0	$1.3 \cdot 10^{15}$					
200$^{(f)}$	0.17	8.5	$1.4 \cdot 10^{15}$		89	7		
200	0.15	7.5	$2.1 \cdot 10^{15}$		90	6		
200	0.15	7.5	$2.2 \cdot 10^{15}$		40	n.o.		
210	0.14	7.0	$1.0 \cdot 10^{15}$		88	16		
210	0.10	5.0	$2.7 \cdot 10^{15}$		90	15		
210 $^{(f)}$	0.13	6.5	$4.2 \cdot 10^{15}$		85	9		
180$^{(f)}$	0.24	12.0		$2.8 \cdot 10^{14}$	n.o.	n.o		
190	0.21	10.1		$4.2 \cdot 10^{14}$	n.o.	n.o		
195	0.15	7.7		$4.1 \cdot 10^{14}$	n.o.	n.o		
200	0.14	7.0		$3.2 \cdot 10^{14}$	n.o.	n.o		
200	0.14	7.2		$3.6 \cdot 10^{14}$	n.o.	n.o		
208	0.12	5.9		$2.3 \cdot 10^{14}$	n.o.	n.o		
210	0.08	3.8		$5.4 \cdot 10^{14}$	50	25		
210	0.11	5.3		$7.8 \cdot 10^{14}$	42	21		
				b) Condensed (C)				
180	0.34	17.0	$6.7 \cdot 10^{14}$		5	20	58	34
180$^{(f)}$	0.35	17.5	$1.3 \cdot 10^{15}$		2	21	28	28
180	0.34	17.0	$3.4 \cdot 10^{15}$		9	17	64	26
190	0.30	15.0	$7.0 \cdot 10^{14}$		23	20	45	28
190	0.29	14.5	$1.3 \cdot 10^{15}$		14	19	54	30
200	0.21	10.5	$1.5 \cdot 10^{15}$		71	15	4	n.o.
200	0.25	12.5	$2.0 \cdot 10^{15}$		67	15	6	n.o.
210	0.14	7.0	$1.4 \cdot 10^{15}$		84	11	n.o.	n.o.
211	0.15	7.5	$3.0 \cdot 10^{15}$		100	n.o.	n.o.	n.o.
180	0.38	19.1		$3.4 \cdot 10^{14}$	n.o.	n.o.		
180	0.28	14.0		$3.6 \cdot 10^{14}$	n.o.	n.o.		
180	0.34	16.8		$2.5 \cdot 10^{15}$	9	n.o.		
190	0.27	13.4		$6.6 \cdot 10^{14}$	n.o.	4		
190	0.27	13.5		$7.0 \cdot 10^{14}$	4	20		
190	0.21	10.4		$2.0 \cdot 10^{15}$	12	n.o.		
200$^{(f)}$	0.22	11.0		$3.0 \cdot 10^{14}$	30	14		
200	0.18	9.0		$1.8 \cdot 10^{15}$	16	20		
210	0.16	7.9		$7.3 \cdot 10^{14}$	53	30		
210	0.16	7.9		$1.2 \cdot 10^{15}$	73	35		
				c) Crystal (SC)				
180	0.30	15.0	$1.2 \cdot 10^{15}$		22	4	31	10
180	0.39	19.5	$1.8 \cdot 10^{15}$		23	9		

continued

T [K]	γ_0	k_{uni} [s^{-1}]	Flow(a) [molecule/s]	Dose(b) [molecules]	η_{HOBr} (c) [%]	η_{Br_2O} (c) [%]	η_{HOBr} (d) [%]	η_{Br_2O} (d) [%]
185	0.22	11.0	$1.6 \cdot 10^{15}$		26	13		
190	0.14	7.0	$1.0 \cdot 10^{15}$		37	10		
190(f)	0.15	7.5	$1.5 \cdot 10^{15}$		61	29		
195	0.10	5.0	$1.4 \cdot 10^{15}$		76	15		
200	0.07	3.5	$1.7 \cdot 10^{15}$		118	14		
205	0.04	2.0	$1.3 \cdot 10^{15}$		78	12		
210	0.022	1.1	$1.2 \cdot 10^{15}$		106	10		
210	0.025	1.3	$1.4 \cdot 10^{15}$		94	1		

(a) Steady–state experiments. (b) Pulsed–valve experiments.

(c) HOBr and Br_2O yields during uptake experiments.

(d) HOBr and Br_2O yields during thermal desorption experiments (TDE).

(e) n.o. = not observed.

(f) Experiments performed in the 8 mm escape orifice reactor.

Table E.4: Results of the interaction of $BrONO_2$ on a) Bulk (B) and b) Condensed (C) ice doped with HBr.

T	Flow	Dose	k_{esc}	k_{uni}	γ	ProductYields[(a)]			HBr(c)[(b)]	$BrONO_{2(c)}$ [(c)]	Br_2(p) [(a)]	HOBr (p)[(a)]	Br_2O(p) [(a)]	Br_2(d) [(d)]	HBr(d) [(d)]
[K]	[molecule/s]	[molecules]	[s^{-1}]	[s^{-1}]		Br_2	HOBr	Br_2O	[molecules]	[molecules]	[molecules]	[molecules]	[molecules]	[molecules]	[molecules]
a) Bulk ice (B)															
180	6,8E+14		2,9	14,2	0,28	31%	2%	< 1%	1,8E+18	9,4E+16	2,9E+16	2,2E+15	8,5E+14	6,6E+16	n.o.
180	1,1E+15		2,6	14,5	0,29	50%	5%	n.o.	1,4E+18	2,8E+17	1,4E+17	1,5E+16	n.o.	9,1E+16	2,6E+16
180	1,1E+15		2,7	14,1	0,28	63%	9%	3%	9,1E+17	3,5E+17	2,2E+17	3,0E+16	9,0E+15		
180	2,2E+15		2,2	16,5	0,33	23%	2%	1%	4,7E+18	7,2E+17	1,7E+17	1,4E+16	6,0E+15		
180	2,2E+15		2,3	18,0	0,36	35%	3%	2%	2,6E+18	1,1E+18	3,7E+17	3,3E+16	2,0E+16	2,1E+17	1,3E+17
190	1,8E+15		2,2	16,4	0,33	43%	8%	2%	1,1E+18	2,4E+17	1,0E+17	1,8E+16	4,0E+15	1,2E+17	6,4E+15
190	1,9E+15		2,3	12,1	0,24	82%	10%	3%	1,4E+18	2,8E+17	2,3E+17	2,7E+16	8,5E+15	1,3E+16	6,1E+15
200	3,3E+14		2,3	10,1	0,20	115%	n.o.	n.o.	4,5E+18	1,3E+17	1,5E+17	n.o.	uptake	2,4E+16	1,2E+17
200	1,1E+15		2,2	11,6	0,23	72%	43%	10%	1,2E+18	3,3E+17	2,4E+17	1,4E+17	3,3E+16		
210	1,5E+15		2,3	7,5	0,15	39%	29%	3%	1,1E+18	5,1E+17	2,0E+17	1,5E+17	1,4E+16	n.o.	n.o.
b) Condensed ice (C)															
180	9,1E+14		2,5	15,3	0,31	40%	5%	29%	8,6E+17	2,6E+17	1,1E+17	1,3E+16	7,6E+16	4,5E+17	8,0E+16
180	3,0E+15		2,4	14,8	0,30										
190	2,2E+15		2,5	13,7	0,27	48%	7%	10%	9,8E+17	3,7E+17	1,8E+17	2,7E+16	3,7E+16	3,5E+17	8,9E+16
190	1,9E+15		2,5	13,0	0,26	11%	7%	15%	1,0E+18	1,3E+18	1,4E+17	9,3E+16	1,9E+17	9,8E+16	1,0E+17
200	1,1E+15		2,4	11,9	0,24	28%	31%	54%	1,0E+18	3,9E+17	1,1E+17	1,2E+17	2,1E+17	3,0E+16	1,6E+17
200	2,1E+15		2,2	13,9	0,28	71%	15%	10%	9,9E+17	2,5E+17	1,8E+17	3,8E+16	2,5E+16	1,7E+17	1,9E+17
210	9,3E+14		2,3	9,0	0,18										
180		7,4E+14	2,8	15,0	0,30	n.o.	n.o.	n.o.	5,5E+17	6,4E+14					
180		1,7E+15	2,8	13,7	0,27	17%	n.o.	n.o.	1,1E+18	1,3E+15	2,3E+14				
200		6,8E+14	3,1	11,9	0,24	n.o.	n.o.	n.o.	1,2E+18	5,0E+14					
200		1,2E+15	2,8	10,8	0,22	n.o.	n.o.	n.o.	1,2E+18	1,0E+15					
200		1,9E+15	2,9	9,5	0,19	29%	n.o.	n.o.	1,4E+18	1,5E+15	4,4E+14				

(a) Observed during uptake. (b) HBr condensed prior to experiment. (c) $BrONO_2$ condensed during uptake experiment. (d) Observed during thermal desorption experiment.

References

Abbatt, J. P. D.; Molina, M. J. *Geophys. Res. Lett.* **1992**, *19*, 461.

Abbatt, J. P. D. *Geophys. Res. Lett.* **1994**, *21*, 665.

Abbatt, J. P. D. *Geophys. Res. Lett.* **1997**, *24*, 1479.

Abbatt, J. P. D.; Waschewsky, G. C. G. *J. Phys. Chem* **1998**, *102*, 3719.

Adamson, A. W. *Physical Chemistry of Surfaces*, 3rd edn.; John Wiley & Sons, New-York , **1976**.

Aguzzi, A.; Rossi M. J. *Phys. Chem. Chem. Phys.* **1999**, *1*, 4337.

Al-Abadleh, H. A.; Grassian, V. H. *J. Phys.Chem.* **2000**, *104*, 11926.

Alcala-Jornod, C.; van den Bergh, H.; Rossi, M. J. *Phys. Chem. Chem. Phys.* **2000**, *2*, 5584.

Allan, B. J.; McFiggans, G.; Plane, J. M. C.; Coe, H. *J. Geophys. Res.* **2000**, *105*, 14363.

Anderson, J. G.; Brune, W. H.; Proffitt, M. H. *J. Geophys. Res.* **1989a**, *94*, 11465.

Anderson, J. G.; Brune, W. H.; Lloyd, S. A.; Toohey, D. W.; Sander, S. P.; Starr, W. L.; Loewenstein, M.; Podolske, J. R. *J. Geophys. Res.* **1989b**, *94*, 11480.

Anderson, J. G., Toohey, D. W.; Brune, W. H. *Science* **1991**, *251*, 39.

Allanic, A.; Oppliger, R.; Rossi M. J. *J. Geophys. Res.* **1997**, *102*, 23529.

Allanic, A.; Oppliger, R.; van den Bergh, H.; Rossi M. J. *Z. Phys. Chem.* **2000**, *214*, 1479.

Allanic, A.; Rossi M. J. *J. Geophys. Res.* **2000b**, *104*, 18689.

Allen, H. C.; Laux, J. M.; Vogt, R.; Finlayson-Pitts, B. J.; Hemminger, J. C. *J. Phys.Chem.* **1996**, *100*, 6371.

Atmospheric Particles Chap. 9, Harrison, R. M.; van Grieken, R., Eds.; John Wiley & Sons, **1998**, Vol. 5.

Barnaal, D.; Slotfeldt-Ellingsen, D. *J. Phys. Chem.*, **1983**, *87*, 4321.

Barnes, I.; Bastian, V.; Becker, K. H.; Overath, R.; Tong, Z. *Int. J. Chem. Kinet.* **1989**, *21*, 499.

Barrie, L. A.; Bottenheim, J. W.; Schnell, R. C.; Crutzen, P. J.; Rasmussen, R. A. *Nature* **1988**, *334*, 138.

Behnke, W; Krüger,H.-U.; Scheer, V.; Zetzsch, C. *J. Aerosol Sci.*, **1992**, *23*, 933.

Behnke, W; Scheer, V.; Zetzsch, C. *J. Aerosol Sci.*, **1993**, *24*, 115.

Beichert, P.; Finnlayson-Pitts, B. J. *J. Phys. Chem.*, **1996**, *98*, 15218.

Biermann U. M.; Crowley, J. N.; Huthwelker, T.; Moortgat, G. K.; Crutzen P. J.; Peter, T. *Geophys. Res. Lett.* **1998**, *25*, 3939.

Blacet, F. E. *Ind. Eng. Chem.* **1952**, *44*, 1339.

Blanchard, D. C.; Cipriano, R. J. *Nature* **1987**, *330*, 526.

Bottenheim, J. W.; Barrie, L. A.; Atlas, E.; Heidt, L. E.; Niki, H.; Rasmussen, R. A.; Shepson, P. B. *J. Geophys. Res.* **1990**, *95*, 18555.

Boudries, H.; Bottenheim, J. W. *Geophys. Res. Lett.* **2000**, *27*, 517.

Caloz, F.; Fenter, F. F.; Rossi, M. J. *J. Phys. Chem* **1996**, *100*, 7494.

Caloz, F.; Fenter F. F.; Tabor K.; Rossi M. J. *Rev. Sci. Instrum.* **1997**, *68*, 3172.

Caloz, F.; Seisel, S.; Fenter, F. F.; Rossi, M. J. *J. Phys. Chem* **1998**, *102*, 7470.

Carlotti, M.; Ade, P. A. R.; Carli, B.; Ciarpallini, P.; Cortesi, U.; Griffin, M. J.; Lepri, G.; Mencaraglia, F.; Murray, A. G.; Nolt, I. G.; Park, J. H.; Radostitz, J. V. *Geophys. Res. Lett.* **1995**, *22*, 3207.

Carslaw, K. S.; Luo, B. P.; Clegg, S. L.; Brimblecombe, P; Crutzen, P. J. *Geophys. Res. Lett.* **1994**, *21*, 2479.

Chaix, L.; van den Bergh, H.; Rossi, M. J. *J. Phys. Chem.* **1998**, *102*, 10300.

Chaix, L.; Allanic, A.; Rossi, M. J. *J. Phys. Chem.* **2000**, *104*, 7268.

Chu, L.; Chu, L. T. *J. Phys. Chem.* **1999**, *103*, 8640.

Chu, L. T.; Chu, L. *J. Phys. Chem.* **1999b**, *103*, 384.

Crutzen, P. J. *J. Geophys. Res.* **1971**, *76*, 7311.

Crutzen, P. J. *Faraday Discuss.* **1995**, *100*, 1.

Dancer, W. *Liebigs Ann. Chem.* **1893**, *125*, 237.

Davies, J.; Cox, R. A. *J. Phys.Chem.* **1998**, *102*, 7631.

De Haan, D. O.; Finlayson-Pitts, B. J. *J. Phys.Chem.* **1997**, *101*, 9993.

Dentener, F. J.; Carmichael, G. R.; Zhang, Y.; Lelieveld, J.; Crutzen, P. J. *J. Geophys. Res.* **1996**, *101*, 22869.

Dessler, A. E.; Wu, J.; Santee, M. L.; Schoeberl, M. R. *J. Geophys. Res.* **1999**, *104*, 13993.

Dianxun, W.; Peng, J. *J. Phys. Chem.* **1996**, *100*, 4382.

Diehl, K; Mitra, S. K.; Pruppacher, H. R. *Atmospheric Research* **1998**, *47-48*, 235.

Evans, W. F. J.; McElroy, C. T.; Galbally, I. E. *Geophys. Res. Lett.* **1985**, *12*, 825.

Fan, S.-M.; Jacob, D. J. *Nature* **1992**, *359*, 522.

Farman, J. C.; Gardiner, B. G.; Shanklin, J. D. *Nature* **1985**, *315*, 207.

Fenter, F. F.; Caloz, F.; Rossi, M. J. *J. Phys. Chem.* **1994**, *98*, 9801.

Fenter, F. F.; Caloz, F.; Rossi, M. J. *J. Phys. Chem.*, **1996**, *100*, 1008.

Fernandez, M.A.; Hynes, R.; Cox, R. A., manuscript in preparation, **2001**.

Finlayson-Pitts, B. J.; Pitts, J. N. *Atmospheric Chemistry: Fundamentals and Experimental Techniques*; John Wiley & Sons, New-York, **1986**.

Finlayson-Pitts, B. J.; Johnson, S. N. *Atmos. Environ.* **1988**, *22*, 1107.

Finlayson-Pitts, B. J.; Ezell, M. J.; Pitts, J. N. *Nature* **1989**, *337*, 241.

Fluckiger, B; Thielman, A.; Gutzwiller, L.; Rossi, M. J. *Ber. Bunsenges. Phys. Chem.* **1998**, *102*, 915.

Fluckiger, B; Chaix, L.; Rossi, M. J. *J. Phys. Chem.* **2000**, *104*, 11739.

Foster, K. L.; Plastridge, R. A.; Bottenheim, J. W.; Shepson, P. B.; Finlayson-Pitts, B. J.; Spicer, C. W. *Science* **2001**, *291*, 471.

Gane, M. P. PhD Thesis, University of East Anglia **2000**.

Golden, D. M.; Spokes, G. N.; Benson, S. W. *Angew. Chem* **1973**, *14*, 602.

Gong, S. L.; Barrie, L. A.; Propero, J. M.; Savoie, D. L.; Ayers, G. P.; Blanchet, J.–P.; Spacek, L. *J. Geophys. Res.* **1997**, *102*, 3819.

Grædel, T. E.; Keene, W. C. *Global Biogeochemical Cycles* **1995**, *9*, 47.

Hampston, J. *"Chemical Instability of the Stratosphere"* **1964**, presented at the International Assocation of Meteorological and Atmospheric Physics (IUGG), Leningrad.

Hanson, D. R. *Geophys. Res. Lett.* **1992**, *20*, 2063.

Hanson, D. R. *Geophys. Res. Lett.* **1997**, *24*, 1087.

Hanson, D. R. *J. Phys. Chem.* **1998**, *102*, 4794.

Hanson, D. R.; Mauersberger, K. *Geophys. Res. Lett.* **1988**, *15*, 855.

Hanson, D. R.; Mauersberger, K. *J. Phys. Chem.* **1990**, *94*, 4700.

Hanson, D. R.; Ravishankara, A. R. in *The Tropospheric Chemistry of Ozone in the Polar Regions*, Niki, H and Becker, K. H. (Eds), *NATO ASI Ser.* **1993**, *17*, 281.

Hanson, D. R.; Ravishankara, A. R. *J. Phys. Chem.* **1994**, *98*, 5728.

Hanson, D. R.; Ravishankara, A. R. *Geophys. Res. Lett.* **1995**, *22*, 385.

Harrison, R. M.; van Grieken, R. (Eds) *Atmospheric Particles*, John Wiley and Sons, New York, **1998**, vol. 5.

Harwood, M. H.; Burkholder, J. B.; Ravishankara, A. R. *J. Phys. Chem.* **1998**, *102*, 1309.

Hausmann, M.; Platt, U. *J. Geophys. Res.* **1994**, *99*, 25399.

Hebestreit, K.; Stutz, J.; Rosen, D.; Matveiv, V.; Peleg, M.; Luria, M.; Platt, U. *Science* **1999**, *283*, 55.

Herring, J. A.; Ferek, R. J.; Hobbs, P. V. *J. Geophys. Res.* **1996**, *101*, 14451.

Hindmarsh, A. C. ODEPACK, A Systemized Collection of ODE Solver's *Scientific Computing*, Ed. Stephen R. S. *et al.*, IMACS *Trans. On Scientific Computation* (North-Holland, Amsterdam), **1983**, *1*, 55.

Hobbs, P. V. *Ice Physics*, Clarendon Press: Oxford **1974**.

Horn, A. B.; Sully, J. J. *Chem. Soc., Faraday Trans.* **1997**, *16*, 2741.

Hudson, P. K.; Foster, K. L.; Tolbert, M. A.; George, S. M.; Carlo, S. R.; Grassian, V. H. *J. Phys. Chem.* **2001**, *105*, 694.

Impey, G. A.; Shepson, P. B.; Hastie, D. R.; Barrie, L. A.; Anlauf, K. G. *J. Geophys. Res.* **1997**, *102*, 16005.

Impey, G. A.; Mihele, C. M.; Anlauf, K. G.; Barrie, L. A.; Hastie, D. R.; Shepson, P. B. *J. Atmos. Chem.* **1999**, *34*, 21.

Johnson, D. G.; Traub, W. A. Chance, K. V.; Jucks, K. W. *Geophys. Res. Lett.* **1995**, *22*, 1373.

Johnston, H. S.; Chang, S.; Whitten, G. *J. Phys. Chem.* **1974**, *78*, 1.

Jones, A. E.; Shanklin, J. D. *Nature*, **1995**, *376*, 409.

Kalberer, M.; Ammann, M.; Arens, F.; Gaggeler, H. W., Baltensperger, U. *J. Geophys. Res.* **1999**, *104*, 13832.

Kaye, J. A.; Penkett, S. A.; Ormund, F. M. (*Eds*), *Reports on Cconcentrations, Lifetimes, and Trends of CFC's, Halons, and Related Species* **1994**, NASA Refence Publication No. 1339.

Kee, R. J.; Rupley, F. M.; Miller, J. A. *CHEMKIN: A Fortran Chemical Kinetics Package for the Analysis of Gas-Phase Chemical Kinetics* march **1991**, Sandia National Laboratories Report.

Keppler, F.; Eiden, R.; Nieden, V.; Pracht, J.; Schüler, H. F. *Nature* **2000**, *99*, 25399.

Keyser, L. F.; Moore, S. B.; Leu, M.-T.*J. Phys. Chem.* **1991**, *95*, 5496.

Keyser, L. F.; Leu, M.-T.; Moore, S. B. *J. Phys. Chem.* **1993**, *97*, 2800.

Khalil, M. A. K.; Rasmussen, R. A.; Gunawerdena, R. *J. Geophys. Res.* **1993**, *98*, 2887.

Knauth, H. D.; Alberti, H.; Clausen, H. *J. Phys. Chem.*, **1979**, *83*, 1604.

Knight, C. A. *Journal of Glaciology* **1996**, *42*, 585.

Koch, T. G.; Rossi, M. J. *J. Phys. Chem.* **1998**, *102*, 9193.

Kondo, Y.; Irie, H.; Koike, M.; Bodeker, G. E. *Geophys. Res. Lett.* **2000**, *27*, 337.

Krishnan, P. N.; Salomon, R. E. *J. Phys. Chem.* **1969**, *73*, 2680.

Laaksonen, A.; Hienola, J.; Kulmala, M.; Arnold, F. *Geophys. Res. Lett.* **1997**, *24*, 3009.

Lary, D. J. *J. Geophys. Res.* **1996**, *101*, 1505.

Lary, D. J.; Shallcross, D. E.; Toumi, R. *J. Geophys. Res.* **1999**, *104*, 15929.

LeBel, P. J.; Huebert, B. J.; Schiff, H. I.; Vay, S. A.; Vanbramer, S. E.; Hastie, D. R. *J. Geophys. Res.* **1990**, *95*, 10199.

Lee-Taylor, J. M.; Holland, E. A. *J. Geophys. Res.* **2000**, *105*, 8857.

Lelieveld, J.; Bregman, B.; Arnold, F.; Bürger, V.; Crutzen, P. J.; Fischer, H.; Waibel, A.; Siegmund, P.; van Velthoven, P. F. J. *Geophys. Res. Lett.* **1997**, *24*, 603.

Leu, M. T.; Moore, S. B.; Keyser, L. F. *J. Phys. Chem.* **1991**, *95*, 7763.

Levy, H. *Science* **1971**, *173*, 141.

Livingston, F. E.; George, S. M. *J. Phys. Chem. A* **1998**, *102*, 10280.

Livingston, F. E.; Smith, J. A.; George, S. M. *Anal. Chem.* **2000**, *72*, 5590.

Lovelock, J. E. *Nature* **1974**, *252*, 292.

McConnell, J. C.; Henderson, G. S.; Barrie, L.; Bottenheim, J.; Niki, H.; Langford, C. H.; Templeton, E. M. J. *Nature* **1992**, *355*, 150.

McElroy, M. B.; Salawitch, R. J.; Wofsy, S. C. *Geophys. Res. Lett.* **1986**, *13*, 1296.

McElroy, C. T.; McLinden, C. A.; McConnell, J. C. *Nature* **1999**, *397*, 338.

Miller, M. S.; Friedlander, S. K.; Hidy, G. M. *J. Coll. Int. Sc.* **1972**, *39*, 165.

Mochida, M.; Akimoto, H.; van den Bergh, H.; Rossi, M. J. *J. Phys. Chem.* **1998**, *102*, 4819.

Molina, M. J.; Rowland, F. S. *Nature* **1974**, *249*, 810.

Molina, M. J.; Tso, T.; Molina, L. T.; Wang, C. Y. *Science* **1987**, *238*, 1253.

Mozurkewich, M.; Calvert, J. G. *J. Geophys. Res.* **1988**, *93*, 15889.

Mozurkewich, M. *J. Geophys. Res.* **1995**, *100*, 14199.

Müller, R.; Peter, T.; Crutzen, P. J.; Oelhaf, H.; Adrian, G. P.; Von Clarmann, T.; Wegner, A.; Schmidt, U.; Lary, D. *Geophys. Res. Lett.* **1994**, *21*, 1427.

Nolt, I. G.; Ade, P. A. R.; Alboni, F.; Carli, B.; Carlotti, M.; Cortesi, U.; Epifani, M.; Griffin, M. J.; Hamilton, P. A.; Lee, C.; Lepri, G.; Mencaraglia, F.; Murray, A. G.; Park, J. H.; Park, K.; Raspollini, P.; Ridolfi, M.; Vanek, M. D. *Geophys. Res. Lett.* **1997**, *24*, 281.

O'Dowd, D. C.; Smith, M. H. *J. Geophys. Res.* **1993**, *98*, 1137.

Oppliger, R.; Allanic, A.; Rossi, M. J. *J. Phys. Chem.* **1997**, *101*, 1903.

Orlando, J. J.; Burkholder, J. B. *J. Phys. Chem.* **1995**, *99*, 1143.

Orlando, J. J.; Tyndall, G. S., *J. Phys. Chem.* **1996**, *100*, 19398.

Oum, K. W.; Lakin, M. J.; DeHaan, D. O.; Brauers, T.; Finlayson-Pitts, B. J. *Science* **1998a**, *279*, 74.

Oum, K. W.; Lakin, M. J.; Finlayson-Pitts, B. J. *Geophys. Res. Lett.* **1998b**, *25*, 3923.

Pandis, S. N.; Wexler, A. S.; Seinfeld, J. H. *J. Phys. Chem.* **1995**, *99*, 9646.

Percival, C. J.; Mössinger, J. C.; Cox, R. A. *Phys. Chem. Chem. Phys.* **1999**, *1*, 4565.

Peter, T.; Müller, R.; Crutzen, P. J.; Deshler, T. *Geophys. Res. Lett.* **1994**, *21*, 1331.

Platt, U.; Lehrer, E. *ARCTOC, Final Report to the European Union* **1995**.

Prather, M. J.; Watson, R. T. *Nature* **1990**, *344*, 729.

Rhew, R. C.; Miller, B. R.; Weiss, R. F. *Nature* **2000**, *403*, 292.

Reihs, C. M.; Golden, D. M.; Tolbert, M. A. *J. Geophys. Res.* **1990**, *95*, 16545.

Salawitch, R.J.; Wofsy, S. C.; Gottlieb, E. W.; Lait, L.R.; Newman, P. A.; Schoeberl, M. R.; Loewenstein, M.; Podolske, J. R.; Strahan, S. E.; Proffitt, M. H.; Webster, C. R.; May, R. D.; Fahey, D. W.; Baumgardner, D.; Dye, J. E.; Wilson, J. C.; Kelly, K. K.; Elkins, J. W.; Chan, K. R.; Anderson, J. G. *Science* **1993**, *261*, 1146.

Sander, R.; Crutzen, P. J. *J. Geophys. Res.* **1996**, *101*, 9121.

Santschi, C. *Personal Communication* **1999**.

Schneider, J.; Arnold, F.; Bürger, V.; Droste-Franke, B.; Grimm, F.; Kirchner, G.; Klemm, M.; Stilp, T.; Wohlfrom, K.-H., Siegmund, P.; van Velthoven, P. F. J. *J. Geophys. Res.* **1998**, *103*, 25337.

Schreiner, J.; Voigt C.; Kohlmann, A.; Arnold, F.; Mauersberger, K.; Larsen, N. *Science* **1999**, *283*, 968.

Seisel, S.; Rossi, M. J. *Ber. Bunsenges. Phys. Chem.* **1997**, *101*, 943.

Seisel, S.; Flückiger, B.; Rossi, M. J. *Ber. Bunsenges. Phys. Chem.* **1998**, *102*, 811.

Seisel, S.; Flückiger, B.; Caloz, F.; Rossi, M. J. *Phys. Chem. Chem. Phys.* **1999**, *1*, 2257.

Shen, T.–L.; Wooldridge, P. J.; Molina, M. J.; in *Composition, Chemistry and Climate of the Atmosphere*, ed. by H. B. Singh, van Nostrand Reinhold, 1995.

Singh, H. B.; Chen, Y.; Gregory, G. L.; Sachse, G. W.; Talbot, R.; Blake, D. R.; Kondo, Y.; Bradshaw, J. D.; Heikes, B.; Thornton, D *Geophys. Res. Lett.* **1997**, *24*, 127.

Solomon, S.; Garcia, R. R.; Rowland, F. S.; Wuebbles, D. J. *Nature* **1986**, *321*, 755.

Solomon, S. *Rev. Geophys.* **1988**, *26*, 131.

Spicer, C. W.; Chapman, E. G.; Finlayson-Pitts, B. J.; Plastridge, R. A.; Hubbe, J. M.; Fast, J. D.; Berkowitz, C. M. *Nature* **1998**, *394*, 353.

Stadler, D.; Rossi, M. J. *Phys. Chem. Chem. Phys.* **2000**, *2*, 5420.

Stull, D. R.; Prophet, C. B. *JANAF Thermochemical Tables, Publication NSRDS-NBS 37*, **1971**, National Bureau of Standards.

Stutz, J.; Hebestreit, K.; Alicke, B.; Platt, U. *J. Atmos. Chem.* **1999**, *34*, 65.

Tabazadeh, A.; Turco, R. P.; Drdla, P.; Jacobson, M. Z.; Toon, O. B. *Geophys. Res. Lett.* **1994**, *21*, 1619.

Tabor, K.; Gutzwiller, L.; Rossi, M. J. *J. Phys.Chem.* **1994**, *98*, 6172.

Tevault, D. E.; Walker, N.; Smardzewski, R. R.; Fox, W. B. *J. Phys. Chem.*, **1978**, *82* 2733.

Thibert, E.; Dominé, F. *J. Phys. Chem. B*, **1997**, *101* 3554.

Thibert, E.; Dominé, F. *J. Phys. Chem. B*, **1998**, *102* 4432.

Thompson, A. M. *Science* **1992**, *256*, 1157.

Tie, X. X.; Brasseur, G. *Geophys. Res. Lett.* **1996**, *23*, 2505.

Timonen, R. S.; Chu, L. T.; Leu, M.-T.; Keyser, L. F. *J. Phys. Chem.*, **1994**, *98*, 9509.

Tolbert, M. A.; Rossi, M. J.; Golden, D. A. *Geophys. Res. Lett.* **1988**, *15*, 847.

Turco, R.; Toon, O. B.; Hamill, P. *J. Geophys. Res.* **1989**, *94*, 16493.

Van Doren, J. M.; Watson, L. R.; Davidovits, P.; Worsnop, D. R.; Zahniser, M. S.; Kolb, C. E. *J. Phys. Chem.* **1991**, *95*, 1684.

Vogt, R.; Crutzen, P. J.; Sander, R. *Nature* **1996**, *383*, 327.

Wagner, T.; Platt, U. *Nature* **1998**, *395*, 486.

Wallington, T. J.; Skewes, L.; Siegl, W. O.; Japar, S. M. *Int. J. Chem. Kinet.* **1989**, *21*, 1069.

Warshawsky, M. S.; Zondlo, M. A.; Tolbert, M. A. *Geophys. Res. Lett.* **1999**, *26*, 823.

Wayne, R. P.; Poulet, G.; Biggs, P.; Burrows, J. P.; Cox, R. A.; Crutzen, P. J.; Hayman, G. D.; Jenkin, M. E.; Le Bras, G.; Moortgat, G. K.; Platt, U.; Schindler, R. N. *Atmos. Environ.* **1995**, *29*, 2677.

Weis, D. D.; Ewing, G. E. *J. Phys.Chem.* **1999**, *103*, 4865.

Wennberg, P. O. *Nature* **1999**, *397*, 299.

Wilson, W. W.; Christe, K. O. *Inorg. Chem.*, **1987**, *26* 1573.

Wingenter, O. W.; Kubo, M. K.; Blake, N. J.; Smith, T. W.; Blake, D. R.; Rowland, F. S. *J. Geophys. Res.* **1999**, *101*, 4331.

WMO **1995**, *Scientific Assessment of Ozone Depletion, 1994*, Global Ozone Research and Monitoring Project Report No. 37, World Meteorological Organizationn, Geneva.

Wofsy, S. C.; Molina, M. J.; Salawitch, R. J.; Fox, L. E.; McElroy, M. B. *J. Geophys. Res.* **1988**, *93*, 2442.

Wofsy, S. C.; Salawitch, R. J.; Yatteau, J. H.; McElroy, M. B.; Gandrud, B. W.; Dye, J. E.; Baumgardner, D. *Geophys. Res. Lett.* **1990**, *17*, 449.

Wolff, E. W.; Mulvaney, R.; Oates, K. *Geophys. Res. Lett.* **1989**, *16*, 487.

Yokouchi, Y.; Noijiri, Y.; Barrie, L. A.; Toom-Sauntry, D.; Machida, T.; Inuzuka, Y.; Akimoto, H.; Li, H.-J.; Fujinuma, Y.; Aoki, S *Nature* **2000**, *403*, 295.

Zetzsch, C.; Behnke, W. *Ber. Bunsenges., Phys. Chem.* **1992**, *96*, 488.

Zhang, R.; Leu, M.-T.; Keyser, L. F. *Geophys. Res. Lett.* **1995**, *22*, 1493.

Zondlo, M. A.; Barone, S. B.; Tolbert, M. A. *Geophys. Res. Lett.* **1997**, *24*, 1391.

Zondlo, M. A.; Barone, S. B.; Tolbert, M. A. *J. Phys. Chem.* **1998**, *102*, 5735.

Curriculum vitae

Arnaud AGUZZI

Date of Birth:	May 27, 1970 in Belfort, France
Nationalities:	Swiss and French
Marital Status:	Married, 2 children

EDUCATION

June 2001	Ph.D. thesis ”Atmospheric Heterogeneous Reactions of Chlorine and Bromine Containing Molecules: A Laboratory Study“ under the supervision of Dr Michel J. Rossi.
1996–2001	Ph.D. student in the Laboratoire de Pollution Atmosphérique directed by Prof. Hubert van den Bergh, at the Swiss Federal Institute of Technology in Lausanne, Switzerland (EPFL).
1996	Physics Diploma in experimental physics: spectroscopy (absortion, UV and Raman spectra) of antibiotic molecules under the supervision of Prof. Majed Chergui.
1991–1996	Undergraduate studies of physics at the University of Lausanne (UNIL), Switzerland.
1989–1991	Undergraduate studies of physics at the Swiss Federal Institute of Technology in Zurich (ETHZ), Switzerland.
1989	High School at the Lycée Cantonal in Porrentruy, Switzerland.

LANGUAGES

French:	Mother tongue
English:	Good knowledge
German:	Good knowledge
Italian:	Spoken

PUBLICATIONS

1 Aguzzi, A; Rossi, M. J. The Kinetics of the Heterogeneous Reaction of $BrONO_2$ with Solid Alkali Halides at Ambient Temperature. A Comparison with the Interaction of $ClONO_2$ on NaCl and KBr, *Phys. Chem. Chem. Phys.* **1999**, *1*, 4337.

2 Aguzzi, A; Rossi, M. J. The Kinetics of the Uptake of HNO_3 on Ice, Solid H_2SO_4/H_2O and Solid Ternary Solutions of $H_2SO_4/HNO_3/H_2O$ in the Temperature Range 180–211 K. Accepted in *Phys. Chem. Chem. Phys.* **2001**.

3 Aguzzi, A; Rossi, M. J. The Heterogeneous Hydrolysis and Reaction of $BrONO_2$ and Br_2O on Ice and Ice Doped with HBr. (In preparation)

4 Aguzzi, A; Flückiger, B.; Rossi, M. J. The Nature of the Interface of the HCl/ice and HBr/ice Systems in the Temperature Range 190–205 K. (In preparation)

Remerciements

Je remercie le *Professeur Hubert van den Bergh* pour l'accueil qu'il m'a réservé dans son laboratoire et pour l'intérêt qu'il a porté à mon travail. Je le remercie également pour les nombreuses discussions autour de la préparation des cours qui ont contribué à me faire voir que tout n'est pas que chimie hétérogène.

Je tiens également à remercier le *Dr Michel Rossi*, mon directeur de thèse préféré. Il a su, grâce à son soutien permanent, ses nombreuses connaissances et sa disponibilité, me guider dans les voies parfois impénétrables de la chimie atmosphérique.

Je souhaite également remercier les membres du jury pour leur travail d'expertise et leurs commentaires vis–à–vis de mon travail. Je remercie à ce titre le *Dr Geert Moortgat*, le *Professeur Philippe Mirabel* et le *Dr Wolfgang Harbich*. L'intérêt qu'ils ont porté à ma thèse a été pour moi la meilleure des récompenses. Je remercie également le *Professeur François Golay* d'avoir accepter la présidence du jury.

Je remercie tous les membres du groupe "hétéro" du LPAS avec qui j'ai eu l'occasion de collaborer tout au long de ces années:

Un merci particulier à *François Caloz*, scientifique rigoureux. Il a été pour moi un exemple à suivre de Zürich à Lausanne. De plus, il m'a offert l'opportunité de rencontrer Michel Rossi.

Merci aussi à *Arnaud "Arnie" Allanic*, le plus irlandais des normands. Les nombreuses heures passées en sa compagnie au labo de chimie ont été fort agréables et très utiles pour les synthèses chimiques. Il a été un compagnon de voyage fort motivant, pouvant résoudre n'importe quels problèmes scientifiques ou autres.

Les mots me manquent pour remercier *Benoît Flückiger*; son aide a été inestimable lors de la rédaction. Ses conseils, les nombreuses discussions que nous avons eues ont grandement faciliter la rédaction des parties expérimentales sur la glace. 24 heures par jour, 7 jours par semaine, il a toujours été présent pour répondre à mes nombreuses questions au travers des nombreux SMS échangés. De plus, je ne le remercierai jamais assez de l'aide apportée la veille du dépôt de thèse jusque tard dans la nuit pour avoir reliés mes copies.

Je remercie chaleureusement *Carine Alcala-Jornod* de m'avoir supporté dans ”mon“ bureau. Mes fréquentes sautes d'humeur lors de la période de rédaction devaient être insupportables, mais elle a tout supporté. Merci aussi à *Christophe ”LaTeX“ Delval* pour son aide à ”débuger“ régulièrement mon compilateur. Une spécialité à faire avec LaTeX, *Christophe* a toujours la réponse. Sans toi, j'aurais peut-être dû écrire ma thèse avec *W...*, je n'ose même pas y penser... Pour la mise à jour de l'acquisition de la machine II, je remercie vivement *Christian Santschi*. Ses dons pour l'électronique, ainsi que sa maîtrise du SEM ont été pour moi d'un grand secours.

Sans oublier *Laurent Chaix, Frederick Fenter, Lukas Gutzwiller, Meike Klinger, Thomas Koch, Olivier Le Bihan, Michihiro Mochida, Raoul Oppliger, Sabine Seisel, Dominik Stadler, Bernadett Toth* et *Noremichi Takenaka*. Qu'ils soient toutes et tous remerciés pour la fantastique ambiance de travail durant ces années. Merci aussi à tous les autres membres du LPAS pour la bonne ambiance qui règne en permanence au sein du laboratoire.

Flavio Comino, notre mécanicien hors pair, que le monde entier nous envie, a été d'un grand secours. Un problème insurmontable, une pièce irréalisable pour moi, ont été simplifiés à l'extrême et sont devenus tout de suite réalisable pour lui. Et ça fonctionne... Un grand merci pour tout ce que tu as fait dans la joie et la bonne humeur. En plus d'être fonctionnelles, les pièces qu'il confectionne sont très esthétiques. Je remercie également *Alfred Neuenschwander*, LE souffleur de verre. Toujours disponible, toujours jovial, c'est un artiste du verre.

Un énorme merci à mes parents, ma soeur et ma belle–famille pour l'intérêt porté à mon travail ainsi que pour leur soutien permanent. Merci à mes amis *Rénald Schaub, Charles Currat, Olivier Kuffer, Claude et Laure Beyeler, Sonia Jimenez et Henry Montenegro*, dont le support m'a été indispensable.

Finalement, je remercie *Hortense*, mon épouse, *Evan* et *Hugo*, mes fils pour m'avoir soutenu tout au long de ces années de thèse et plus spécialement lors de la période de rédaction. Lors de cette période, ils ne m'ont que trop rarement vu; je leur exprime ma plus profonde gratitude d'avoir consenti à de tels sacrifices. Combien de fois j'ai entendu de la bouche d'Evan: ” Tu travailles trop, restes avec moi! “. Et combien de fois j'aurais voulu effectivement rester à la maison. Evan et Hugo, vos sourires permanents ont été pour moi un grand soutien moral quand je ne l'avais pas. Soyez–en remerciés!

Je tiens également à témoigner ma gratitude à toute personne qui de près ou de loin m'aurait apporté de l'aide et que je n'ai pas citée ici.